A Parallel Monte–Carlo Partial–Differential–Equation Procedure for the Analysis of Multicomponent Random Media

by

Manuel Ernani de Carvalho Cruz

B.S., Federal University of Rio de Janeiro (1984)
M.S., Federal University of Rio de Janeiro (1988)

Submitted to the Department of Mechanical Engineering
in partial fulfillment of the requirements for the degree of

DOCTOR OF PHILOSOPHY

at the

MASSACHUSETTS INSTITUTE OF TECHNOLOGY

May 1993

Author .....
Department of Mechanical Engineering
May 7, 1993

Certified by .....
Anthony T. Patera
Professor of Mechanical Engineering
Thesis Supervisor

Accepted by .....
Professor Ain A. Sonin
Chairman, Departmental Committee on Graduate Studies

A Parallel Monte–Carlo Partial–Differential–Equation Procedure for the Analysis of Multicomponent Random Media

by

Manuel Ernani de Carvalho Cruz

Submitted to the Department of Mechanical Engineering
on May 7, 1993, in partial fulfillment of the
requirements for the degree of
DOCTOR OF PHILOSOPHY

Abstract

Multicomponent random media play an important role in many natural and industrial processes. Analysis of such media is complicated by the presence of disparate length scales, and thus engineering focus has been on the understanding of macroscopic behavior. Many techniques have been proposed to analyze multicomponent problems: heuristic approaches can address a broad class of complex physical phenomena, but must introduce strong assumptions; bound methods can produce rigorous estimates, but typically provide only limited accuracy; various particle–expansion analytical and semi–analytical methods can efficiently treat many–particle systems, but are essentially restricted to linear media; first–principle computational studies (typically serial) can readily accomodate nonlinear media, but have been, to date, technologically confined to single–particle periodic cells, simple geometries, relatively few particles, or small sample sizes.

The broad goal of this research is to develop a new first–principle methodology for the study of macroscopic behavior of random multicomponent systems through the determination of effective properties and statistical correlation lengths. The methodology combines the relative strengths of earlier analytical and computational approaches, and is based upon a variational hierarchical decomposition procedure which recasts the original multiscale problem as a sequence of three scale–decoupled subproblems. The micro–, meso–, and macroscale subproblems are formulated, and a parallel nested Monte–Carlo partial–differential–equation procedure is used to solve the computationally intensive mesoscale subproblem. Specifically, the methodology includes: Monte-Carlo sampling, domain generation and partition based on Voronoi tesselation, Delaunay mesh generation, homogenization theory, finite element discretization, and parallel iterative solution techniques. Two problems of practical importance are addressed: heat conduction in random composites and creeping flow through random porous media, both in two space dimensions. The results are consis-

tent with previous analytical, semi-analytical, and some experimental investigations, and further extend the understanding of random media behavior.

Thesis Supervisor: Anthony Tyr Patera
Title: Professor of Mechanical Engineering

Dedication

I dedicate this work to my grandmother, Maria Bevilacqua Tedeschi, and to my parents, Cid de Carvalho Cruz and Therezinha Tedeschi de Carvalho Cruz.

Acknowledgements

First of all, I would like to thank Prof. Anthony Patera for his excellent and enthusiastic supervision. It has been an enjoyable learning experience working with him!

I also thank CNPq, the federal Brazilian agency for the development of science and technology, for financially supporting me for four years.

In the first two years of my stay, I enjoyed the help of Dr. Einar Rønquist, Prof. Paul Fischer, Dr. Lee Ho and Dr. Ed Bullister. Thank you very much.

Finally, I would like to thank the students and staff of the Fluid Mechanics Laboratory for providing me with a unique and exciting working environment.

This research effort was partially supported by DARPA under Grant N00014-91-J-1889, and by the ONR under Grants N00014-90-J-4124 and N00014-89-J-1610.

Contents

1 Introduction 9

1.1 Motivation 9

1.2 Review of Prior Work 12

1.2.1 Bound Methods 13

1.2.2 Phenomenological Methods 15

1.2.3 Analytical and Semi-Analytical Methods 16

1.2.4 First-Principle Computational Methods 20

1.2.5 Experimental Work 21

1.3 Objectives of This Thesis 22

2 Problem Formulations 25

2.1 Conduction in Unidirectional Fibrous Composites 25

2.1.1 Description of the Original Multiscale Problem 25

2.1.2 Macroscale 29

2.1.3 Mesoscale 30

2.1.4 Microscale 43

2.2 Creeping Flow Through Fibrous Porous Media 49

2.2.1 Description of the Original Multiscale Problem 49

2.2.2 Macroscale 50

2.2.3 Mesoscale 52

2.2.4 Microscale 57

3 Numerical Methods **60**

3.1 Overview 60

3.2 Partial–Differential–Equation Solution 62

3.2.1 Domain Generation and Partition 63

3.2.2 Mesh Generation 72

3.2.3 Discretization 77

3.2.4 Iterative Solution 87

3.2.5 Parallel Implementation 93

3.3 Monte–Carlo 97

3.3.1 Sampling from the Inclusion JPDF 98

3.3.2 Statistical Analysis 101

4 Results and Conclusions **104**

4.1 Results for Regular Arrays 105

4.1.1 Conduction 105

4.1.2 Creeping Flow 106

4.2 Results for Random Arrays: Conduction 107

4.3 Results for Random Arrays: Creeping Flow 117

4.4 Conclusions 122

4.5 Future Work 123

A Application of Homogenization Theory to the Conduction Problem 143

A.1 Definition 144

A.2 Overview 146

A.3 A Model Problem 148

A.3.1 Strong form 148

A.3.2 Method of asymptotic expansions 148

A.4 Application to the Conduction Problem 152

B Derivation of Equations (2.52) and (2.56) **157**

B.1 Derivation of equation (2.52) 157

B.2 Derivation of equation (2.56) 159

C Extension to Sedimentation **160**

D The ϵ-Smoothing Procedure **167**

E A Stopping Criterion for the Conjugate Gradient Iteration **176**

F Parallel Direct Stiffness Summation: Implementation Details **180**

G Random Number Generation **186**

G.1 Random Numbers 186

G.2 Linear Congruential Generators 187

G.3 Description of Tests 188

G.4 Results of Tests 191

Chapter 1

Introduction

1.1 Motivation

Many real systems of fundamental and practical importance are multicomponent in nature, in that several phases and/or dissimilar constituents are present. Typically, e.g. for two–component systems, one component is dispersed as particles or inclusions in a continuous matrix of the other component. When the spatial distribution of the dispersed phase is adequately described by a probability density function, the medium is said to be random. Representative multicomponent systems in mechanics are composite materials, porous media, suspensions of particles, fluidized beds, multiphase flows, and clouds of drops and bubbles. Such systems are generally dependent on numerous parameters, which makes their complete analysis an extremely difficult task. From an engineering perspective, the understanding of the macroscopic behavior of these systems generally suffices, and therefore the determination of effective (bulk) properties, e.g. conductivity, elastic modulus, permeability etc., is crucial for their description. These properties are determined from microstructural and microdynamical quantities pertaining to the system being investigated.

The aforementioned systems are present in a wide variety of processes, equipment, and machines occurring in the manufacturing, energy, aeronautical, and food industries, to name a few; also, porous media are encountered in biomedical [Curry & Michel (1980), Levick (1987)] and environmental [Davies (1973)] processes as well.

Important current problems involving such systems are design, optimization and evaluation of parts (e.g. thermal composites, filtration devices) and equipment (e.g. sedimentation tank, heat exchanger), as well as their proper operation, while minimizing material, manufacturing and replacement costs, and energy consumption. *In this thesis*, in particular, we will be dealing with two multicomponent random systems, namely, unidirectional fibrous composites and fibrous porous media (more details are given in Sections 1.3, 2.1 and 2.2). We will characterize heat conduction in the former, and creeping flow through the latter. It should be noted that by means of mathematical analogy, results obtained for the thermal properties of composites can be readily extended to electrical, magnetic, and diffusive properties.

Composite materials are attractive because of the wide range of properties they can attain, usually at a lower cost and a higher efficiency as compared to the individual components. In broad terms, they are classified into particulate or fibrous composites. The dispersed phase in particulate composites consists of small particles or voids either naturally present or inserted by design; examples of this type are consolidated rocks, artificial diamond–particle–filled composites, or even "solid" stainless steel (which in fact possesses a gas–filled pore space). Their analysis is essentially three–dimensional. Fibrous composites are typically man–made, and they consist of fibers, short or long, with specifically selected properties, embedded in or bonded to a matrix. Three–dimensional effects are present in short–fiber composites or laminates; unidirectional composites can be properly treated in two dimensions transversely to the fibers.

Unidirectional fibrous composites are highly anisotropic, since the longitudinal and transverse properties are very different; they usually have large values of conductivity (or resistivity) and elastic modulus in the fibers direction. The fibers can be, in general, randomly distributed; statistical homogeneity (and also transverse isotropy) is commonly assumed for analysis purposes. Unidirectional fibrous composites can be manufactured, for instance, with the process of pultrusion [Spencer (1983)], and often have fiber volume fractions above 50%. In the context of heat transfer, fibrous composites are used, mostly, as thermal insulators or conductors, either because they are

designed for that purpose, or due to the working conditions. For example, carbon–fiber reinforced ceramic matrices are used as refractory composites with improved mechanical characteristics (fracture toughness, impact resistance), which work at high temperatures; their conduction behavior is important for assessment of thermal losses. Graphite fibers are often used to enhance thermal conductivity, for instance in graphite–glass, and graphite–polymer composites. Overheating (or charge build–up) under certain working conditions due to the poor conductivity of the matrix can be avoided with the inclusion of such fibers. They are also used in metal matrix composites due to their high strength and low density. On the other hand, ceramic fibers in carbon matrices can be used to lower thermal conductivity, as in certain aeronautical applications. Some superconducting materials are made of aligned superconducting wires embedded in a copper matrix. It is not surprising that, today, composite design is aided by commercial software, which uses databases constructed from known mechanical and thermal properties of various individual and combined materials. For further description and applications of composites, the reader is referred to Mallick (1988), and Kelly (1987).

Similarly, porous media may comprise particles (i.e., granules) or fibers. In the first case, the pore space is very complex, and realistic models of its geometry are inevitably three–dimensional (of course, one may bypass this difficulty by introducing [non–universal] empirical factors). Examples of such media are naturally occurring unconsolidated sands and soil, and industrial granular beds. Fibrous porous media can also have complex geometry, as in fiber mats or biological macromolecular networks, but two–dimensional analysis, when not exact, often yields satisfactory results. Fibrous filters are an important example of this type; also, and interestingly enough, the mold–fibers set–up for the composite manufacturing technique of resin transfer molding is another example. Notice that sometimes it is convenient to interpret a porous medium as a composite material, where the (fluid–filled) pores are one component (as in oil–saturated sands). Good general references for porous media are Scheidegger (1974) and, more recently, Adler (1992).

Fibrous filters are used for the clean–up of fluids, like air and water, either for

control of environmental pollution, or for proper operation of fluid lines. Knowledge of their permeability is important to determine the power needed to drive the flow; also, in order to determine filtration efficiency and to estimate filter lifetime, one may need to model the flow at the pore scale, to be able to quantify particle capture. In the currently appealing resin transfer molding technique, a low viscosity polymeric resin is forced through a mold with pre-positioned fibers. Again, the permeability is a key parameter for the mold design, and in determining power requirements.

1.2 Review of Prior Work

The literature on the subjects of composites and porous media, due to their importance and "age" [Rayleigh (1892)], is indeed very vast. The purpose of this section is not to provide a comprehensive review, but rather to establish a background, and to touch upon, in a broad sense, some of the various methods previously developed to study problems of the type we are interested in. More complete treatments can be found in the review paper by Hashin (1983) on composites, and in the books by Happel & Brenner (1983), and Kim & Karrila (1991) on creeping flows.

In the review paper by Batchelor (1974), various results for different physical multicomponent systems are presented under a common theoretical framework, based on analogies in their mathematical formulation. The basic problem is to determine, in the constitutive equation for a statistically homogeneous medium, the coefficient of proportionality (in general, tensorial) between an average flux and an average imposed gradient. This coefficient is characteristic of the medium, and is defined to be its effective transport property for the conditions being considered. The difficulty of solving this problem in a particular situation depends on many factors, some of which are mentioned here, with increasing level of complexity from left to right:

- uniform and unimodal distribution of particles → nonuniform, multimodal;
- 2-D → 3-D geometries;
- regular → irregular shapes;

- ordered → random arrangement of inclusions;
- low → high volume fraction (i.e., interaction) of inclusions;
- linear → nonlinear transport phenomenon;
- prescribed (e.g. solid) → free (e.g. fluid) interfaces;
- noncolloidal → colloidal inclusions;
- steady (e.g. distribution input) → unsteady (e.g. distribution output) regime.

Several approaches have been devised to solve various multicomponent system problems, differing in generality, accuracy, efficiency, and ease of use. We review key contributions for the problems of conduction in composites and creeping flow through porous media. They are grouped here into bound, phenomenological, analytical and semi-analytical, and first-principle computational methods, and experimental work.

1.2.1 Bound Methods

Bound methods consist of determining upper and lower bounds for the effective properties, preferrably within a narrow gap. Although they provide rigorous results that are useful for checking more detailed calculations, they typically have limited accuracy, and sometimes are difficult to evaluate. Coarse bounds may be obtained, for example, with series and parallel resistance models, which are a simple way of weighing the component properties with their volume fractions. More accurate bounds are based on variational principles: the effective property is first shown to have an extremizing property, and trial functions are subsequently chosen to evaluate the bounds.

Conduction Using variational theorems applicable to magnetic permeability and electric and heat conductivities of macroscopically homogeneous isotropic materials, Hashin & Shtrikman (1962) developed explicit optimal (i.e., narrowest for the available information) bounds using minimal input about the underlying medium, namely,

the component properties and volume fractions. Later, Hashin (1970) obtained narrower bounds for the specific class of transversely isotropic fiber–reinforced materials. Improvement of these general bounds is necessary for materials with very different components, and (typically) requires statistical information about the spatial distribution of the phases. Beran (1965) improved Hashin & Shtrikman's bounds by introducing three–point correlation functions to partially describe the microstructure; Corson (1974) evaluated Beran's bounds using empirical techniques, and Milton (1981) expressed them as functions of two geometrical parameters. McPhedran & Milton (1981) showed convergence (as progressively more information is supplied about the medium's microstructure) of Milton's bounds for the cases of regular arrays of cylinders and spheres. Torquato & Lado (1988) calculated Milton's bounds for random arrays of cylinders, using three–point probability functions developed by Torquato & Stell (1982); their results are narrower than Hashin's, in certain cases, by a factor of almost 5. Notice that for the case of insulating (or infinitely conducting) inclusions, the above bounds are one–sided, in that the lower bound (or upper bound) is trivial, i.e., zero (or infinity). More recently, Chau & Chinh (1991) derived inequalities from classical variational principles, dependent on several coefficients characterizing the medium's microstructure. The coefficients were calculated exactly for a type of composite with ellipsoidal inclusions, and narrower bounds than Hashin & Shtrikman's were obtained.

Creeping Flow Three–point correlation functions were used by Prager (1961) and Weissberg & Prager (1970) to derive upper bounds for the permeability of porous media. However, they used heuristic arguments to simplify their ensemble averaging approach; Berryman & Milton (1985) used volume–averaging to derive rigorous bounds. More recently, Rubinstein & Torquato (1989), using ensemble–averaging and variational principles, derived rigorous upper and (new) lower bounds for the permeability of random porous media.

1.2.2 Phenomenological Methods

Phenomenological approaches can normally address a very broad class of complex problems, often yielding simple useful results and new physical insights; on the other hand, they must introduce strong, often debatable, assumptions. Therefore, they require *a posteriori* testing on known solutions; their range of validity is not easily established, and must rely on experimental verification.

Conduction Springer & Tsai (1967) obtained approximate expressions for the effective conductivity of square arrays of cylindrical and square inclusions; they used a thermal model in which the total heat flow across the composite, due to a constant temperature difference, was thought to occur through three independent, parallel paths. Acrivos & Chang (1986) calculated the effective conductivity of a random dispersion of equal spheres by treating the composite medium surrounding a test sphere as a continuum, but having a varying thermal conductivity proportional to the local inclusion volume density; the same technique was employed to a (dilute–regime) sedimentation problem. Acrivos & Shaqfeh (1988) considered longitudinal heat conduction in aligned slender rods composites, and obtained an expression for the effective conductivity to second–order in the particle concentration for the semidilute regime; they locally used an equation for the conditional ensemble average temperature that strictly applies to the macroscale only. More recently, Pitchumani & Yao (1991) attempted to correlate effective conductivity of unidirectional fibrous composites using local fractal techniques. Their results are within 10% of the exact values reported for ordered arrangements.

Creeping Flow In Kozeny's theory, as discussed in Scheidegger (1974), the porous medium is modelled as a bundle of straight channels parallel to the direction of flow, and with arbitrary cross–sections. The permeability is derived, from one–dimensional Navier–Stokes, to be proportional to the cube of the porosity, and to the square of the inverse specific surface; the inverse "constant" of proportionality (termed Kozeny's constant), for example, was found by Carman (1937), for fluid flow through granu-

lar beds, to be around 5. Kozeny's theory, apart from being non–universal, is not accurate for highly porous media. Cell models, see e.g. Happel (1959) and Happel & Brenner (1983), calculate the permeability by determining the force on one inclusion surrounded by fluid in a unit cell. which has the same volume fraction as in the whole medium. Based on symmetry arguments, no shear boundary conditions are used at the outer fluid envelope. As the concentration increases (i.e., as the porosity decreases), Happel's permeability results for flow perpendicular to cylinder arrays are such that a Kozeny's constant of about 5.3 is approached (for flow parallel to the cylinders, the constant is about 3.4).

Brinkman (1947), using an effective–medium approach, proposed a modification of the Stokes' momentum equation, adding to it a damping force term to account for the presence of the porous mass around one test (spherical) particle. He notes that, with some parameter choices, his results satisfactorily agree with previous experimental evidence in the low concentration regime. Spielman & Goren (1968) extended Brinkman's method to fibrous porous media (for various fiber orientation distributions), obtaining somewhat complex expressions involving Bessel functions. Their predictions for the permeability, more applicable in the low concentration range (less than 0.13), underestimate empirical data for fibrous filters (made of glass wool, cotton etc., as compiled by Davies (1952)), but not as much as cell model results do.

1.2.3 Analytical and Semi–Analytical Methods

Particle–expansion analytical and semi–analytical (i.e., also involving symbolic numerical computations) methods can efficiently solve single– and multiple–particle problems, allowing a through investigation of the underlying physics. The essence of particle–expansion methods is linear superposition: the desired field quantity (e.g. temperature, potential, velocity, vorticity) is written as a summation of fundamental solutions or Green's functions of the governing equations [Rayleigh (1892), Hasimoto (1959), Kim & Karrila (1991)]; numerical computations are then often performed to evaluate the (truncated) sums. Extensions of these methods to accomodate nonlinearities (e.g. inertia) are not easily accomplished.

Many analytical and semi–analytical results, for either conduction or creeping flow in multicomponent systems, were developed for media having a periodic microstructure, which are simplified models of real (random) media. The mathematical analysis of these models is greatly simplified by the periodic boundary conditions, which make proofs of existence and uniqueness of solution in periodic homogenization theory possible [Bensoussan, Lions & Papanicolaou (1978); see also Appendix A for a discussion and further references about homogenization theory]. Solutions of periodic models can exactly account for multiple–body interactions, and they are easily compiled due to smaller parameter spaces. However, due to the simplified and somewhat arbitrary microstructure, care is needed when applying the results in practice.

Conduction Behrens (1968) used the method of long waves of solid state physics to calculate the principal thermal conductivities of an infinite composite, made of periodic cells with orthorhombic symmetry. The method consists in considering travelling waves of long wavelengths compared to inter–inclusion spacings, and calculating their damping coefficients in the principal directions of the medium. Han & Cosner (1981) employed the boundary collocation method (whereby boundary conditions are satisfied at a selected number of points along the boundary) to solve for the effective conductivity of fibrous composites in various unit–cell geometries.

J. Keller (1964) demonstrated a reciprocity theorem for rectangular lattices of identical parallel cylinders, which relates the component conductivities and the effective conductivities along the two orthogonal coordinate directions. In the particular case of isotropic regular arrays, Keller's relation takes the form

$$\frac{k_e(c,\, k_{di}/k_{co})}{k_{co}} = \left[\frac{k_e(c,\, 1/(k_{di}/k_{co}))}{k_{co}}\right]^{-1}, \tag{1.1}$$

where k_e is the (scalar) effective conductivity function, k_{co} and k_{di} are the continuous phase and dispersed phase conductivities, respectively, and c is the concentration (i.e., cylinders volume fraction). Notice that the second argument of k_e corresponds to the dispersed phase conductivity normalized with respect to the continuous phase

conductivity. We will be interested in the case with $k_{di} = 0$ (see Chapters 2 and 4), so that the inverse of reported effective conductivity results for infinitely conducting cylinders are appropriate for comparison. Keller's proof relies on the properties of harmonic functions. He also claimed that equation (1.1) is applicable to a medium with statistically homogeneous and isotropic random distribution of cylinders, a result later made rigorous by Mendelson (1975).

Perrins, McKenzie & McPhedran (1979) and McPhedran & McKenzie (1978) solved, respectively, the two- and three-dimensional problems of heat conduction through ordered arrays of cylinders and spheres. They extended Rayleigh's superposition analysis to include an arbitrary number of terms in the series expansion of the potential (or temperature) in terms of harmonic functions. Their results for square and hexagonal arrays are tabulated for various values of the concentration and the ratio of dispersed to continuous phase conductivities.

Sangani & Yao (1988a) calculated the effective conductivities of *random* arrays of cylinders. They extended the periodic fundamental solutions of Laplace's equation [Hasimoto (1959)] to include many particles in the (periodic) domain, and subsequently truncated the resulting infinite series expressions. Effective conductivity values were determined for computer generated arrays, and average results (corresponding to small sample sizes, $O(10)$) are presented in terms of the concentration and the ratio of component conductivities. Sangani & Yao's results are, to the author's knowledge, the only ("exact") ones for random arrays of cylinders; in Chapter 4, our results are compared to theirs.

Tzou (1991) analysed the problem of determining the thermal conductivity of porous media, thought of as "particulate" composite materials with insulating spherical cavities or penny-shaped cracks. He used a volume averaging approach to define bulk quantities; the cavity or crack was subjected to the following boundary conditions: zero flux at the surface, and an incoming unidirectional heat flux at a great distance. Tzou's expression for the effective conductivity in the case of penny-shaped cracks overestimates experimental data; this is mathematically explained in Section 2.1.3.

It should be pointed out that most procedures developed for the analysis of thermal conduction in composite materials extend directly to the structural composite problem [Hashin (1983), Kibler (1991)]. In fact, expressions similar to the ones derived in this thesis [see Chapter 2] and elsewhere for the effective conductivity can also be derived for the elastic moduli of composites [see e.g. Hashin (1983), Bendsøe & Kikuchi (1988), Rodin & Hwang (1990)].

Creeping Flow Childress (1972) showed that Brinkman's approach is indeed rigorous for point particles, by obtaining an asymptotic expansion for the permeability in powers of concentration, using a perturbation method. Saffman (1973) gave a unified analytical treatment for the point particle approximation, explaining different qualitative dependence of effective properties (permeability, sedimentation rate) on concentration. Notice that the point particle approximation has been extensively used for the low concentration range, i.e., dilute regime [Batchelor (1974), Kim & Karrila (1991)].

Kim & Mifflin (1985) use the boundary collocation technique, in which series representations of the velocity field in terms of Green's functions are truncated, and the coefficients calculated by satisfying the boundary conditions at a finite number of boundary nodes, to (completely) solve for the resistance and mobility functions of two equal spheres in a creeping flow. Later, Kim and co-workers [see Kim & Karrila (1991)] developed a completed double-layer boundary integral equation method (CDL-BIEM) to deal with general multi-particle systems in creeping flow; the method uses Stokes double layer densities completed to form a basis, and linear operator theory. Karrila, Fuentes & Kim (1989) developed computational strategies for the CDL-BIEM to make use of parallel processing.

Brady & Bossis (1985, 1988) developed a dynamic simulation technique, termed Stokesian Dynamics, applicable to a variety of situations, including flow through porous media. It is based on known analytical expressions of mobility-resistance functions for particular categories of Stokes flow (thus linear); these expressions are used to approximate the lubrication (near-field) and far-field contributions to hydro-

dynamic particle interactions. Ladd (1990; see also references therein) uses similar near–field and far–field approximation techniques to determine, through simulation, transport coefficients of random dispersions of hard spheres. Brady & Bossis' and Ladd's simulation techniques are not exact, and were mainly explored for spherical particles, due to ready availability of analytical expressions.

Sangani & Acrivos (1982a, 1982b) solved the problems of creeping flow through periodic arrays of cylinders and spheres; for the former, they used a somewhat non–conventional numerical method to calculate values of the force on one cylinder, resulting from series expansions of the vorticity and streamfunction; for the latter, they basically modified Hasimoto's treatment for the dilute regime, to solve for the complete range of concentration. Sangani & Yao (1988b), by extending their conduction solution technique to a streamfunction–vorticity formulation of the Stokes problem, calculated permeabilities of random arrays of cylinders. Notice that, since Sangani & Yao's approach is based on solutions to Laplace's equation, further extension of the method to flow in three dimensions is not possible.

1.2.4 First–Principle Computational Methods

First–principle computational methods (based on the conservation equations of continuum mechanics), typically developed for serial machines, can more easily treat nonlinearities and complex shapes, but they have been, to date, technologically confined to single–particle periodic cells, simple geometries, relatively few particles, and small sample sizes.

Conduction Winterfeld, Scriven & Davis (1981) investigated percolation and conductivity of random two–dimensional composites. The composites were generated by labelling a fraction of the convex polygons of a (random) Voronoi tesselation [Preparata & Shamos (1988)] as conducting, and the rest as insulating. They used the finite element method to numerically compute the effective conductivity for one realization of the random medium; average values corresponding to small sample sizes, $O(10)$, are reported as a function of the conducting fraction. Beyond the percolation

threshold (about 0.5), the composite appears as if it contained insulating, irregular polygonal inclusions.

Creeping Flow Edwards, Shapiro, Bar–Yoseph & Shapira (1990) used the finite element method to compute the effect of moderate Reynolds number (between 0 and 200) in the permeability of square and hexagonal periodic arrays of cylinders. For a given concentration, they found a decrease of the permeability relative to Stokes flow. They also comment, based on their permeability results for bidisperse square arrays, that by increasing the polydispersivity of ordered arrays, real porous media behavior can presumably be approached. Hu, Joseph & Crochet (1992) performed numerical simulations of the motion of two interacting cylinders falling under gravity with moderate Reynolds numbers ($O(100)$). They also used finite elements, and were able to reproduce some typical motions observed experimentally. The Navier–Stokes equations were used to describe the fluid motion, and Newton's equations to describe the particles motion. Notice that although both of the above investigations included nonlinear inertial effects (unlike analytical approaches), they were basically restricted to simple geometries and small number of particles.

1.2.5 Experimental Work

Obviously, experimental data is crucial for any realistic assessment of any theories. Much experimental work has been done in the field of multicomponent media; here, we mention *only* two investigations, which are more directly related to our current work on effective properties of fibrous media.

Conduction Hasselman, Bhatt, Donaldson & Thomas (1992) conducted experiments to investigate the effect of fiber orientation (with respect to the heat flux) on the effective conductivity of a unidirectional carbon fiber–reinforced glass matrix composite. The diameter of the fibers was about 10μm, and the specimens were 2–8 milimeters thick. The conductivity of the carbon fibers is larger (by a factor of roughly 100) than that of the glass matrix. For a concentration of about 60% of fibers,

the effective conductivity decreases by a factor of 21 as the angle changes from 0 (longitudinal conduction) to 90 (transverse conduction, as in this thesis) degrees. The effective conductivity value of 4.47 W/mK was reported for transverse conduction.

Creeping Flow Gebart (1992) measured the permeability of unidirectional reinforcements for the composite manufacturing technique of resin transfer molding (RTM). The fibers are first placed in a mold, and it is then filled with a (Newtonian, low viscosity) resin which is forced through the arrangement; the mold is opened after curing of the resin, and the composite is then extracted. The mold fill time depends on the permeability, and hence on the fiber content, of the medium; the concentration in the experiments varied from 0.35 to 0.55. The fiber diameter was about 10μm; the fibers, however, were seen to be assembled into larger fiber bundles, with cross–sections a little flattened instead of perfectly round. Essentially all of the flow occurred in between the bundles, since the fibers within them were highly packed. Gebart's original measurements are dimensional (meter^2); by fitting the experimental data, for flow aligned with the fibers, with square array model predictions, he estimates an effective fiber radius of 42μm. The use of such radius with square array model predictions for flow perpendicular to the fibers overestimates the empirical data for cross–flow, by about 10% (at the lower concentrations) to 50% (at the higher concentrations).

1.3 Objectives of This Thesis

In general terms, previous investigations, although they have led to many significant results, have been limited to techniques that either cannot be systematically extended to handle more complex situations, particularly nonlinearities, or cannot allow for error control in a specific problem. More general methodologies are then needed to solve new problems arising from the more sophisticated operation and design requirements of various devices or equipment, and to impact existing and new multicomponent technologies (such as, e.g., particle tailoring in suspensions).

With the above considerations in mind, this research has the *broad goal* of developing a new general first–principle methodology for the study of multicomponent random media, which combines the relative strengths of earlier analytical and computational approaches. The methodology, presented in detail in Chapters 2 and 3, is based upon:

- a variational hierarchical decomposition procedure which recasts the original multiscale problem as a sequence of three *scale–decoupled* subproblems;
- solution of the resulting (micro–, meso–, and macroscale) subproblems by *parallel* Monte–Carlo and finite–element methods.

The variational scale decomposition procedure keeps the number of degrees of freedom to within tractable amounts; Monte–Carlo methods make possible the analysis of random media; and parallel finite–element methods not only provide the necessary geometric flexibility for complex (2-D or 3-D) domains, but also exploit the well–demonstrated order–of–magnitude cost and performance benefits associated with distributed–memory commodity–chip parallel processors.

The *specific goals* of this research are:

- to develop fully automated parallel processing partial–differential–equation (PDE) tools which permit ready integration of PDE solvers into higher–level, multiple–PDE, inquiries, such as Monte–Carlo or optimization methods;
- to develop a parallel *nested* Monte–Carlo finite–element procedure for first–principle analysis of multicomponent random media;
- to apply the methodology to study two selected problems of practical importance, namely, conduction in unidirectional fibrous composites and creeping flow through fibrous porous media; in particular, we will
  - explore the micro–meso–macro variational decomposition procedure, which easily permits, as we will show, incorporation of analytical results into the finite element framework;

– determine effective properties and statistical correlation lengths to understand, through simulation, essential physical aspects of those systems, with focus on concentration ranges not amenable to other forms of analysis.

We have deliberately chosen problems for which semi-analytical results are available; however, our methodology is more general as regards geometry, nonlinear media, and three dimensionality. We have pursued the physics more deeply than in past work, including: variational interpretation of effective properties and implications; statistical correlation length definition and determination; comparison to a multiscale calculation and to some experimental data.

The proposed methodology can conceptually handle the different levels of complexity indicated in Section 1.2, though the technical difficulties associated with a particular implementation can significantly increase (e.g. adding the third dimension). Finally, it should be pointed out that present and future results obtained with this methodology, besides their availability for incorporation into existing analysis-oriented software [e.g. CLASS, see Kibler (1991)], can be used to develop engineering models for multicomponent media, appropriate for subsequent design and optimization studies. Model construction and validation based on computational inquiry and systematic surrogate techniques is subject of intensive current research [see e.g. Yeşilyurt and Patera (1993)].

Overview of Thesis This thesis is divided into four Chapters and seven Appendices. In Chapter 2, we develop the continuous formulations of the problems we are interested in: heat conduction in composites and creeping flow through porous media. In Chapter 3, the numerical methods used for the solution of these continuous problems are presented. In Chapter 4, the results obtained are shown and discussed, and the conclusions stated. The Appendices give further details of various components of the methodology presented in the text.

Chapter 2

Problem Formulations

In this chapter, we formulate the continuous problems of heat conduction in unidirectional fibrous composites (Section 2.1) and creeping flow through fibrous porous media (Section 2.2). The original multiscale problem in each case is hierarchically decomposed into three scale–decoupled subproblems; conservation principles are then used to derive the macroscale, mesoscale and microscale equations. We show that both the effective conductivity and permeability satisfy extremum principles; these variational formulations can be used to derive rigorous bounds for nearfield behavior of clustered inclusions for the purpose of reducing computational cost.

2.1 Conduction in Unidirectional Fibrous Composites

2.1.1 Description of the Original Multiscale Problem

A unidirectional fibrous composite, shown in Figure 2-1, consists of a matrix, the continuous phase, and the dispersed phase, here (randomly and homogeneously distributed) parallel cylindrical inclusions. Both phases are assumed solid, homogeneous, and isotropic; the constant (scalar) thermal conductivity of the matrix is denoted k_{co}, and that of the inclusions k_{di}. In this work, the inclusions will be considered circular, of diameter d, and insulating, $k_{di} = 0$, in which case they can also be thought of as

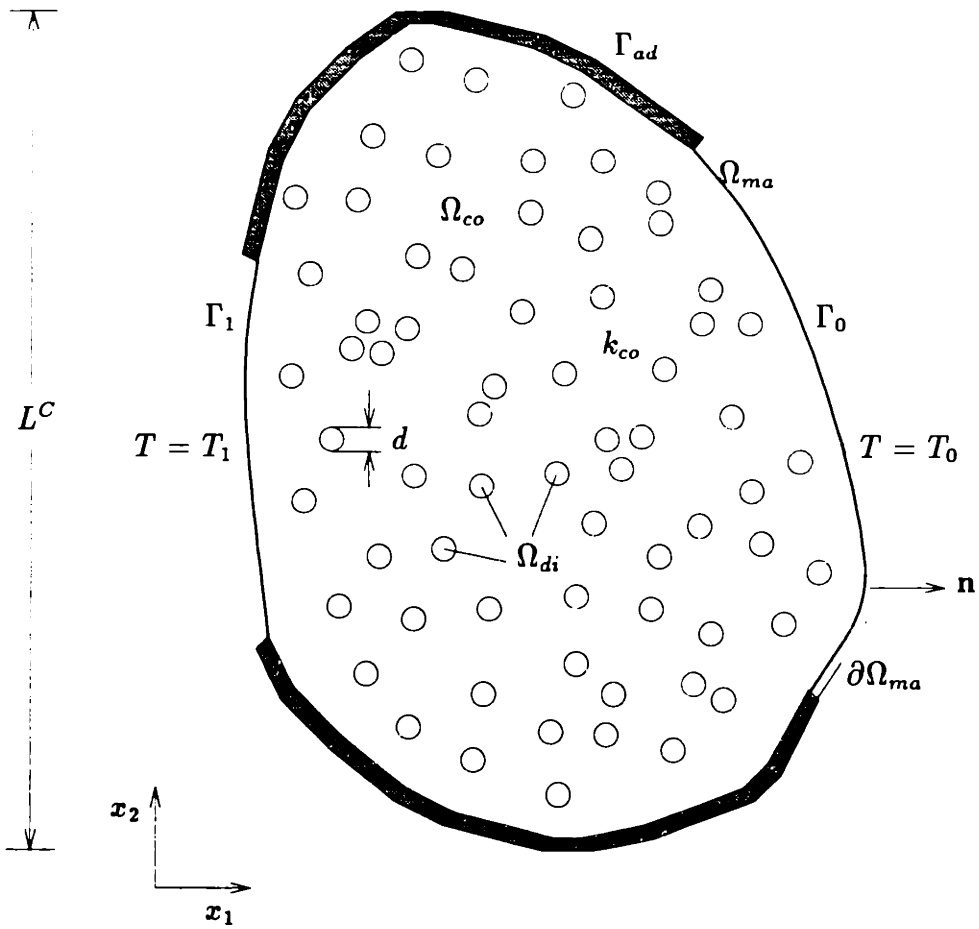

Figure 2-1: Unidirectional fibrous random composite.

voids. By virtue of Keller's relation discussed in Section 1.2.3, the results that we will obtain are also valid for infinitely conducting inclusions (which can be thought of as superconducting wires), provided the composite is isotropic, and the inverse values are used.

In Figure 2-1, the (two–dimensional) space coordinates are $(x_1, x_2) = \mathbf{x} \in \mathcal{R}^2$, and the *geometric* regions occupied by the matrix and the dispersed phase are, respectively, Ω_{co} and Ω_{di}. Physically, the composite extends throughout a characteristic length L^C. The large scale over which (temperature) gradients are imposed is called the *macroscale*, denoted by L (L is proportional to L^C). The macroscale region is indicated by $\Omega_{ma} = \Omega_{co} \cup \Omega_{di}$. The smallest scale present is the characteristic size of the inclusions, d, called the *microscale*. The boundary conditions are specified on the

external surface of the composite, which we denote $\partial\Omega_{ma}$. For definiteness, we have shown $\partial\Omega_{ma} = \Gamma_0 \cup \Gamma_1 \cup \Gamma_{ad}$, where Γ_0, Γ_1, and Γ_{ad} are sub–regions of the boundary on which, respectively, uniform temperatures T_0 and T_1, and adiabatic conditions are imposed.

Consistently with the nature of many real multicomponent systems, it is assumed here that

$$\gamma \equiv \frac{d}{L} \ll 1 . \tag{2.1}$$

The problem then intrinsically possesses a clear separation of scales, as opposed, for instance, to turbulence, in which energy is transferred from larger to progressively smaller scales, where it is finally dissipated. In general, the volume fraction of inclusions is specified as a concentration function, $c(\mathbf{x}) : \Omega_{ma} \rightarrow [0, 1]$, varying significantly only on the macroscale. Also, the inclusion distribution function (see Section 2.1.3) may change appreciably only on the macroscale; transverse isotropy is *not* assumed *a priori*. It is natural to assume, given statistical homogeneity, that there exists an intermediate characteristic length λ, $d < \lambda < L$, which is the scale of the region surrounding one test inclusion, over which "most" of its interactions with neighboring inclusions occur; we call λ the *mesoscale*.

Clearly for such a composite, it is an enormous task to solve a complete boundary value problem on Ω_{ma}: analytically, due to its geometric complexity; numerically, due to the excessive number of degrees of freedom required to resolve both the microscale and the macroscale. However, it is not usually necessary to solve the problem in such detail, since in engineering practice one is typically interested in bulk quantities, such as, say, the steady–state heat transfer rate per unit depth, Q, passing through the boundary segment Γ_0 due to the imposed temperature difference $\Delta T = T_1 - T_0$. It is thus natural to treat the composite as a continuous homogeneous material possessing *effective properties* [Beran (1968)]. For a particular set of positions of the inclusions, an effective property associated with a given transport phenomenon is the coefficient in the (now postulated) medium's constitutive equation relating the volume averaged flux to the volume averaged (imposed) gradient. In particular, for heat conduction

we write Fourier's law for the composite as

$$< \mathbf{q} >_v = - \underline{\mathbf{k}}'_e \cdot < \nabla T >_v , \tag{2.2}$$

where $<>_v$ denotes volume average, $\mathbf{q}$ is the local heat flux, $\underline{\mathbf{k}}'_e$ is the effective conductivity tensor, and ∇T is the local temperature gradient. The prime in $\underline{\mathbf{k}}'_e$ indicates a particular configuration of the random medium. A more useful quantity in practice is obtained by performing *ensemble* averaging over all the possible configurations (see Section 2.1.3); the resulting effective property, $\underline{\mathbf{k}}_e$, can be applied, with known uncertainty, to any configuration.

In the next sections, we describe our variational hierarchical scale–decoupling procedure: the original problem is decomposed into the microscale, mesoscale, and macroscale (sub–)problems. In the microscale problem, we analyse local effects, such as the nearfield behavior of clustered inclusions and matrix–inclusion interfacial phenomena. In the mesoscale problem, by introducing periodic supercells incorporating *many* microscale–modelled particles and clusters, we not only determine effective properties, but also seek the length scales at which, statistically periodic and truly random microstructures behave in a sufficiently close manner (note: although in our context we should really use the word *meso*structure instead of *micro*structure, we employ the latter throughout the thesis, because of its widespread use in the literature). In the macroscale problem, we treat the now-smooth, potentially anisotropic, homogenized medium in order to predict the quantities of engineering interest, here represented by Q. Although from a physical point of view it is more natural to consider the microscale problem first, for purposes of clarity of exposition, we begin with the simpler macroscale problem. The equations and boundary conditions are presented in dimensional form; however, for the numerical implementation (Chapter 3) and presentation and analysis of the results (Chapter 4), the nondimensional form is more convenient. We then briefly indicate, when appropriate, the various nondimensional parameters and their interdependence.

2.1.2 Macroscale

The steady-state heat conduction equation for the homogenized medium extending over the macroscale reads

$$-\frac{\partial}{\partial x_i}\left[\, k_{e_{ij}}(c(\mathbf{x}))\,\frac{\partial T_{ma}}{\partial x_j}\,\right] = 0 \ \text{ in } \Omega_{ma}\,, \tag{2.3}$$

with Dirichlet and Neumann boundary conditions

$$T_{ma} = T_1 \ \text{ on } \Gamma_1\,, \tag{2.4}$$

$$T_{ma} = T_0 \ \text{ on } \Gamma_0\,, \tag{2.5}$$

and

$$-\,k_{e_{ij}}\,\frac{\partial T_{ma}}{\partial x_j}\,n_i = 0 \ \text{ on } \Gamma_{ad}\,, \tag{2.6}$$

where $T_{ma}(\mathbf{x})$ is the macroscale temperature, $\underline{\mathbf{k}}_e(c) \equiv k_{e_{ij}}(c)$, $i,j = 1,2$, is the effective conductivity tensor–concentration function, $\mathbf{n} = n_i$ denotes the unit outward normal to the boundary, and the summation convention over repeated indices is assumed. Note that the *original* problem of Figure 2-1 can be expressed by equations (2.3)–(2.6) if we replace: T_{ma} with T; $k_{e_{ij}}(c)$ with k_{co} and Ω_{ma} with Ω_{co} in (2.3); Γ_{ad} with $\Gamma_{ad} \cup \partial\Omega_{di}$ in (2.6) ($\partial\Omega_{di}$ is the boundary of Ω_{di}, i.e., the union of all inclusion surfaces).

Given the relative geometric complexity of Ω_{ma} and Ω_{co}, it is easy to conclude that the homogenized problem requires only a small fraction, $O(\gamma^2)$, of the number of degrees of freedom demanded by the original problem. The macroscale problem can then be routinely solved with state–of–the–art commercial software packages. From T_{ma} the requisite (global) heat transfer rate can be calculated as

$$Q_{ma} = \int_{\Gamma_0} -k_{e_{ij}}(c(\mathbf{x}))\,\frac{\partial T_{ma}}{\partial x_j}\,n_i\,ds \tag{2.7}$$

(ds is a surface element). From homogenization theory [Bensoussan, Lions & Papanicolaou (1978)], it is known that, for a medium with λ–periodic microstructure, in the

limit $\epsilon = \frac{\lambda}{L} \rightarrow 0$, the macroscale temperature T_{ma} locally approximates, with error $O(\epsilon)$, the original temperature T.

In nondimensional terms, the ratio $\frac{k_{e_{ij}}}{k_{co}} \equiv k^*_{e_{ij}}$, $k_{co} \neq 0$, in general depends on inclusion geometry, expressed by shape factors, on the ratio of component conductivities, $\varsigma = \frac{k_{di}}{k_{co}}$, and on the concentration c. Only the latter dependence is indicated, as the former are, for the purposes of this thesis, fixed.

2.1.3 Mesoscale

The mesoscale problem encompasses four nested levels, and it is the most computationally intensive; its solution, simply put, provides the proper function $\underline{\mathbf{k}}_e(c(\mathbf{x}))$ to the macroscale problem. The analysis done at the microscale (see Section 2.1.4) can be incorporated into the mesoscale problem, modifying (and complicating) its equations, but reducing the overall computational cost. In this section, we will present the mesoscale equations with *no* microscale preparation; these are the actual equations solved in this thesis. The modified equations due to the microscale analysis will be presented in Section 2.1.4, but their implementation is left for future work (see Section 4.5). We now introduce the four levels of the mesoscale procedure. In order to simplify the presentation, we assume the inclusion distribution to be isotropic. Although *not* essential, this assumption permits us to discuss scalar, rather than tensor, effective properties; the notation is thus greatly condensed by the omission of indices. In Chapter 4, results for all components of the effective conductivity tensor are reported.

Level 1

At the first, innermost, level, the microstructure is set-up and analysed: first, a concentration value, c, is assumed; next, a particular realization (i.e., configuration) of the composite medium is considered, by introducing a periodic supercell containing many inclusions (which account for the prefix *super*). The supercell geometry is depicted in Figure 2-2 as a square region, $(y_1, y_2) = \mathbf{y} \in \Omega_{sc}$, of given edge-length λ;

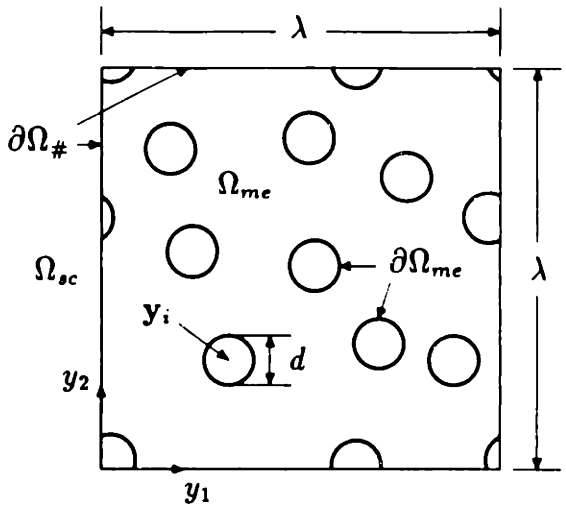

Figure 2-2: Periodic supercell geometry.

by removing N disks of diameter d,

$$N = \frac{4c}{\pi}\frac{\lambda^2}{d^2}\,, \tag{2.8}$$

with *prescribed* centers $\{\mathbf{y}\}_N = \mathbf{y}_1, \ldots, \mathbf{y}_N$, we obtain the mesoscale region, Ω_{me}. In Section 3.2.1, we show the actual geometry used for the (computational) supercell region. The union of the boundaries of the N voids is denoted $\partial\Omega_{me}$, and the union of the pairs of periodic edges, $\partial\Omega_{\#}$ (note that segments inside "cut" inclusions are not part of the periodic edges).

The partial differential equation for the mesoscale temperature, $T_{me} = \epsilon\,\chi(\mathbf{y})$,

$$\epsilon = \frac{\lambda}{L}\,,$$

is given by

$$-\frac{\partial}{\partial y_i}(k_{co}\frac{\partial \chi}{\partial y_i}) = 0 \ \text{ in } \Omega_{me}\,, \tag{2.9}$$

with Neumann and periodic boundary conditions,

$$-k_{co}\frac{\partial \chi}{\partial y_i}n_i = -k_{co}\frac{\Delta T}{L}n_1 \ \text{ on } \partial\Omega_{me}\,, \tag{2.10}$$

and

$$\chi(\mathbf{y}) = \chi(\mathbf{y} + \lambda(m_1\mathbf{e}_1 + m_2\mathbf{e}_2)) \text{ on } \partial\Omega_{\#} , \tag{2.11}$$

where the y_1 direction has been chosen for the driving temperature gradient, the scaling $\frac{\Delta T}{L}$ is included to preserve dimensionality, $m_1 , m_2 \in \{0, \pm 1, \pm 2, \ldots\}$, and the $\mathbf{e}_i$, $i = 1, 2$, are orthonormal basis vectors. Since adding a constant to a solution of the boundary value problem (2.9)–(2.11) yields another solution, we further require for uniqueness that

$$\int_{\Omega_{me}} \chi \, d\mathbf{y} = 0 , \tag{2.12}$$

where $d\mathbf{y} = dy_1 \, dy_2$.

In order to *motivate* equation (2.9), we first assume an asymptotic expansion for the original temperature T, in the infinite *periodic* medium, of the form

$$T(\mathbf{x}) = T_{ma}(\mathbf{x}) + \epsilon \, \chi(\mathbf{x}, \mathbf{y}) + O(\epsilon^2) , \tag{2.13}$$

where $\mathbf{x}$ and $\mathbf{y} \equiv \mathbf{x}/\epsilon$ represent, respectively, slowly and rapidly varying coordinates. Taking the gradient of equation (2.13) with respect to $\mathbf{x}$, multiplying by k_{co} , and taking the divergence of the flux terms so obtained, we get

$$\frac{\partial}{\partial x_i}(k_{co} \frac{\partial T}{\partial x_i}) = \frac{\partial}{\partial x_i}(k_{co} \frac{\partial T_{ma}}{\partial x_i}) + \epsilon \, \nabla_{\mathbf{x}} \cdot [k_{co} \nabla_{\mathbf{x}} \chi(\mathbf{x}, \mathbf{y})] . \tag{2.14}$$

Noting that the macroscale, on the mesoscale, appears linear to order $O(\epsilon^2)$, we set to within an arbitrary constant

$$T_{ma} = -\frac{\Delta T}{L} x_1 ; \tag{2.15}$$

using (2.15) and the conservation of energy principle for the original problem (with no heat generation), we can rewrite equation (2.14) as

$$\nabla_{\mathbf{x}} \cdot [k_{co} \nabla_{\mathbf{x}} \chi(\mathbf{x}, \mathbf{y})] = 0 . \tag{2.16}$$

Since, for χ,

$$\frac{\partial}{\partial x_i} = \frac{\partial}{\partial x_i} + \frac{1}{\epsilon}\frac{\partial}{\partial y_i}, \tag{2.17}$$

equation (2.16) becomes

$$\frac{\partial}{\partial x_i}(k_{co}\frac{\partial \chi}{\partial x_i}) + \frac{2}{\epsilon}\frac{\partial}{\partial x_i}(k_{co}\frac{\partial \chi}{\partial y_i}) + \frac{1}{\epsilon^2}\frac{\partial}{\partial y_i}(k_{co}\frac{\partial \chi}{\partial y_i}) = 0\,. \tag{2.18}$$

Multiplying equation (2.18) by ϵ^2, and neglecting terms of $O(\epsilon^2)$ and $O(\epsilon)$ with respect to $O(1)$, we finally obtain equation (2.9). The boundary condition on $\partial\Omega_{me}$, equation (2.10), is *motivated* in a similar manner: the divergence of the flux terms in (2.14) is replaced by their inner product with $\mathbf{n}$, and zero flux is imposed at the inclusion surfaces. The key physical fact to realize is that the macroscale ($T_{ma}(\mathbf{x})$) and mesoscale ($T_{me} = \epsilon\,\chi(\mathbf{x},\mathbf{y})$) temperature components will contribute to the flux at $\partial\Omega_{me}$ *to the same order*: the former will be order ΔT and vary over a scale $O(L)$, giving a gradient of $O(\frac{\Delta T}{L})$; the latter will be order $\epsilon\Delta T$ and vary over a scale $O(\lambda)$, giving a gradient of $O(\frac{\Delta T}{L})$.

The effective conductivity of the supercell (assumed isotropic), or of the infinite medium, for the particular configuration $\{\mathbf{y}\}_N$, $k_e'(c,\lambda,\{\mathbf{y}\}_N)$, is defined in equation (2.2), and takes the (scalar) form

$$k_e'(c,\lambda,\{\mathbf{y}\}_N) = k_{co}\,\{(1-c) - \frac{L}{\Delta T\,\lambda^2}\int_{\Omega_{me}}\frac{\partial \chi}{\partial y_1}\,d\mathbf{y}\}\,. \tag{2.19}$$

Equation (2.19) can be obtained as follows. In equation (2.2), the average heat flux in a supercell (which must be equal to the average over the whole medium, given periodicity) is

$$< \mathbf{q} >_v = \frac{1}{\int_{\Omega_{sc}} d\mathbf{y}}\left[\int_{\Omega_{me}} -k_{co}\nabla_{\mathbf{x}} T\,d\mathbf{y}\right]\,. \tag{2.20}$$

Using equations (2.13), (2.15) and (2.17), and neglecting terms of $O(\epsilon)$ with respect to $O(1)$, we obtain

$$< \mathbf{q} >_v = \frac{1}{\int_{\Omega_{sc}} d\mathbf{y}}\left[\int_{\Omega_{me}} k_{co}\frac{\Delta T}{L}\,d\mathbf{y} + \int_{\Omega_{me}} -k_{co}\frac{\partial \chi}{\partial y_1}\,d\mathbf{y}\right]\mathbf{e}_1\,; \tag{2.21}$$

identifying the ratio $\frac{\int_{\Omega_{me}} dy}{\int_{\Omega_{sc}} dy}$ as the matrix volume fraction $(1-c)$, equation (2.21) becomes

$$< \mathbf{q} >_v = k_{co} \left[(1-c) \frac{\Delta T}{L} - \frac{1}{\lambda^2} \int_{\Omega_{me}} \frac{\partial \chi}{\partial y_1} \, d\mathbf{y} \right] \mathbf{e}_1 \, . \tag{2.22}$$

Now, the average temperature gradient is given by

$$< \nabla T >_v = \frac{1}{\int_{\Omega_{sc}} d\mathbf{y}} \left[\int_{\Omega_{sc}} -\frac{\Delta T}{L} \, d\mathbf{y} + \int_{\Omega_{sc}} \frac{\partial \chi}{\partial y_1} \, d\mathbf{y} \right] \mathbf{e}_1 \, , \tag{2.23}$$

or, equivalently,

$$< \nabla T >_v = \left[-\frac{\Delta T}{L} + \frac{1}{\lambda^2} \int_{\partial \Omega_{sc}} \chi \, n_1 \, ds \right] \mathbf{e}_1 \, . \tag{2.24}$$

By periodicity of χ, the second term on the right-hand-side of (2.24) is zero, and we finally obtain

$$< \nabla T >_v = -\frac{\Delta T}{L} \mathbf{e}_1 \, , \tag{2.25}$$

which is the imposed macroscale temperature gradient, as expected. From (2.2), (2.22) and (2.25), we easily obtain (2.19). The reason for integrating over Ω_{sc} in the denominators of (2.20) and (2.23) can be physically motivated by observing that the homogenized medium has no voids; equation (2.19) is derived rigorously in Appendix A using homogenization theory.

Equation (2.19) can be alternatively obtained with a surface, rather than volume, approach. First we write, based on Fourier's law,

$$k_e' = - \frac{\bar{q}}{-(\Delta T/L)} \, , \tag{2.26}$$

where $\bar{q}$ is the average heat flux in a supercell, and $-(\Delta T/L)$ is the imposed macroscopic temperature gradient, with respect to which the effective property is desired. The total heat transfer rate per unit length, $\dot{q}_l$, across a line of constant y_1 *inside* Ω_{me} is given by

$$\dot{q}_l = \int_0^{\lambda} k_{co} \left[\frac{\Delta T}{L} - \frac{\partial \chi}{\partial y_1} \right] dy_2 \, ; \tag{2.27}$$

the superficial heat flux is therefore

$$q_s = \frac{1}{\lambda}\int_0^{\lambda} k_{co}\left[\frac{\Delta T}{L} - \frac{\partial \chi}{\partial y_1}\right] dy_2 \,. \tag{2.28}$$

By conservation of energy and periodicity, $\dot{q}_l$, and hence q_s, are constant along $0 \leq y_1 \leq \lambda$, so that

$$\bar{q} = q_s = \frac{1}{\lambda}\int_0^{\lambda} q_s \, dy_1 = \frac{1}{\lambda^2}\int_0^{\lambda}\int_0^{\lambda} k_{co}\left[\frac{\Delta T}{L} - \frac{\partial \chi}{\partial y_1}\right] dy_2 \, dy_1 \,; \tag{2.29}$$

we then write

$$\bar{q} = \frac{1}{\lambda^2} k_{co}\left[\frac{\Delta T}{L}\lambda^2(1-c) - \int_0^{\lambda}\int_0^{\lambda} \frac{\partial \chi}{\partial y_1} \, dy_2 \, dy_1\right] . \tag{2.30}$$

Notice that the integrations from 0 to λ over y_2 in (2.27)–(2.30) include only segments inside the matrix portion of the supercell, Ω_{me}; this gives rise to the factor $(1-c)$ in (2.30). From (2.26) and (2.30) we finally get the desired expression (2.19).

Defining the functional I^C_Ω,

$$I^C_\Omega(v) = \frac{\Delta T}{L}\int_\Omega \frac{\partial v}{\partial y_1} \, d\mathbf{y} \,, \tag{2.31}$$

equation (2.19) can be rewritten as

$$k'_e(c, \lambda, \{\mathbf{y}\}_N) = k_{co}\left\{(1-c) - \frac{L^2}{\Delta T^2 \, \lambda^2} I^C_{\Omega_{me}}(\chi)\right\} ; \tag{2.32}$$

we also introduce the functional J^C_Ω,

$$J^C_\Omega(v) = \int_\Omega \frac{\partial v}{\partial y_k}\frac{\partial v}{\partial y_k} \, d\mathbf{y} - 2\, I^C_\Omega(v) \,, \tag{2.33}$$

which possesses a positive–definite bilinear form. Multiplying (2.9) by χ, integrating over Ω_{me}, and using the divergence theorem and equation (2.10), we derive

$$I^C_{\Omega_{me}}(\chi) = -J^C_{\Omega_{me}}(\chi) = \int_{\Omega_{me}} \frac{\partial \chi}{\partial y_k}\frac{\partial \chi}{\partial y_k} \, d\mathbf{y} \,. \tag{2.34}$$

From (2.32) and (2.34) we note that, in the general anisotropic case, the diagonal components of the effective conductivity tensor $\underline{\mathbf{k}}'_e$ will always be less than k_{co}, as physically expected from the insulating nature of the inclusions, *and* also less than $k_{co}(1-c)$. The same comments apply to the off–diagonal components, but due to the positive–definiteness of $\underline{\mathbf{k}}'_e$, shown in Appendix A.

It is interesting to note that, although no new principles are involved in the derivation of (2.19), one can still find recent models proposed in the literature which violate the implication that $\frac{k'_e}{k_{co}} < (1-c)$ (notice this result is not restricted to two dimensions). As mentioned in Section 1.2.3, Tzou (1991) proposed an expression for the effective conductivity of porous media containing (insulating) penny–shaped cracks; he obtained (using our notation)

$$\frac{k'_e}{k_{co}} = 1 - \frac{8}{9}c\,. \tag{2.35}$$

Clearly, the ratio in (2.35) is larger than $(1-c)$; it is therefore not surprising that (2.35) overestimated experimental data, as reported by Tzou.

It is advantageous to work with the equivalent, well–known, variational form associated with the strong form (2.9)–(2.11); analytically, because it will allow derivation of the microscale bounds shown in Section 2.1.4, and numerically because it will blend naturally with the finite element method (Chapter 3). We write [see e.g. Kikuchi (1986), pp. 28-30]:

$$\chi \;=\; \arg \min_{v \in H^1_{\#,0}} J^C_{\Omega_{me}}(v)\,, \tag{2.36}$$

where $H^1_{\#,0}(\Omega_{me}) = \{v \in H^1_{\#}(\Omega_{me}) \mid \int_{\Omega_{me}} v\, d\mathbf{y} = 0\}$, and $H^1_{\#}(\Omega_{me})$ is the space of all λ–doubly periodic functions for which both the function and the derivative are square–integrable over Ω_{me}. The weak form for χ then derives from the first variation of the functional $J^C_{\Omega_{me}}(v)$: Find $\chi \in H^1_{\#,0}(\Omega_{me})$ such that

$$\int_{\Omega_{me}} k_{co} \frac{\partial v}{\partial y_k} \frac{\partial \chi}{\partial y_k}\, d\mathbf{y} = \frac{\Delta T}{L} \int_{\Omega_{me}} k_{co} \frac{\partial v}{\partial y_1}\, d\mathbf{y} \quad \forall v \in H^1_{\#,0}(\Omega_{me}) \tag{2.37}$$

(again, equation (2.37) is derived rigorously in Appendix A using homogenization

theory). The linear functional on the right-hand-side of (2.37), somewhat non-standard, represents the flux inhomogeneity in (2.10) in a (integrated-by-parts) form which trivially ensures solvability (take $v = const.$, say) of subsequent finite element discretizations. In fact, integrating (2.37) by parts, we obtain

$$k_{co} \int_{\partial\Omega_{me}} v \frac{\partial\chi}{\partial y_k} n_k \, ds - k_{co} \int_{\Omega_{me}} v \frac{\partial^2\chi}{\partial y_k \, \partial y_k} \, d\mathbf{y} = \frac{\Delta T}{L} \int_{\partial\Omega_{me}} k_{co} \, v \, n_1 \, ds \, . \tag{2.38}$$

Since (2.38) has to hold for all $v \in H^1_{\#,0}(\Omega_{me})$, equation (2.10) follows immediately.

From (2.32), (2.34), and (2.36) it follows that

$$k'_e(c, \lambda, \{\mathbf{y}\}_N) = k_{co} \{(1 - c) + \frac{L^2}{\Delta T^2 \, \lambda^2} \min_{v \in H^1_{\#,0}} J^C_{\Omega_{me}}(v)\} \, ; \tag{2.39}$$

defining the bilinear form

$$a^C_\Omega(v, v) = k_{co} \frac{1}{\lambda^2} \int_\Omega \frac{\partial}{\partial y_k} (\frac{L}{\Delta T} v - y_1) \frac{\partial}{\partial y_k} (\frac{L}{\Delta T} v - y_1) \, d\mathbf{y} \, , \tag{2.40}$$

we can write equation (2.19) in the equivalent form

$$k'_e(c, \lambda, \{\mathbf{y}\}_N) = a^C_{\Omega_{me}}(\chi, \chi) = \min_{v \in H^1_{\#,0}} a^C_{\Omega_{me}}(v, v) \, . \tag{2.41}$$

For the general anisotropic case, analogous relations to (2.37) and (2.40) can be derived more directly — and rigorously — by applying periodic homogenization theory (see Appendix A). It is then readily demonstrated that the effective conductivity tensor $\underline{\mathbf{k}}'_e$ is symmetric and positive-definite. The extremizing property (here, minimum) (2.41) extends to the off-diagonal components of $\underline{\mathbf{k}}'_e$ in a form similar to the inequalities derived, from variational principles, in Nir, Weinberger & Acrivos (1975), for the components of the shearing tensor.

Finally, we nondimensionalize equations (2.19) and (2.37). Choosing (arbitrarily) the characteristic temperature $T^C = \Delta T(d/L)$, and the diameter d as the characteristic length, we define: $\chi^* = \chi/T^C$, $v^* = v/T^C$, $\mathbf{y}^* = \mathbf{y}/d$ and $\lambda^* = \lambda/d$; equations

(2.19) and (2.37) take, respectively, the normalized forms

$$k_e'^* = \frac{k_e'}{k_{co}} = (1-c) - \frac{1}{\lambda^{*2}} \int_{\Omega_{me}} \frac{\partial \chi^*}{\partial y_1^*} \, d\mathbf{y}^* \,, \tag{2.42}$$

and

$$\int_{\Omega_{me}} \frac{\partial v^*}{\partial y_k^*} \frac{\partial \chi^*}{\partial y_k^*} \, d\mathbf{y}^* = \int_{\Omega_{me}} \frac{\partial v^*}{\partial y_1^*} \, d\mathbf{y}^* \quad \forall v^* \in H^1_{\#,0}(\Omega_{me}) \,. \tag{2.43}$$

Equation (2.43) is the actual supercell problem numerically solved in Chapter 3, in order to determine $k_e'^*$ as given in (2.42). Notice that the functional dependence is $k_e'^* = k_e'^*(c, \lambda^*, \{\mathbf{y}^*\}_N)$. □

Level 2

In the Level 1 procedure described above, the concentration c and the supercell size λ were input; furthermore, the configuration of the N inclusions, expressed by their positions $\{\mathbf{y}\}_N$, was assumed given. The effective conductivity of the supercell was then determined as $k_e'(c, \lambda, \{\mathbf{y}\}_N)$ (equation (2.19)). In Level 2, since our objective is to analyse random media, we must address the question concerning the spatial distribution of inclusions in the supercell. To this end, the positions of the inclusions are now regarded as (continuous) random variables (represented by capital letters): $\{\mathbf{Y}\}_N = \mathbf{Y}_1, \ldots, \mathbf{Y}_N$, where $\mathbf{Y}_1, \ldots, \mathbf{Y}_N \in \Omega_{sc}$. There are various types of mathematical functions that can be used to characterize such spatial distribution; due to the medium randomness, they must involve probabilities. A joint probability density function (JPDF) [see e.g. Mood, Graybill & Boes (1974)], $P_{\mathbf{Y}_1,\ldots,\mathbf{Y}_N}(\mathbf{y}_1, \ldots, \mathbf{y}_N)$ or, simply, $P_N(\mathbf{y}_1, \ldots, \mathbf{y}_N)$, is defined such that $P_N(\mathbf{y}_1, \ldots, \mathbf{y}_N) d\mathbf{y}_1, \ldots, d\mathbf{y}_N$ represents the probability that the N inclusion centers are simultaneously located in the neighborhoods $d\mathbf{y}_1, \ldots, d\mathbf{y}_N$ around the points $\mathbf{y}_1, \ldots, \mathbf{y}_N$. It is normalized such that

$$\int_{\{\mathbf{y}\}_N \in \Omega_{sc}^N} P_N(\mathbf{y}_1, \ldots, \mathbf{y}_N) \, d\mathbf{y}_1, \ldots, d\mathbf{y}_N = 1 \,. \tag{2.44}$$

A conditional joint probability density function,

$$P_{\mathbf{Y}_{M+1},\ldots,\mathbf{Y}_N|\mathbf{Y}_1,\ldots,\mathbf{Y}_M}(\mathbf{y}_{M+1},\ldots,\mathbf{y}_N|\mathbf{y}_1,\ldots,\mathbf{y}_M)\,,$$

or, simply, $P_{M+1,N}(\mathbf{y}_{M+1},\ldots,\mathbf{y}_N|\mathbf{y}_1,\ldots,\mathbf{y}_M)$, is defined such that

$$P_{M+1,N}(\mathbf{y}_{M+1},\ldots,\mathbf{y}_N\,|\,\mathbf{y}_1,\ldots,\mathbf{y}_M)\,d\mathbf{y}_{M+1},\ldots,d\mathbf{y}_N$$

expresses the probability that $N-M$ inclusion centers are simultaneously located in the neighborhoods $d\mathbf{y}_{M+1},\ldots,d\mathbf{y}_N$ around the points $\mathbf{y}_{M+1},\ldots,\mathbf{y}_N$, given that there are already M centers at $\mathbf{y}_1,\ldots,\mathbf{y}_M$. It is normalized such that

$$\int_{\{\mathbf{y}_{M+1},\ldots,\mathbf{y}_N\}\in\Omega_{ic}^{N-M}} P_{M+1,N}(\mathbf{y}_{M+1},\ldots,\mathbf{y}_N\,|\,\mathbf{y}_1,\ldots,\mathbf{y}_M)\,d\mathbf{y}_{M+1},\ldots,d\mathbf{y}_N = 1\,. \quad (2.45)$$

Alternatively, n–point probability functions can also be used to describe the microstructure of the medium. An n–point probability function, S_n, gives the probability of finding a certain subset of n points in the continuous phase and the remainder in the dispersed phase. Torquato & Stell (1982) derived an infinite series representation of the S_n involving correlation functions [Beran (1968)], ultimately related to P_N. In this study, we use P_N rather than S_n; P_N can be more directly implemented, but more difficult to find in practice.

The technical question to be posed is, therefore, what joint probability density function characterizes the microstructure of the composites we are dealing with. There is no unique answer. The JPDF may be known *a priori* from the manufacturing process; it could thus be used as input to a Monte–Carlo sampling method, provided there were no deforming effects which might systematically change it. However, the JPDF may change between different manufacturing processes, or even with time using the same process, due to machinery changes. In the absence of such information, it seems natural to assume that any configuration in the ensemble of all possible configurations is as likely as any other, with the physical constraint that no two inclusions overlap. The practical construction of a JPDF associated with this assumption is not

trivial, both analytically and computationally.

The actual JPDF used in this work is constructed recursively from conditional joint density functions, in the following way. The position of the first inclusion, $\mathbf{Y}_1$, is assumed to be uniformly distributed over the entire supercell region Ω_{sc}. The position of the second inclusion, $\mathbf{Y}_2$, is now assumed to be uniformly distributed over the *available* region of the supercell, $\Omega_{sc} \setminus \Omega_{2d}$, where Ω_{2d} consists of the circular region centered at $\mathbf{Y}_1$ of diameter $2d$; this ensures no overlapping of inclusions. The assumption of uniform distribution over the available space is then carried on successively to the position of the N^{th} inclusion, $\mathbf{Y}_N$. Mathematically, the postulated JPDF can be expressed as

$$\begin{aligned} P_{\mathbf{Y}_1,\ldots,\mathbf{Y}_N}(\mathbf{y}_1,\ldots,\mathbf{y}_N) = P_{\mathbf{Y}_1}(\mathbf{y}_1)\cdot P_{\mathbf{Y}_2\,|\,\mathbf{Y}_1}(\mathbf{y}_2\,|\,\mathbf{y}_1)\cdot\ldots \\ \ldots\cdot P_{\mathbf{Y}_{N-1}\,|\,\mathbf{Y}_1,\ldots,\mathbf{Y}_{N-2}}(\mathbf{y}_{N-1}\,|\,\mathbf{y}_1,\ldots,\mathbf{y}_{N-2})\cdot \\ \cdot P_{\mathbf{Y}_N\,|\,\mathbf{Y}_1,\ldots,\mathbf{Y}_{N-1}}(\mathbf{y}_N\,|\,\mathbf{y}_1,\ldots,\mathbf{y}_{N-1})\,. \end{aligned} \tag{2.46}$$

In Chapter 3 we discuss the implementation of (2.46). While such a JPDF may seem arbitrary, it can be tested *a posteriori* by carrying out sensitivity studies. We also assume that the statistical properties of P_N given in (2.46) approach well-defined limits as λ, and hence N, tend to infinity.

The effective conductivity of the medium is now a random variable, K_e, which is advantageously expressed as a deterministic function of the random inclusion positions, $K_e = k_e'(c,\lambda,\{\mathbf{Y}\}_N)$, calculated in Level 1. The objective of Level 2 is to determine the average effective conductivity of the composite medium over the ensemble of configurations, $< K_e > (c,\lambda)$:

$$< K_e > (c,\lambda) = \int_{\{\mathbf{y}\}_N \in \Omega_{sc}^N} k_e'(c,\lambda,\{\mathbf{y}\}_N)\, P_N(\{\mathbf{y}\}_N)\, d\mathbf{y}_1,\ldots,d\mathbf{y}_N\,; \tag{2.47}$$

in nondimensional form, we write

$$< K_e^* > (c,\lambda^*) = \frac{< K_e >}{k_{co}} = \int_{\{\mathbf{y}^*\}_N \in \Omega_{sc}^N} k_e'^*(c,\lambda^*,\{\mathbf{y}^*\}_N)\, P_N(\{\mathbf{y}^*\}_N)\, d\mathbf{y}_1^*,\ldots,d\mathbf{y}_N^*\,. \tag{2.48}$$

We use Monte–Carlo methods (see Chapter 3) to evaluate the multi–dimensional integral in (2.48), which require repetition of the Level 1 procedure for many realizations of the composite medium (i.e., many different sets of configurations $\{\mathbf{y}^*\}_N$). It should be pointed out that the relevance of our results either requires that the assumption (2.46) is correct, or that the extent to which it is incorrect is attenuated by low sensitivity of the results to the JPDF chosen. In other words, the resulting $< K_e >$ in (2.47) will be practically relevant only if the random composite of interest is either well characterized as regards inclusion distribution (and geometry), or insensitive to inclusion distribution (and geometry). □

Level 3

In Level 3 we determine, for a given concentration c, the composite medium correlation length, $\lambda^C(c)$, by repeating the Level 2 procedure for evaluating $< K_e > (c, \lambda)$ for several values of λ. The correlation length concept is based on the regularity assumption that the limit

$$\lim_{\lambda \to \infty} < K_e > (c, \lambda) \equiv k_e(c)$$

exists. The correlation length is defined as that value of the supercell edge–length for which: $< K_e > (c, \lambda > \lambda^C(c))$ differs by no more than a prescribed small tolerance, $\varepsilon_e = \varepsilon_1 \, k_e$, from the assumed–to–exist asymptotic value, $k_e(c)$; the standard deviation of $K_e(c, \lambda > \lambda^C(c))$ is less than a prescribed small fraction, ε_2, of $k_e(c)$. The condition on the mean $< K_e >$ ensures that, as the supercell edge–length increases beyond λ^C (thus incorporating more particles), the mean (or the basic physics) does not change appreciably; the condition on the standard deviation of K_e at $\lambda > \lambda^C$ ensures that a particular realization of the medium in this range of λ has as effective conductivity which is not too far away from the mean $< K_e >$.

The importance of the correlation length is due, basically, to the fact that it allows the transition *periodic* → *random*: by systematically using long–range–periodic and short–range–random description of multicomponent media, one is able, if all assump-

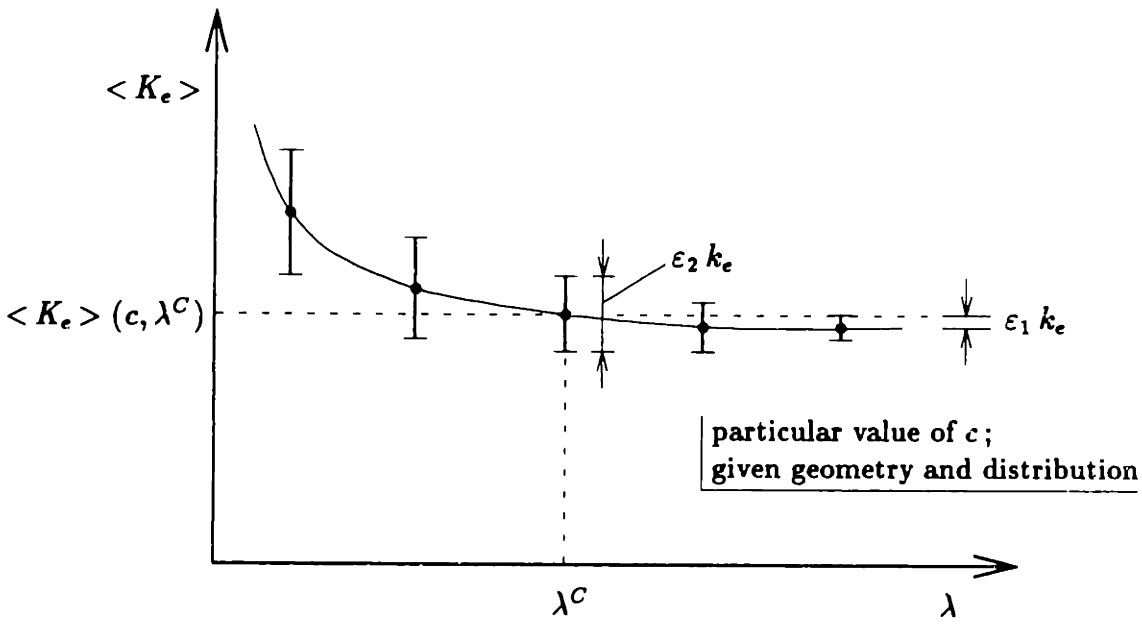

Figure 2-3: Illustration of the correlation length $\lambda^C(c)$. Dots represent $< K_e >$, and I-shaped bars represent $\sigma(K_e)$.

tions hold, to obtain results applicable to truly (real) random media. Notice that the periodicity of the supercell is a practical (not conceptual) constraint in simulation, or even analytical, studies.

The correlation length is illustrated schematically in Figure 2-3. The dots represent computed values for $< K_e >$, and the I-shaped bars represent the standard deviation of K_e, $\sigma(K_e)$. As λ increases, we expect that a spatial averaging effect will contribute to lowering the standard deviation of the ensemble. We remark that $\lambda^C(c)$ and $< K_e > (c, \lambda^C(c))$ will be useful for truly random unidirectional fibrous composites provided $\frac{\lambda^C}{L} \ll 1$, in which case the composites behavior can be investigated in a cost-effective manner in comparison with the original multiscale problem.

The most important practical application of the correlation length λ^C is simply that it allows one to know whether a composite body is large enough to apply $k_e(c)$ to compute bulk quantities. Additional applications of $\lambda^C(c)$ include determining whether a material sample is large enough, so that measurements (transients in particular, see e.g. Pitchumani & Yao (1992)) performed on it are representative of the

whole. Also, in simulations or theories requiring detailed field calculations, $\lambda^C(c)$ can be used in (periodic) supercell models as the proper size of the supercell; although it should lead to more accurate results, these will be more expensive than those obtained with single–inclusion cell models. □

Level 4

Finally, in Level 4, we determine, by repeating the evaluation procedure of Level 3 for different values of c, the functional dependencies of $\lambda^C(c)$ and $< K_e > (c, \lambda^C(c))$ for $0 < c < c_{max}$, where c_{max} is an appropriate maximum packing for the particular inclusion geometry and distribution under consideration [see e.g. Berryman (1983)]. More generally, in this Level one might construct $\lambda^C(\mathbf{p})$ and $< K_e > (\mathbf{p})$, where $\mathbf{p}$ is a vector of parameters related to the properties, geometry, and distribution of the continuous and dispersed phases; this more complex task might involve efficient statistical modelling techniques [see e.g. Yeşilyurt & Patera (1993)]. □

Given the four–level mesoscale process described above, the problem of heat conduction in a unidirectional fibrous composite for which the prescribed concentration distribution, $c(\mathbf{x})$, varies appreciably only on the macroscale, L, and for which the macroscale is large compared to $\max_{\mathbf{x}\in\Omega_{ma}} \lambda^C(c(\mathbf{x}))$, is basically solved: with high (quantifiable) probability, the macroscale result Q_{ma} based on (2.7), (2.19), and $k_e(c) \approx < K_e > (c, \lambda^C(c))$ from (2.47) will accurately predict the heat transfer rate Q of the original problem of Figure 2-1 *for any particular realization of the random composite.*

2.1.4 Microscale

The microscale analysis is concerned with the dispersed phase and its immediate neighborhood. It can take two forms: the development of appropriate models for the dispersed phase and for the continuous phase–dispersed phase interface; the development of appropriate models for clusters of very close inclusions or particles. The former is important to account for internal inclusion heat transfer or contact resis-

tance at the interface between the matrix and inclusions. Here, we assume perfect contact between the phases; since we are dealing with insulating inclusions, details of the interfacial interaction are embedded in the inclusion shape, here circular cylindrical. Also, we assume no internal physics, in that possible radiative or convective heat transfer inside the voids are neglected (if the inclusions are made of a nontransparent solid, these processes cannot occur). Notice that in the case of conducting inclusions, contact resistance play a very important role in the overall composite conduction capability; addition of bonding chemicals at the manufacturing stage can help reduce such thermal resistance. Also, when the composite is subjected to oscillating thermal loads, contact between the phases, due to differential thermal expansion, may be very good when heating, but poor when cooling.

We focus here on cluster models, which are critical in moderating the mesoscale computational burden: in most of our calculations to date — in which no cluster models are included — a large fraction (particularly at higher c) of the computational degrees of freedom are associated with couples or triples of nearly touching inclusions (see Chapter 3). We describe here a variational approximation technique possessing both reasonable approximation properties and readily obtained *a posteriori* error bounds. The bounds we construct rely on the minimization property of k_e', equation (2.41), and are, for the most part, not new. They derive, generally, from the classical variational estimation techniques of space expansion, space restriction, domain embedding and inclusion, and functional analysis [Hill & Power (1956), Keller, Rubenfeld & Molyneux (1967), Kim & Karrila (1991), Maday & Patera (1993)]; specifically, from earlier work on heat transfer variational bounds [Hashin & Shtrikman (1962), Elrod (1974), Magen, Mikiç & Patera (1988)]. The techniques by which we integrate these bounds into a numerical procedure are, however, new.

Consider a (initially single) pair of inclusions, shown in Figure 2-4, with centers, say, $\mathbf{y}_1$ and $\mathbf{y}_2$ in Ω_{sc} separated by a distance $d + a$, $\alpha = \frac{a}{d} \ll 1$, for which the segment connecting the inclusion centers, $\overline{\mathbf{y}_1\mathbf{y}_2}$, is inclined by an angle θ from the unit–vector in the y_1 direction. Denoting the unit–vector perpendicular to $\overline{\mathbf{y}_1\mathbf{y}_2}$ as $\mathbf{r}$, we define the "nip" region, Ω_{ni} (hatched area in Figure 2-4), as the intersection

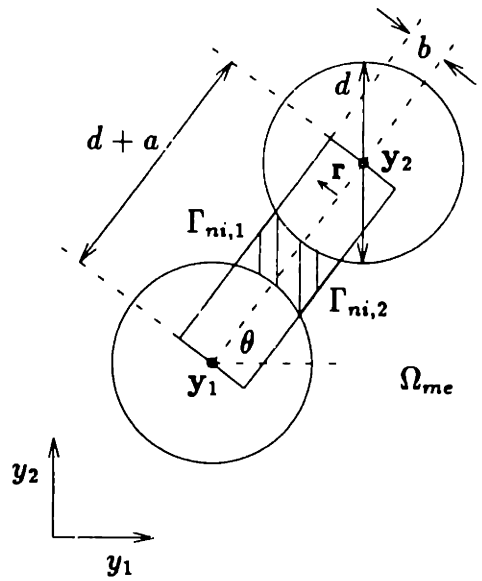

Figure 2-4: The nip region.

of Ω_{me} with the rectangle described by the four corners $\mathbf{y}_1 + b\mathbf{r}, \mathbf{y}_2 + b\mathbf{r}, \mathbf{y}_2 - b\mathbf{r}$, and $\mathbf{y}_1 - b\mathbf{r}$, where $\beta = \frac{b}{d} < \frac{1}{2}$. The parts of the segments $\overline{(\mathbf{y}_1 + b\mathbf{r})\,(\mathbf{y}_2 + b\mathbf{r})}$ and $\overline{(\mathbf{y}_1 - b\mathbf{r})\,(\mathbf{y}_2 - b\mathbf{r})}$ which lie within Ω_{me} are denoted $\Gamma_{ni,1}$ and $\Gamma_{ni,2}$, respectively. We now consider the *modified* mesoscale domain, $\tilde{\Omega}_{me} = \Omega_{me} \setminus \Omega_{ni}$, in which the nip region has been *removed*. It is then possible to construct rigorous lower and upper bounds for the effective conductivity,

$$k'_{e,LB}(c, \lambda, \{\mathbf{y}\}_N) \leq k'_e(c, \lambda, \{\mathbf{y}\}_N) \leq k'_{e,UB}(c, \lambda, \{\mathbf{y}\}_N)\,, \tag{2.49}$$

based only on solutions defined over $\tilde{\Omega}_{me}$: we avoid the computationally intensive nip region, while maintaining strict control over the resulting error. In this section, bounds are derived for the scalar k'_e, given in (2.19); extension to the full conductivity tensor can be pursued similarly to the treatment in Nir, Weinberger & Acrivos (1975). We first describe the bounds, and then discuss the actual micro–mesoscale interaction.

To arrive at an upper bound, we assume that, in the nip region, the temperature, χ_{UB}, is only a function of the direction perpendicular to the inter-center segment $\overline{\mathbf{y}_1\,\mathbf{y}_2}$. This is equivalent to pursuing the minimization (2.39) over a restricted class of

functions, and thus yields an *upper bound* for the actual effective conductivity; this is readily motivated physically by noting that our assumption of one-dimensionality is equivalent to an infinite continuous-phase conductivity parallel to $\overline{\mathbf{y}_1\mathbf{y}_2}$. The bound $k'_{e,UB}(c,\lambda,\{\mathbf{y}\}_N)$ will comprise two components: an outer contribution from minimization over $\tilde{\Omega}_{me}$, and an inner contribution from minimization over the nip region, Ω_{nip}. The Euler equation for the inner contribution can be solved analytically in terms of the unknown temperatures $\chi_{UB}|_{\Gamma_{ni,k}}$, $k=1,2$; this inner solution is then reflected in the *modified* outer problem as an inter-boundary "Robin" condition.

Specifically, we present the detailed equations for the algebraically simple case of $\theta = 0$, though the formulation applies for all θ. We now want to find the function χ_{UB} that minimizes $J^C_{\tilde{\Omega}_{me}}(v)$ over a restricted space $X_{\#,UB}(\Omega_{me})$, where $X_{\#,UB}(\Omega_{me})$ is the space of all functions $v(\mathbf{y}) \in H^1_{\#,0}(\Omega_{me})$ for which $v|_{\Gamma_{ni,k}} = C_k$, $k=1,2$. The functional $J^C_{\tilde{\Omega}_{me}}(v)$, given in (2.33), can be expressed as the sum $J^C_{\tilde{\Omega}_{me}}(v) = J^C_{\tilde{\Omega}_{me}}(v) + J^C_{\Omega_{nip}}(v)$; because $v = v(y_2)$ in the nip region,

$$\int_{\Omega_{nip}} \frac{\partial v}{\partial y_1}\, d\mathbf{y} = 0\,, \tag{2.50}$$

so that $J^C_{\tilde{\Omega}_{me}}(v)$ simplifies to $J^C_{\tilde{\Omega}_{me}}(v) + L^C_{\Omega_{nip}}(v)$, where

$$L^C_{\Omega_{nip}}(v) = \int_{\Omega_{nip}} \frac{\partial v}{\partial y_k}\frac{\partial v}{\partial y_k}\, d\mathbf{y}\,. \tag{2.51}$$

We can then minimize $L^C_{\Omega_{nip}}(v)$ over the space $X_{UB}(\Omega_{nip})$, where $X_{UB}(\Omega_{nip})$ is the space of all functions $v(\mathbf{y}) \in H^1_0(\Omega_{me})$ for which $v|_{\Gamma_{ni,k}} = C_k$, $k=1,2$; after solving the resulting Euler equation, we find that the minimizing functions $\chi_{UB,ni} \in \Omega_{nip}$ are of the form (see Appendix B for the derivation)

$$\frac{\partial \chi_{UB,ni}}{\partial y_2} = \frac{1}{l}\, G(\alpha,\beta)\,(\chi_{UB,ni}|_{\Gamma_{ni,1}} - \chi_{UB,ni}|_{\Gamma_{ni,2}})\,, \tag{2.52}$$

where l is the variable inter-inclusion distance parallel to $\overline{\mathbf{y}_1\mathbf{y}_2}$,

$$l = (1 + \alpha - \sqrt{1-4\eta^2}\,)\,d\,, \tag{2.53}$$

$\eta = \frac{y_2}{d}$, and $G(\alpha,\beta)$ is the integral geometric factor

$$G(\alpha,\beta) = \left(2\int_0^\beta \frac{d\eta}{1+\alpha-\sqrt{1-4\eta^2}}\right)^{-1} \tag{2.54}$$

($k_{co}\,G(\alpha,\beta)$ is the inner–solution nip conductance). Now, we want to minimize $J^C_{\tilde{\Omega}_{me}}(v)$ over the functions v in the space $X_{\#,UB}(\Omega_{me})$ *further* restricted by the form in (2.52) inside the nip. Taking the first variation of the functional $J^C_{\tilde{\Omega}_{me}}(v)$ and equating to zero, we then finally obtain the modified outer problem for $\theta = 0$: Find $\chi_{UB} \in X_{\#,UB}(\tilde{\Omega}_{me})$ such that

$$\begin{aligned}\int_{\tilde{\Omega}_{me}} k_{co}\frac{\partial v}{\partial y_k}\frac{\partial \chi_{UB}}{\partial y_k}\,d\mathbf{y} \;&+\; k_{co}\,(v|_{\Gamma_{ni,1}} - v|_{\Gamma_{ni,2}})\,G(\alpha,\beta)\,(\chi_{UB}|_{\Gamma_{ni,1}} - \chi_{UB}|_{\Gamma_{ni,2}}) \\ &= \frac{\Delta T}{L}\int_{\tilde{\Omega}_{me}} k_{co}\frac{\partial v}{\partial y_1}\,d\mathbf{y} \quad \forall v \in X_{\#,UB}(\tilde{\Omega}_{me})\,,\end{aligned} \tag{2.55}$$

where $v|_{\Gamma_{ni,k}} = C_k$, $k = 1,2$, are *part* of the solution. The above minimization procedure is somewhat analogous to minimizing a function of two variables, by first fixing one variable and finding the minimum with respect to the other, in terms of the constraint; next, we allow the artificial constraint to vary, and then minimize the now single–variable function.

The effective conductivity is now given by (see Appendix B for the derivation)

$$k'_{e,UB}(c,\lambda,\{\mathbf{y}\}_N) = k_{co}\left\{(1-c) - \frac{L^2}{\Delta T^2\,\lambda^2} I^C_{\tilde{\Omega}_{me}}(\chi_{UB})\right\}\,; \tag{2.56}$$

other representations for $k'_{e,UB}$ based on $J^{C,UB}_{\tilde{\Omega}_{me}}(v)$, the functional of which (2.55) is the first variation, are also possible. Note that the variational problems posed above involve slightly non–standard "torsion" boundary conditions, in which the solution is constrained to be, say, constant, over certain boundary segments; these boundary conditions can be shown to lead to well–posed problems.

A crude lower bound is even more easily obtained: we simply assume the nip region is filled with an insulator, or, equivalently, that χ_{LB} satisfies homogeneous natural (adiabatic) conditions on the $\Gamma_{ni,k}$, $k = 1,2$. That is, we find $\chi_{LB} \in X_{\#,LB}(\tilde{\Omega}_{me})$

such that

$$\int_{\tilde{\Omega}_{me}} k_{co} \frac{\partial v}{\partial y_k} \frac{\partial \chi_{LB}}{\partial y_k} \, d\mathbf{y} = \frac{\Delta T}{L} \int_{\tilde{\Omega}_{me}} k_{co} \frac{\partial v}{\partial y_1} \, d\mathbf{y} \quad \forall v \in X_{\#,LB}(\tilde{\Omega}_{me}) \,, \tag{2.57}$$

where $X_{\#,LB}(\tilde{\Omega}_{me})$ is the space of all λ–doubly periodic functions $v(\mathbf{y})$ for which both the function and derivative are square–integrable over the domain $\tilde{\Omega}_{me}$, and for which $\int_{\tilde{\Omega}_{me}} v \, d\mathbf{y} = 0$ (in fact, $X_{\#,LB}(\tilde{\Omega}_{me}) = H^1_{\#,0}(\tilde{\Omega}_{me})$). The resulting effective conductivity is

$$k'_{e,LB}(\tilde{c}, \lambda, \{\mathbf{y}\}_N) = k_{co} \left\{ (1 - \tilde{c}) - \frac{L^2}{\Delta T^2 \, \lambda^2} I^C_{\tilde{\Omega}_{me}}(\chi_{LB}) \right\} , \tag{2.58}$$

where

$$1 - \tilde{c} = \frac{\int_{\tilde{\Omega}_{me}} d\mathbf{y}}{\int_{\Omega_{sc}} d\mathbf{y}} \tag{2.59}$$

(notice that $\tilde{c}$ appears above, because the nip is filled with an insulator, and therefore it conducts no heat due to the imposed $\frac{\Delta T}{L}$). The physically plausible claim that the resulting quantity is a lower bound is readily shown mathematically by embedding (or inclusion),

$$k'_{e,LB} = \min_{v \in X_{\#,LB}} a^C_{\tilde{\Omega}_{me}}(v, v) \leq a^C_{\tilde{\Omega}_{me}}(\chi|_{\tilde{\Omega}_{me}}, \chi|_{\tilde{\Omega}_{me}}) \leq a^C_{\tilde{\Omega}_{me}}(\chi, \chi) = k'_e \,, \tag{2.60}$$

where the first inequality follows from the minimization property (2.41), with $\chi|_{\tilde{\Omega}_{me}}$ meaning χ restricted over $\tilde{\Omega}_{me}$ *and* shifted by a constant to satisfy $\int_{\tilde{\Omega}_{me}} \chi \, d\mathbf{y} = 0$, and the second inequality follows from the positive–definiteness of the bilinear form (2.40). (In practice, at low and moderate concentrations, this locally crude bound may be globally rather sharp, since the close–particle nip regions will typically *not* be the preferred conduits of heat.)

It is important to note that, within this general formulation, other local analyses are possible; in particular, by properly selecting the shape of the nip region and the form of candidate solutions, precise analytical microsolutions can be directly incorporated into large–scale simulations in a rigorously *quantifiable* fashion. Once we have obtained satisfactory microscale bounding procedures, the mesoscale procedure is modified accordingly: the nip regions of close–particle pairs (n–tuples are treated

pairwise) are eliminated, and the resulting bounds calculated through, say, (2.56) and (2.58). If the bounds, (2.49), are sufficiently sharp (i.e., bound "gap" on the order of the discretization error), the calculation is concluded; if the bounds are not sufficiently sharp, some or all of the nip regions are reduced in size, and the calculation is repeated. For the suggested, rather crude, lower bound, the bound "gap" in (2.49) can remain order unity even as β tends to zero; for more sophisticated insulator choices, the bound gap will decrease to $O(\alpha)$ as $\beta \rightarrow 0$. In any event, the *combined* analytical-numerical procedure is systematic and convergent. The procedure can result in very significant computational economies, and extends — in some cases rigorously, in other cases heuristically — to a large class of problems.

2.2 Creeping Flow Through Fibrous Porous Media

In this section, we present the formulation of the creeping flow problem; we follow the same structure/approach of the previous Section on the conduction problem. We take advantage of the similarities to shorten the presentation; this in itself is an example of the extendability/generality of the methodology, to treat different problems.

2.2.1 Description of the Original Multiscale Problem

Figure 2-5 shows an example of a (unidirectional) fibrous porous medium, where the continuous phase is now a fluid ("matrix"), and the inclusions are now solid obstacles. The same notation and overall description of Section 2.1.1, when applicable, is assumed.

The fluid is assumed Newtonian with density ρ_{co} and viscosity μ_{co}. The porous medium physically extends throughout a characteristic length L^P (the macroscale L is proportional to L^P); sub-regions of the external boundary may be walls, Γ_w, or upstream (inlet) and downstream (outlet) sections, Γ_{in} and Γ_{out}, where constant pressures p_{in} and p_{out} are maintained, respectively. The bulk quantity of interest is

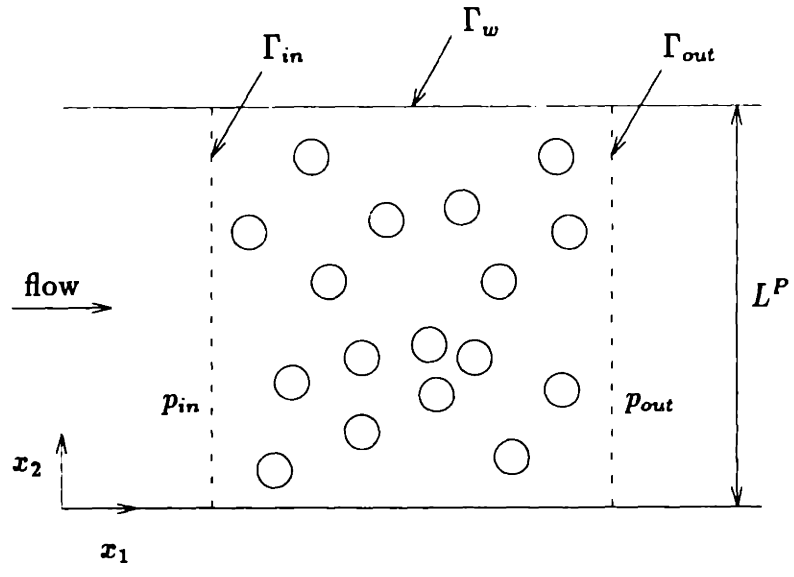

Figure 2-5: An example of a fibrous porous medium: a filter.

the volumetric flow rate, Q_v , passing through the filter. The effective property is now the permeability, defined by Darcy's law as

$$< \mathbf{u}_{orig} >_v = -\frac{1}{\mu_{co}} \underline{\kappa}' \cdot < \nabla p_{orig} >_v , \tag{2.61}$$

where $\mathbf{u}_{orig}$ is the local fluid velocity, $\underline{\kappa}'$ is the permeability tensor, and ∇p_{orig} is the local pressure gradient. In the following three sections, we present the macroscale, mesoscale, and microscale problems for creeping flow through a porous medium.

2.2.2 Macroscale

The steady-state creeping flow equation for the homogenized medium (a flowing fluid) in the macroscale region, from conservation of mass and Darcy's law, reads

$$-\frac{\partial}{\partial x_i}\left[\frac{\kappa_{ij}(c(\mathbf{x}))}{\mu_{co}}\frac{\partial p_{ma}}{\partial x_j}\right] = 0 \text{ in } \Omega_{ma} , \tag{2.62}$$

with Dirichlet and Neumann boundary conditions

$$p_{ma} = p_{in} \text{ on } \Gamma_{in} , \tag{2.63}$$

$$p_{ma} = p_{out} \text{ on } \Gamma_{out} , \tag{2.64}$$

and

$$-\frac{\kappa_{ij}}{\mu_{co}} \frac{\partial p_{ma}}{\partial x_j} n_i = 0 \text{ on } \Gamma_w , \tag{2.65}$$

where $p_{ma}(\mathbf{x})$ is the macroscale pressure, $\underline{\kappa} \equiv \kappa_{ij}(c)$, $i,j = 1,2$, is the permeability tensor–concentration function, $\mathbf{n} = n_i$ denotes the unit outward normal to the boundary, and the summation convention over repeated indices is assumed. [Note that the *original* problem of Figure 2-5 can be expressed by equations (2.62)–(2.65) if we replace: p_{ma} with p_{orig} ; $\kappa_{ij}(c)$ with 1 (from mass and momentum conservation, pressure is a harmonic function) and Ω_{ma} with Ω_{co} in (2.62); Γ_w with $\Gamma_w \cup \partial\Omega_{di}$ in (2.65). Once p_{orig} is found, the velocity $\mathbf{u}_{orig}$ is determined by solving the corresponding Poisson equation in Ω_{co} with no–slip boundary condition on $\Gamma_w \cup \partial\Omega_{di}$, and inflow–outflow on $\Gamma_{in} - \Gamma_{out}$.] Solving (2.62)–(2.65) for p_{ma} , e.g. numerically with a software package, the requisite (global) volumetric flow rate can be calculated as

$$Q_{v_{ma}} = \int_{\Gamma_{out}} -\frac{\kappa_{ij}(c(\mathbf{x}))}{\mu_{co}} \frac{\partial p_{ma}}{\partial x_j} n_i \, ds . \tag{2.66}$$

The integrand of equation (2.66), from the differential form of Darcy's law [Scheidegger (1974)], is simply $\mathbf{u}_{ma} \cdot \mathbf{n}$, where $\mathbf{u}_{ma}(\mathbf{x})$ is the macroscale velocity. From homogenization theory [Bensoussan, Lions & Papanicolaou (1978), Mei & Auriault (1989)], it is known that, for a medium with λ–periodic microstructure, in the limit $\epsilon = \frac{\lambda}{L} \to 0$, the macroscale pressure p_{ma} and macroscale velocity $\mathbf{u}_{ma}$ locally approximate, with error $O(\epsilon)$, the original pressure p_{orig} and original velocity $\mathbf{u}_{orig}$, respectively.

The permeability is a characteristic of the porous medium as a whole, and has dimension of length squared; in nondimensional terms, the ratio $\kappa^*_{ij} \equiv \frac{\kappa_{ij}}{d^2}$ in general depends on inclusion geometry, expressed by shape factors, and on the concentration c. Only the latter dependence is indicated, as the former is, for the purposes of this thesis, fixed.

2.2.3 Mesoscale

The mesoscale problem again encompasses four nested levels, exactly analogous to their conduction counterparts, the main difference being that the equations are a little more complicated. Its solution provides the proper function $\underline{\kappa}'(c(\mathbf{x}))$ to the macroscale problem. Again, microscale analysis can be incorporated into the mesoscale equations, though in this work the ones actually solved have no microscale preparation. In what follows, the inclusion distribution is also assumed isotropic.

Level 1

The mesoscale supercell depicted in Figure 2-2, and described in Section 2.1.3, is appropriate for the creeping flow problem, the N disks now representing impermeable fibers. The partial differential equations for the mesoscale pressure, $p_{me} = \epsilon\, p(\mathbf{y})$, and mesoscale velocity vector, $\mathbf{u}_{me} = \epsilon\, \mathbf{u}(\mathbf{y}) = \epsilon\,(u_1(y_1, y_2), u_2(y_1, y_2))$, express conservation of momentum and mass, and are given by

$$-\frac{\partial}{\partial y_j}(\mu_{co}\frac{\partial u_i}{\partial y_j}) + \frac{\partial p}{\partial y_i} = \frac{\Delta P}{L}\delta_{1i} \text{ in } \Omega_{me} \text{ for } i = 1, 2\,, \tag{2.67}$$

where δ_{ij} is the Kronecker delta, and

$$-\frac{\partial u_i}{\partial y_i} = 0 \text{ in } \Omega_{me}\,, \tag{2.68}$$

with no–slip Dirichlet and periodic boundary conditions

$$\mathbf{u} = 0 \text{ on } \partial\Omega_{me}\,, \tag{2.69}$$

and

$$\mathbf{u}(\mathbf{y}) = \mathbf{u}(\mathbf{y} + \lambda(m_1\mathbf{e}_1 + m_2\mathbf{e}_2)) \text{ on } \partial\Omega_{\#}\,, \tag{2.70}$$

$$p(\mathbf{y}) = p(\mathbf{y} + \lambda(m_1\mathbf{e}_1 + m_2\mathbf{e}_2)) \text{ on } \partial\Omega_{\#}\,, \tag{2.71}$$

where the y_1 direction has been chosen for the driving pressure gradient, the scaling $\frac{\Delta P}{L}$ is included to preserve dimensionality, $m_1\,, m_2 \in \{0, \pm 1, \pm 2, \ldots\}$, and the $\mathbf{e}_i\,,\ i =$

1, 2, are orthonormal basis vectors. Since adding a constant to a pressure solution of the boundary value problem (2.67)–(2.71) yields another solution, we further require for uniqueness that

$$\int_{\Omega_{me}} p \, d\mathbf{y} = 0 \,, \tag{2.72}$$

where $d\mathbf{y} = dy_1 \, dy_2$. The forcing term on the right–hand–side of (2.67) is the linearized macroscale pressure gradient analogous to the linear macroscale temperature gradient appearing in (2.10).

The Level–1 permeability of the (isotropic) supercell, or of the infinite medium, for the particular configuration $\{\mathbf{y}\}_N$, $\kappa'(c, \lambda, \{\mathbf{y}\}_N)$, is defined in equation (2.61), and takes the form

$$\kappa'(c, \lambda, \{\mathbf{y}\}_N) = \mu_{co}^2 \, \frac{L^2}{\Delta P^2 \, \lambda^2} I^P_{\Omega_{me}}(\mathbf{u}) \,, \tag{2.73}$$

where

$$I^P_{\Omega}(\mathbf{v}) = \frac{\Delta P}{\mu_{co} \, L} \int_{\Omega} v_1 \, d\mathbf{y} \,. \tag{2.74}$$

In order to obtain equation (2.73), we first observe that, in equation (2.61), we have $< \nabla p_{orig} >_v = -\frac{\Delta P}{L} \mathbf{e}_1$, which is the imposed macroscale pressure gradient (analogous to $-\frac{\Delta T}{L}$ in Section 2.1.3); next, we recognize that $< \mathbf{u}_{orig} >_v \equiv \frac{1}{\lambda^2} \int_{\Omega_{me}} u_1 \, d\mathbf{y}$, since on the mesoscale, the macroscale velocity appears to be zero, to $O(\epsilon^2)$ ($< \mathbf{u}_{orig} >_v$ can be viewed as a superficial flow rate across the supercell). Notice that, by periodicity, the average over one supercell must equal the average over the entire medium. A more general form of equation (2.73) is derived rigorously in Mei & Auriault (1989) with (periodic) homogenization theory. We also introduce the functional $J^P_{\Omega}(\mathbf{v})$ (related to the "excess dissipation"),

$$J^P_{\Omega}(\mathbf{v}) = 2 \, I^P_{\Omega}(\mathbf{v}) - \int_{\Omega} \frac{\partial v_i}{\partial y_k} \frac{\partial v_i}{\partial y_k} \, d\mathbf{y} \,. \tag{2.75}$$

By multiplying (2.67) by $\mathbf{u}$, integrating over Ω_{me}, and using the divergence theorem and equation (2.68), we derive

$$I^P_{\Omega_{me}}(\mathbf{u}) = J^P_{\Omega_{me}}(\mathbf{u}) = \int_{\Omega_{me}} \frac{\partial u_i}{\partial y_k} \frac{\partial u_i}{\partial y_k} \, d\mathbf{y} \,. \tag{2.76}$$

From (2.73) and (2.76) we note that the permeability will always be positive, as required for well-posedness of the macroscale problem.

Similarly to the conduction problem, both our microscale analytical techniques and numerical methods will be founded upon the well-known variational form of (2.67) and (2.68) [Girault & Raviart (1986), pp. 80-84],

$$\mathbf{u} = \arg \max_{\mathbf{v} \in Z} J^P_{\Omega_{me}}(\mathbf{v}) , \tag{2.77}$$

where $Z = \{(v_1, v_2) \in (H^1_{0\#}(\Omega_{me}), H^1_{0\#}(\Omega_{me})) \,|\, \mathrm{div}\, \mathbf{v} = 0\}$, and $H^1_{0\#}(\Omega_{me})$ is the space of all λ-doubly periodic functions which vanish on $\partial\Omega_{me}$, and for which both the function and derivative are square-integrable over Ω_{me}. In order to arrive at the standard velocity-pressure weak form, we first transform the constrained maximization (2.77) into an unconstrained saddleproblem: that is, we enlarge the velocity space to include *all* functions (v_1, v_2) in $(H^1_{0\#}(\Omega_{me}), H^1_{0\#}(\Omega_{me}))$, and introduce a Lagrange multiplier — the pressure, p — to impose the incompressibility constraint. Taking the first variation of the resulting Lagrangian, we obtain the weak form: Find $(u_1, u_2, p) \in (H^1_{0\#}(\Omega_{me}), H^1_{0\#}(\Omega_{me}), L^2_{\#,0}(\Omega_{me}))$ such that

$$\mu_{co} \int_{\Omega_{me}} \frac{\partial v_i}{\partial y_k} \frac{\partial u_i}{\partial y_k} \, d\mathbf{y} - \int_{\Omega_{me}} \frac{\partial v_i}{\partial y_i} \, p \, d\mathbf{y} = \frac{\Delta P}{L} \, \delta_{1i} \int_{\Omega_{me}} v_1 \, d\mathbf{y} \quad \forall (v_1, v_2) \in (H^1_{0\#}(\Omega_{me}))^2 , \tag{2.78}$$

$$- \int_{\Omega_{me}} q \, \frac{\partial u_i}{\partial y_i} \, d\mathbf{y} = 0 \quad \forall q \in L^2_{\#,0}(\Omega_{me}) , \tag{2.79}$$

where $L^2_{\#,0}(\Omega_{me})$ is the space of all λ-doubly periodic functions $q(\mathbf{y})$ which are square-integrable over Ω_{me} (note that candidate pressures need not be continuous), and for which $\int_{\Omega_{me}} q \, d\mathbf{y} = 0$. From (2.73), (2.76), and (2.77) we can derive the following expression for the permeability,

$$\kappa'(c, \lambda, \{\mathbf{y}\}_N) = \mu^2_{co} \, \frac{L^2}{\Delta P^2 \, \lambda^2} \max_{\mathbf{v} \in Z} J^P_{\Omega_{me}}(\mathbf{v}) . \tag{2.80}$$

The expression (2.80) is, of course, related to the Helmholtz stationary-dissipation principle [Batchelor (1967), Hill & Power (1956), Keller, Rubenfeld & Molyneux

(1967), Kim & Karrila (1991)] Again, in the anisotropic case, analogous expressions for the components of the permeability tensor can be obtained following the development in Nir, Weinberger & Acrivos (1975).

Finally, we nondimensionalize equations (2.73), (2.78) and (2.79). Choosing (arbitrarily) the characteristic pressure $p^C = \Delta P(d/L)$, and the diameter d as the characteristic length, we define: $\mathbf{u}^* = \mathbf{u}/U$, $\mathbf{v}^* = \mathbf{v}/U$, $p^* = p/[\Delta P(d/L)]$, $q^* = q/[\Delta P(d/L)]$, $\mathbf{y}^* = \mathbf{y}/d$ and $\lambda^* = \lambda/d$, where $U = \Delta P\, d^2/\mu_{co}\, L$ is the velocity scale; equations (2.73), (2.78) and (2.79) take, respectively, the normalized forms

$$\int_{\Omega_{me}} \frac{\partial v_i^*}{\partial y_k^*} \frac{\partial u_i^*}{\partial y_k^*}\, d\mathbf{y}^* - \int_{\Omega_{me}} \frac{\partial v_i^*}{\partial y_i^*}\, p^*\, d\mathbf{y}^* = \delta_{1i} \int_{\Omega_{me}} v_1^*\, d\mathbf{y}^* \quad \forall (v_1^*, v_2^*) \in (H^1_{0\#}(\Omega_{me}))^2\,, \tag{2.81}$$

$$-\int_{\Omega_{me}} q^* \frac{\partial u_i^*}{\partial y_i^*}\, d\mathbf{y}^* = 0 \quad \forall q^* \in L^2_{\#,0}(\Omega_{me})\,, \tag{2.82}$$

and

$$\kappa'^* = \frac{\kappa'}{d^2} = \frac{1}{\lambda^{*2}} \int_{\Omega_{me}} u_1^*\, d\mathbf{y}^*\,. \tag{2.83}$$

Equations (2.81) and (2.82) constitute the actual supercell problem numerically solved in Chapter 3, in order to determine κ'^* as given in (2.83). Notice that the functional dependence is $\kappa'^* = \kappa'^*(c, \lambda^*, \{\mathbf{y}^*\}_N)$. □

Level 2

Similarly to the conduction problem, in Level 1 the concentration c (often the porosity, equal to $1 - c$, is used in the literature) and the supercell size λ were input; furthermore, the configuration of the N inclusions, expressed by their fixed positions $\{\mathbf{y}\}_N$, was assumed given. The permeability of the supercell was then determined as $\kappa'(c, \lambda, \{\mathbf{y}\}_N)$ (equation (2.73)). In Level 2, we use the *same* joint probability density function assumed for the composites, expressed by equation (2.46) (see Section 2.1.3). Again, *a posteriori* sensitivity studies can test such JPDF for porous media. We also assume asymptotically uniform statistical properties of P_N as λ, and hence N, tend to infinity.

The permeability of the medium is now a random variable, κ, expressed as a

deterministic function of the random inclusion positions, $\kappa = \kappa'(c, \lambda, \{\mathbf{Y}\}_N)$, determined in Level 1. The objective of Level 2 is to determine the average permeability of the porous medium over the ensemble of configurations, $< \kappa > (c, \lambda)$:

$$< \kappa > (c, \lambda) = \int_{\{\mathbf{y}\}_N \in \Omega_{ic}^N} \kappa'(c, \lambda, \{\mathbf{y}\}_N)\, P_N(\{\mathbf{y}\}_N)\, d\mathbf{y}_1, \ldots, d\mathbf{y}_N\,; \tag{2.84}$$

in nondimensional form, we write

$$< \kappa^* > (c, \lambda^*) = \frac{< \kappa >}{d^2} = \int_{\{\mathbf{y}^*\}_N \in \Omega_{ic}^N} \kappa'^*(c, \lambda^*, \{\mathbf{y}^*\}_N)\, P_N(\{\mathbf{y}^*\}_N)\, d\mathbf{y}_1^*, \ldots, d\mathbf{y}_N^*\,. \tag{2.85}$$

Again, we use Monte–Carlo methods (see Chapter 3) to evaluate (2.85), which require repetition of the Level 1 procedure for many realizations of the porous medium (i.e., many different sets of configurations $\{\mathbf{y}^*\}_N$). It should be pointed out that the resulting $< \kappa >$ in (2.84) will be practically relevant only if the random porous medium of interest is either well characterized with respect to inclusion distribution and geometry, or insensitive to inclusion distribution and geometry. □

Level 3

In Level 3 we determine, for a given concentration c, the porous medium correlation length, $\lambda^P(c)$, by repeating the Level 2 procedure for evaluating $< \kappa > (c, \lambda)$ for several values of λ. The regularity assumption for $< \kappa > (c, \lambda)$, and the definition of $\lambda^P(c)$ are exactly analogous to the ones given in Section 2.1.3, with permeabilities, κ, in place of effective conductivities, k_e.

The most important practical application of the correlation length λ^P is simply that it allows one to know whether a porous body is large enough to apply $\kappa(c)$ to compute bulk quantities. Additional practical applications of $\lambda^P(c)$ include determination of filtration efficiency and particle (e.g. dust) capture: recently, Shapiro & Brenner (1990) presented a more sophisticated filtration theory (as compared to conventional, e.g. in Davies (1973)) in which a numerically obtained velocity field, in a single–inclusion periodic cell, is used in the calculations of macroscopic dispersion

coefficients. These are related to the overall filter behavior, and can be used to assess its performance. Periodic (super)cells of edge–length $\lambda^P(c)$ should lead to more accurate and useful results (though more expensive), as the basic physics of the *random* porous medium will be captured. □

Level 4

Finally, in Level 4, we determine, by repeating the evaluation procedure of Level 3 for different values of c, the functional dependencies of $\kappa(c)$ and $\lambda^P(c)$ for the range $0 < c < c_{max}$, where c_{max} is an appropriate maximum packing for the particular inclusion geometry and distribution under consideration. Again, richer parameter spaces may be investigated using statistical modelling techniques. □

Given the four–level mesoscale process described above, the problem of creeping flow through fibrous porous media for which the prescribed concentration distribution, $c(\mathbf{x})$, varies appreciably only on the macroscale, L, and for which the macroscale is large compared to $\max_{\mathbf{x}\in\Omega_{ma}} \lambda^P(c(\mathbf{x}))$, is basically solved: with high (quantifiable) probability, the macroscale result $Q_{v_{ma}}$ based on (2.66), (2.73), and $\kappa(c) \approx < \kappa > (c, \lambda^P(c))$ from (2.84) will accurately predict the volumetric flow rate Q_v of the original problem of Figure 2-1 *for any particular realization of the random porous medium.*

2.2.4 Microscale

The microscale analysis for the porous medium problem is somewhat simpler than that for the conduction problem, due to complete lack of internal physics and interfacial interaction (fiber surface changes due to, e.g., dust accumulation or chemical reactions being ignored). Those factors account for much of the complexity in the study of multicomponent media systems involving drops and bubbles [Clift, Grace & Weber (1978)]. We are thus mainly concerned with cluster models, which we briefly discuss; they are based on the variational principle (2.80).

Again, the purpose of cluster models is to avoid computationally intensive regions

between close inclusions; relative to the conduction problem, they play a more important role here, since the Stokes equations, on the same domain, are more complex. Nip-region-based lower and upper bounds for the components of the permeability tensor can be constructed; here we discuss only the (scalar) isotropic case (variational principles in Nir, Weinberger & Acrivos (1975) can be used for extension to the anisotropic case). For example, to generate a crude upper bound, κ'_{UB}, we can simply *enlarge* the nip region, as shown in Figure 2-6a. To construct a crude lower bound, κ'_{LB}, it suffices to replace the nip region with a *blockage*, as shown in Figure 2-6b. These physically plausible enlargement and blockage constructions can be rigorously proven to produce upper and lower bounds, respectively; the proofs are based on variational embedding arguments, in which a maximizing (or dissipation-minimizing) solution on a smaller (fluid) domain is extended (by zero, due to no-slip boundary conditions) to construct a non-maximizing candidate (test function) on a larger domain. A much sharper lower bound can be obtained by requiring that candidate velocities in the nip region reduce to parallel parabolic profiles; this bound results in a modified outer Stokes problem analogous to (2.55). The resulting permeability is a lower bound: mathematically, because the space of functions over which we maximize the functional $J^P_{\Omega_{m\epsilon}}(\mathbf{v})$ is a subspace of Z; physically, because the fluid viscosity in the nip region in the direction parallel to the inter-center segment is now effectively infinite. As for the conduction problem, these local-modification bounding techniques permit us to address exceptional — computationally intensive — events with resolution *no greater* than that required to accurately predict the *macroscopic* properties (e.g., at low concentrations, nip regions are unlikely to play an important role, so it is very expensive *not* to use the bounds, due to unnecessary deteriorated conditioning, see Section 3.2.3).

We should also note that velocities in the nip regions may be obtained with a resistance matrix formulation to account for the near-field lubrication effects, similarly to the approach by Brady & Bossis (1985, 1988) in the Stokesian dynamic technique (Section 1.2.3). An outer problem can then be obtained to resolve the flow outside the nip regions, thus allowing for accurate determination of the permeability, while

avoiding the nips. The implementation of this formulation is more involved.

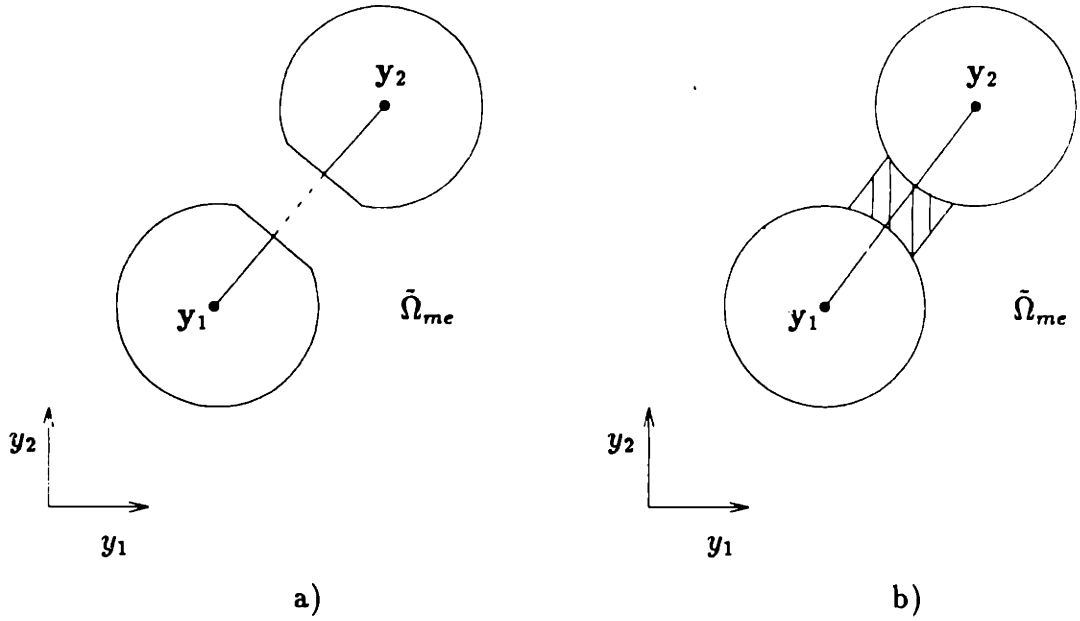

Figure 2-6: Microscale cluster models: a) nip region enlargement; b) nip region blockage.

◇

Extension to Sedimentation In closing Chapter 2, we remark that a further extension of the methodology is set forth in Appendix C, where the (two–dimensional) sedimentation problem is considered. Only the formulation and a brief discussion of attendant numerical issues are presented; no implementation was pursued.

Chapter 3

Numerical Methods

In this Chapter, we concentrate on the first three Levels of the mesoscale problems described in Chapter 2; since in this study the concentration is the only parameter for both the conduction and creeping flow problems, Level 4 thus just consists of repeating Levels 1, 2, and 3 for different concentration values. The microscale nip–region analyses (Sections 2.1.4 and 2.2.4) lead to the modified mesoscale equations; numerical methods for modified outer problems, e.g. equation (2.55), which require only minimal modification of standard finite–element discretizations and bases, are briefly discussed in the last section of Appendix C, in the more complex case of sedimentation. The macroscale problems require relatively little computation, and can be solved with conventional (analytical or numerical) methods. In what follows, unless specifically discriminated, the conduction and creeping flow problems are treated identically.

3.1 Overview

As mentioned in Section 1.3, our methodology for the analysis of multicomponent random media is based on a parallel nested Monte–Carlo partial–differential–equation procedure. The Monte–Carlo part brings the computational task within reach; the (automated) parallel partial–differential–equation (PDE) solution part exploits well–known advantages of parallel processing. A schematic of our procedure, to solve the

computationally–intensive four–level mesoscale problems of Sections 2.1.3 and 2.2.3, is given below:

START

Level 4: for each concentration value c_i , $i = 1, 2, \ldots, n_c$,

Level 3: for each supercell size λ_j , $j = 1, 2, \ldots, n_\lambda$,

Level 2: Outer Monte–Carlo; on a serial platform:

draw a sample, $\{\mathbf{y}\}_N$, from the inclusion JPDF

construct supercell domain for the configuration $\{\mathbf{y}\}_N$

export to parallel processors

Level 1: Inner PDE Solution; on a parallel machine:

loop: for each realization (i.e., sampled configuration),

mesh, discretize, and solve mesoscale problem

compute and save effective property, $EP(c_i, \lambda_j, \{\mathbf{y}\}_N)$

endloop

End of Level 1

perform statistical analysis

(i.e., estimate $< EP > (c_i, \lambda_j)$ and associated uncertainties)

End of Level 2

determine correlation length, $\lambda^{EP}(c_i)$

record $< EP > (c_i, \lambda^{EP}(c_i))$

End of Level 3

construct function $< EP > (c)$

End of Level 4

END

In Section 3.2, we describe the inner parallel partial–differential–equation solution part, and in Section 3.3, the outer Monte–Carlo part. For clarity of exposition, we include the supercell domain construction and partition at the beginning of Section 3.2, since a domain is needed before mesh generation and the subsequent steps of Level 1.

3.2 Partial–Differential–Equation Solution

The Level 1 procedure of the mesoscale problem is the inner loop of our nested Monte–Carlo partial–differential–equation solution approach. Its essential aspect is the solution of equations (2.37), (2.55), or (2.57) for the conduction problem, or equations (2.67)–(2.68) for the porous medium problem, which must be repeated *many* times as evoked by Levels 2, 3, and 4. The driving requirements are first, automation, and second, distributed–memory parallel processing: the former is required in order to ensure minimal intervention in the production–run stage, which may require solutions of hundreds of equations to determine a single effective–property (Level 1) data point; the latter is required to ensure, first, that adequate — scalable — speed and memory are available as problem size increases, and second, that the computations exploit the very considerable cost advantage of commodity–chip–based supercomputing. From these broad constraints we derive the following general algorithmic skeleton: geometry description and pre–mesh data–parallel domain partition (Section 3.2.1); automatic and parallel simplex mesh generation (Section 3.2.2); finite element discretization and energy–based calculation of effective properties (Section 3.2.3); iterative parallel solution of the finite element equations and incomplete–iteration error control (Sections 3.2.4 and 3.2.5).

We summarize the motivation for the essential elements of this computational plan. First, *pre*–mesh domain partition followed by parallel and subdomain–based mesh generation attenuates two typical limitations: the workstation–to–parallel bottleneck associated with workstation–based mesh generation, and the node–memory and internode–parallel communication bottlenecks associated with parallel global mesh generation. Second, simplex elements both efficiently represent the general, complex geometries associated with multicomponent random media *and* admit relatively robust automatic mesh generation procedures. Third, variational discretization procedures readily incorporate our variational nip–region bounds, and, furthermore, provide optimal order accuracy for the energy–norm effective properties of interest, (2.41) and (2.80); *volume*–based finite element methods are most appropriate for

nonlinear media. Fourth, iterative solution techniques, for the problems of interest, require both much less memory and significantly fewer operations than direct solution methods, in particular in three space dimensions; iterative techniques are also more readily and efficiently parallelized. Lastly, incomplete–iteration error estimation and control ensures solution integrity without disruption of the higher–Level mesoscale processes. These essential elements are described next.

3.2.1 Domain Generation and Partition

Each configuration $\{\mathbf{y}\}_N$ of the inclusions in the supercell, corresponding to a realization of the random medium, requires the solution of a boundary value problem in the periodic domain Ω_{me} (Level 1). Since we have to generate many such domains as required by the outer (Level 2) Monte–Carlo driver (Section 3.3), we need an automatic and robust preprocessor that can take a sequence of $\{\mathbf{y}\}_N$'s as input, and systematically output periodic supercells, each pre–partioned for subsequent distribution among parallel processors.

Our domain generation and partition procedure is entirely based on the *Voronoi diagram*. In two dimensions, given a set of N_G points (called generators) in a plane, the Voronoi diagram identifies N_G regions (called Voronoi tiles, or simply tiles) whose interior points are closest to the corresponding generator; clearly, given an Euclidean norm, it can be defined more generally in n–dimensional space [Preparata and Shamos (1988)]. A typical Voronoi diagram is shown in Figure 3-1. Note that the outermost tiles may be bounded (as shown) or unbounded, depending on whether or not an artificial box is placed around the region of interest.

As indicated in Figure 3-1, each Voronoi edge shares two generators (or tiles), and each Voronoi point is the intersection of three Voronoi edges. A Voronoi edge, by construction, is equidistant from its two associated generators, so that any Voronoi point is the center of the circle that goes through the three closest generators around it. A Voronoi tile is always a convex, in general irregular, polygon. An example of a degeneracy that may occur is shown in Figure 3-2, where four edges meet at one point. This and other types of degeneracies make it very difficult to construct and

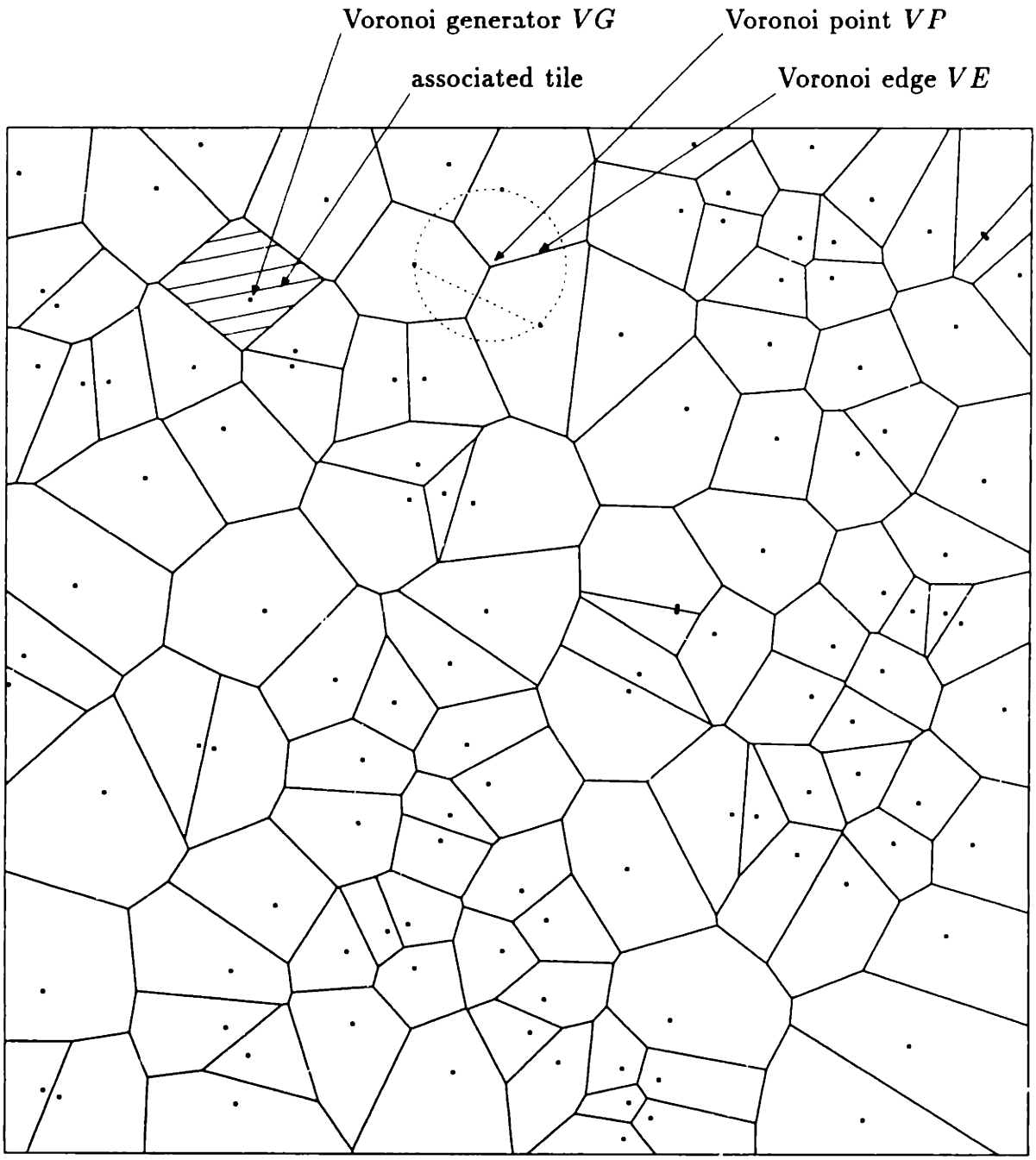

Figure 3-1: A typical Voronoi diagram.

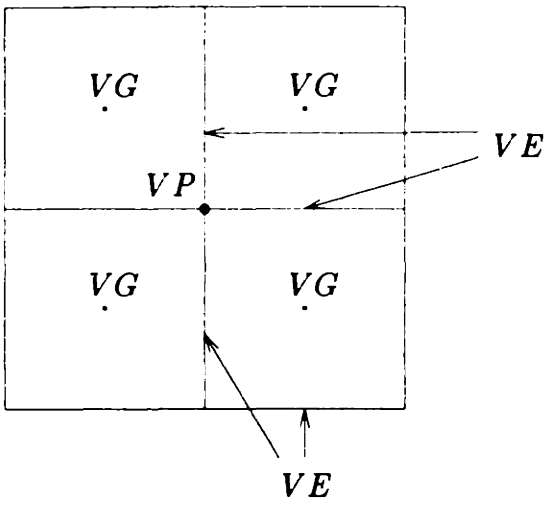

Figure 3-2: An example of a degenerate Voronoi diagram: four edges (VE) meet at one point (VP).

implement robust algorithms to produce Voronoi diagrams (in 2–D or 3–D) for a given set of generators.

The Voronoi diagram has been used in many previous applications. Winterfeld, Scriven & Davis (1981) studied percolation and conductivity of random two–dimensional composites (Section 1.2.4). The composites were generated by assigning binary values to the tiles, corresponding to either a conducting or an insulating constituent. The Voronoi diagram is also used in mesh generation algorithms, where three Voronoi generators, around one Voronoi point, make one triangle. The dual diagram so generated (a mesh) is called the Delaunay, and the mesh generation process, Delaunay triangulation [see e.g. Preparata & Shamos (1988)].

We used a FORTRAN program developed by Sugihara & Iri (1989a, 1989b), called VORONOI2, to construct plane Voronoi diagrams for our specific purposes. The program is a topology–oriented, $O(N_G)$ time, implementation of the incremental (or divide–and–conquer) method, in which the generators are sequentially added, and their tiles are determined by expanding trees from the neighboring Voronoi points. VORONOI2 is very robust, and can generate a diagram for up to one million generators in single precision. Robustness is attained by placing more emphasis on topo-

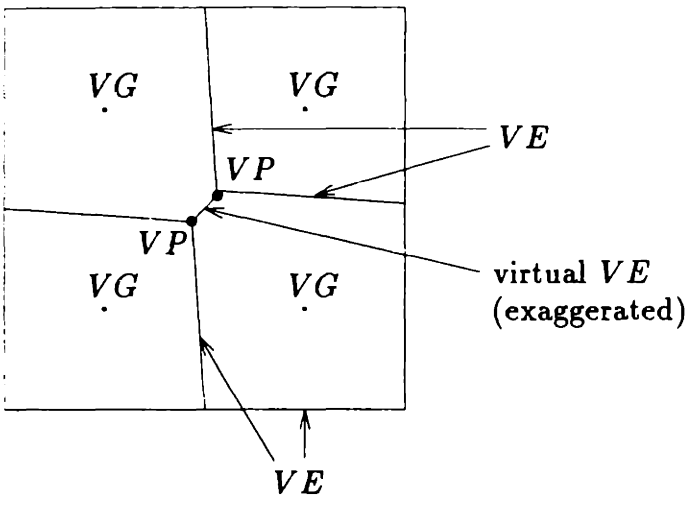

Figure 3-3: Virtual (topological, zero–length) edge inserted by VORONOI2 to avoid a degenerate Voronoi diagram.

logical structures than on numerical values. As an example, the degeneracy shown in Figure 3-2 is simply handled, by inserting a *virtual*, zero–length, Voronoi edge at the point where the four (original) edges meet, as illustrated in Figure 3-3.

Our algorithm to generate periodic supercells, based on the properties of the Voronoi diagram and its construction by VORONOI2, is described next. We assume a particular realization, i.e., the inclusion positions $\{\mathbf{y}\}_N \in \Omega_{sc}$, to be given; the sampling method to generate many $\{\mathbf{y}\}_N$'s is described in Section 3.3.1. A square box of edge–length 5λ, shown in Figure 3-4, is first constructed. It consists of 25 square supercells of edge–length λ each (like the one shown in Figure 2-2), called S–supercells. The origin of the coordinate system $\mathbf{y} = (y_1, y_2)$ is placed at the lower left corner of the middle S–supercell, which contains the N inclusions located at $\mathbf{y}_1, \ldots, \mathbf{y}_N$. The set $\{\mathbf{y}\}_N$ is then replicated over the other 24 S–supercells, and a new set of $N_G = 25N$ generators is obtained; each element in the set, a generator $\mathbf{y}_{G_i}$, $i = 1, \ldots, N_G$, is given by

$$\mathbf{y}_{G_i} = \mathbf{y}_j + \lambda(m_{1i}\,\mathbf{e}_1 + m_{2i}\,\mathbf{e}_2)\,, \tag{3.1}$$

where $i = 1, \ldots, N_G$, $j = 1 + \text{int}(\frac{i-1}{25})$ (int(arg) is the largest nonnegative integer

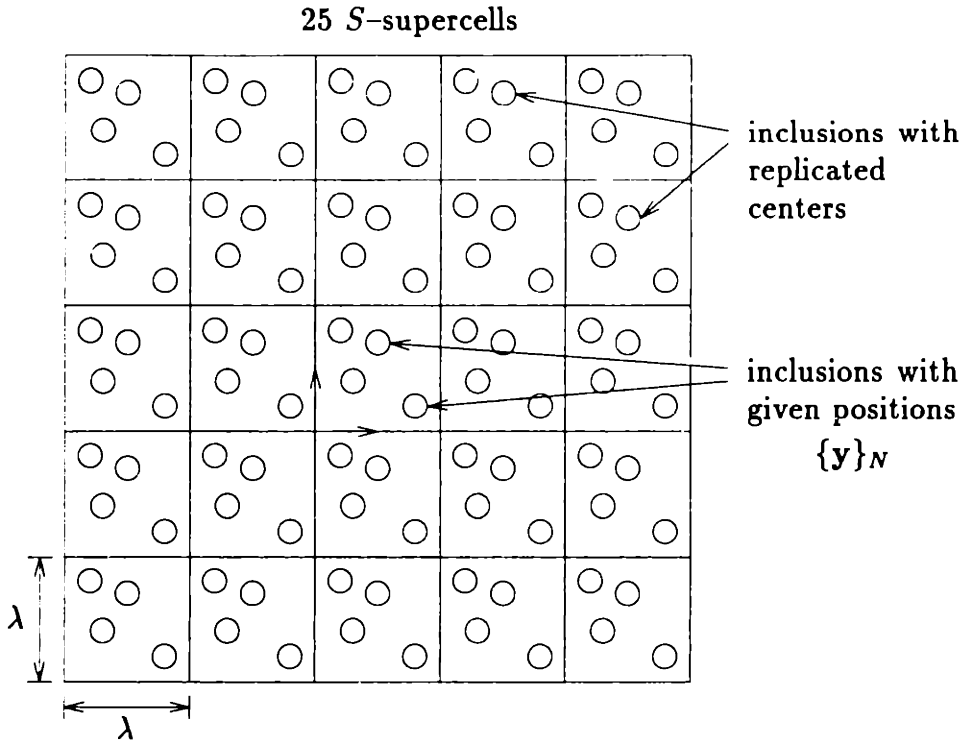

Figure 3-4: Special supercell generation set–up: square box of edge–length 5λ.

smaller than or equal to arg), so that j varies from 1 to N, $m_{1i}, m_{2i} \in \{0, \pm 1, \pm 2\}$, and $\{m_{1i}, m_{2i}\} \neq \{m_{1k}, m_{2k}\}$, $k = 1, \ldots, N_G$, $k \neq i$. The generators and associated tiles which originate from the same center $\mathbf{y}_j$ in the middle square, are said to be of the type j.

Next, the Voronoi diagram corresponding to the input set $\{\mathbf{y}_G\}_{N_G}$ is constructed. The special geometric set–up just described ensures that a *periodic*, Voronoi–based, supercell containing N inclusions is "buried" inside the diagram, and can be extracted in the following way ($N > 1$): starting at any one tile of type j, $j \in \{1, \ldots, N\}$, in the middle S–supercell, we look for another tile of distinct type j' connected to it (i.e., sharing one Voronoi edge), *and* inside the region of the inner nine S–supercells; next, we look for another tile of type j'' that must connect either to j or to j', and inside the same region; the process is repeated successively until a set of N connected tiles of different types has been identified. This connected set of N tiles is guaranteed to exist, and to have matching periodic edges (i.e., with same length and parallel to each other)

on the outer boundary; such set of tiles is denoted a V–supercell, and shown with darker contour in Figure 3-5. Figures 3-6 (a) and (b) show two (isolated) V–supercells, both with 32 inclusions, with concentrations $c = 0.10$ ($\lambda = 15.9\,d$) and $c = 0.30$ ($\lambda = 9.2\,d$), respectively. The fundamental difference between the V–supercell and the original S–supercell is that the former, in addition to having all the necessary properties of the latter, is naturally partitioned in N tiles by the construction process; this partitioning allows the subdomains to be easily distributed to parallel processors, and to be independently meshed (parallel data constructs ensure global mesh integrity, see Section 3.2.5). The existence and plane–filling property (i.e., periodicity) of the V–supercell derives from the symmetries *imposed* in the construction algorithm, and from the properties of the Voronoi diagram described earlier. The two layers of S–supercells surrounding the middle one, guarantee that the V–supercell will be free of boundary (periodicity–deforming) effects, that could otherwise arise when searching for the different–type connected tiles. [Note: In this work, the centers $\{\mathbf{y}\}_N$ were replicated over 15, rather than 24, S–supercells (Figure 3-5); this simpler approach reduces computational time. Although boundary effects could potentially distort V–supercell configurations containing tiles in the outermost layer (with 12, rather than 16, S–supercells), such approach worked (i.e., periodicity tests passed) for *all* sampled $\{\mathbf{y}\}_N$'s.]

There are a number of features of the V–supercell that should be pointed out. In general, it is not a square region (Figure 3-6), but has the same (matrix) area (and thus the same concentration) of the original S–supercell: any deformation of the boundary of the middle square due to intruding or protruding tiles, by periodicity, is matched on the opposite side by protruding or intruding tiles of the same type. Since a Voronoi edge is equidistant from the two corresponding generators (here, centers), and since the distance between any two generators is at least two inclusion radius (no overlapping condition), it follows that no inclusion is "cut" by an edge, which simplifies the mesh generation task (see Section 3.2.2). Each Voronoi tile then contains one and only one *entire* inclusion. Finally, the outer boundary of the V–supercell, as well as of the N tiles, is composed of only rectilinear segments, simplifying the

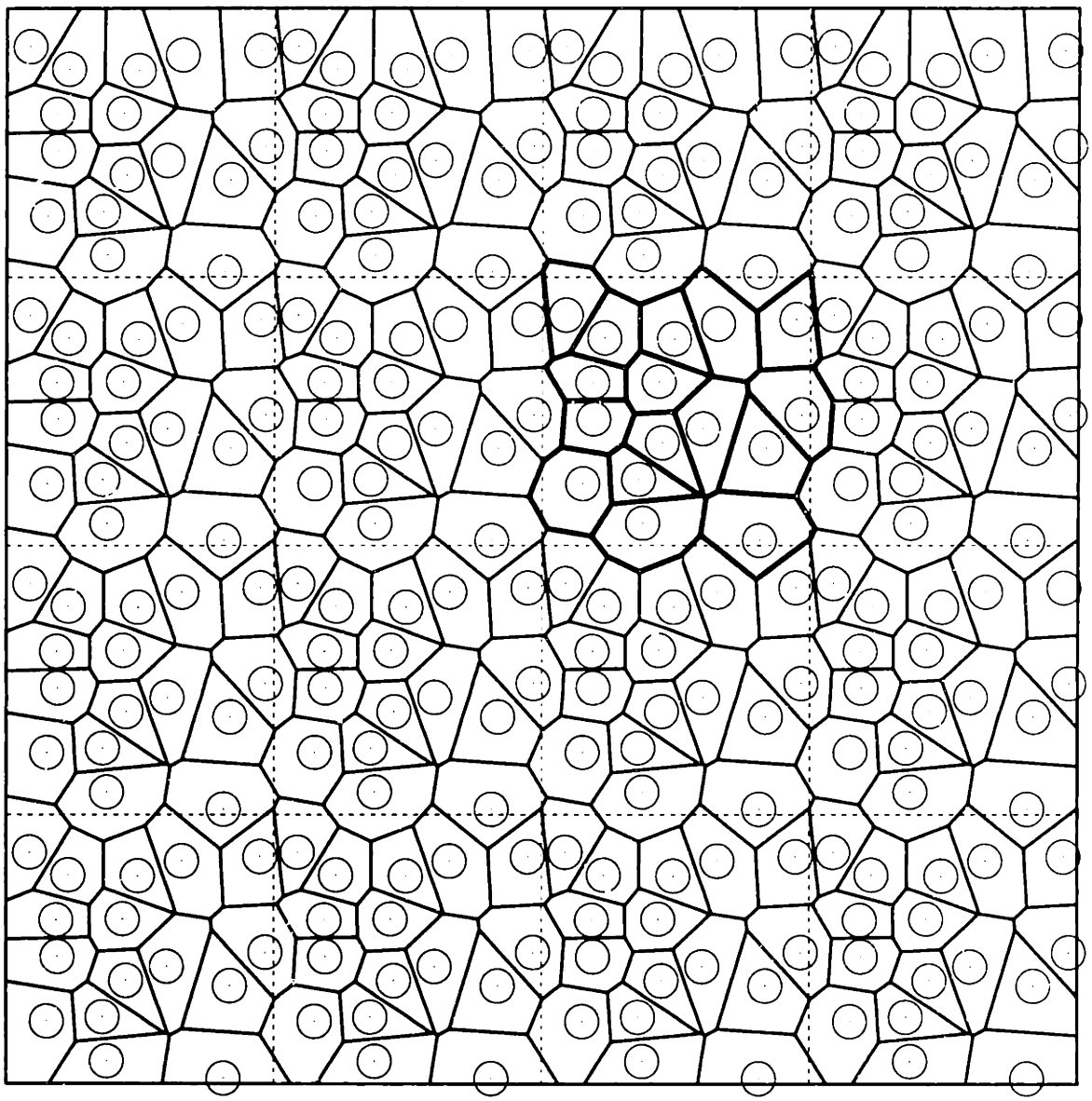

Figure 3-5: Special supercell generation set–up: Voronoi diagram based on replication of $\{\mathbf{y}\}_N$ ($c = 0.20$, $N = 16$, $\lambda = 7.9\,d$); the V–supercell is shown with darker contour.

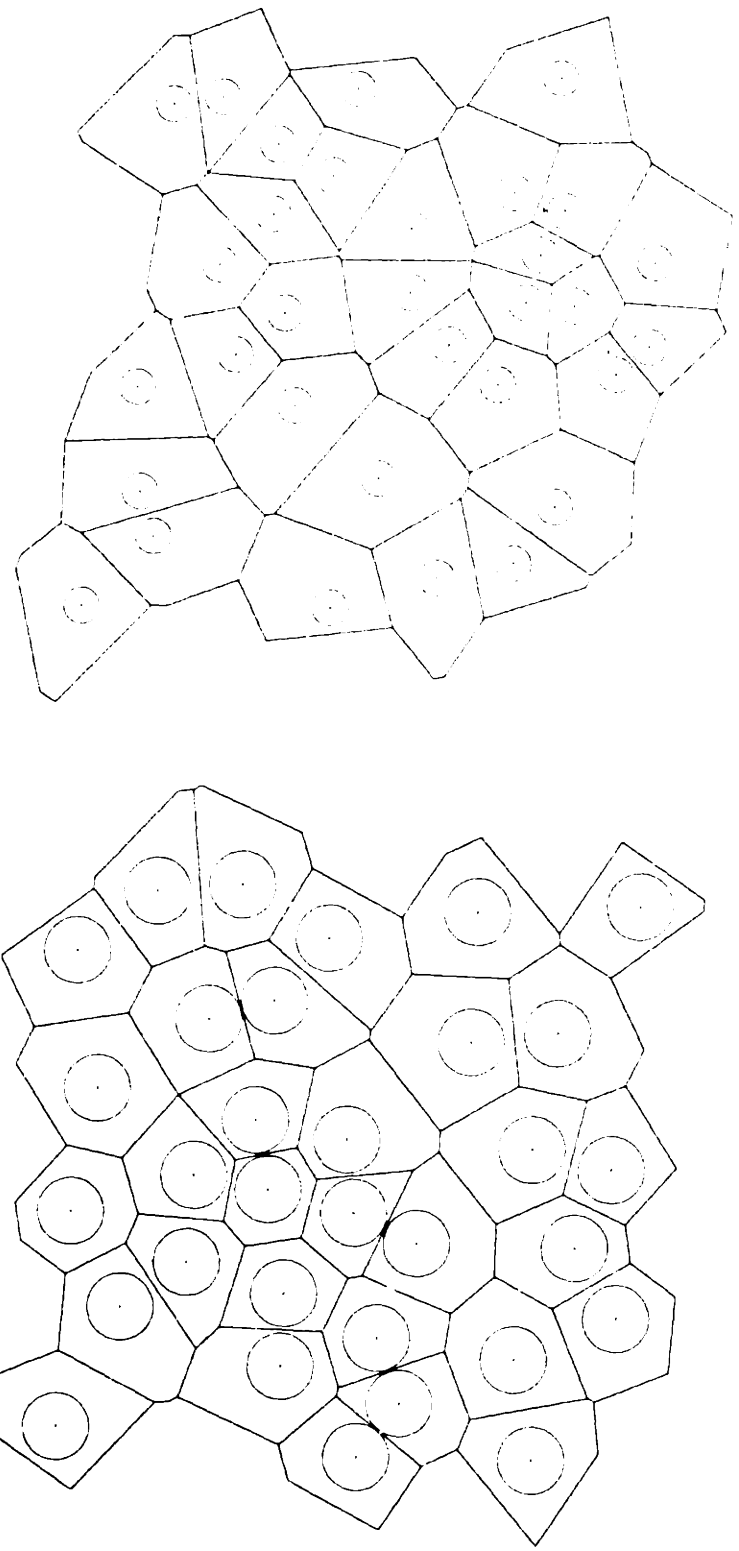

Figure 3-6: Two typical 32–inclusion V–supercells, with concentrations (a) $c = 0.10$ ($\lambda = 15.9\,d$) and (b) $c = 0.30$ ($\lambda = 9.2\,d$).

V–supercell geometry and topological description to be transferred to the parallel processors.

The VORONOI2 program supplies all the geometrical and topological data needed to extract the V–supercell as described, and to identify and match its periodic edges. One undesired by–product of the Voronoi diagram–VORONOI2 usage, is the presence of virtual edges (Figure 3-3), and of very small edges (on the order of machine precision) that must be eliminated for successful mesh generation and subsequent discretization/solution. We call this edge–elimination procedure $\epsilon - smoothing$, and it is described in Appendix D. The advantages of the adopted domain generation and partition procedure, with respect to the conventional S–supercell approach, are:

- it is a simple (given availability of tools) way of generating periodic, multiple–inclusion, domains;
- it automatically provides a natural, reasonably good, supercell domain partition for parallel processing;
- it provides regular regions (the convex polygonal tiles and uncut inclusions) for parallel sub–mesh generation;
- it facilitates the use of Hausdorff distances for sub–mesh generation (see Section 3.2.2).

The relative disadvantages of the V (versus S) approach are:

- it requires ϵ–smoothing (see Appendix D);
- it generates many more local/global vertices and edges (see Section 3.2.5 and Appendix F), which affect overall parallel performance;
- it cannot be readily extended to deal with non–circular inclusion geometries;
- its extension to three dimensions is non–trivial.

The generation of 100 50–inclusion V–supercells takes on the order of 4 minutes on a standard desktop workstation. The ratio of the maximum to the minimum tile area

for one V–supercell ranges from 1 to about 4; since the number of global degrees of freedom scales with area, this ratio gives an indication of the load balance that can be expected from the Voronoi partitioning alone. Final load balance also depends on the meshing procedure, described in Section 3.2.2. The S–supercell approach has to be revisited for performing future three–dimensional simulations with the methodology proposed in this work. New partitioning techniques, applicable to both 2–D and 3–D, have to be devised; to say the least, a VORONOI3 is, to the author's knowledge, unavailable.

3.2.2 Mesh Generation

Parallel computation within the Level 1 procedure starts with mesh generation for the V–supercell. After one V–supercell has been constructed, and its geometry and topology properly defined, it is distributed among parallel processors. If the number of tiles (or inclusions) matches, or is a multiple of, the number of processors, then each processor will separately work on the same number of tiles; otherwise, some processors will have one more tile than others. Load balancing, which can be expressed by the maximum ratio between the number of degrees of freedom in any two processors (ideally should be one), is dependent entirely on how well the Voronoi diagram partioned the domain in terms of area, and more importantly, as we will show, on how close the inclusion in one tile is to one of the Voronoi edges around it. Notice that when two inclusions are very close to each other, forming a cluster, the Voronoi edge between them is almost a tangent.

Since we use finite elements, as opposed for instance to finite–differences, the mesh generation takes place in the physical domain, rather than on a transformed domain. The union of all Voronoi edges (or tile boundaries) of the V–supercell is denoted $\partial\Omega_{VE}$, and the union of all inclusion circumferences (or void boundaries), as defined in Section 2.1.3, is $\partial\Omega_{me}$; notice that $\partial\Omega_{\#} \subset \partial\Omega_{VE}$. Clearly, the mesh generation procedure has to start at $\partial\Omega_{VE}$ and $\partial\Omega_{me}$, by specifying the positions of simplex element nodes, or simply nodes, on such boundaries. Because two tiles that share one edge may be on two different processors, a conforming mesh to be generated with

no parallel communication requires that the *same* nodes be specified on that edge on each processor. The parallel data structures that make such a task simple, are described in Section 3.2.5. An inclusion surface lies *entirely* on one processor (Section 3.2.1), and thus requires no special data structures. The process of generating sub-domain meshes independently on different processors, all of which belonging to the same global mesh, is called sub-meshing.

As mentioned earlier, simplex elements are appropriate for our multicomponent media problems: they provide the necessary geometric flexibility, while allowing robust implementations. Their geometry matches the outer tile boundaries, which are rectilinear, however it does not match curvilinear inclusion surfaces. This limitation generates a "skin effect," discussed in Section 3.2.3; elimination of such effect requires iso-parametric elements, not implemented in this work.

The main question in generating the mesh is then how to distribute nodes along $\partial\Omega_{VE}$ and $\partial\Omega_{me}$. The following boundary-node distribution-function (analogous to finite-difference stretching functions) is used for this purpose:

$$h_r(\mathbf{y}_{bn,j}) = \left[\frac{1}{\frac{m}{d_H(\mathbf{y}_{bn,j})} + \frac{1}{h_0}}\right] \cdot r^{-1} , \tag{3.2}$$

where $\mathbf{y}_{bn,j}$, $j = 1, \ldots, n_{bn}$, denotes a boundary node either on a Voronoi edge in $\partial\Omega_{VE}$ or on an inclusion surface in $\partial\Omega_{me}$, possessing a total of n_{bn} nodes; h_r is the actual mesh spacing that should be advanced from $\mathbf{y}_{bn,j}$, along the edge or circumference, to determine the next node $\mathbf{y}_{bn,j+1}$; $d_H(\mathbf{y}_{bn,j})$ is the Hausdorff distance [Preparata and Shamos (1988)] associated with the node $\mathbf{y}_{bn,j}$, with respect to an inclusion surface (if $\mathbf{y}_{bn,j} \in \partial\Omega_{VE}$) or to a Voronoi edge (if $\mathbf{y}_{bn,j} \in \partial\Omega_{me}$); m is the near-cylinder refinement parameter; h_0 is the input default mesh spacing; and r is the global mesh refinement parameter.

The Hausdorff distance associated with the boundary node $\mathbf{y}_{bn,j} = \mathbf{y}_{ve,j} \in \partial\Omega_{VE}$, $d_H(\mathbf{y}_{ve,j})$, with respect to the inclusion inside the corresponding tile, is defined as the minimum distance from that node to the inclusion surface; it is then given by the distance between $\mathbf{y}_{ve,j}$ and the point of intersection between the inclusion surface

and the line joining $\mathbf{y}_{ve,j}$ to the inclusion center, as shown in Figure 3-7. Similarly, the Hausdorff distance associated with the node $\mathbf{y}_{bn,j} = \mathbf{y}_{is,j} \in \partial\Omega_{me}$, $d_H(\mathbf{y}_{is,j})$, with respect to a Voronoi edge of the same tile, is defined as the minimum distance from $\mathbf{y}_{is,j}$ to the edge; it is then given by the length of the perpendicular from $\mathbf{y}_{is,j}$ to the edge, also shown in Figure 3-7. It should be pointed out that the actual Hausdorff distance input to equation (3.2) for a boundary node on $\partial\Omega_{me}$, $\mathbf{y}_{is,j}$, is the minimum over the Hausdorff distances associated with $\mathbf{y}_{is,j}$, with respect to all the Voronoi edges around the node (this is implied below).

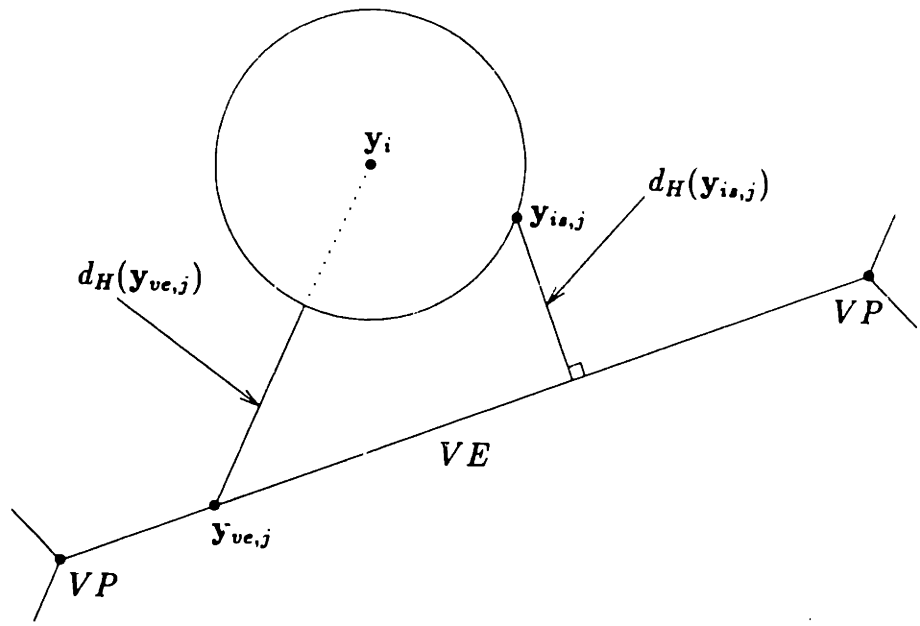

Figure 3-7: Hausdorff distances d_H for nodes on a Voronoi edge, and on an inclusion surface.

The Hausdorff distances just defined measure how close a particular boundary node is to the nearest inclusions, *and*, for nodes on $\partial\Omega_{VE}$, how close these inclusions are. Notice that the latter information is crucial for deciding on mesh fineness, and the properties of the Voronoi diagram allow easy computation of inter-inclusion spacing based on the d_H values: for nodes on $\partial\Omega_{me}$, it is simply twice the value of $d_H(\mathbf{y}_{is,j})$; for nodes on a Voronoi edge, in $\partial\Omega_{VE}$, the minimum neighboring-inclusions gap is simply twice the minimum value of $d_H(\mathbf{y}_{ve,j})$. The symmetry of the Voronoi

diagram may be slightly disturbed by the elimination of small Voronoi edges in the ϵ–smoothing procedure, which causes displacement of neighboring edges; this is discussed in Appendix D.

Nip–regions between clustered inclusions require finer mesh spacings relative to regions far away from inclusion boundaries, due to potentially higher gradients. The Hausdorff distances provide a quantitative, uniform, basis for mesh sizing. Even after implementation of the microscale bounds derived in Sections 2.1.4 and 2.2.4, such distances, d_H, are important to provide relative fineness among various regions of the mesh, therefore allowing resolution of all the field scales in the V–supercell. For an S–supercell, on the other hand, Hausdorff distances associated with the edges on $\partial\Omega_\#$ do not necessarily reflect inter–inclusion spacing, and therefore additional interpolation techniques are necessary [Ghaddar (1994)].

Equation (3.2) possesses some nice characteristics that we now discuss. First of all, the global refinement parameter r allows for uniform mesh refinement throughout the entire domain, since a typical size of a simplex element side within the domain scales with h_r; such uniformity is necessary for convergence tests (and for mesh adaptivity). The parameter r is a positive real number, and its value is set to 1 in production runs. Second, h_r automatically and smoothly handles various edge and inclusion surface sub–regions demanding different resolution: for a node far away from any neighboring inclusions, the Hausdorff distance is large, such that the ratio $\frac{1}{h_0}$ dominates $\frac{m}{d_H(\mathbf{y}_{bn,j})}$, in which case the mesh spacing assumes, as expected, the default value h_0 ($r = 1$); for a node very close to a neighboring inclusion, the ratio $\frac{m}{d_H(\mathbf{y}_{bn,j})}$ dominates $\frac{1}{h_0}$, so that the mesh spacing assumes the value $\frac{d_H(\mathbf{y}_{bn,j})}{m}$; a smooth transition occurs between the two asymptotic values. Clearly, the purpose of the parameter m is to guarantee that at least m simplex elements exist between any pair Voronoi edge–inclusion surface; typically, m is set to 2. Third, the mesh spacing h_r at a Voronoi point is the same for all three edges around it; such equality ensures continuity of the mesh, avoids distorted (potentially vanishing Jacobian) elements, and holds no matter on what processors the corresponding tiles are (no communication, e.g. of minimum h_r value, required). Again, this is due to the efficient coupling Voronoi–Hausdorff; minimal

differences may occur due to ϵ–smoothing. Finally, rewriting equation (3.2) as

$$h_r(\mathbf{y}_{bn,j}) = \frac{h_0}{r}\left[\frac{\zeta}{\zeta+1}\right], \tag{3.3}$$

where $\zeta \equiv \frac{d_H(\mathbf{y}_{bn,j})}{m\,h_0}$, it is seen that, for a particular configuration for which the minimum d_H value is known (corresponding to the minimum edge–inclusion gap), h_r can be made independent of d_H by setting mh_0 very small compared to this minimum value (if memory allows).

The (interior) mesh generation step, in Ω_{me}, follows the placement of nodes on $\partial\Omega_{VE}$ and $\partial\Omega_{me}$, as governed by equation (3.2). In this work, we used a FORTRAN subroutine developed in INRIA, France, by F. Hecht and E. Saltel [see Hecht & Saltel (1990)], called MSHPTG. It is an implementation of a Voronoi–based, Delaunay triangulation algorithm, which takes boundary nodes, and corresponding topological description of the boundary, as input. The positions of the nodes, and their numbering, are honored in MSHPTG. After the mesh has been created, MSHPTG (optionally) performs a smoothing operation, whereby it makes all triangles as close to equilateral as possible.

The subroutine MSHPTG is very robust, and is capable of meshing domains composed of multiply–connected subdomains, just like the V–supercells, which are composed of (multiply–connected) Voronoi tiles. It was found convenient to mesh the Voronoi tiles *on one* processor individually, rather than all tiles simultaneously. The subroutine MSHPTG has also been used by Hu, Joseph & Crochet (1992) in their particle motion simulation studies mentioned in Section 1.2.4.

Typical values used for $h_0^* \equiv \frac{h_0}{d}$ are 0.1 and 0.2 for the conduction and creeping flow runs, respectively (see also Chapter 4). The generation of 100 meshes for 32–inclusion V–supercells takes on the order of 10 minutes on 16 processors. Figures 3-8, 3-9 and 3-10 show typical meshes for 32–inclusion V–supercells with concentrations $c = 0.10$, $c = 0.30$ and $c = 0.50$, respectively; all meshes have $(h_0^*, m, r) = (0.2, 2, 1)$. The fraction of the total number of global nodes that lies inside nip regions depends on the concentration: it is about 10% for $c = 0.10$, 25% for $c = 0.30$, and 60% for

$c = 0.50$.

3.2.3 Discretization

Finite element discretization is used for both the conduction and creeping flow problems, following standard procedures [Strang & Fix (1973), Gunzburger (1989)]. In this section, we write the discrete equations for the unknown field variables and the effective properties. The finite element method provides optimal approximations of the latter; we show that the effective conductivity has quadratic convergence, with (linear–triangles) mesh spacing, in the energy norm. In Chapter 4, this fact is verified numerically for the case of regular arrays, for which exact solutions are known (see Section 1.2.3). In what follows, we deal only with nondimensional quantities, denoted previously (see Sections 2.1.3 and 2.2.3) with the superscript *; for clarity of presentation, the superscript is, for the most part, omitted.

Conduction Problem

Finite element formulation In the mesoscale conduction problem, the field variable of interest in the V–supercell is the temperature $\chi(\mathbf{y}) \in H^1_{\#,0}(\Omega_{me})$ given by equation (2.43), rewritten here in the form

$$a(\chi, v) = \ell(v) \quad \forall v \in H^1_{\#,0}(\Omega_{me}) \,, \tag{3.4}$$

where $a(v, v)$ is the standard bilinear form defined on Ω_{me},

$$a(v, v) = \int_{\Omega_{me}} \frac{\partial v}{\partial y_k} \frac{\partial v}{\partial y_k} \, d\mathbf{y} \,, \tag{3.5}$$

and $\ell(v)$ is the linear functional on the right–hand–side of (2.43). We now introduce a triangulation T_h of Ω_{me}, which consists in the subdivision of Ω_{me} in $\mathcal{K}$ non–overlapping conforming triangles t_k, $k = 1, \ldots, \mathcal{K}$, such that

$$\Omega_{me} = \bigcup_{k=1}^{\mathcal{K}} t_k \,, \; t_k \in T_h \,. \tag{3.6}$$

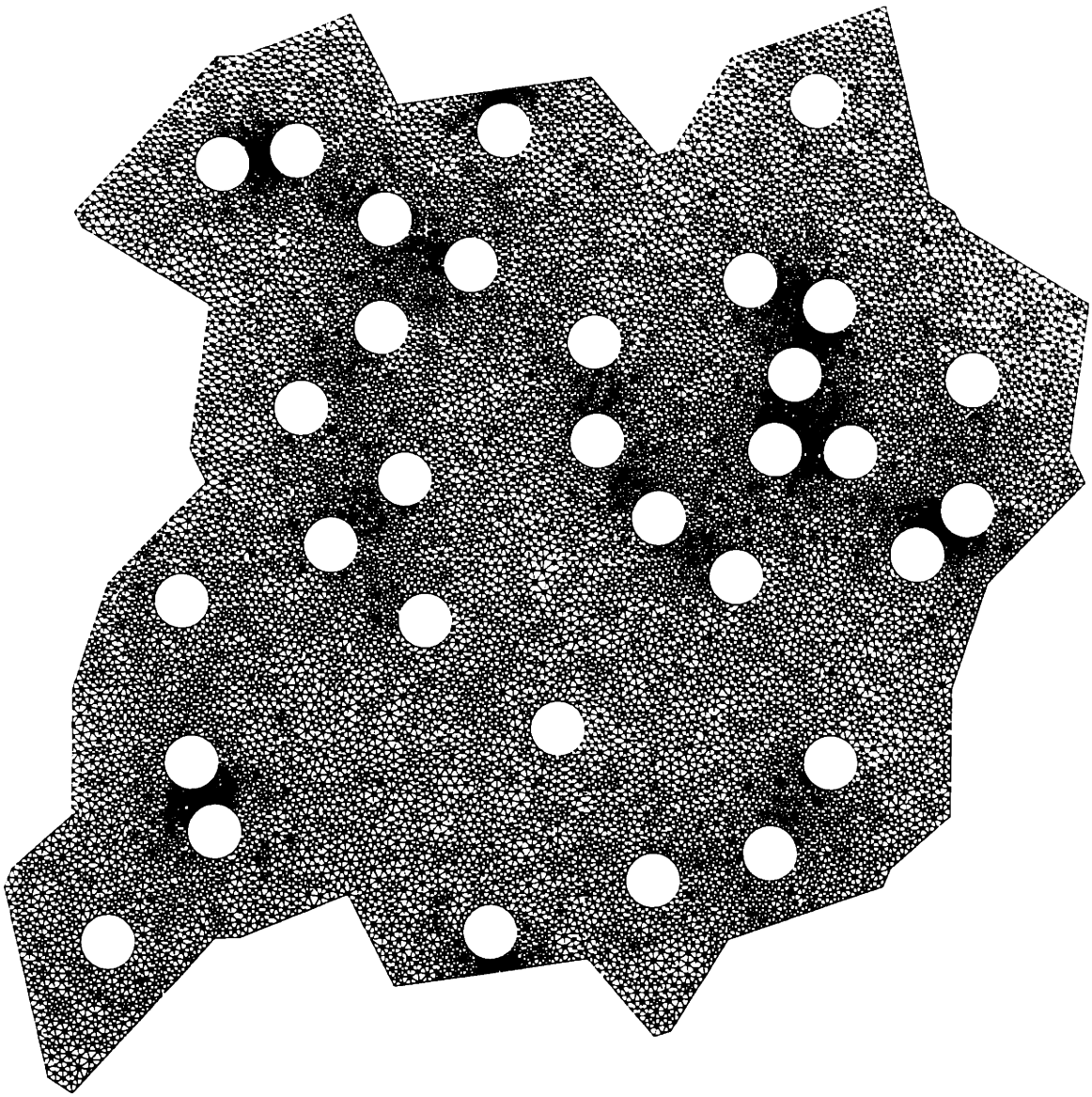

Figure 3-8: Mesh for a 32–inclusion V–supercell with concentration $c = 0.10$ ($\lambda = 15.9\,d$): total of 30900 triangles, 15900 global nodes.

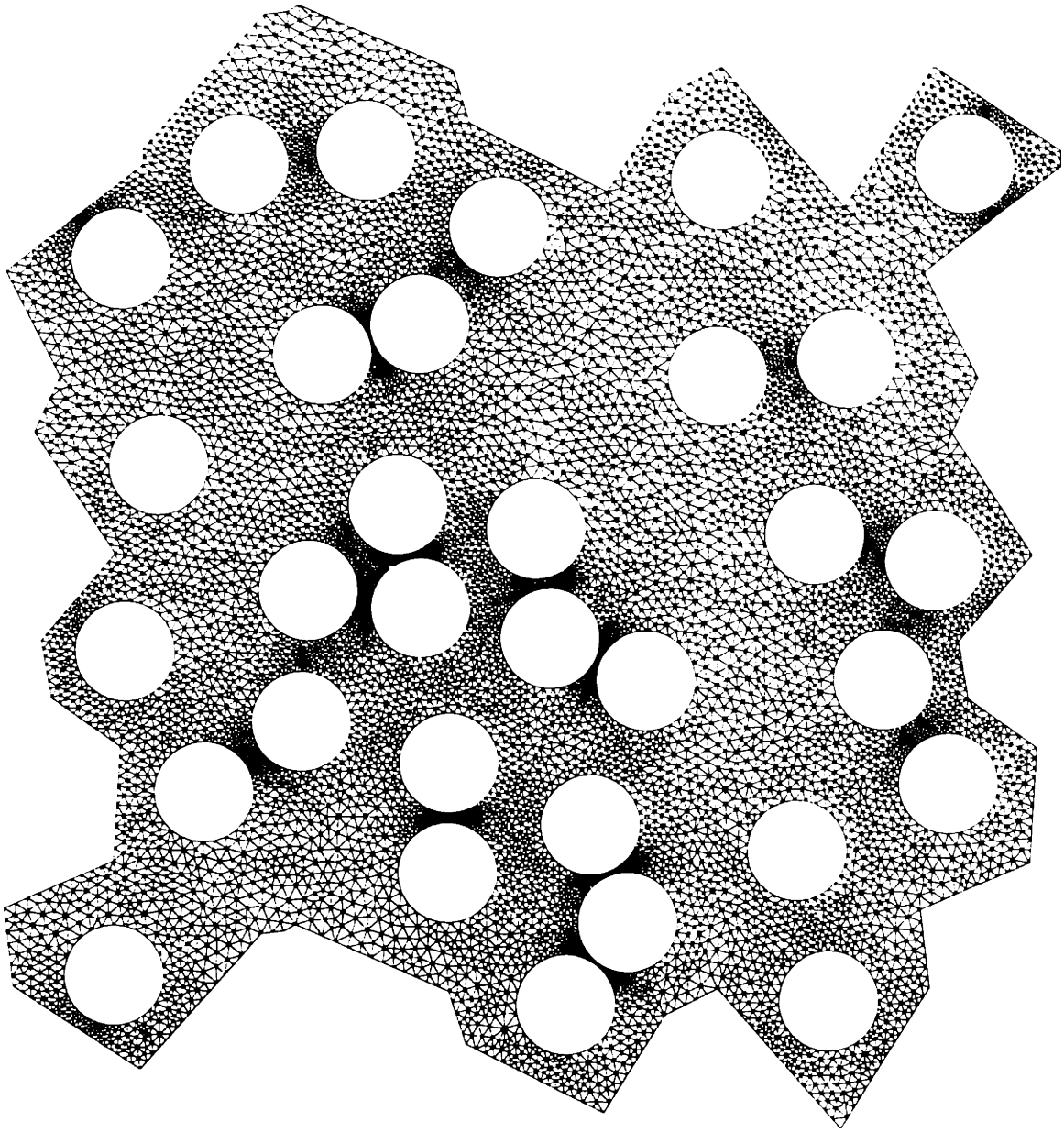

Figure 3-9: Mesh for a 32-inclusion V-supercell with concentration $c = 0.30$ ($\lambda = 9.2\,d$): total of 18500 triangles, 10000 global nodes.

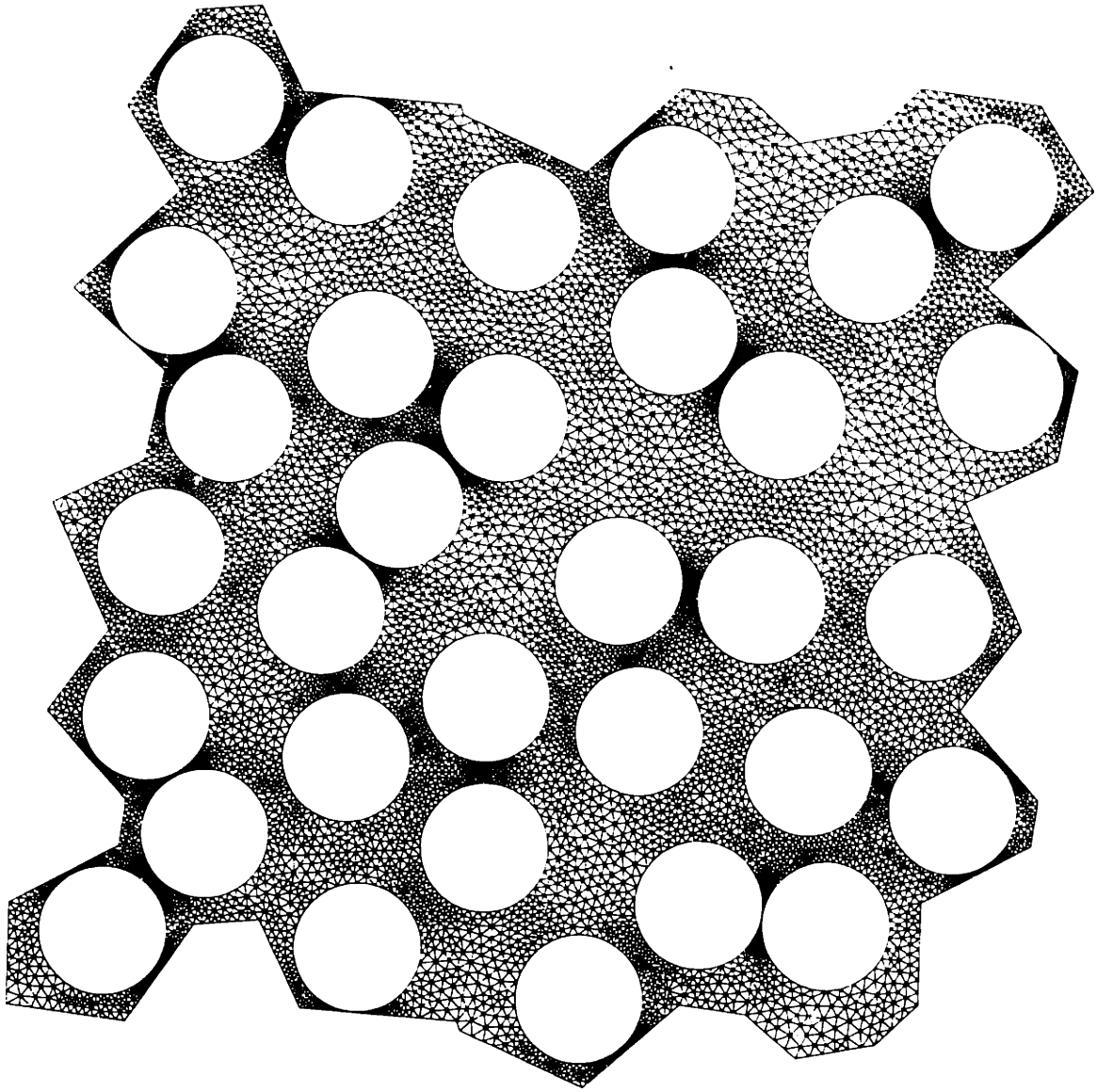

Figure 3-10: Mesh for a 32–inclusion V–supercell with concentration $c = 0.50$ ($\lambda = 7.1\,d$): total of 19700 triangles, 11200 global nodes.

Clearly, the mesh generation procedure described in Section 3.2.2 provides T_h. The Galerkin approximation corresponds to restricting the function space in which we look for the numerical solution, and leads to

$$a(\chi_h, v) = \ell(v) \quad \forall v \in X_h \,, \tag{3.7}$$

where χ_h is the (discrete) approximation for χ, $X_h = \{v\,|_{t_k \in T_h} \in \mathcal{P}_{\mathcal{N}_o}(t_k)\} \cap H^1_{\#,0}(\Omega_{me})$ and $\mathcal{P}_{\mathcal{N}_o}(t_k)$, $\mathcal{N}_o = 1, 2$, $k = 1, \ldots, \mathcal{K}$, is the space of all polynomials of degree $\mathcal{N}_o$ defined on the element (i.e., triangle) t_k. (Notice that second–order triangles, $\mathcal{N}_o = 2$, are optional for the conduction problem, but, as indicated below, effectively necessary for the creeping flow problem.) From equations (3.4) and (3.7), we conclude

$$a(\chi - \chi_h, v) = 0 \quad \forall v \in X_h \,, \tag{3.8}$$

which is the usual finite element result that χ_h is the best possible fit to χ in X_h, in the H^1–seminorm.

We next choose nodal Lagrangian interpolants for the basis functions, $\phi_i \in X_h$, such that

$$\phi_i(\mathbf{y}_j) = \delta_{ij} \,, \; i, j = 1, \ldots, N_{gn} \,, \tag{3.9}$$

where $\mathbf{y}_j \in \Omega_{me}$ is a global node of T_h (notice that N_{gn}, the total number of global nodes in T_h, is equal to $1 + N_{dof}$, where N_{dof} is the total number of algebraic degrees of freedom, due to the uniqueness condition for the conduction problem); it follows that a function $v(\mathbf{y}) \in X_h$ can be written as

$$v(\mathbf{y}) = \sum_{i=1}^{N_{gn}} v_i \, \phi_i(\mathbf{y}) \,, \tag{3.10}$$

with $v_i = v(\mathbf{y}_i)$. Note that the ϕ_i have degree $\mathcal{N}_o$, and $\text{span}\{\phi_i\} = X_h$. Expressing χ_h and v in (3.7) in terms of the basis functions ϕ_i, and also choosing the ϕ_i as test

functions, we finally obtain the following discrete linear system of equations

$$\underline{\mathbf{A}}\,\underline{\chi}_h = \underline{F}\,; \tag{3.11}$$

here, $\underline{\mathbf{A}} \equiv A_{ij} = a(\phi_i\,,\phi_j)$, $i,j = 1,\ldots,N_{gn}$, is the global system matrix corresponding to the (weak) discrete Laplacian operator, $\underline{\chi}_h$ is the vector (i.e., one–column matrix) of unknown (global) nodal values of the scalar field χ_h, and $\underline{F}$ is the vector of (global) nodal values corresponding to the inhomogeneity $\ell(v)$,

$$F_i = \int_{\Omega_{me}} \frac{\partial \phi_i}{\partial y_1}\, d\mathbf{y} \tag{3.12}$$

(unit dimensionless imposed temperature gradient in the y_1 direction). Notice that the functional $\ell(v)$ in (3.4) (or in (3.7)) automatically imposes the correct flux conditions on χ (or on χ_h) (see Section 2.1.3, equation (2.38)); the uniqueness condition (given in continuous form in equation (2.12)) is discretely imposed with the simple zero algebraic average requirement:

$$\sum_{i=1}^{N_{gn}} \chi_{h_i} = 0\,. \tag{3.13}$$

Due to algebraic simplicity, all the quadratures are performed exactly at the elemental level (see Section 3.2.4) for either value of $\mathcal{N}_o$. The global matrix $\underline{\mathbf{A}}$, and global vectors $\underline{\chi}_h$ and $\underline{F}$, are then obtained by performing direct stiffness summation of the elemental contributions. It follows from the bilinear form (3.5) that $\underline{\mathbf{A}}$ is symmetric and positive–definite; these properties are exploited later in the choice of the iterative solver. The details of the (parallel) solution of equation (3.11) are given in Sections 3.2.4 and 3.2.5.

Numerical expressions for the effective conductivity Substituting χ_h for χ in the equation for the effective conductivity, (2.42), and using the basis functions ϕ_i, we arrive at the following discrete equation for $k'^{*}_{e_h}$,

$$k'^{*}_{e_h} = \frac{k'_{e_h}}{k_{co}} = (1-c) - \frac{1}{\lambda^{*2}}\,\chi_{h_i} \int_{\Omega_{me}} \frac{\partial \phi_i}{\partial y_1}\, d\mathbf{y}\}\,, \tag{3.14}$$

where summation over the global nodes, $i = 1, \ldots, N_{gn}$, is implied.

It is convenient, as we will show below, to write an alternative expression for $k'^{*}_{e_h}$ (corresponding to the continuous equation (2.41)). After inspection of equations (3.11), (3.12) and (3.14), we conclude that

$$k'^{*}_{e_h} = (1 - c) - \frac{1}{\lambda^{*2}} \underline{\chi}_h^T \underline{\mathbf{A}} \underline{\chi}_h \,, \tag{3.15}$$

where the superscript ^{T} denotes the transpose operation; equivalently,

$$k'^{*}_{e_h} = (1 - c) - \frac{1}{\lambda^{*2}} a(\chi_h \,, \chi_h) \,. \tag{3.16}$$

Necessary agreement between equations (3.14) and (3.15) provides a useful check for the numerical implementation of the finite element equations and their solver.

Properties of $k'^{*}_{e_h}$ Finally, we can now derive two properties of the numerically determined effective conductivity, $k'^{*}_{e_h}$. We define the (normalized) absolute error

$$E'^{C}_h \equiv k'^{*}_{e_h} - k'^{*}_{e} \approx \frac{1}{\lambda^{*2}} \left[a(\chi \,, \chi) - a(\chi_h \,, \chi_h) \right] . \tag{3.17}$$

The approximate sign has been used due to the presence of the "skin effect" mentioned earlier, arising from the use of sub-parametric elements to represent the circular surface of the inclusions (the equal sign would have been used if the surface of the inclusions was composed of rectilinear segments). The "skin effect" is $O(h^2)$, where h here represents the maximum side of an element $t_k \in T_h$, generated with the distribution function h_r given in (3.2). Using symmetry of the bilinear form $a(v, v)$ given in (3.5), (3.17) becomes

$$E'^{C}_h \approx \frac{1}{\lambda^{*2}} a(\chi - \chi_h \,, \chi + \chi_h) \,; \tag{3.18}$$

choosing $v = -2\chi_h \in X_h$ in equation (3.8) and summing to (3.18), we obtain

$$E'^{C}_h \approx \frac{1}{\lambda^{*2}} a(\chi - \chi_h \,, \chi + \chi_h - 2\chi_h) \,, \tag{3.19}$$

so that

$$E_h'^C \approx \frac{1}{\lambda^{*2}}\, a(\chi - \chi_h, \chi - \chi_h)\,. \tag{3.20}$$

Clearly from equation (3.20), the error $E_h'^C$ is seen to be positive, yielding the property

$$k_{e_h}'^* \geq k_e'^*\,, \tag{3.21}$$

a result verified in Chapter 4 for regular arrays. Equation (3.21) is consistent with the standard finite element result [see Strang & Fix (1973), p. 98] that the numerical solution underestimates the energy in comparison to the continuous solution, since the numerical system is stiffer (due to restricted space) than the real one. We can rewrite the right-hand-side of (3.20) as

$$E_h'^C \approx \frac{1}{\lambda^{*2}}\, a^{\frac{1}{2}}(\chi - \chi_h, \chi - \chi_h)\, a^{\frac{1}{2}}(\chi - \chi_h, \chi - \chi_h)\,, \tag{3.22}$$

where $a^{\frac{1}{2}}(\cdot,\cdot) = |\cdot|_{H^1}$; it is known from finite element theory that, for linear elements ($\mathcal{N}_o = 1$), the H^1–seminorm in (3.22) is proportional to h, yielding the property

$$E_h'^C \leq C\, h^2\, ||\chi||_{H^2}\, ||\chi||_{H^2}\,, \tag{3.23}$$

where C is a constant independent of h, and $||\ \ ||_{H^2}$ represents the H^2–norm. The quadratic convergence predicted by equation (3.23) is, again, verified in Chapter 4 for regular arrays. The effective conductivity $k_{e_h}'^*$ depends on the derivative of χ_h, equation (3.14). It should be pointed out that although the error in the derivative of χ_h (H^1 error) varies only linearly with h, second–order convergence in $k_{e_h}'^*$ is obtained due to its particular, special functional relation to the derivative, expressed by equation (3.16).

Creeping Flow Problem

Finite element formulation In the mesoscale creeping flow problem, the field variables of interest in the V–supercell are the velocity $\mathbf{u}(\mathbf{y}) \in [H^1_{0\#}(\Omega_{me})]^2$, and the

pressure $p(\mathbf{y}) \in L^2_{\#,0}(\Omega_{me})$, given by equations (2.81) and (2.82), rewritten here in the form (superscript * omitted)

$$a(\mathbf{u},\mathbf{v}) - b(p,\mathbf{v}) = (\mathbf{f},\mathbf{v}) \quad \forall \mathbf{v} \in [H^1_{0\#}(\Omega_{me})]^2 \,, \tag{3.24}$$

and

$$-b(q,\mathbf{u}) = 0 \quad \forall q \in L^2_{\#,0}(\Omega_{me}) \,, \tag{3.25}$$

where $(t,w) = \int_{\Omega_{me}} t(\mathbf{y}) w(\mathbf{y})\, d\mathbf{y}$ is the inner product of two scalar (or vector, if boldface) functions, $a(\mathbf{u},\mathbf{v}) = (\nabla\mathbf{u}, \nabla\mathbf{v})$, $b(t,\mathbf{w}) = (t, \nabla\cdot\mathbf{w})$, and $\mathbf{f} = (1,0)$ (unit dimensionless imposed pressure gradient in the y_1 direction).

The key issue in discretizing equations (3.24)–(3.25) relates to the choice of compatible velocity and pressure spaces, in order to ensure satisfaction of the div–stability condition [see Gunzburger (1989), Chapter 2], also known as the inf–sup condition. Here, given a triangulation T_h, we use Taylor–Hood $\mathcal{P}_1 - \mathcal{P}_2$ elements: linear ($\mathcal{N}_o = 1$) and quadratic ($\mathcal{N}_o = 2$) piecewise continuous basis functions are used to represent the pressure and velocity, respectively. The discrete equations become

$$a(\mathbf{u}_h,\mathbf{v}) - b(p_h,\mathbf{v}) = (\mathbf{f},\mathbf{v}) \quad \forall \mathbf{v} \in [Y_h(\Omega_{me})]^2 \,, \tag{3.26}$$

and

$$-b(q,\mathbf{u}_h) = 0 \quad \forall q \in W_h(\Omega_{me}) \,, \tag{3.27}$$

where the reduced function spaces are now $Y_h(\Omega_{me}) = \{v\,|_{t_k \in T_h} \in \mathcal{P}_2(t_k)\} \cap H^1_{0\#}(\Omega_{me})$, and $W_h(\Omega_{me}) = \{v\,|_{t_k \in T_h} \in \mathcal{P}_1(t_k)\} \cap C^0_{\#,0}(\Omega_{me})$. Using the same basis and test functions, of appropriate order, as those used in the conduction problem, and performing all quadratures exactly, we arrive at the system

$$\underline{\mathbf{A}}\,\underline{u}_{h_i} - \underline{\mathbf{D}}_i^T\,\underline{p}_h = \underline{\mathbf{M}}\,\underline{f}_i \,, \quad i = 1,2 \,, \tag{3.28}$$

and

$$-\underline{\mathbf{D}}_i\,\underline{u}_{h_i} = 0 \,. \tag{3.29}$$

In (3.28)–(3.29), $\underline{\mathbf{A}}$, as before, is the discrete Laplacian operator; $\underline{u}_h$ and $\underline{p}_h$ are, respectively, the velocity and pressure vectors of unknown (global) values; $\underline{\mathbf{D}}_i^T$ is the discrete gradient operator, given by

$$\underline{\mathbf{D}}_i^T \equiv D_{nm_i} = (\phi_{m,1}\,, \frac{\partial \phi_{n,2}}{\partial y_i})\,, \tag{3.30}$$

where $\phi_{m,1}$ and $\phi_{m,2}$ are, respectively, the linear and parabolic basis functions, $m = 1, \ldots, (1 + N_{dof,1})$, $n = 1, \ldots, N_{dof,2}$, and $N_{dof,1}$ and $N_{dof,2}$ are, respectively, the total number of pressure and velocity (one component) degrees of freedom; $\underline{\mathbf{M}} \equiv M_{mn} = (\phi_{m,2}\,, \phi_{n,2})$, $m, n = 1, \ldots, N_{dof,2}$, is the global mass matrix; finally, $\underline{f}_i$ is the vector of global values corresponding to the unit forcing term. All Dirichlet boundary conditions were incorporated into the matrix operators. The uniqueness condition for the pressure, given in continuous form in equation (2.72), is discretely imposed with the simple zero algebraic average requirement:

$$\sum_{m=1}^{N_{gn,1}} p_h \,|_{\text{node } m} = 0\,, \tag{3.31}$$

$N_{gn,1} = 1 + N_{dof,1}$ is the number of pressure global nodes. The linear algebraic system (3.28)–(3.29) constitutes a classical symmetric saddlepoint (min–max) problem.

Numerical expressions for the permeability Substituting $\mathbf{u}_h$ for $\mathbf{u}$ in the equation for the permeability, (2.83), and using the basis functions $\phi_{n,2}$, we arrive at the following discrete equation for $\kappa_h'^*$,

$$\kappa_h'^* = \frac{\kappa_h'}{d^2} = u_{1,h_n} \int_{\Omega_{me}} \phi_{n,2}\, d\mathbf{y}\}\,, \tag{3.32}$$

where summation over the velocity global nodes, $n = 1, \ldots, N_{gn,2}$, is implied.

An alternative, dissipation–related, expression for $\kappa_h'^*$, corresponding to the continuous equation (2.80), is given by

$$\kappa_h'^* = \frac{1}{\lambda^{*2}} \left[\underline{u}_{i,h}^T \, \underline{\mathbf{A}} \, \underline{u}_{i,h} \right], \tag{3.33}$$

where summation over i, $i = 1, 2$, is implied; the right-hand-side of (3.33) is based on equation (2.75) for the functional $J^P_{\Omega_{me}}$, related to the permeability. Again, necessary agreement between equations (3.32) and (3.33) provides a useful check for the numerical implementation of the creeping flow problem.

The convergence rate of the permeability κ'^*_h, with mesh spacing, is not expected to be third-order, $O(h^3)$, because the "skin effect" introduces second-order inaccuracy (note that the midpoint on the edge of a second-order triangle on the surface of an inclusion is actually *inside* the inclusion, and therefore outside the domain of interest, Ω_{me}); for more details on the behavior of the "error in energy," see Strang & Fix (1973), pp. 105-116 and pp. 192-204.

3.2.4 Iterative Solution

Both discrete problems, (3.11) for conduction, and (3.28)-(3.29) for creeping flow, are solved iteratively: the algorithms of choice are conjugate gradient [Golub & Van Loan (1989)] for the former, and Uzawa [Fischer & Patera (1991), Maday, Meiron, Patera & Rønquist (1993)] for the latter. Conjugate gradient iteration is *only* applicable for symmetric, positive-definite systems. The presence of the $\underline{\mathbf{A}}$ operator in (3.11) makes it directly applicable to the conduction problem. The saddlepoint creeping flow (Stokes) problem can be converted into two symmetric, positive-(semi) and positive-definite systems by the Uzawa algorithm, described below.

Conduction Problem

The (non-preconditioned) conjugate gradient iteration for the (model) system $\underline{\mathbf{A}}\,\underline{\chi}_h = \underline{F}$ has the form:

$$\text{initialization}: \; m = 0\,, \;\; \text{pick } \underline{\chi}^0_h\,, \;\; \underline{r}^0 = \underline{F} - \underline{\mathbf{A}}\,\underline{\chi}^0_h\,, \;\; \underline{w}^0 = \underline{r}^0\,;$$

$$a^m = (\underline{r}^m\,, \underline{r}^m)/(\underline{w}^m\,, \underline{\mathbf{A}}\,\underline{w}^m)\,; \tag{3.34}$$

$$\underline{\chi}^{m+1}_h = \underline{\chi}^m_h + a^m\,\underline{w}^m\,; \tag{3.35}$$

$$\underline{r}^{m+1} = \underline{r}^m - a^m\underline{\mathbf{A}}\,\underline{w}^m\,; \tag{3.36}$$

$$b^m = (\underline{r}^{m+1}, \underline{r}^{m+1})/(\underline{r}^m, \underline{r}^m) ; \tag{3.37}$$

$$\underline{w}^{m+1} = \underline{r}^m + b^m \underline{w}^m , \tag{3.38}$$

where m is the iteration number, $\underline{\chi}_h^m$ is the m^{th} iterate of $\underline{\chi}_h$, $\underline{r}^m$ is the residual, $\underline{w}^m$ is the search direction, and $(\cdot, \cdot)$ denotes the discrete scalar product. The iteration proceeds until a stopping criterion is satisfied; typically, the incomplete iteration error is based on the H^1–seminorm $|\underline{\chi}_h - \underline{\chi}_h^m|_{H^1}$, and expressed in terms of the (computable) L^2–norm of the residual. In Appendix E we present in detail one approach to a conjugate gradient stopping criterion for the discrete Poisson problem; the result, equation (E.14), is employed in both the conduction and creeping flow problems (implicitly in the former — see below —, and explicitly in the latter). The discrete condition (3.13) is easily incorporated into the algorithm, by subtracting out from each component of $\underline{\chi}_h^m$, at every iteration m, the average value of $\underline{\chi}_h^m$ over the global nodes; this corresponds to orthogonalization of $\underline{\chi}_h^m$ with respect to the 1–vector (all components equal to one), since then

$$(\underline{\chi}_h^m, \mathbf{1}) = 0 . \tag{3.39}$$

The special incomplete–iteration error bounding method for the conduction problem is described next. The stopping criterion for the conjugate gradient iteration presented in Appendix E, can be transformed into a direct error control on the (discrete) effective conductivity, $k'^*_{e_h}$. This derives from the relation (3.16) between $k'^*_{e_h}$ and the energy norm of χ_h, as we now show. The relative error in the effective conductivity present at iteration m, ξ^m, is defined by

$$\xi^m = \frac{1}{(k'^*_{e_h})_m} \left| (k'^*_{e_h})_m - k'^*_{e_h} \right| , \tag{3.40}$$

where $|\cdot|$ indicates absolute value, and $(k'^*_{e_h})_m$ is the effective conductivity based on the m^{th} iterate of $\underline{\chi}_h$, chosen as the denominator of (3.40) due to its availability during the iteration process; notice that this is appropriate because χ_h^m approaches

χ_h as m increases. From equation (3.15), we deduce

$$\xi^m = \frac{1}{\lambda^{*^2}(1-c) - \underline{\chi}_h^{m^T}\,\underline{\mathbf{A}}\,\underline{\chi}_h^m}\,|\,\underline{\chi}_h^T\,\underline{\mathbf{A}}\,\underline{\chi}_h - \underline{\chi}_h^{m^T}\,\underline{\mathbf{A}}\,\underline{\chi}_h^m\,|\,. \tag{3.41}$$

We want to stop after performing m_f iterations, and achieve

$$\xi^{m_f} \leq \epsilon_{tol}\,, \tag{3.42}$$

where ϵ_{tol} is the desired accuracy; therefore, we need to bound ξ^m at iteration m to obtain (3.42).

Since $\underline{\mathbf{A}}$ is positive–definite, we can decompose $\underline{\mathbf{A}} = \underline{\mathbf{A}}^{\frac{1}{2}^T}\,\underline{\mathbf{A}}^{\frac{1}{2}}$ (e.g., by performing Cholesky factorization); we then define

$$\underline{s} = \underline{\mathbf{A}}^{\frac{1}{2}}\,\underline{\chi}_h^m \tag{3.43}$$

and

$$\underline{t} = \underline{\mathbf{A}}^{\frac{1}{2}}\,\underline{\chi}_h\,, \tag{3.44}$$

so that

$$\xi^m = \frac{1}{\lambda^{*^2}(1-c) - |\,\underline{\chi}_h^m\,|_{H^1}^2}\,|\,\underline{t}^T\underline{t} - \underline{s}^T\underline{s}\,|\,, \tag{3.45}$$

where $|\,\underline{\chi}_h^m\,|_{H_1}^2 \equiv \underline{\chi}_h^{m^T}\,\underline{\mathbf{A}}\,\underline{\chi}_h^m = \underline{s}^T\underline{s} \equiv ||\,\underline{s}\,||^2$, the last equality following from (3.43). At high concentrations, the effective conductivity $k_{e_h}^{\prime *}$ is small; at low concentrations, its deviation from $(1-c)$ is small. In the former case, we want to ensure that the relative error in $k_{e_h}^{\prime *}$ itself is small; in the latter case, we want to ensure that the deviation of $k_{e_h}^{\prime *}$ from $(1-c)$, given by $(\underline{\chi}_h^T\,\underline{\mathbf{A}}\,\underline{\chi}_h/\lambda^{*^2})$, has small relative error. Therefore, we rewrite (3.45) as

$$\xi^m \leq \frac{1}{R^2}\,|\,\underline{t}^T\underline{t} - \underline{s}^T\underline{s}\,|\,, \tag{3.46}$$

where R is a *known* quantity at iteration m, given by

$$R^2 = \min\left(\,\lambda^{*^2}(1-c) - |\,\underline{\chi}_h^m\,|_{H_1}^2\,,\,|\,\underline{\chi}_h^m\,|_{H^1}^2\,\right). \tag{3.47}$$

Equation (3.46), due to trivial symmetry of scalars, is equivalent to

$$\xi^m \leq \frac{1}{R^2} \left| (\underline{t}^T - \underline{s}^T)(\underline{t} + \underline{s}) \right| . \tag{3.48}$$

From the Cauchy-Schwarz inequality, (3.48) becomes

$$\xi^m \leq \frac{1}{R^2} \| \underline{t} - \underline{s} \| \cdot \| \underline{t} + \underline{s} \| , \tag{3.49}$$

or

$$\xi^m \leq \frac{1}{R^2} \| \underline{t} - \underline{s} \| \cdot \| \underline{t} - \underline{s} + 2\underline{s} \| . \tag{3.50}$$

Now, from the triangle inequality, (3.50) becomes

$$\xi^m \leq \frac{1}{R^2} \| \underline{t} - \underline{s} \| (\| \underline{t} - \underline{s} \| + 2 \| \underline{s} \|) , \tag{3.51}$$

or

$$\xi^m \leq \left(\frac{\| \underline{t} - \underline{s} \|}{R} \right)^2 + 2 \frac{\| \underline{s} \|}{R} \frac{\| \underline{t} - \underline{s} \|}{R} . \tag{3.52}$$

We now impose that ξ^m be smaller than a prescribed small tolerance ϵ_{tol}, to get

$$\left(\frac{\| \underline{t} - \underline{s} \|}{R} \right)^2 + 2 \frac{\| \underline{s} \|}{R} \frac{\| \underline{t} - \underline{s} \|}{R} \leq \epsilon_{tol} . \tag{3.53}$$

Solving the quadratic in (3.53), we find that the following condition must hold

$$\frac{\| \underline{t} - \underline{s} \|}{R} \leq -\frac{\| \underline{s} \|}{R} + \sqrt{\left(\frac{\| \underline{s} \|}{R} \right)^2 + \epsilon_{tol}} . \tag{3.54}$$

From the expression for R in equation (3.47) and the equality $| \underline{\chi}_h^m |_{H_1} = \| \underline{s} \|$, we easily conclude that the left-hand-side in (3.54) satisfies

$$\frac{\| \underline{t} - \underline{s} \|}{R} \leq -1 + \sqrt{1 + \epsilon_{tol}} . \tag{3.55}$$

Notice that the numerator on the left-hand-side of (3.55) is equal to $| \underline{\chi}_h - \underline{\chi}_h^m |_{H^1}$, due to (3.43) and (3.44); also, the right-hand-side of (3.55) is $O(\epsilon_{tol})$ ($\approx \frac{\epsilon_{tol}}{2}$ for small

ϵ_{tol}). Using the result (E.9) derived in Appendix E, namely,

$$|| \underline{t} - \underline{s} || = | \underline{\chi}_h - \underline{\chi}_h^m |_{H_1} \leq \frac{1}{\varrho_{min}^{1/2}} (\underline{r}^{m^T} \underline{\mathbf{M}}^{-1} \underline{r}^m)^{\frac{1}{2}} , \tag{3.56}$$

we conclude that if we choose

$$(\underline{r}^{m^T} \underline{\mathbf{M}}^{-1} \underline{r}^m)^{\frac{1}{2}} < \varrho_{min}^{1/2} R(\sqrt{1+\epsilon_{tol}} - 1) , \tag{3.57}$$

then, from (3.55) and (3.56), we are guaranteed that $\xi^m \leq \epsilon_{tol}$. The practical realization is thus, finally (see Appendix E),

$$\left\{ \sum_{i=1}^{N_{dof}} \frac{(r_i^m)^2}{\bar{M}_i} \right\}^{\frac{1}{2}} < \frac{\pi}{\lambda^*} R(\sqrt{1+\epsilon_{tol}} - 1) . \tag{3.58}$$

It should be pointed out that an automatic *a posteriori* estimation for the discretization error, and its propagation to the effective conductivity, is necessary for control of the total, or final, error. We therefore need solution techniques appropriate for adaptive meshes as well. These automatic procedures were not implemented in this work (see Section 4.5).

Creeping Flow Problem

Our main (framework–preserving) strategy to solve the Stokes problem is to transform equations (3.28)–(3.29) into discrete equivalents suitable for conjugate gradient iteration. This is accomplished with the Uzawa saddle–decoupling algorithm, which essentially consists in the application of block Gaussian elimination to the system (3.28)–(3.29): formally multiplying the first equation on the left by $\underline{\mathbf{D}}_i \underline{\mathbf{A}}^{-1}$, and using the second, we obtain

$$\underline{\mathbf{S}} \underline{p}_h = - \underline{\mathbf{D}}_i \underline{\mathbf{A}}^{-1} \underline{\mathbf{M}} \underline{f}_i , \; i = 1, 2 , \tag{3.59}$$

where $\underline{\mathbf{S}} \equiv \underline{\mathbf{D}}_i \, \underline{\mathbf{A}}^{-1} \underline{\mathbf{D}}_i^T$ is a symmetric, positive–(semi)definite operator, and

$$\underline{\mathbf{A}} \, \underline{u}_{h_i} = \underline{\mathbf{D}}_i^T \, \underline{p}_h + \underline{\mathbf{M}} \, \underline{f}_i \, , \; i = 1, 2 \, . \tag{3.60}$$

The solution $(\mathbf{u}_h \, , p_h)$ of the system (3.59)–(3.60) is found by a nested conjugate gradient iteration to obtain the pressure, followed by another conjugate gradient iteration to obtain the velocity. Inversion of the $\underline{\mathbf{S}}$ operator in equation (3.59) is performed with an outer conjugate gradient solve, analogous to (3.34)–(3.38). Since $\underline{\mathbf{S}}$ is not known explicitly, its action on the search direction for the pressure, $\underline{q}$, cannot be evaluated directly; therefore, for every outer iteration, an inner conjugate gradient solve is necessary, in which $\underline{\mathbf{S}} \, \underline{q}$ is determined as follows:

$$\underline{w}_i = \underline{\mathbf{D}}_i^T \, \underline{q} \;\; ; \;\; \underline{\mathbf{A}} \, \underline{z}_i = \underline{w}_i \;\; ; \;\; \underline{\mathbf{S}} \, \underline{q} = \underline{\mathbf{D}}_i \, \underline{z}_i \, , \tag{3.61}$$

where $i = 1, 2$, and summation over i is implied in the third equation. Notice that the $\underline{\mathbf{A}}$ system has exactly the same form of the conduction equation (3.11). Once $\underline{p}_h$ has been obtained, the right–hand–side of (3.60) can be evaluated, and another $\underline{\mathbf{A}}$–conjugate gradient solve is needed to find the velocity field.

The Uzawa algorithm is chosen here because of its efficiency in terms of computational complexity and memory requirements as compared to a direct solver approach. Also, it can be efficiently parallelized due to the use of conjugate gradient iterations (see Section 3.2.5). The algorithm's critical result is that for finite elements which satisfy a uniform inf–sup condition, the condition number of $\underline{\mathbf{S}}$ is independent of the mesh size, and for not overly distorted domains, order unity; unfortunately, many domains (V–supercells) in which we solve the system (3.59)–(3.60) are indeed very distorted, originating bad conditioned meshes/systems which require a large number of outer iterations. Notice that the elimination of nip regions due to the microscale bounds (Section 2.2.4) should reduce overall distortion, and a reduction in computation time is expected.

Equation (E.14) of Appendix E is used for the incomplete–iteration error control (with no modifications, unlike the conduction case); small tolerances, $O(10^{-5})$, are

chosen for both the inner and outer iterations, and for the velocity solve. Notice that the residual in the outer iteration is precisely the discrete divergence, which can then be directly controlled with ϵ_{tol} [Rønquist (1988)].

3.2.5 Parallel Implementation

The two crucial evaluation operations of the conjugate gradient algorithm (Section 3.2.4) as regards computational complexity are the matrix–vector product in (3.34), and the inner products in (3.34) and (3.37). In this work, we use the now–standard, well–documented [Fischer (1989), Fischer & Patera (1991], technique of *elemental evaluation of operators*. The global system matrix $\underline{\mathbf{A}}$ is never formed or stored; instead, the quadratures are performed (exactly) to assemble elemental matrices (3×3 when $\mathcal{N}_o = 1$, 6×6 when $\mathcal{N}_o = 2$), which may or may not be stored. The requisite global matrix–vector products are then calculated by, first, performing the elemental matrix–vector multiplications, followed by direct stiffness summation; the latter operation ensures that, at a global node, integral contributions from test functions on neighboring elements are properly summed. A global node typically corresponds to a system degree of freedom, and to physically coincident elemental local nodes; in our implementation, values of the field variables, e.g. $\underline{\chi}_h$, are stored at every local node. Lastly, the inner products are calculated similarly, with local evaluations followed by summation over all the elements in T_h; notice that the contribution from a local node has to be divided by its multiplicity (number of coincident local nodes). The data structures that allow efficient execution of such conjugate gradient operations in a parallel environment, are described below.

Implementation of a particular PDE *parallel* solution algorithm (here, conjugate gradient) requires, first, the postulation of a model architecture (allowing for development of data constructs, and analysis of computational complexity associated with the algorithm/architecture coupling), and second, the practical implementation on an actual machine (hardware–software pair). Our adopted model architecture is described in detail in Fischer (1989), and has three essential ingredients: distributed–memory MIMD (multiple instruction multiple data) processors; message passing capability

(for direct stiffness summation); $O(\log_2 P)$ communication steps for inner product (global vector reduction) operations, P being the number of procesors.

The purpose of our PDE parallel solution algorithm is mainly to support the conjugate gradient iteration operations (3.34)–(3.38) on a parallel environment; the algorithm is, of course, applicable to both the conduction and creeping flow problems, and consists of: *data* partition (we use the SPMD — single program multiple data — paradigm), parallel direct stiffness summation and inner product (or vector reduction). These components are described separately next.

Data Partition

All the parallel data structures that we now describe are illustrated in Figure 3-11. The mesoscale domain (V–supercell) is divided into *collections*, which are, by construction, indivisible structured units, geometrically identified as subdomains; if mesh adaptivity is pursued, they may be divided into sub–units to allow for better load–balancing. The collections correspond, in our case, to the Voronoi tiles described in Section 3.2.1: after generation, on a workstation (i.e., serially), of the V–supercell, its tile–structured, geometrically and topologically described, skeleton is split among (parallel) processors. These will then operate on locally resident data, e.g. by individually performing sub–mesh generation (Section 3.2.2). Each collection is further subdivided into local data structures: at the highest level, it is composed of *local edges* and *local vertices*, and at the lowest level, of *elements*. Local edges correspond to collection boundary regions shared with another collection (note they need not be rectilinear), and local vertices delimit (but are not included in) the local edges. The elements are the volume building blocks of the collections, and are clearly identified with the simplex finite elements, here triangles. The length scales in a collection range from $O(d)$ for the local edges, to $O(h_r)$ for the elements.

In order to perform the conjugate gradient global operations, higher level global data structures are needed. *Global edges* are "mortars" between collections: to every pair of coincident local edges, there corresponds one global edge; notice that, due to periodicity, the local edges on the external boundary of the V–supercell "wrap–

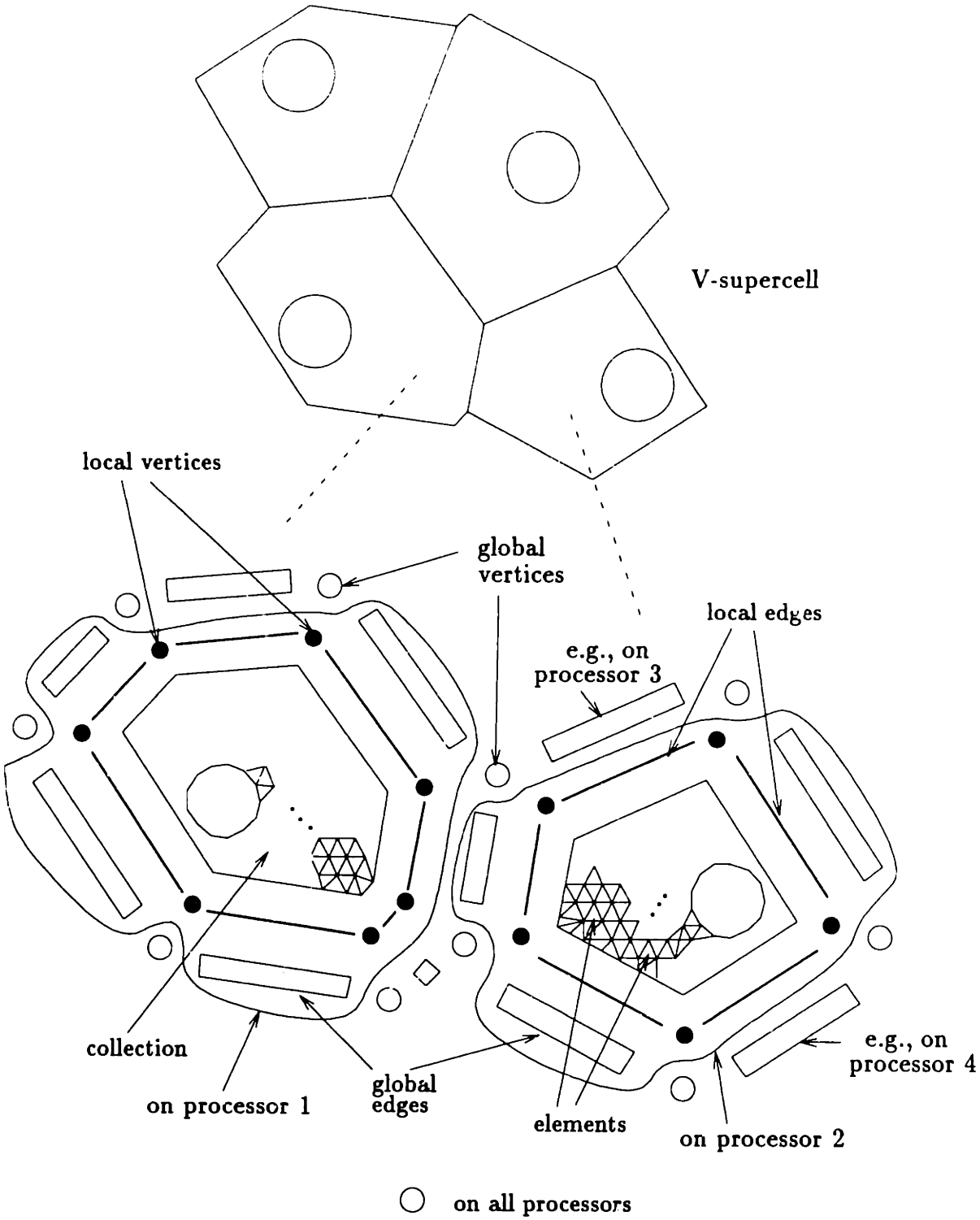

Figure 3-11: Parallel data structures.

around" and coincide. Regions of the domain boundary on which Dirichlet or Neumann boundary conditions are specified (such as $\partial\Omega_{me}$) do not have to be associated with local or global edges, since these boundary conditions are not *part* of the solution process. The inclusion surfaces inside the collections lie in this category, and therefore have no special data structures linked to them. A *global vertex* corresponds to coincident local vertices, so that they interface with three or more collections. For reasons presented below, the global edges, like the collections, are also distributed among the processors, and the global vertices are distributed to *all* processors. □

Direct Stiffness Summation

Communication (e.g., message passing) is needed at every iteration of the conjugate gradient solve, in order to exchange proper data for completion of the global operations; the higher level global data structures described above were designed to allow for efficient communication. Global edges, like the collections, are distributed among the processors, since they contain a significant amount of data. This distribution results in an acceptable overhead due to latency time when sending messages. Also, due to the structured nature of global edge data, contention is minimized. Global vertices, on the other hand, contain very little (one word per vertex), unstructured data, and therefore they can reside on all processors.

Direct stiffness summation updates, at each local node, local field variable values (computed from elemental evaluation of operators) to global values. Details of the parallel direct stiffness procedure are described in Appendix F; here, only the main steps are described.

First, a serial-type direct stiffness operation is performed within the collections on every processor; this step involves all the local data structures, and completely updates the values of the elemental nodes inside the collections. The local vertices and edges, and the nodes on the boundaries are only partially updated. Next, on each processor, global vertices accumulate the values from corresponding local vertices, and then a global gather–scatter operation is invoked to update all the global vertices. The correct (global) values are subsequently redistributed to the local vertices and

elemental nodes. Finally, sets of local edge data are sent to corresponding global edges, where they are summed. Subsequently, the correct data is sent back to the local edges, and then redistributed to the elemental nodes. □

Inner Product

Evaluation of inner products does not involve local, or global, edges or vertices. Each processor loops over the elements of all resident collections, accumulating the elemental contributions (divided by appropriate multiplicities) to the inner product in one partial result. Next, a global gather–scatter, architecture–supported, operation is invoked, which sums the partial results across the P processors, and broadcasts the final result. Such operation takes $\log_2 P$ communication steps on the hypercube architecture. □

The actual machine we used is an Intel iPSC/860 hypercube, with 32 8–Mb processors (or nodes). The code performed at about 30 MFLOPS (32–bit) on 16 processors, twice as fast as the Cray X-MP; this can represent a factor of 10 savings in the actual cost of the computation. The parallel efficiency was around 50%. Typically, on 16 processors, a complete three–level computation takes on the order of 50 hours, and a 16–inclusion realization requires a few minutes.

3.3 Monte–Carlo

In Section 3.2 we presented the Level 1 mesoscale computational procedure, namely, parallel solution of the discretized governing partial differential equations ((3.11) for conduction, and (3.28)–(3.29) for creeping flow). In this Section, we concentrate on the numerical methods for Level 2, which comprise: (i) sampling from the inclusion joint probability density function (JPDF) postulated in Section 2.1.3, equation (2.46); (ii) standard statistical methods for determining the ensemble average multi–dimensional integrals (2.48), for the effective conductivity, and (2.85), for the permeability, and the standard deviations and confidence intervals associated with them. We employ Monte–Carlo methods for both tasks (i) and (ii); the Monte–Carlo strat-

egy is described below. At the end of this section, we briefly discuss, in a separate paragraph, the simpler implementations of Levels 3 and 4.

The analytical construction of (2.46) involves an infinite series of n–point probability functions [Torquato & Stell (1982)]; this fact basically impedes any closed form results, unless the infinite series is truncated, as routinely done in bound methods (Section 1.2.1). Monte–Carlo techniques do not require explicit construction of the JPDF, and are superior to (e.g., tensor–product based) deterministic procedures, at least for evaluating these higher dimensional integrals (2.48) and (2.85) (notice $N \approx O(50)$). The actual probability density function of the random effective conductivity, K_e, or permeability, κ, is never formed; its relevant statistics are computed through the inclusion JPDF. Given the complexity of the latter, the integrals are evaluated by: first — task (i) —, *sampling* from P_N, which results in various configurations (or realizations) of the random medium (for fixed c and λ^*); second — task (ii) —, after solution of the pertinent mesoscale problem (Level 1, Section 3.2) for *many* realizations, a statistical analysis of the sample results is performed, from which the final Level 2 quantities are derived.

3.3.1 Sampling from the Inclusion JPDF

In this section we describe the implementation of the Level 2 task concerned with the successive generation of supercell configurations by sampling from the prescribed inclusion JPDF specified in (2.46). The sequence of configurations is denoted $[\{\mathbf{y}\}_N]_\nu$, $\nu = 1, \ldots, N_S$, where N_S is the sample size; again, in one configuration, the inclusion centers are located at $\mathbf{y}_i \in \Omega_{sc}$, $i = 1, \ldots, N$.

The standard acceptance–rejection sampling method [von Neumann (1951), Rubinstein (1981)] is used to generate the sequence $[\{\mathbf{y}\}_N]_\nu$. It is based upon the uniform conditional densities in (2.46) and the no–overlapping condition. The algorithmic steps of the method are enumerated below:

1. **start:** set counters C_{outer}, $C_{outer} = 1, \ldots, N_S$, and C_{inner}, $C_{inner} = 1, \ldots, N$, to zero

2. generate a first pair of *p*seudo–random numbers, $\mathbf{Y}_{p,1} = (Y^1_{p,1}, Y^2_{p,1})$, uniformly distributed in $\Omega_{box} = \{[0,1) \times [0,1)\}$, i.e., with probability density function

$$P_{\mathbf{Y}_p}(\mathbf{y}_p) = 1 \ , \quad \mathbf{y}_p \in \Omega_{box} \tag{3.62}$$

3. scale $\mathbf{Y}_{p,1}$ from Ω_{box} to Ω_{sc}

4. set $\mathbf{Y}_1$ equal to $\mathbf{Y}_{p,1}$, and identify $\mathbf{y}_1 = \mathbf{Y}_1$

5. accept first inclusion position $\mathbf{y}_1$

6. generate another pair $\mathbf{Y}_{p,i} = (Y^1_{p,i}, Y^2_{p,i})$, $i > 1$, and scale $\mathbf{Y}_{p,i}$ from Ω_{box} to Ω_{sc}

7. set $\mathbf{Y}_i$ equal to $\mathbf{Y}_{p,i}$, and identify $\mathbf{y}_i = \mathbf{Y}_i$

8. compute $\text{dist}(\mathbf{y}_i, \mathbf{y}_j)$: the distance between centers $\mathbf{y}_i$ and $\mathbf{y}_j$, $j = 1, \ldots, i-1$

9. if $\text{dist}(\mathbf{y}_i, \mathbf{y}_j)$ is greater than d, accept $\mathbf{y}_i$ and increment C_{inner} ; otherwise, reject $\mathbf{y}_i$, do not increment C_{inner} and go back to step 6

10. if C_{inner} is less than N, go back to step 6; otherwise, since then one set $\{\mathbf{y}\}_N$ is complete, call the domain generation process (Section 3.2.1 and Appendix D); next, increment C_{outer}

11. if C_{outer} is less than N_S, go back to step 2; otherwise, stop; **end**

The acceptance–rejection method is based on the fact that a uniform density over, say, Ω_{sc} is also uniform over any part of Ω_{sc}, so that a conditional density is obtained by restricting sampled values of the uniform density to the part of interest. Figure 3-12 illustrates the uniformity of the conditional densities (with the evenly shaded areas), and the no–overlapping constraint (with the "impenetrable" disks of diameter $2d$). Notice that the entire sequence $[\{\mathbf{y}\}_N]_\nu$ and associated V–supercells are generated on a workstation (i.e., in series), and later exported to the parallel processors. The serial–parallel processing phases could be integrated in a heterogeneous computing

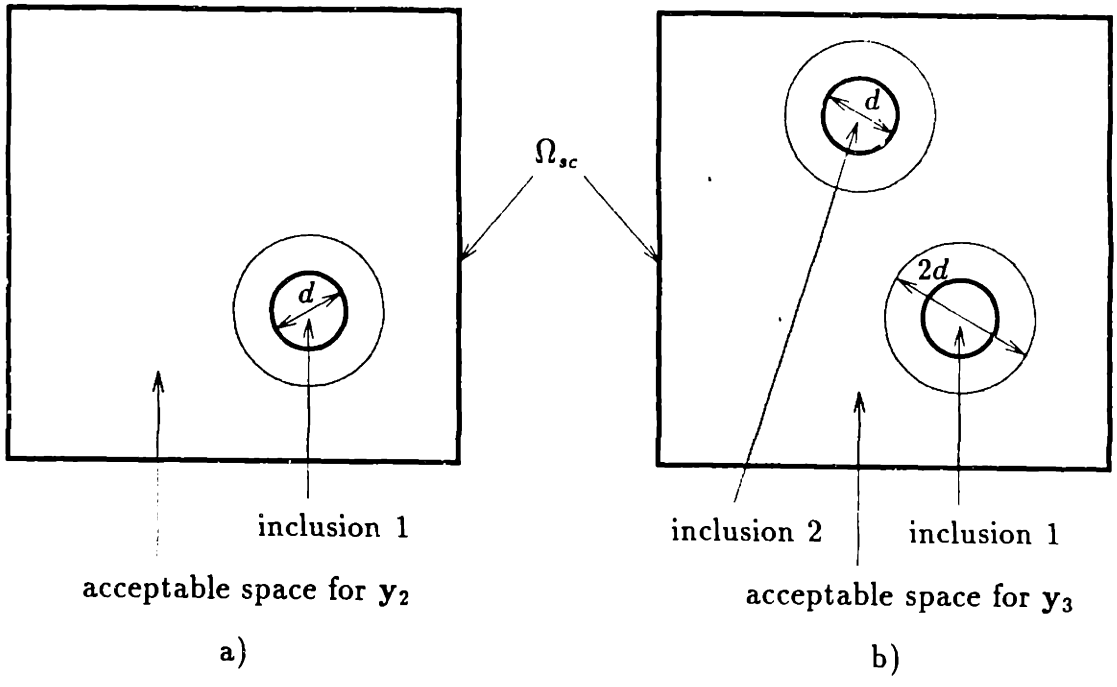

Figure 3-12: Acceptance–rejection method: a) step 2; shaded area represents the uniform conditional $P_{\mathbf{Y}_2|\mathbf{Y}_1}(\mathbf{y}_2|\mathbf{y}_1)$, and b) step 6, with $i = 2$; shaded area represents the uniform conditional $P_{\mathbf{Y}_3|\mathbf{Y}_1,\mathbf{Y}_2}(\mathbf{y}_3|\mathbf{y}_1,\mathbf{y}_2)$.

environment, in which N_S is not input, but rather open–ended: an acceptable statistical error on an effective property is specified, and the serial–parallel computations would proceed until such tolerance was achieved (sequential testing).

The key ingredient for the above algorithm is the pseudo–random number generator for executing steps 2 and 6. In this thesis, we used a linear congruential pseudo–random number generator, coupled with the shuffling algorithm due to Bays and Durham, implemented and recommended by Press, Flannery, Teukolsky & Vetterling (1989). The former generates uniform random deviates in the segment $[0, 1) \in \mathcal{R}$; the latter breaks any sequential correlations that might arise due to the pairing of successive deviates into the $\mathbf{Y}_{p,i}$'s. In Appendix G we report the actual generator and shuffling routine used, and present the results of the chi–square and Kolmogorov–Smirnov goodness–of–fit tests that were performed, to verify the adequacy of the coupling; in short, the results show that the coupling can satisfactorily generate *uniform* random pairs $\mathbf{Y}_{p,i}$'s in Ω_{box}. The main limitation of the adopted algorithm is

its failure to generate $O(10)$ supercells containing $O(10)$ inclusions for concentrations greater than about $c = 0.60$. It is common practice in the literature [Sangani & Yao (1988a), (1988b)], for such higher concentrations, to initially place the N inclusions on a regular lattice, and then perturb their positions with a normally distributed, random displacement. More detailed studies are necessary in this concentration range, to establish the relationship between practically realizable and postulated JPDF's.

3.3.2 Statistical Analysis

In this section we describe the implementation of the Level 2 task concerned with the evaluation of the integrals in (2.48) and (2.85).

We use standard statistical methods [Mood, Graybill & Boes (1974)] to estimate the ensemble averages (2.48) and (2.85), and associated uncertainties. Here, an ensemble average effective property is estimated by the corresponding (unbiased) sample mean; the ensemble variance is estimated by the corresponding (unbiased) sample variance; a confidence interval for the mean is determined in terms of the estimated variance and sample size, based on the assumption of normality of the mean (true when $N_S \to \infty$) and the asymptotic normality of the t–distribution. After parallel solution of the conduction and creeping flow problems for the sequence $[\{\mathbf{y}\}_N]_\nu$, the following Level 2 (nondimensional) quantities are then finally computed (estimated):

- sample mean effective conductivity, $\bar{K}_e^*$,

$$< K_e^* > (c, \lambda^*) \approx \bar{K}_e^* \approx \bar{K}_{e_h}^* = \frac{1}{N_S} \sum_{\nu=1}^{N_S} k_{e_h}'^*(c, \lambda^*, [\{\mathbf{y}^*\}_N]_\nu)\,, \qquad (3.63)$$

  and permeability, $\bar{\kappa}^*$,

$$< \kappa^* > (c, \lambda^*) \approx \bar{\kappa}^* \approx \bar{\kappa}_h^* = \frac{1}{N_S} \sum_{\nu=1}^{N_S} \kappa_h'^*(c, \lambda^*, [\{\mathbf{y}^*\}_N]_\nu)\,; \qquad (3.64)$$

- sample variance of the effective conductivity, $S^2(K_e^*)$,

$$\sigma^2(K_e^*) \approx S^2(K_e^*) \approx S^2(K_{e_h}^*) = \frac{1}{N_S - 1} \sum_{\nu=1}^{N_S} \left[k_{e_h}'^*(c, \lambda^*, [\{\mathbf{y}^*\}_N]_\nu) - \bar{K}_{e_h}^* \right]^2 , \tag{3.65}$$

and of the permeability, $S^2(\kappa^*)$,

$$\sigma^2(\kappa^*) \approx S^2(\kappa^*) \approx S^2(\kappa_h^*) = \frac{1}{N_S - 1} \sum_{\nu=1}^{N_S} [\, \kappa_h'^*(c, \lambda^*, [\{\mathbf{y}^*\}_N]_\nu) - \bar{\kappa}_h^* \,]^2 , \tag{3.66}$$

where σ^2 represents the true variance;

- confidence interval for the effective conductivity, $CI^C = CI(< K_e^* >)$,

$$CI^C = \left[\bar{K}_e^* - z_\alpha \frac{S^2(K_e^*)}{\sqrt{N_S}} \, , \, \bar{K}_e^* + z_\alpha \frac{S^2(K_e^*)}{\sqrt{N_S}} \right] , \tag{3.67}$$

and for the permeability, $CI^P = CI(< \kappa^* >)$,

$$CI^P = \left[\bar{\kappa}^* - z_\alpha \frac{S^2(\kappa^*)}{\sqrt{N_S}} \, , \, \bar{\kappa}^* + z_\alpha \frac{S^2(\kappa^*)}{\sqrt{N_S}} \right] , \tag{3.68}$$

where z_α is such that

$$2\,[1 - \Phi(z_\alpha)] = \alpha \, , \tag{3.69}$$

$1 - \alpha$ is the confidence level, i.e., the probability that $< \cdot >$ is indeed inside $CI(< \cdot >)$, and Φ is the standard normal cumulative distribution function.

It is seen from (3.67) and (3.68) that the Monte–Carlo error decreases as $\sqrt{N_S}$. Notice that although S^2 and the confidence interval CI are related, S^2 is the variance of the process, and CI is related to the sampling error for the mean; also, a confidence interval for the variance is needed as well, since the Level 3 correlation length should reliably guarantee that the variance of the effective property, at such length, is small.

Level 3 and Level 4 The Level 3 procedure is concerned with the determination of the composite and porous medium correlation lengths, $\lambda^{*C} = \lambda^C/d$ and $\lambda^{*P} = \lambda^P/d$, respectively. The essential computational element of Level 3 is the construction

of a functional representation of $< K_e^* > (c, \lambda^*)$ or $< \kappa^* > (c, \lambda^*)$, from which to extrapolate the large–λ^* behavior. As we are primarily interested in those values of λ^* for which, say, $< K_e^* > (c, \lambda^*)$, is, by plausible assumption, smooth, many techniques are appropriate. In particular, once an estimate of the asymptotic value of the effective property is obtained, then prescription of the tolerances ε_1 and ε_2 (Section 2.1.3), and simple interpolation procedures between values of k_e^* or κ^* are enough to determine the correlation length, shown in Chapter 4 (for the conduction problem).

The Level 4 procedure is trivial in this single–parameter study of the effective properties, and just consists of repeating Levels 1, 2, and 3 for different values of the concentration c. The more complete multi–parameter function–construction task, with the objective of developing a model for the effective conductivity or permeability as a function of a parameter vector, $\mathbf{p}$, given a set of individual calculations at isolated parameter values, is not addressed here; the reader is referred to Yeşilyurt & Patera (1993) for such statistical modelling techniques.

Chapter 4

Results and Conclusions

In this chapter, we present and analyse our results. In Section 4.1, we validate our implementation by reproducing the well-known effective conductivity and permeability results for the square and hexagonal periodic arrays of cylinders; in particular, we show the expected second-order convergence, with mesh spacing, of the effective properties (see Section 3.2.3). In Sections 4.2 and 4.3, the effective conductivity and the permeability results for the *random* periodic arrays generated in this study (see Sections 3.2.1 and 3.3.1) are discussed, respectively. Finally, in Section 4.4 we state our conclusions, and in Section 4.5 we indicate relevant future work in the field of multicomponent media suggested by our conclusions.

We remark that all the results presented in this chapter are nondimensional: the effective conductivity is normalized with respect to the matrix conductivity k_{co}, and the permeability is normalized with respect to the diameter d of the inclusions. The (general) symbols used are k_e^* for the former, and κ^* for the latter. Other quantities are defined as they appear. We also note that all the figures for this chapter have been placed after the text of Section 4.5.

4.1 Results for Regular Arrays

4.1.1 Conduction

As mentioned in Section 1.2.3, exact effective conductivity results are known for regular arrays of cylinders; they are tabulated in Perrins, McKenzie & McPhedran (1979) for various values of the concentration c, and of the ratio of inclusion to matrix conductivities, ς, for both the square (Figure 4-1 (a)) and hexagonal (Figure 4-1 (b)) periodic arrangements. In order to obtain the exact values for insulating inclusions (since here, $k_{di} = 0$), we invert the results reported for infinitely conducting inclusions, based on Keller's relation for isotropic arrays, equation (1.1). Figures 4-2 (a) and (b) show (scalar) effective conductivity data points with varying concentration for the square and hexagonal arrays, respectively. It is seen that our numerical results match the exact ones for *all* tabulated values. We should note that the domain generation procedure described in Section 3.2.1 had to be slightly modified to produce the hexagonal one–inclusion V–supercells.

More importantly, Figures 4-3 (a) and (b) show, for the same arrays, the (normalized) absolute error E_h^C, defined by

$$E_h^C = k_{e_h}^* - k_e^* , \tag{4.1}$$

versus the nominal mesh spacing h^*, identified with

$$h^* = \frac{h_0^*}{r} \tag{4.2}$$

(Section 3.2.2), for three values of the concentration; k_e^* is the exact conductivity value (determined from table), and $h_0^* = h_0/d$. Notice that, as shown in Section 3.2.3 (for $E_h'^C$), the error E_h^C is positive. Indeed, the expected second–order convergence of the effective conductivity with mesh spacing, using $\mathcal{P}_1$ triangles, as derived in Section 3.2.3, is clearly obtained. In the convergence tests, the value of h_0^* was fixed at 0.5, the parameter m was fixed at 2, and the refinement parameter r varied from 1 to

12.5. The incomplete iteration error tolerance, ϵ_{tol} (Section 3.2.3), varied from 10^{-4} to $6 \cdot 10^{-3}$. The number of degrees of freedom typically ranged from 150 to 25000 as r increased; the CPU time ranged from a few seconds to a few hours for each data point. All these one-inclusion tests were performed on a workstation. The accuracy of the tabulated effective conductivity values for $k_{di} = \infty$ for both the square and hexagonal arrays, about 10^{-4}, yields absolute errors in k_e^* of 10^{-5} to 10^{-7} for concentrations from 0.10 to close to maximum packing, respectively, due to the use of inverse values for insulating inclusions ($k_{di} = 0$). In the case $c = 0.78$ for the square array, or $c = 0.90$ for the hexagonal array, and $r = 2.5$, the lowest tolerance ϵ_{tol} for which the iteration converged was $6 \cdot 10^{-3}$ (notice that at these high concentrations the conditioning of the discrete system is very bad), allowing reliable absolute error in $k_{e_h}^*$ only on the order of 10^{-4}. This explains the anomalous position of the lower left point of the $c = 0.78$ (Figure 4-3 (a)) and $c = 0.90$ (Figure 4-3 (b)) curves.

Similar convergence tests were carried out using second-order ($\mathcal{P}_2$) triangles. For a convex problem [Strang & Fix (1973)], third-order convergence of $k_{e_h}^*$ (whose error varies with the square of H^1-seminorm of χ_h) is expected. In our case, the problem is not convex (see Figures 4-1 (a) and (b)), and skin-effects only allow second-order convergence (notice that the midpoint on the side of a triangle touching an inclusion surface lies *inside* the inclusion). For the same set (h_0^*, m, r), the absolute error E_h^C in (4.1) with $\mathcal{P}_2$ triangles is half the error with $\mathcal{P}_1$ triangles.

4.1.2 Creeping Flow

Similarly, exact results for creeping flow through periodic square and hexagonal arrays are plotted (and also tabulated) in Sangani & Acrivos (1982a) in the nondimensional form $\frac{F}{\mu_{co} U}$ versus c, where F is the force per unit length exerted on one cylinder by the fluid, and U is the (volume) average fluid velocity. The (normalized) permeability, from equation (2.61), can thus be calculated, by dividing $(\lambda/d)^2$ by $\frac{F}{\mu_{co} U}$. Figures 4-4 (a) and (b) show (scalar) permeability data points with varying concentration for the square and hexagonal arrays, respectively. It is seen, again, that our numerical results match the exact ones for *all* tabulated values.

Again, more importantly, Figure 4-5 shows, for the square array, the (normalized) absolute error E_h^P, defined by

$$E_h^P = |\kappa_h^* - \kappa^*|, \tag{4.3}$$

versus the nominal mesh spacing h^*, given in (4.2); κ^* is the exact permeability value (determined from table). Second–order convergence of the permeability is seen to be obtained with $\mathcal{P}_2 - \mathcal{P}_1$ triangles (notice that third–order convergence is not attainable with sub–parametric elements, due to the skin–effect mentioned in Section 3.2.3). In the convergence tests, the value of h_0^* was fixed at 0.5, the parameter m was fixed at 2, and the refinement parameter r varied from 1 to 3. The incomplete iteration tolerances for the inner and outer Uzawa iterations (and for the velocity solve) were set equal, and varied from 10^{-8} to 10^{-5}. The number of (one–component) velocity degrees of freedom typically ranged from 450 to 6000 as r increased; the CPU time ranged from a few seconds to a couple of hours for each data point. The accuracy of the tabulated values, about 10^{-2}, yields absolute errors in κ^* of 10^{-4} to 10^{-8} for concentrations from 0.10 to 0.50, respectively.

4.2 Results for Random Arrays: Conduction

We next present and discuss the effective conductivity results for the mesoscale problem of heat conduction in unidirectional fibrous random composites (Section 2.1), as solved by the numerical methods in Chapter 3 (note: in what follows, for the sake of notation simplicity, the subscript $_h$ indicating numerical quantities is omitted). The production runs had the following characteristics:

- Level 1: for each c, λ^*, and realization $\{\mathbf{y}^*\}_N$, $\mathcal{P}_1$ triangles were used, with h_0^* set to 0.1, m to 2, r to 1, and ϵ_{tol} to 10^{-2};
- Level 2: for each c and λ^*, typically, $N_S = 100$ realizations;
- Level 3: for each c, 10 different values of λ^*, corresponding to number of inclusions in the set $N \in \{2, 4, 6, 8, 12, 16, 24, 32, 40, 48\}$;

- Level 4: 5 different concentration values, $c \in \{0.10, 0.20, 0.30, 0.40, 0.50\}$.

It should be pointed out that in some cases, the mesh generation procedure or the conjugate gradient iteration failed, due to the presence of nearly touching inclusions (distance between them on the order of machine (single) precision). For these critical cases (i.e., configurations with nearly touching inclusions), an effective conductivity value could not be computed with $\mathcal{P}_1$ triangles, and the attempted ensemble was left incomplete (obviously, the sample size N_S was correspondingly reduced). This problem was alleviated by using, in such instances, $\mathcal{P}_2$ triangles with same h_0^* and m, but with r changed from 1 to $1/\sqrt{2} \approx 0.707$. This value for r is based on the fact that $\mathcal{P}_2$ triangles, as mentioned in Section 4.1.1, have half the error of $\mathcal{P}_1$ triangles with same (h_0^*, m, r). Since the triangles sides on the boundaries $\partial\Omega_{VE}$ and $\partial\Omega_{me}$ become a little larger when r is decreased (see Section 3.2.2), meshing is easier (i.e., fails less), and the conditioning is improved. This measure allowed solution of many realizations previously rejected with $\mathcal{P}_1$ elements, with *same* discretization error as in the other normal cases (empirical tests on realizations for which both $\mathcal{P}_1$ and $\mathcal{P}_2$ worked confirmed this claim). Overall, the vast majority of the Level 2 calculations had at most 2 realizations missing; in four cases, at the highest concentrations $c = 0.40$ and $c = 0.50$, 8 to 10 realizations were rejected. Also, due to limited performance of the acceptance–rejection method for higher concentrations (see Section 3.3.1), more than one seed was used for the concentration $c = 0.50$.

The meshing/iteration failing problem mentioned above is technical, rather than conceptual. In fact, calculations in double precision were performed on the MIT Cray X-MP which allowed successful solution of some critical configurations with $\mathcal{P}_1$ elements. The development of the nip–region bounds presented in Section 2.1.4 allows rigorous and definitive solution of this problem; also, even for non–critical configurations, appropriate solutions may be obtained faster, by avoiding element–dense nip–regions. We estimate that the number of degrees of freedom after elimination of nip–regions may decrease, in extreme cases, by 20% (at $c = 0.10$) to 75% (at $c = 0.50$), and the conditioning may improve by a factor of 100; therefore, a reduction in the computation time by a factor of 10 or more can be easily accomplished.

Figure 4-6 (a) shows the Level–3 results for the behavior of the effective conductivity $< K^*_{e_{11}} >$ as a function of the normalized supercell size λ^*, for all the Level–4 concentration values. The two points at the lowest value of λ^* for each c (i.e., the square and the hexagonal symbols), correspond to the conductivities of the square and hexagonal arrays, the latter having higher values than the former, more so at higher c. It is seen, first of all, that all data points for a particular c lie below $1 - c$, as expected from equation (2.19), Section 2.1.3. Also, there are some oscillations of the conductivity values in the lower λ^* range, but they ultimately disappear, and the conductivity seems to approach an asymptotic limit; this behavior allows determination of correlation lengths, as described below. Finally, the results for the random arrays lie systematically below those for either one of the regular arrays. We comment on this random versus regular behavior below.

Figure 4-6 (b) shows the behavior of the effective conductivity $< K^*_{e_{22}} >$ as a function of λ^*, for all the Level–4 concentration values. Again, the leftmost points for each c are for the regular arrays. The vertical, I–shaped, bars represent the Monte–Carlo confidence intervals (Section 3.3.2) for $< K^*_{e_{11}} >$, i.e., $CI(< K^*_{e_{11}} >)$; the confidence intervals $CI(< K^*_{e_{22}} >)$ are not shown for clarity of the Figure. Notice that this type of plot allows easy comparison between $< K^*_{e_{11}} >$ and $< K^*_{e_{22}} >$. It is seen that both diagonal components of the effective conductivity tensor behave very similarly, both qualitatively and quantitatively; clearly, to within statistical errors (since confidence intervals for $< K^*_{e_{11}} >$ and $< K^*_{e_{22}} >$ are roughly of the same size and overlap), the random arrays as constructed from equation (2.46) (Sections 2.1.3 and 3.3.1) are isotropic *on the average*. This is further evidenced by Figures 4-7 (a) and (b): the former shows a definite approach of $< K^*_{e_{12}} >$ to zero as λ^* increases; more importantly, the latter shows that all the computed confidence intervals for $< K^*_{e_{12}} >$ contain the value zero. Notice that higher absolute values of $< K^*_{e_{12}} >$ at lower λ^* simply indicate that larger sample sizes are necessary to average out any anisotropic contributions, since at larger λ^*, spatial averaging reduces the variance of $< K^*_{e_{12}} >$. The (average) isotropy of the random arrays is not at all surprising, given that there was no distinction between the y_1 and y_2 directions in the construction

process (Sections 3.2.1 and 3.3.1). Based on the above conclusions, in what follows, only the results for $< K^*_{e_{11}} >$ are presented; also, for simplicity, we drop the indices and write $< K^*_e >$ instead of $< K^*_{e_{11}} >$.

Figure 4-8 shows the standard deviation in the effective conductivity, $\sqrt{S^2(K^*_e)}$ (Section 3.3.2), as a function of λ^*. Clearly, it decreases for all concentrations, though with a few "bumps"; notice that the significance of such "bumps" cannot be assessed without confidence intervals for the standard deviation, which are absent here. The decreasing behavior of $\sqrt{S^2(K^*_e)}$ is attributed to a spatial averaging effect: as the V–supercell size increases, there is a spatial average contribution to ensemble averaging, which do not occur as much at lower supercell sizes. The dependence of $\sqrt{S^2(K^*_e)}$ on concentration is not so clear: no smooth behavior was found, although the standard deviation, for fixed λ^*, was consistently lowest at $c = 0.10$, and highest at $c = 0.30$, so it appears non–monotonic. This fact can perhaps be motivated in the following way. At lower concentrations, the particular configuration of the particles is not so important, since there are many paths for heat transfer: the variance is small. At medium concentrations, relative increase in the number of particles makes their positioning extremely important, since now there are fewer paths, and small displacements of particles can significantly affect overall heat transfer: the variance is large. At the highest concentrations, heat transfer paths are limited, but there is not much room for significantly changing the relative positions of the particles; also, the particles cover more cell space, and a spatial averaging effect contributes for attenuating variations of the mean: the variance is intermediate.

Figures 4-9, 4-10 and 4-11 show the mean values $< K^*_e >$ and associated 99% confidence intervals for the concentrations of 0.10, 0.30 and 0.50, respectively, with varying λ^*. In these Figures, we also show the conductivity results reported by Sangani & Yao (1988a) for random arrays of cylinders (Section 1.2.3); their λ^* value corresponds to $N = 16$. Here, we simply invert their (major axis) values for infinitely conducting inclusions, though they presented the full conductivity tensor (notice isotropy is required to use Keller's equation, (1.1)). Since their sample sizes are reportedly small (about 10 for each concentration), off–diagonal contributions may not have averaged

out, and are simply disregarded here. Also, we *estimated* confidence intervals (shown in the Figures as dashed I–shaped bars) for their mean values, based on our standard deviations and sample size of 10. Their results are seen to agree with ours to within the Monte–Carlo sampling errors, since the respective confidence intervals overlap.

The oscillations in the mean $< K_e^* >$ at lower λ^* values, mentioned above, for all concentrations in Figures 4-9, 4-10 and 4-11, are more clearly observed (due to magnified vertical scale): they are more pronounced at higher concentrations, and as λ^* increases, they disappear for all concentrations, so that $< K_e^* >$ approaches an asymptotic value. Notice that larger sample sizes (greater than 100) *might* smooth out these oscillations, though, obviously, leaving the (true) standard deviation, $\sigma(K_e^*)$, unaltered. The decaying confidence intervals simply reflect decaying standard deviations with λ^* (Figure 4-8), since the sample sizes were about the same for all cases. Note the results for the regular arrays are shown without confidence intervals.

Given the observed asymptotic behavior of the effective conductivity $< K_e^* >$ mentioned above, we can extract, by inspection of the calculated results, values for:

- (an estimate of) the asymptotic limit $k_e^*(c) \equiv < K_e^* > (c, \lambda^* = \infty)$ (Section 2.1.3), identified with our conductivities at the highest values of λ^* (which correspond to $N = 48$ for each c);

- the correlation length $\lambda^{*C}(c)$ (see Sections 2.1.3 and 3.3.2), by prescribing tolerances ε_1 (for the mean) and ε_2 (for the standard deviation), and performing simple linear interpolation in λ^* between calculated results;

- the number of particles associated with λ^{*C} for each concentration, $N(\lambda^{*C})$ (closest higher integer);

- the practically interesting relation $k_e^{*C}(c) \equiv < K_e^* > (c, \lambda^{*C}(c))$, also by performing linear interpolation in λ^*.

The chosen tolerances for determining $\lambda^{*C}(c)$ are $\varepsilon_1 = 3\%$ and $\varepsilon_2 = 5\%$. Notice that ε_1 includes the incomplete iteration and the Monte–Carlo sampling errors, but not the

c	$k_e^*(c)$	$\lambda^{*C}(c)$	$N(\lambda^{*C})$	$k_e^{*C}(c)$
0.10	0.813	3.0	2	0.817
0.20	0.651	3.6	4	0.654
0.30	0.512	5.4	12	0.513
0.40	0.390	6.1	19	0.390
0.50	0.281	7.0	32	0.281

Table 4.1: Effective conductivity results for various values of c: asymptotic values, correlation lengths and associated quantities.

discretization error. The results are shown in Table 4.1, and plotted in Figures 4-12 and 4-13.

Figure 4-12 shows $\lambda^{*C}(c)$ in terms of c. The behavior of $\lambda^{*C}(c)$ can be mainly explained (mathematically) with one effect: the monotonic decrease of $k_e^*(c)$ (see Table 4.1). A fixed percentage ε_2 of $k_e^*(c)$ is progressively smaller with c, and since the standard deviation $\sigma(K_e^*)$ increases from $c = 0.10$ to around $c = 0.30$, higher values of λ^*, at a given c in this range, are required to satisfy the ε_2 constraint in the definition of the correlation length. In the higher concentration range (above $c = 0.30$, say), the standard deviation slightly decreases, but now the ε_1 constraint predominates, causing an increase in the correlation length to make $k_e^{*C}(c)$ closer to $k_e^*(c)$. The observed non-monotonicity in the standard deviation possibly accounts for the apparent decrease in the rate of variation of $\lambda^{*C}(c)$ with c; however, no slopes can be appropriately quantified from our data. In particular, if two data points for $c = 0.30$ were ignored, due to "bumps" in the standard deviation, a value of 4.8 would be obtained for $\lambda^{*C}(c = 0.30)$. This value would lead to a somewhat linear appearance (i.e., constant rate of change) of the curve in Figure 4-12. Neglect of such points is not strictly allowed without confidence intervals for the standard deviation. A physical motivation for the increasing behavior of λ^{*C} with c, is the fact that there are more particles around one test particle (i.e., within the effect, quantified e.g. with Green's functions, of one test particle) at higher concentrations than at lower concentrations. Therefore, a larger N (in fact, N/c, see Table 4.1) is needed at higher c to take account of the particle interactions.

Figure 4-13 shows $k_e^{*C}(c)$ in terms of c. Clearly, as physically expected from the insulating nature of the inclusions, $k_e^{*C}(c)$ is a decreasing function of c, and, consistently with equation (2.32), lies below the line $(1-c)$. Also, as mentioned before, the effective conductivities of the random arrays are seen to lie below the ones for regular arrays. It is hard to give an explanation for this fact, based on a quantitative estimate of a single parameter, like the average nearest–neighbor interparticle spacing, given the geometrical complexity of the random arrays. The interparticle spacing, at a given c, is higher for hexagonal arrays than for square arrays, and, given their geometrical simplicity, accounts for the difference between them, also seen in Figure 4-13. Notice that such regular arrays have a guaranteed, uniform, path for heat transfer for all concentration values below the associated maximum packing limit; the same is *not true* for random arrays. It is therefore suggested here that this lack of a guaranteed uniform path for heat transfer is a possible structure–based explanation for the observed behavior of the random arrays with respect to the regular arrays.

The difference in effective conductivity between regular and random arrays is progressively larger as the concentration increases. Indeed, Figure 4-14 shows the relative difference between such arrays, expressed by:

$$E^C_{rel,HS} = \frac{1}{k^*_{e,hex}} [k^*_{e,hex} - k^*_{e,sq}] , \tag{4.4}$$

$$E^C_{rel,RS} = \frac{1}{k_e^{*C}} [k^*_{e,sq} - k_e^{*C}] , \tag{4.5}$$

and

$$E^C_{rel,HR} = \frac{1}{k^*_{e,hex}} [k^*_{e,hex} - k_e^{*C}] , \tag{4.6}$$

where $k^*_{e,sq}$ and $k^*_{e,hex}$ represent the effective conductivities of the square and hexagonal arrays, respectively. Notice that the numerators in (4.4), (4.5) and (4.6) were chosen to be positive; the k_e^* values in the denominators are for the array with higher c_{max} of the two being compared, where c_{max} is the maximum two–dimensional close packing ($c_{max} = 0.785, 0.82, 0.907$ for the square, random, and hexagonal arrays, respectively [see Berryman (1983)]). It is seen that $E^C_{rel,HS}$, $E^C_{rel,RS}$ and $E^C_{rel,HR}$ increase with c

(since, mainly, the denominators decrease), and that the latter two are practically identical (ranging from 0.2% at $c = 0.10$ to about 16% at $c = 0.50$). We therefore conclude that: first, the "mechanism" which distinguishes random from regular arrays is independent of the particular regular array configuration; second, any differences in the absolute errors $k^*_{e,sq} - k^{*C}_e$ and $k^*_{e,hex} - k^{*C}_e$, at a given c (Figure 4-13), are due to different maximum packing limits, which force rapid decrease of the conductivity to zero at different values of c. We should also note that, consistently with the above physical argument of dissimilar heat transfer paths, the difference between random and regular arrays is larger than the difference between distinct types of regular arrays, since $E^C_{rel,RS}$ and $E^C_{rel,HR}$ are above $E^C_{rel,HS}$.

As mentioned in Section 1.2.5, Hasselman, Bhatt, Donaldson & Thomas (1992) conducted experiments with a composite made of an aluminoborosilicate glass matrix and high conductivity carbon fibers. At the concentration of approximately $c = 0.60$, the experimental value for the effective conductivity was 4.56 [$\frac{k_e}{k_{co}}$ = (4.47 W/mK) / (0.98 W/mK), Hasselman (1993)], with inverse value $k^*_{e,exp} = 0.22$. If we simply fit, in a least-squares sense, a (third-order) polynomial through our data in Figure 4-13, *enhanced by* the point ($c = 0, k^{*C}_e = 1$), then at $c = 0.60$ we obtain $k^{*C}_e = 0.182$. This estimate is 17% lower than the experimental value $k^*_{e,exp}$; the square array overestimates $k^*_{e,exp}$ by 5%, and the hexagonal overestimates by 13%. However, the fit does not reproduce a sharp decrease in the conductivity at higher values of c: this is evidenced by the substantially lower extrapolated value at $c = 0.70$ as compared to the value calculated by Sangani & Yao. If we then include their $c = 0.70$ data point (since we did not compute a conductivity for this concentration) in a new fit, the new value at $c = 0.60$ is 0.20, 9% below the experimental value; a partial explanation for the better agreement is that Sangani & Yao's result at $c = 0.50$ is higher than ours, Figure 4-11. Notice also that Sangani & Yao employ a different method for sampling from the inclusion JPDF at high concentrations, based on normally distributed random inclusion displacements. A similar fit to Sangani & Yao's (16-inclusion) data yields a conductivity value at $c = 0.60$ of 0.205 (7% below $k^*_{e,exp}$). We remark that a comparison between our (extrapolated) result and the experimental value is

somewhat artificial, given our previous discussion; the purpose of the comparison is to highlight that different "choices" for the composite microstructure lead to fairly different results.

Finally, Torquato & Lado (1988) report (in a plot) lower bounds for the effective conductivity of random arrays of cylinders for infinitely conducting inclusions (the upper bounds diverge to infinity). Transforming their lower bounds into *upper* bounds for the case of insulating inclusions, by using inverse values, we obtain (approximately) 0.78, 0.64, 0.51, 0.39 and 0.29 for the concentrations 0.10, 0.20, 0.30, 0.40 and 0.50, respectively. These results are not consistently *above* our k_e^* values in Table 4.1; differences in the assumed composite microstructure may be the cause for such discrepancy.

An Original Multiscale Problem Calculation

The practical utility of the decomposition procedure of the original problem (Section 2.1.1) into the macroscale–mesoscale–microscale problems (Sections 2.1.2, 2.1.3 and 2.1.4, respectively) is now illustrated by means of one example. In particular, with the objective of comparing the total heat flux in a random medium with the averaged, macroscale heat flux given by equation (2.7) (Section 2.1.2) and using our results for the effective conductivity k_e^{*C}, we performed an original problem calculation with the following characteristics:

- concentration $c = 0.30$;
- $N_{orig} = 128$ inclusions in a square box $((\lambda_{box}/d) = 18.3)$; notice that (see below) periodicity is *not* imposed around the box, i.e., it is *not* a supercell;
- medium's configuration picked *at random*;
- boundary conditions: insulated at the top and bottom faces; imposed constant temperatures $T = 1$ and $T = 0$ at the left and right faces, respectively.

It is convenient to generate such domain (i.e., box) using the Voronoi diagram, since the latter provides the subdomains and partitioning for parallel processing. The

domain generation procedure described in Section 3.2.1 has to be slightly modified for this purpose, in the following way: instead of 25 squares, we now have 9 squares, all of edge length λ_{box} ; the centers are generated in the middle square, but now they are *reflected* across the 4 sides and 4 corners of the middle square into the neighboring 8 squares (there is no replication); the Voronoi diagram is then constructed, and this set–up ensures that Voronoi edges will lie along all the vertical and horizontal faces of the 9 boxes. The middle box can thus be extracted from the diagram, partitioned in tiles ready for distribution to parallel processors. In order to avoid "cut" inclusions by the box vertical and horizontal faces, the centers were forced to be away from such faces by a distance of at least the radius. This constraint slightly changes the inclusion distribution as compared to the one given by equation (2.46). Figure 4-15 shows the Voronoi diagram with the 9 boxes, and Figure 4-16 shows the extracted middle box, actually used in this example.

The domain shown in Figure 4-16 was distributed among 32 parallel processors, and meshed according to the procedure described in Section 3.2.2; the set ($h_0^* = 0.1$, $m = 2$, $r = 1$) was used. A total of approximately 85000 degrees of freedom resulted. The discretization and solution followed the methods described in Sections 3.2.3, 3.2.4 and 3.2.5, the only difference being that Dirichlet and Neumann boundary conditions, rather than periodic, were imposed on the outer boundaries.

We obtained the following results: after 20 hours of computation time, the total heat flux in the x_1 direction for the random medium (Figure 4-16), normalized with respect to $k_{co}(\Delta T/L)$, was $Q^* = 0.0252$; after a few seconds of calculation using $k_e^{*C}(c = 0.30)$ in Table 4.1, the macroscale heat flux in the x_1 direction for the homogenized medium was $Q_{ma}^* = 0.0280$ (notice that even higher values are obtained for regular arrays). The difference, 11%, is consistent with the expected uncertainty associated with the macroscale heat flux: as the ratio $\lambda^{*C}/\lambda_{box}$ decreases, it is expected that Q_{ma}^* approaches Q^*, so that the uncertainty in Q_{ma}^* scales with such ratio; because of practical limitations the box could not be made "very large," and $\lambda^{*C}/\lambda_{box} = 5.4/18.3 \approx 30\%$.

4.3 Results for Random Arrays: Creeping Flow

We next present and discuss the permeability results for the mesoscale problem of creeping flow through fibrous random porous media (Section 2.2), as solved by the numerical methods in Chapter 3 (the subscript $_h$ is also omitted below). The production runs had the following characteristics:

- Level 1: for each c, λ^*, and realization $\{\mathbf{y}^*\}_N$, $\mathcal{P}_2 - \mathcal{P}_1$ triangles were used (Section 3.2.3), with h_0^* set to 0.2, m to 2, r to 1, and ϵ_{iter} to 10^{-5} for both the inner–outer Uzawa, and velocity solve, conjugate gradient iterations;
- Level 2: for each c and λ^*, typically, $N_S = 50$ realizations;
- Level 3: for each c, 8 different values of λ^*, corresponding to number of inclusions in the set $N \in \{2, 4, 6, 8, 12, 16, 24, 32\}$;
- Level 4: 5 different concentration values, $c \in \{0.10, 0.30, 0.35, 0.45, 0.48\}$.

It should be pointed out that in many cases, the outer Uzawa conjugate gradient iteration did not converge to the prescribed tolerance, due to the sensitivity of the Stokes problem to bad conditioning (Section 3.2.3). Again, nip–region bounds (see Section 2.2.4) should greatly alleviate this problem. Empirical incomplete iteration error estimation was performed (since, as opposed to the conduction problem, there is no direct control on the propagation of such error to the permeability), and it was concluded that the associated error induced in the permeability is no greater than 1.5%. In very few realizations the mesh generator failed, since now the mesh spacing is larger than the one used in the conduction problem (Section 4.2). Still, satisfactory accuracy is guaranteed by the use of second–order triangles for the velocity field, on which the permeability depends: though no discretization error estimate is present, a comparison of the numerical with analytical results for regular arrays, in the range of concentration specified above, shows that the error induced in the permeability by the discretization error is less than 1% (naturally, to obtain such a number, the conjugate gradient tolerances were set much lower, $O(10^{-7})$). Overall, it is estimated

that the permeability values reported here have an error around 2% (Monte–Carlo uncertainties excluded).

Figure 4-17 shows the Level–3 results for the behavior of the permeability $< \kappa^* >$ as a function of the normalized supercell size λ^*, for all the Level–4 concentration values (notice that, due to isotropy, indices for κ^* are omitted). The two points at the lowest value of λ^* for each c (i.e., the square and the hexagonal symbols), correspond to the permeabilities of the square and hexagonal arrays. It is seen, first of all, that all data points for a particular c are above the zero line, as expected from equation (2.73), Section 2.2.3. Also, there are some oscillations of the permeability values all throughout the λ^* range covered. For each c, these oscillations are seen to decrease in size as λ^* increases, but no asymptotic limit has been reached; therefore, correlation lengths *cannot* be identified for the creeping flow problem with our data. It is concluded that, first, asymptotic values for the permeability are likely to exist, given the decreasing amplitude of the oscillations, and second, that the creeping flow problem, for a given c, has larger correlation length than the conduction problem. Finally, a dramatic decrease in $< \kappa^* >$ with c is observed: roughly, for the range of c covered, $< \kappa^* >$ goes down by one order of magnitude per 20 percentage points decrease in c.

Figure 4-18 shows the standard deviation in the permeability, $\sqrt{S^2(\kappa^*)}$ (Section 3.3.2), as a function of λ^*. Clearly, it decreases with λ^* for all concentrations, though with a few "bumps", as for the conduction problem. This decreasing behavior is, again, attributed to the spatial averaging effect mentioned earlier (Section 4.2). As opposed to the conduction problem, however, it seems that the standard deviation is, for a given λ^* (and overlooking one or other "bump"), a monotonically *decreasing* function of the concentration c. It is not clear why the standard deviation behaves so differently in the conduction and creeping flow problems.

Figures 4-19 and 4-20 show the mean values $< \kappa^* >$ and associated 99% confidence intervals for the concentrations of 0.10 and 0.30, respectively, with varying λ^*. In these Figures, we also show the permeability results reported by Sangani & Yao (1988b) for random arrays of cylinders (Section 1.2.3). Here, we simply use their values

corresponding to the principal direction, though they presented the full permeability tensor. Also, we *estimated* confidence intervals (shown in the Figures as dashed I-shaped bars) for their mean values, based on our standard deviations, and sample size of 10. Again, their results are seen to agree with ours to within the Monte-Carlo sampling errors, since the respective confidence intervals overlap.

Figures 4-21, 4-22 and 4-23 show the mean values $< \kappa^* >$ and associated 99% confidence intervals for the concentrations of 0.35, 0.45 and 0.48, respectively, with varying λ^*. The oscillations in the mean $< \kappa^* >$ for all concentrations in Figures 4-19–4-23 are more clearly observed, and they do not completely disappear in the range of λ^* covered. However, for each c, $< \kappa^* >$ seems to be approaching an asymptotic value: larger values of λ^* are needed to estimate/determine $\kappa^*(c) =< \kappa^* > (c, \lambda^* \rightarrow \infty)$. Again, the decaying confidence intervals simply reflect decaying standard deviations, since the sample sizes were about the same for all cases (except for the last confidence interval for each c, corresponding to $N = 32$, for which the sample size was about half, i.e., 25). The results for the regular arrays are shown without confidence intervals.

Figure 4-24 shows the permeability $< \kappa^* >_{N=32}$, which corresponds to the mean $< \kappa^* >$ at our highest value of λ^* (associated with $N = 32$ inclusions), as a function of the concentration; permeabilities for the square and hexagonal arrays are also shown. Clearly, $< \kappa^* >_{N=32}$ is a decreasing function of c. Also shown are the confidence intervals $CI(< \kappa^* >_{N=32})$; notice that these confidence intervals *do not* account for any uncertainty related to the fact that the highest λ^*, for each c, was not large enough to allow the mean to reach an asymptotic value. Bearing this fact in mind, a crossover between the behaviors of regular and random arrays is observed: at lower concentrations, the permeability of random arrays is larger than that of regular arrays, whereas it is lower at higher concentrations; the crossover happens around $c = 0.30$ (similar crossover exists between the square and hexagonal arrays, with the latter surpassing the former as c increases, when $0.10 < c < 0.20$).

Figure 4-25 shows the relative differences between the random, square and hexagonal arrays, expressed by:

$$E^P_{rel,HS} = \frac{1}{\kappa^*_{hex}} [\kappa^*_{hex} - \kappa^*_{sq}] , \tag{4.7}$$

$$E^P_{rel,RS} = \frac{1}{< \kappa^* >_{N=32}} [\kappa^*_{sq} - < \kappa^* >_{N=32}] , \tag{4.8}$$

and

$$E^P_{rel,HR} = \frac{1}{\kappa^*_{hex}} [\kappa^*_{hex} - < \kappa^* >_{N=32}] , \tag{4.9}$$

where κ^*_{sq} and κ^*_{hex} represent the permeabilities of the square and hexagonal arrays, respectively. It is seen that $E^P_{rel,HS}$ (shown with a dashed line), $E^P_{rel,HR}$ and $E^P_{rel,RS}$ (shown with a continuous line) increase with c, though the latter decreased between $c = 0.30$ and $c = 0.45$. The crossovers are reflected in the sign changes of the E^P_{rel}'s.

The sharp decrease in $< \kappa^* >$ as the concentration increases (Figure 4-24) is probably related to a channel flow effect. The average velocity and flow rate in a channel flow is proportional to the cube of the plates separation. As c increases, the average nearest–neighbor interparticle spacing plays the role of a decreasing channel separation, which is dependent on the concentration ($O(c^{-1/2})$). The observed crossover between regular and random arrays (Figures 4-24 and 4-25) may result from a percolation phenomenon in the latter. The flow through a random array encounters "large" and "small" passages compared to the fixed passage of a regular array. At low concentrations, the "large" passages dominate, in that they ultimately allow the flow to pass through the medium; therefore, resistance combines in parallel, and the permeability of random arrays is larger. At high concentrations (thus closer to the value at which percolation is not possible), flow conduits become scarcer, and the "small" passages become a bottleneck: resistance then combines in series, and the permeability of random arrays is smaller.

We now compare our permeability results to those obtained in some previous investigations. Spielman & Goren (1968), extending Brinkman's low–concentration approach from 2 to 3 dimensions (Section 1.2.2), obtained $\kappa^* = 0.417$ for the concen-

tration $c = 0.10$, for an arrangement consisting of fibers with axes all lying in planes perpendicular to the direction of the superficial velocity, but having completely random angles in those planes. Such value is about 4.5% higher than ours (notice the difference between their geometry and ours), and underestimates experimental data for filters made of various materials, e.g. cotton [Davies (1952)]. As the concentration increases, our permeability values are such that a Carman–Kozeny constant of about 10 is approached. For the concentration of $c = 0.45$, for example, it is about 10.5; Happel (1959) obtained a value of 5.46, for the same c, for flow perpendicular to a cylinder in a unit cell.

Experimental values for the concentrations 0.35, 0.45 and 0.48 are available in Gebart (1992), who performed permeability measurements in resin transfer moulding (Section 1.2.5). The experimental set–up consists of a mould filled with bundles of fibers, placed parallel to each other and perpendicularly to the flow; inside each bundle, the fibers are practically touching each other. Basically all the flow happens around the bundles, assumed circular in shape. The dashed lines in Figures 4-21, 4-22 and 4-23 represent tentative nondimensional equivalents of Gebart's experimental values. Since these were given in $meter^2$ and the effective radius of the fiber bundles was unknown, we first have to match the permeability values at one concentration, say $c = 0.35$ (this is probably the most "neutral" one, since all arrays are closest around this value, Figure 4-24), and subsequently compute an effective bundle radius, or diameter. Such diameter is then used to normalize the permeability values at the other concentration values, $c = 0.45$ and $c = 0.48$. Matching the values at $c = 0.35$ gives a bundle radius of about 45μm (the fiber diameter is about 10μm). Differences in the geometrical arrangement of the fibers and fiber bundles, and our JPDF given in (2.46), account for the observed discrepancy in the Figures (around 20%).

Finally, we point out that permeability results can be used to compute sedimentation rates, if one assumes that the random array moves in a rigid (locked) fashion. The settling velocity, $\mathcal{U}$, is then given by $\mathcal{U} = -\frac{\kappa \nabla p_{sed}}{\mu_{co}}$, where the permeability κ is known, and the pressure gradient ∇p_{sed} is equated to the total weight of the array, corrected for buoyancy. The velocity $\mathcal{U}$ so calculated may be compared to experimental data;

much data is available for sedimenting spheres, but not for cylinders (sedimenting fibers). The application of our methodology to three–dimensional porous media can thus help to clarify the controversy over the dependence of $\mathcal{U}$ on concentration for *dilute* suspensions of spheres [Batchelor (1972), Saffman (1974)]. The low concentration exponent for the dependence of the permeability on c for fibrous porous media cannot be reliably extracted from our data (more results at low concentrations are needed).

4.4 Conclusions

In the previous three chapters, we have presented a general methodology for the analysis of multicomponent random media, based on a parallel nested Monte–Carlo partial–differential–equation solution paradigm. The methodology was applied to the problems of heat conduction in unidirectional fibrous composites and creeping flow through fibrous porous media; in this chapter, the results were presented, discussed and compared to previous findings. The conclusions of our study, from the physical and algorithmic points of view, may be stated as follows:

- **Physics**
  - For both the conduction and creeping flow problems, the effect of the microstructure of the medium is extremely important; in particular, the important question of what to do if the microstructure is unknown, deserves further investigation (e.g., by studying an appropriate manufacturing process, or by obtaining hierarchical information with experimental techniques), given that fairly different results may be obtained with different assumptions.
  - For the conduction problem,
    * the effective conductivity, at a given concentration, of the hexagonal array is higher than that of the square array, which in turn is higher than the conductivity of the random array;

    * the correlation length was determined, and seen to increase with concentration;
    * possible non-monotonicities exist in the function relating the standard deviation of the effective conductivity to the concentration.
  - For the creeping flow problem,
    * a crossover between the permeabilities of random and regular arrays was observed (the crossover is also present between square and hexagonal arrays);
    * the standard deviation was seen to be a monotonically decreasing function of the concentration;
    * for a given concentration, higher values of the supercell size with respect to the conduction problem are required in order to achieve the correlation length.

- **Algorithmic**
  - A new methodology is available to systematically investigate the complex physics of random multicomponent media; the methodology can help elucidate various aspects of such media which are not totally resolved.
  - The incorporation of parallel algorithms into our scheme makes it more attractive than serial approaches, in terms of computation cost.

4.5 Future Work

Based on our study, we can suggest the following as relevant, related future work in the area of multicomponent random media:

- Investigation of various correlation functions for describing microstructure.
- Implementation of nip-region variational bounds.
- Discretization error estimation and control (adaptivity).

- Determination of confidence intervals for the standard deviation.
- Extension of the methodology to three dimensions.
- Extension of the methodology to sedimentation.
- Extension of the methodology to include inertial effects.

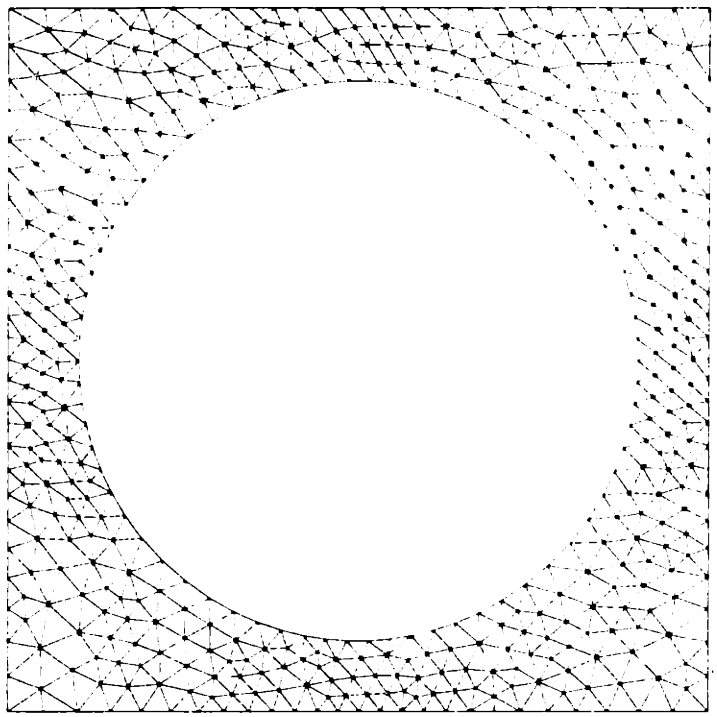

(a)

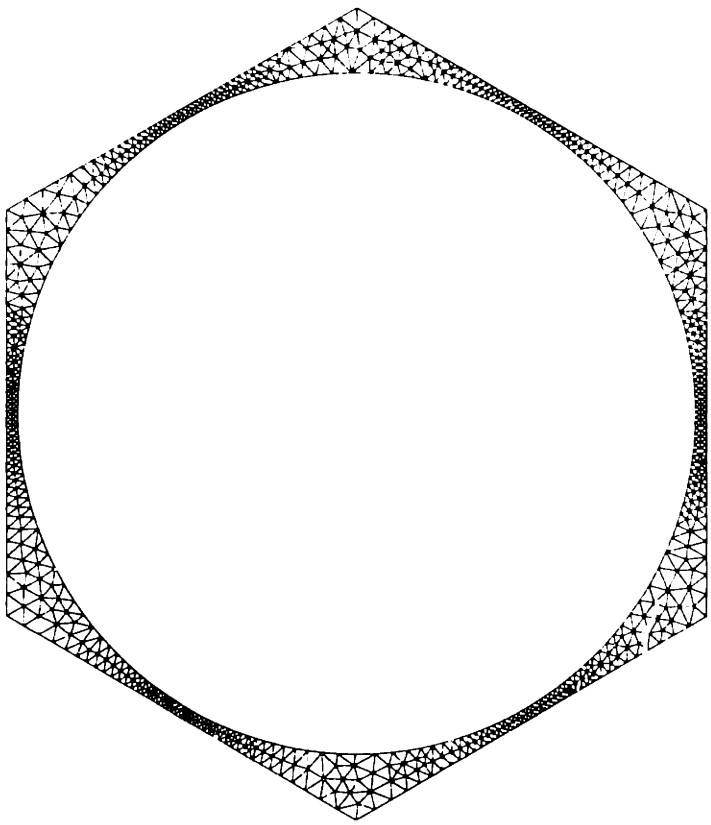

(b)

Figure 4-1: Regular arrays: (a) square ($c = 0.50$, 500 degrees of freedom), and (b) hexagonal ($c = 0.85$, 850 degrees of freedom).

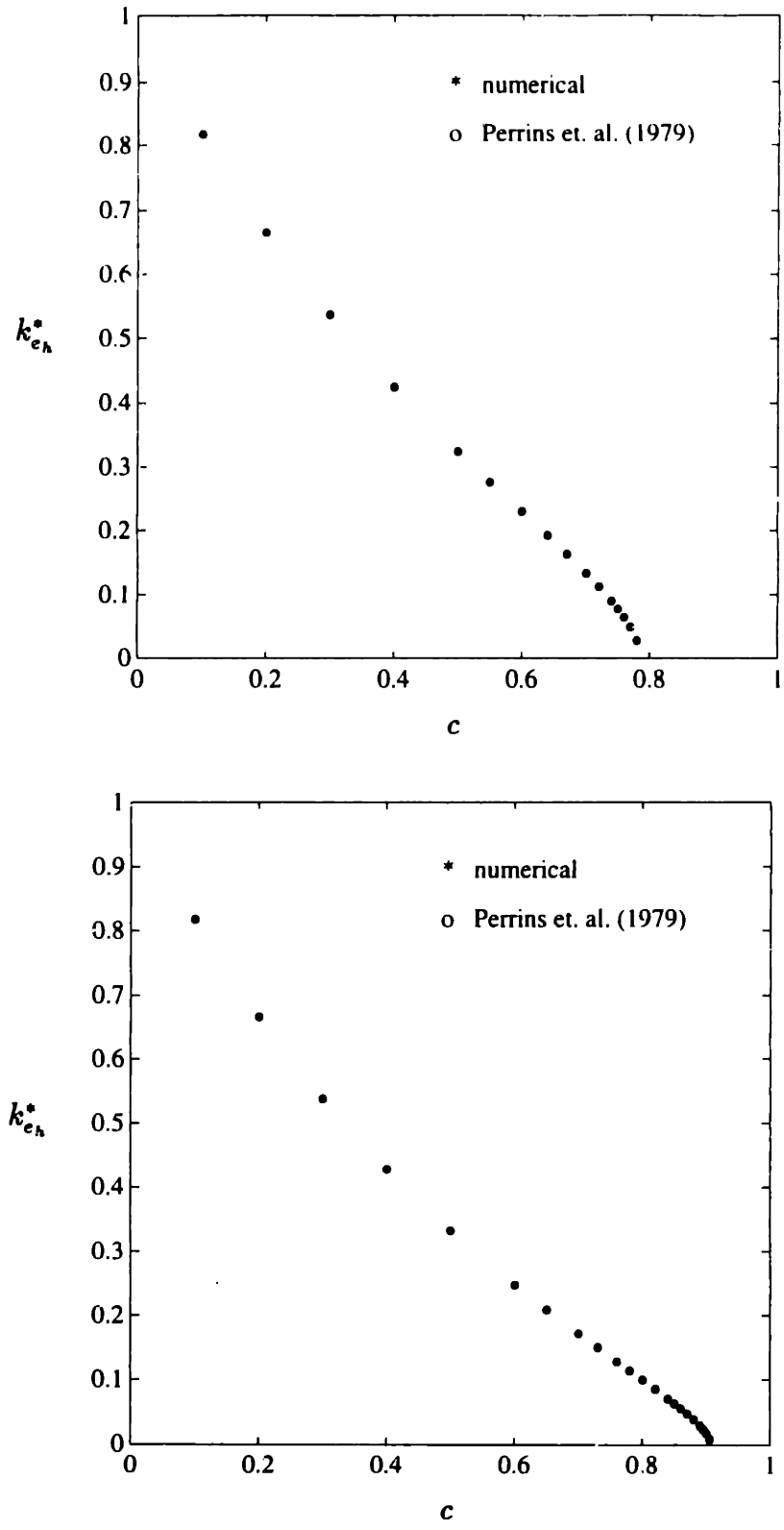

Figure 4-2: Effective conductivities $k^*_{e_h}$ (numerical) and k^*_e (exact) as functions of concentration c for (a) square and (b) hexagonal arrays.

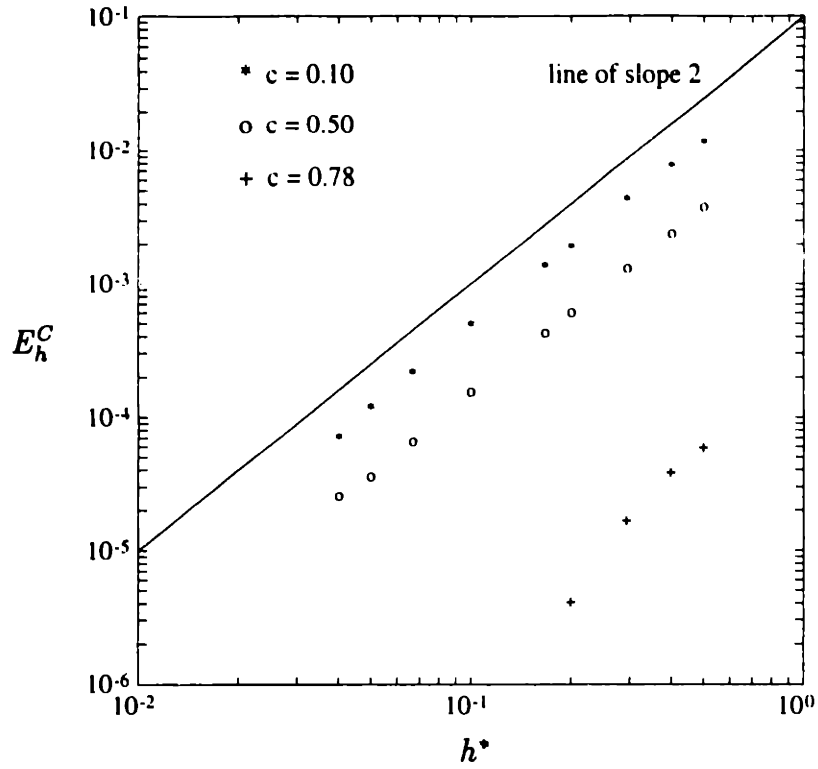

(a)

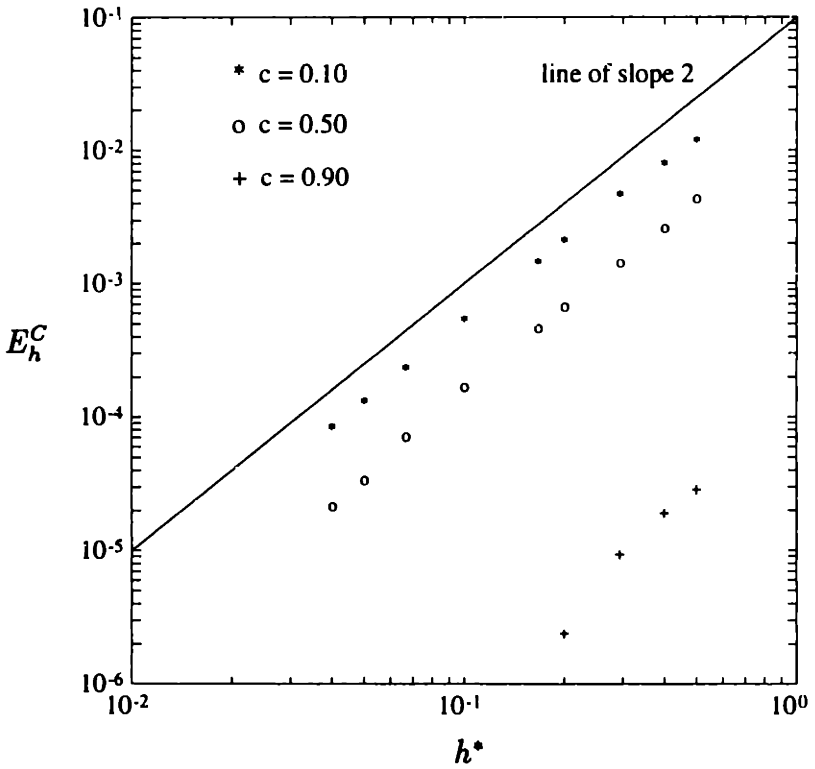

(b)

Figure 4-3: Convergence of the effective conductivity $k_{e_h}^*$ with mesh spacing h^* for the (a) square and (b) hexagonal arrays: the absolute error E_h^C decreases as h^{*2}.

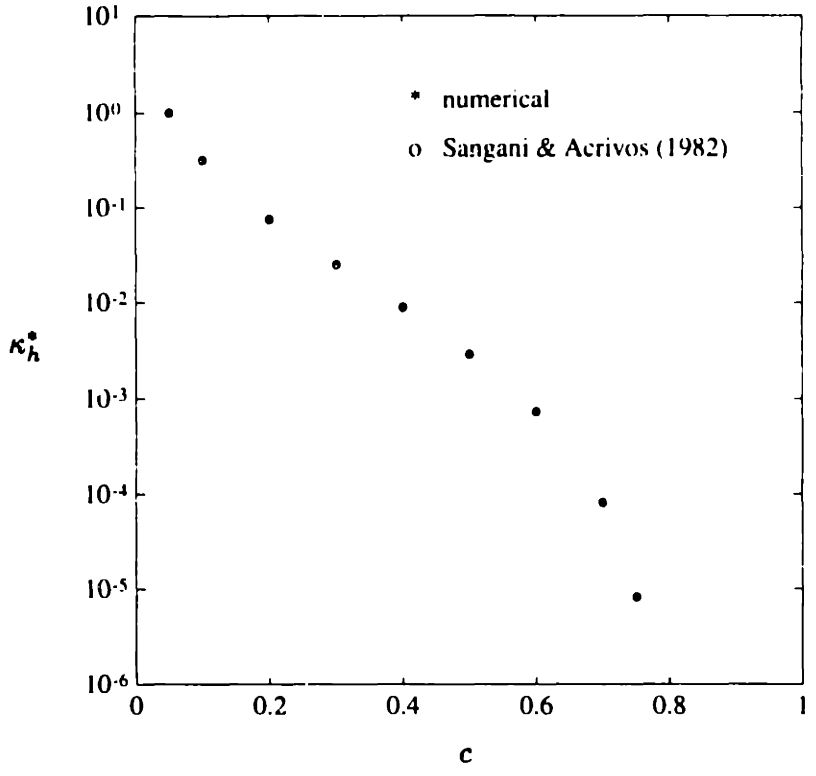

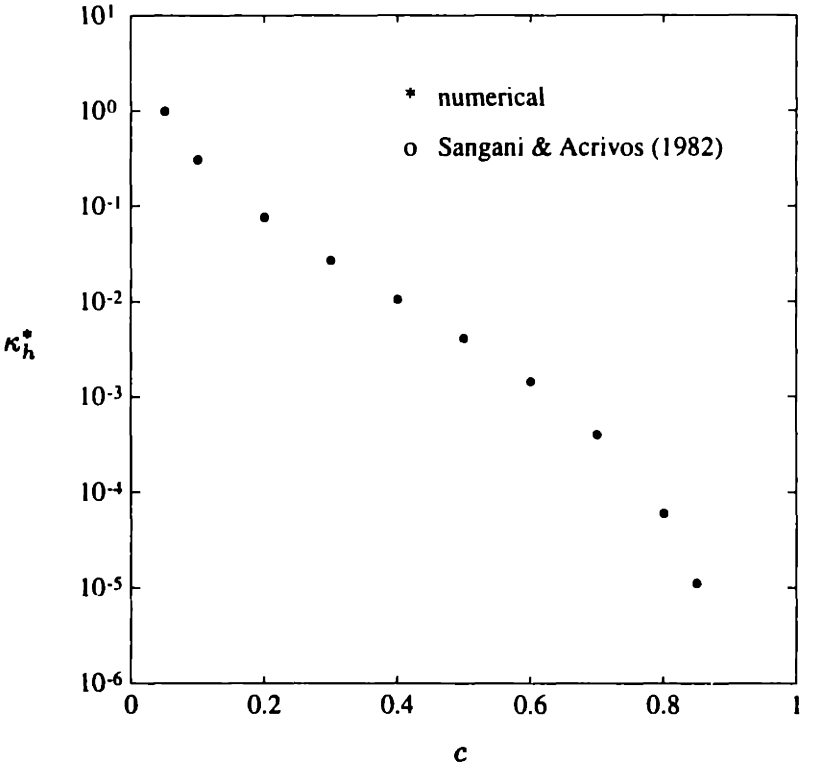

Figure 4-4: Permeabilities κ_h^* (numerical) and κ^* (exact) as functions of concentration c for (a) square and (b) hexagonal arrays.

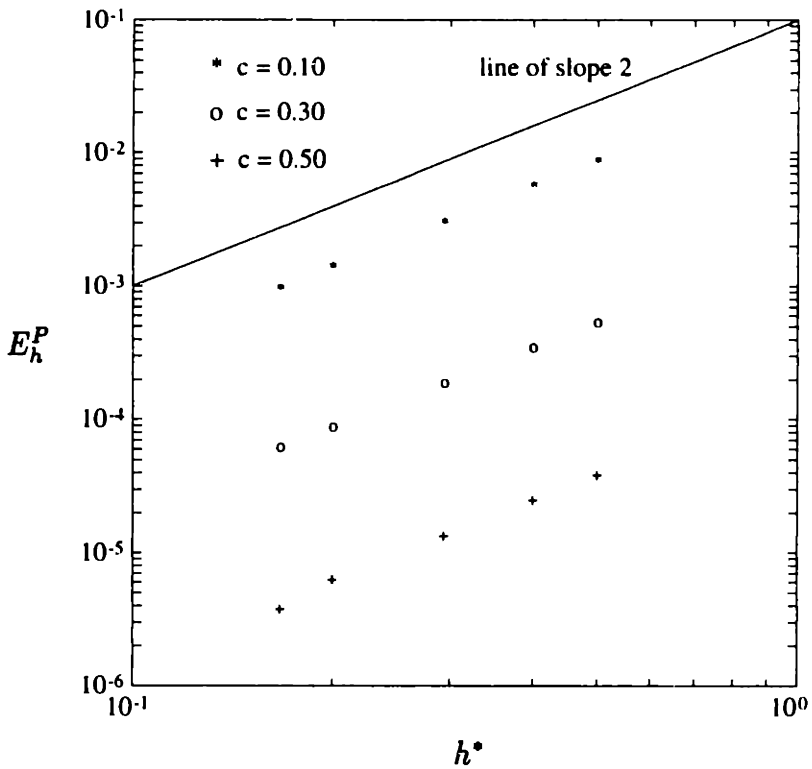

Figure 4-5: Convergence of the permeability κ_h^* with mesh spacing h^* for the square array: the absolute error E_h^P decreases as h^{*2}.

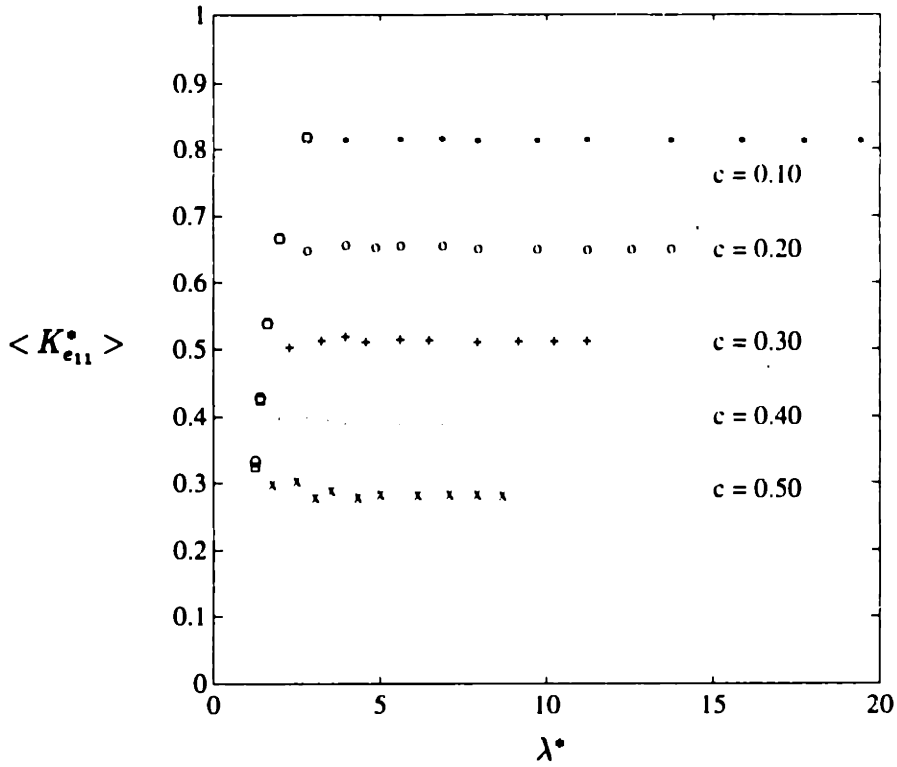

(a)

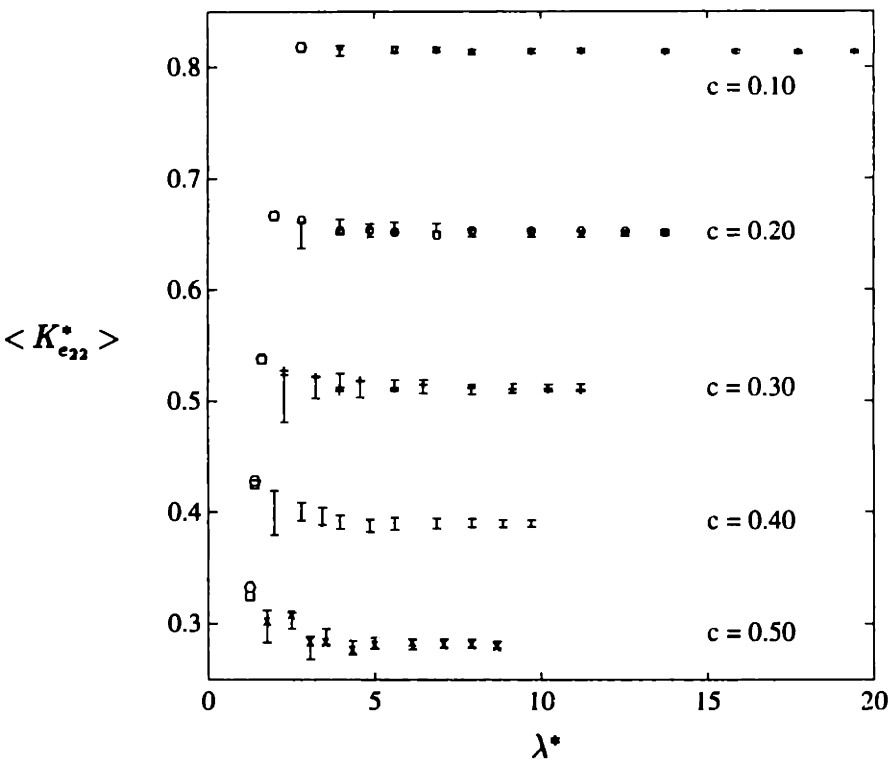

(b)

Figure 4-6: Effective conductivity versus supercell size λ^* for various values of c: (a) $< K^*_{e_{11}} >$; (b) $< K^*_{e_{22}} >$ and confidence intervals $CI(< K^*_{e_{11}} >)$.

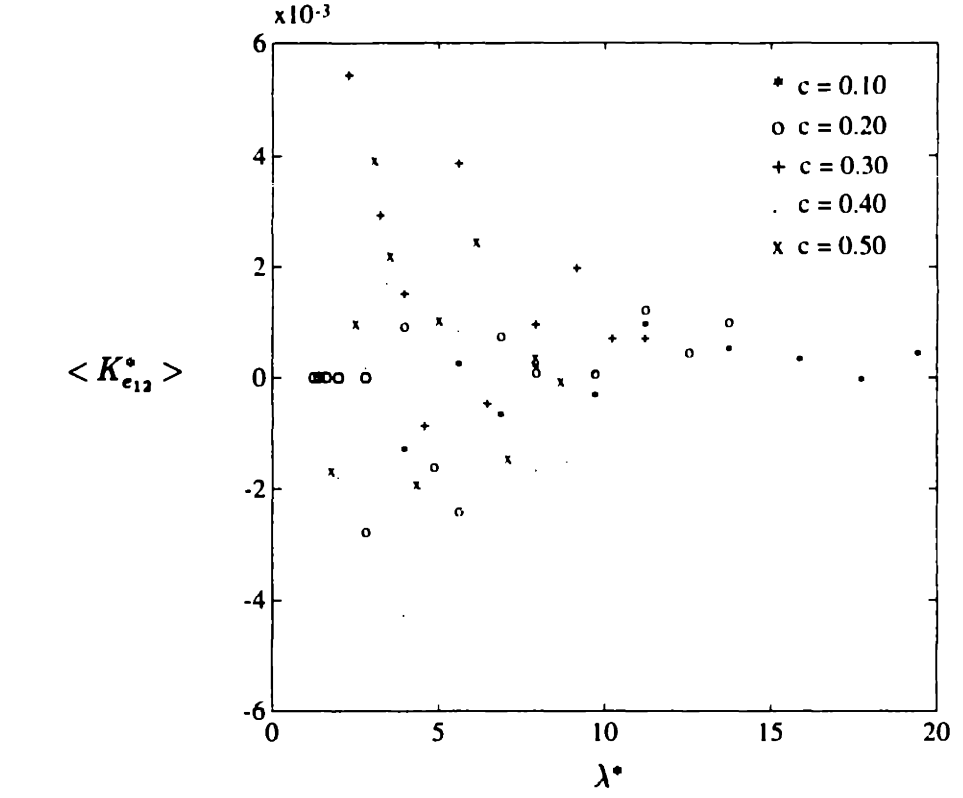

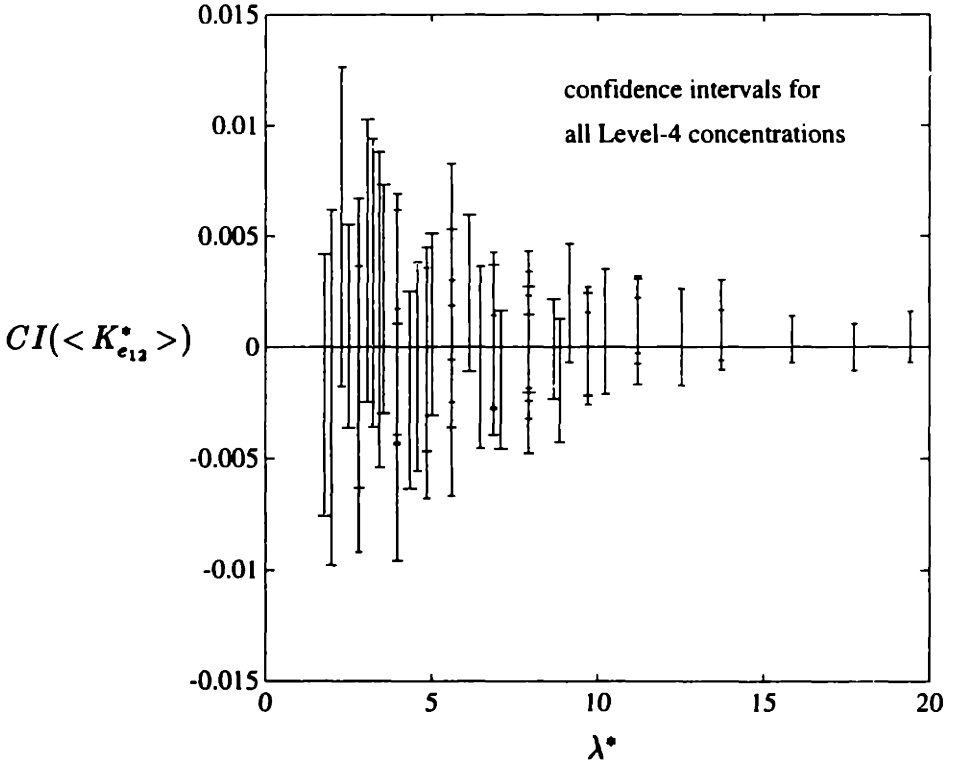

Figure 4-7: Effective conductivity versus supercell size λ^* for various values of c: (a) $< K^*_{e_{12}} >$; (b) confidence intervals $CI(< K^*_{e_{12}} >)$.

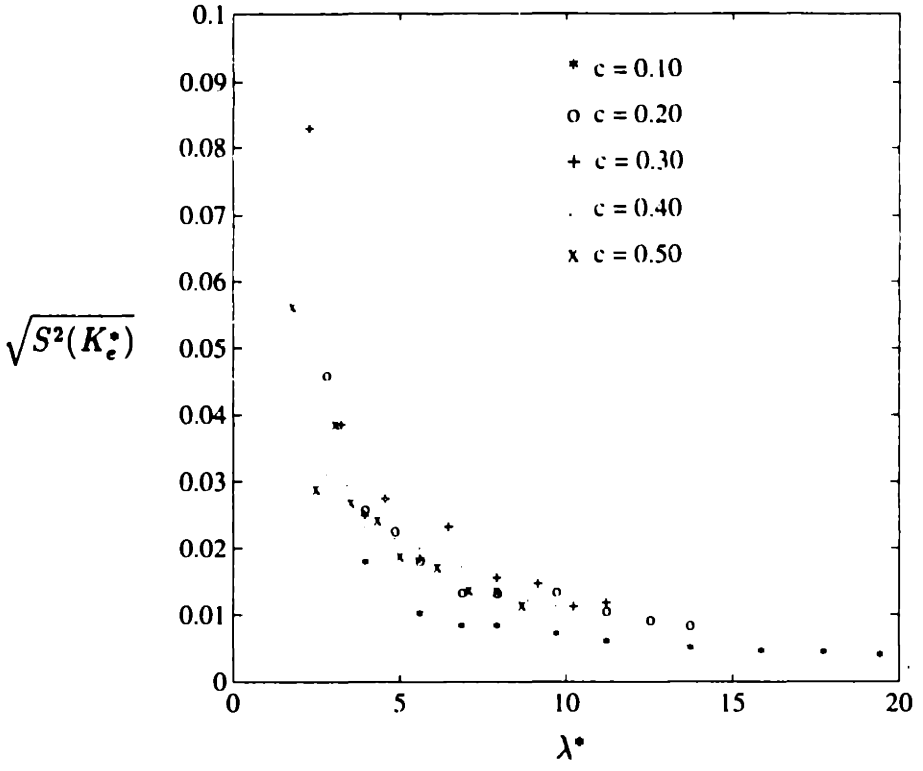

Figure 4-8: Standard deviation of the effective conductivity, $[S^2(K_e^*)]^{\frac{1}{2}}$, versus supercell size λ^* for various values of c.

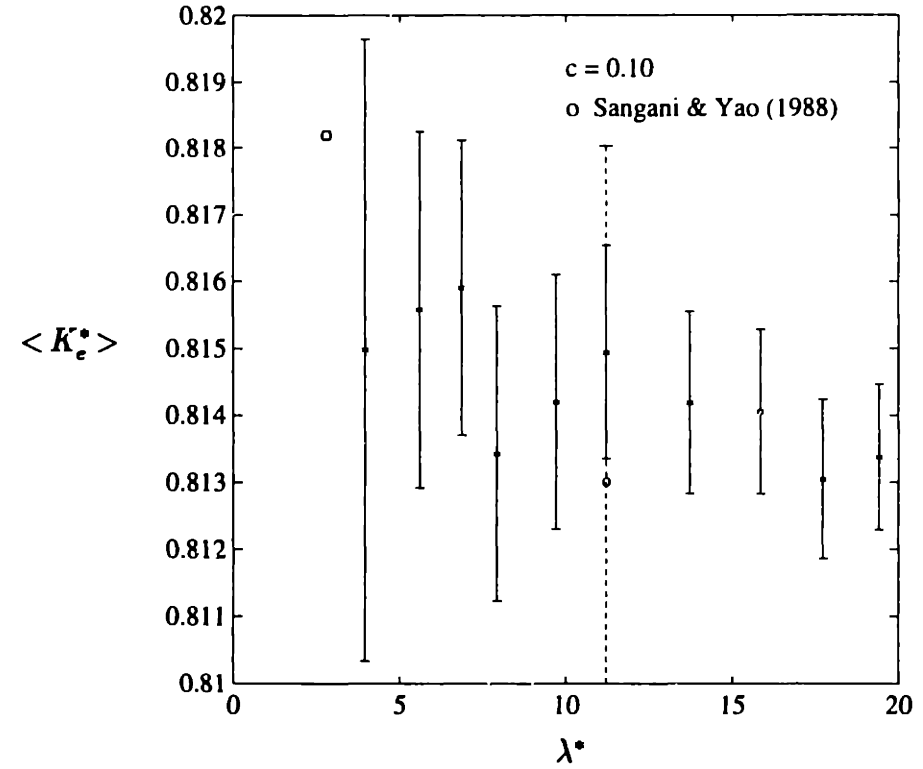

Figure 4-9: Effective conductivity $< K_e^* >$ and corresponding Monte–Carlo confidence intervals $CI(< K_e^* >)$ (I-shaped bars) for the concentration $c = 0.10$.

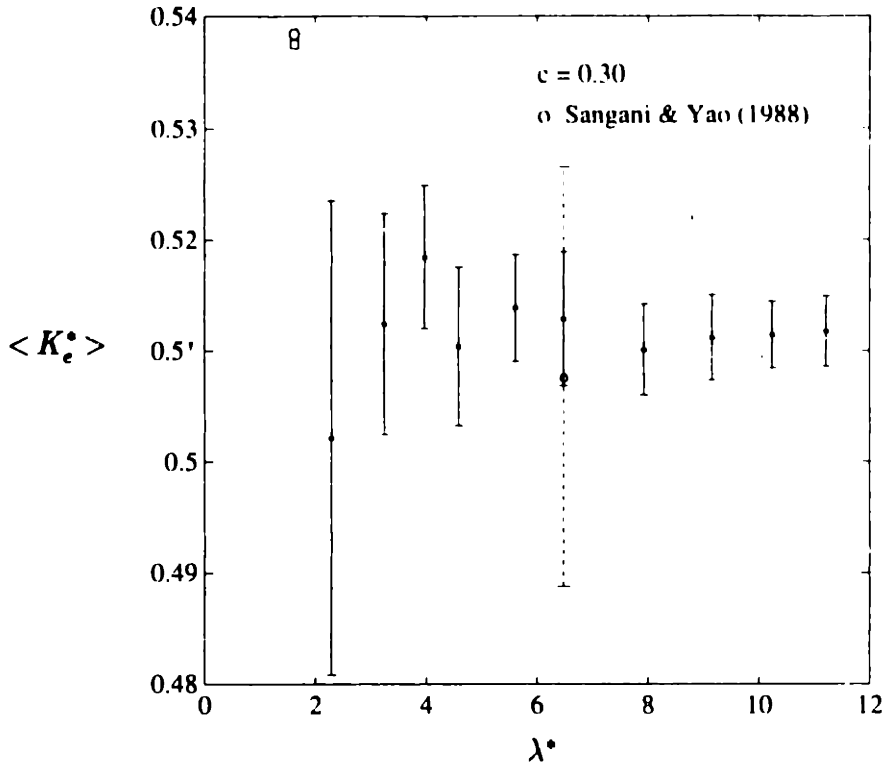

Figure 4-10: Effective conductivity $< K_e^* >$ and corresponding Monte–Carlo confidence intervals $CI(< K_e^* >)$ (I-shaped bars) for the concentration $c = 0.30$.

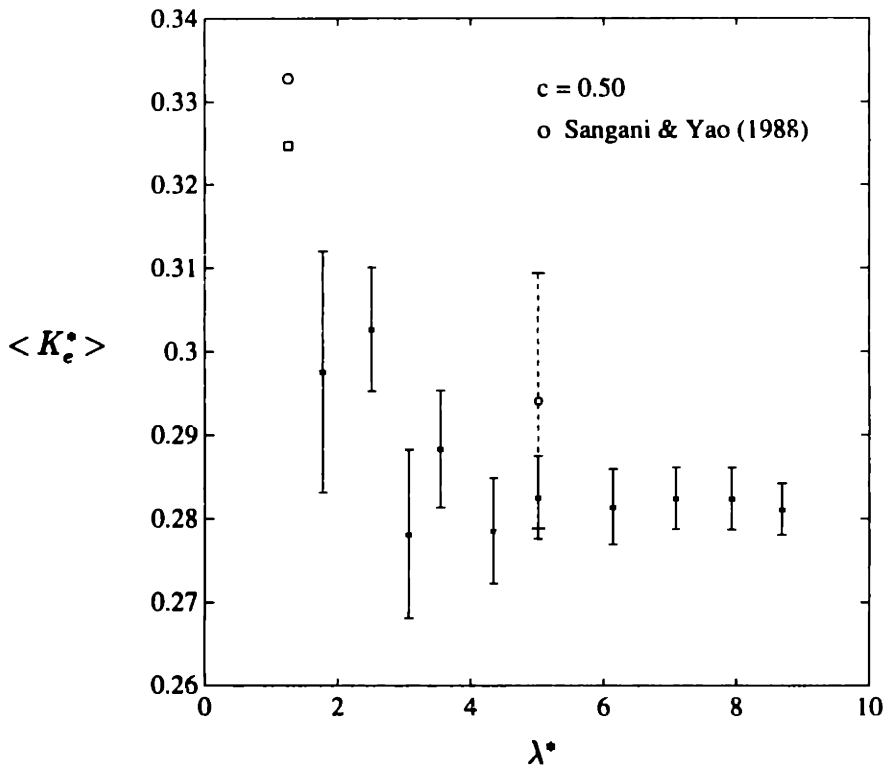

Figure 4-11: Effective conductivity $< K_e^* >$ and corresponding Monte–Carlo confidence intervals $CI(< K_e^* >)$ (I-shaped bars) for the concentration $c = 0.50$.

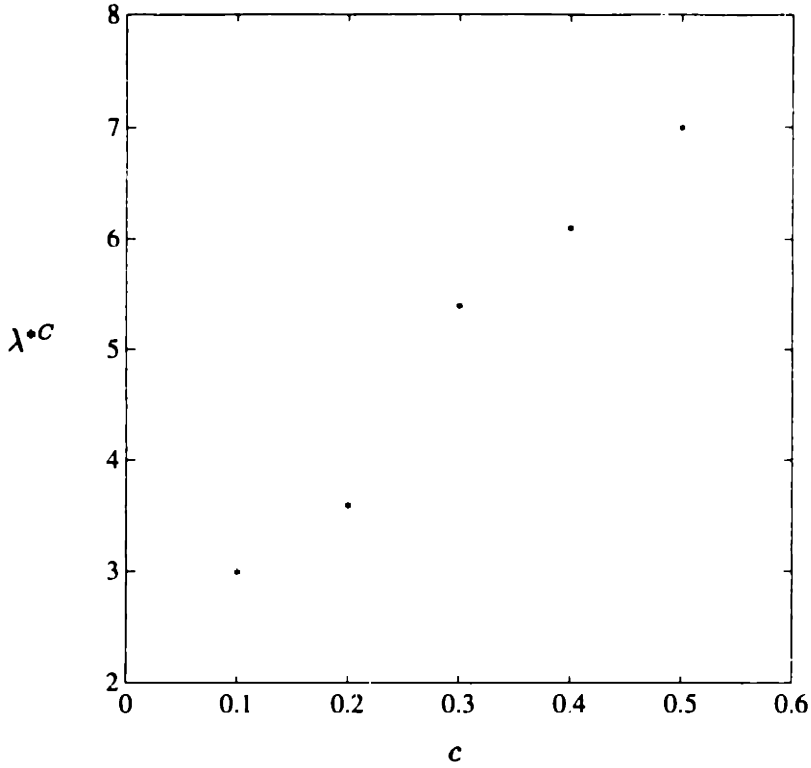

Figure 4-12: Correlation length $\lambda^{*C}(c)$ versus concentration c.

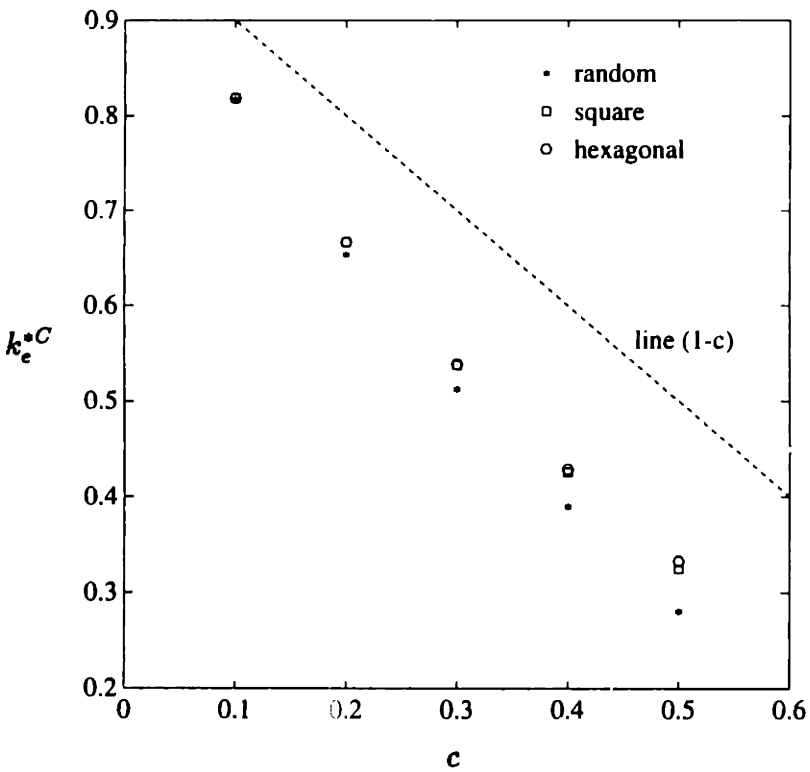

Figure 4-13: Effective conductivity $k_e^{*C}(c)$ versus concentration c.

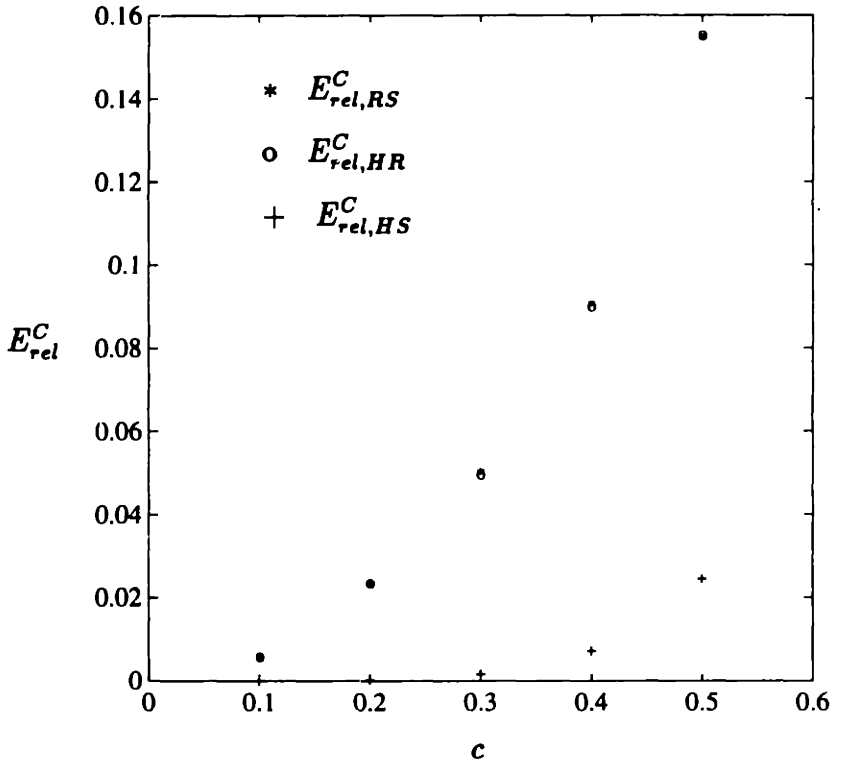

Figure 4-14: Relative differences, E^C_{rel}, between the effective conductivities of random and regular arrays, in terms of the concentration c.

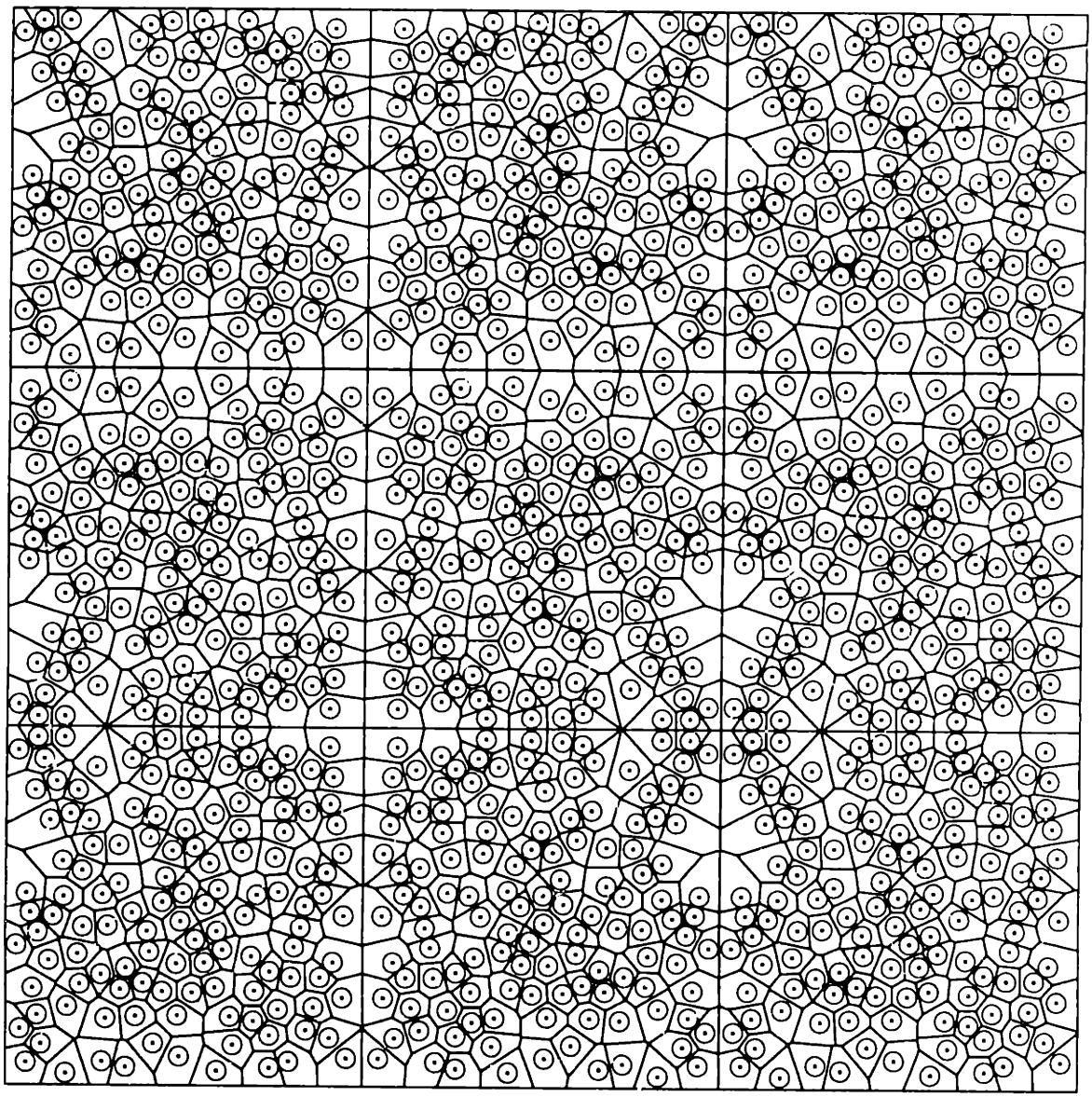

Figure 4-15: Voronoi diagram for the original multiscale problem calculation: the inner box is the desired domain.

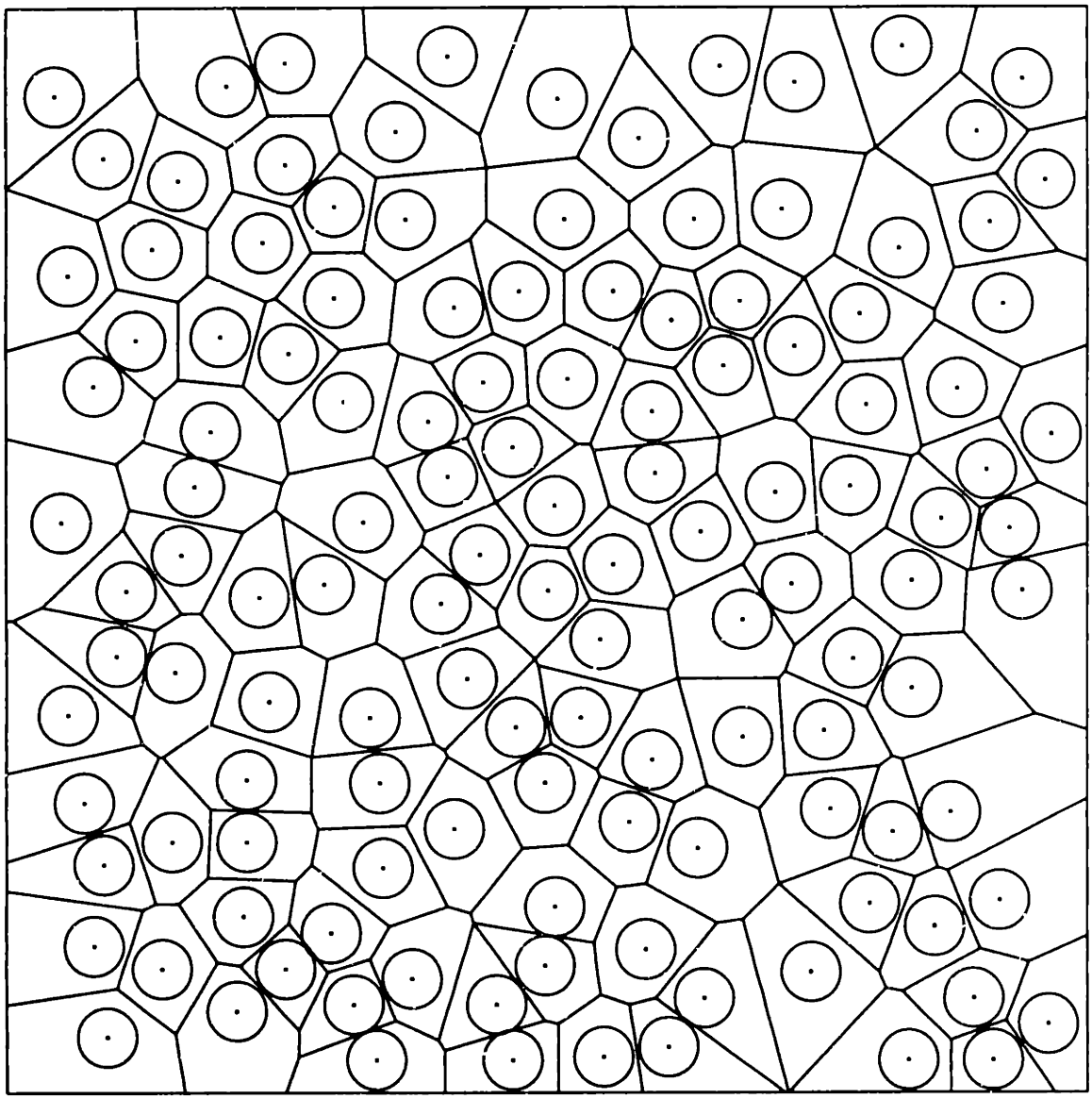

Figure 4-16: Actual, partitioned, domain for the original multiscale problem calculation: $c = 0.30$, $(\lambda_{box}/d) = 18.3$ (128 inclusions), insulated at top and bottom, constant temperature at left ($T = 1$) and right ($T = 0$).

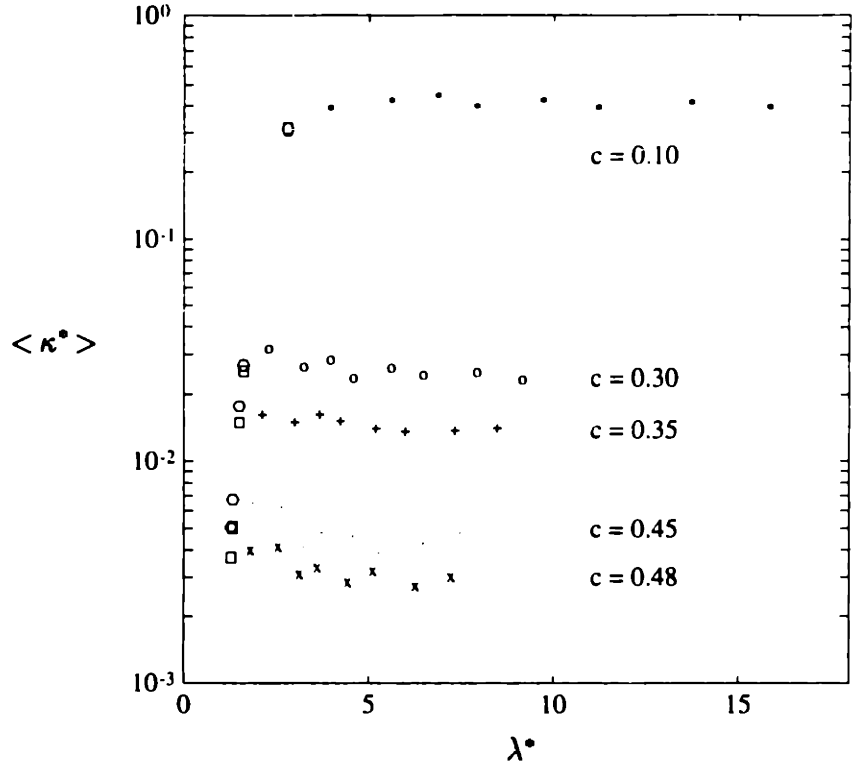

Figure 4-17: Permeability $<\kappa^*>$ versus supercell size λ^* for various values of c.

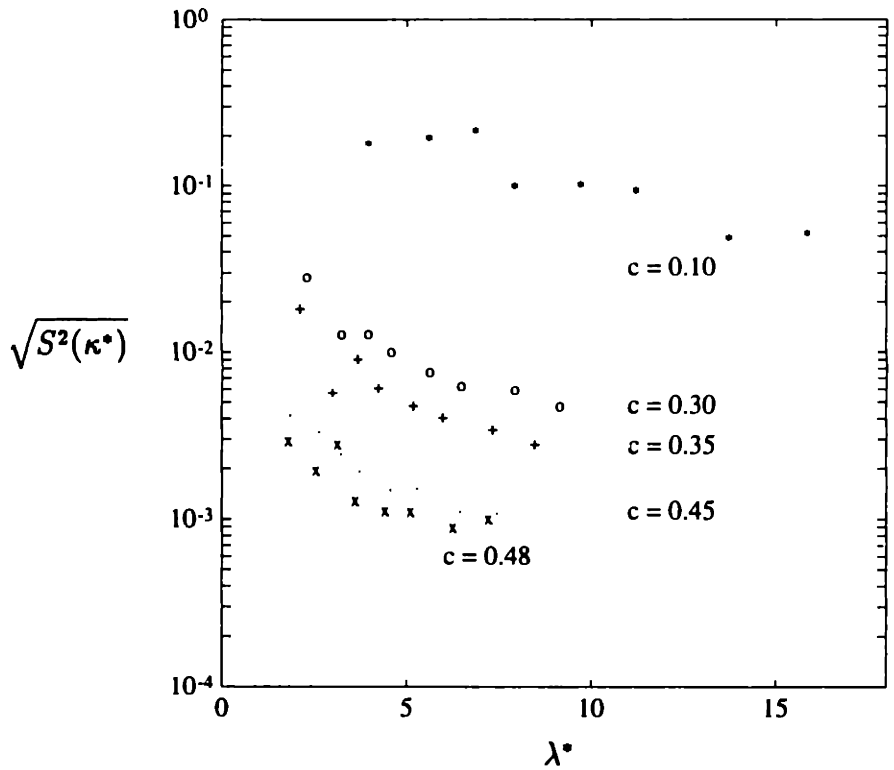

Figure 4-18: Standard deviation of the permeability, $[S^2(\kappa^*)]^{\frac{1}{2}}$, versus supercell size λ^* for various values of c.

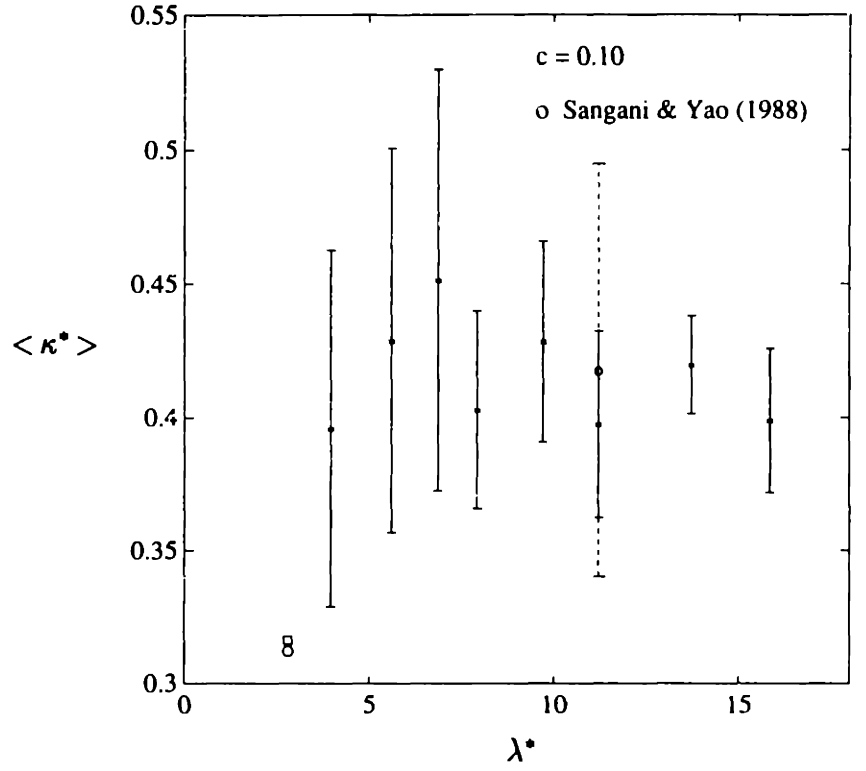

Figure 4-19: Permeability $<\kappa^*>$ and corresponding Monte–Carlo confidence intervals $CI(<\kappa^*>)$ (I–shaped bars) for the concentration $c = 0.10$.

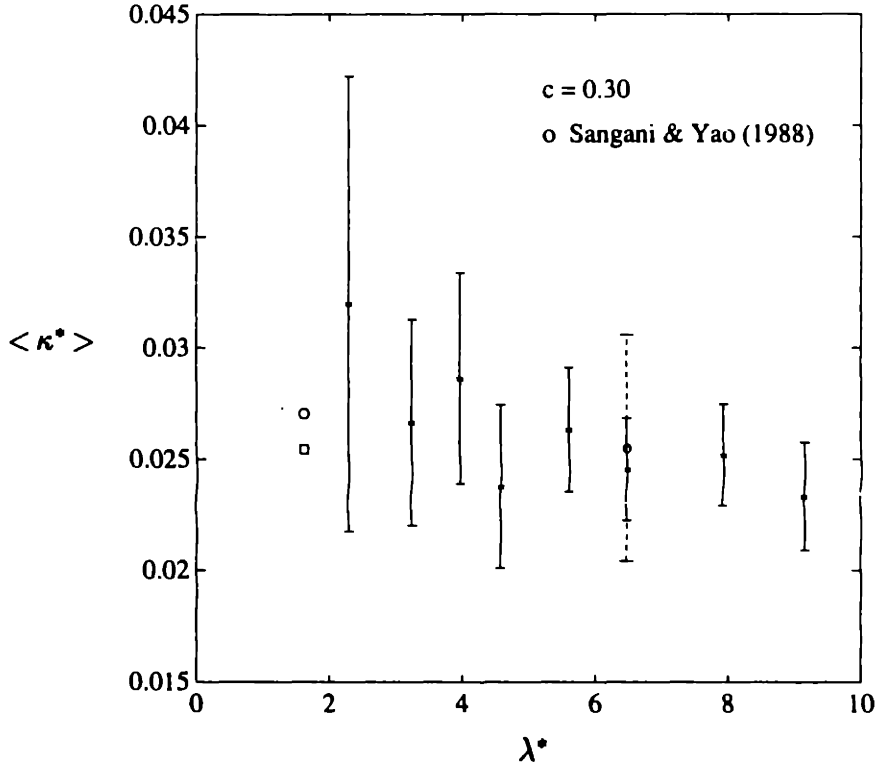

Figure 4-20: Permeability $<\kappa^*>$ and corresponding Monte–Carlo confidence intervals $CI(<\kappa^*>)$ (I–shaped bars) for the concentration $c = 0.30$.

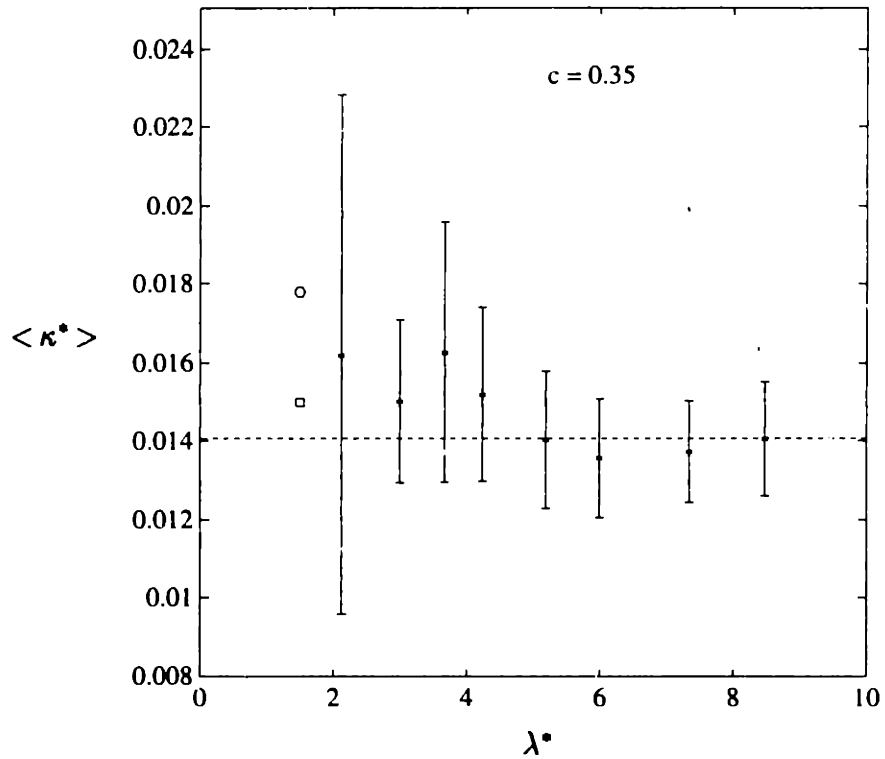

Figure 4-21: Permeability $< \kappa^* >$ and corresponding Monte–Carlo confidence intervals $CI(< \kappa^* >)$ (I–shaped bars) for the concentration $c = 0.35$.

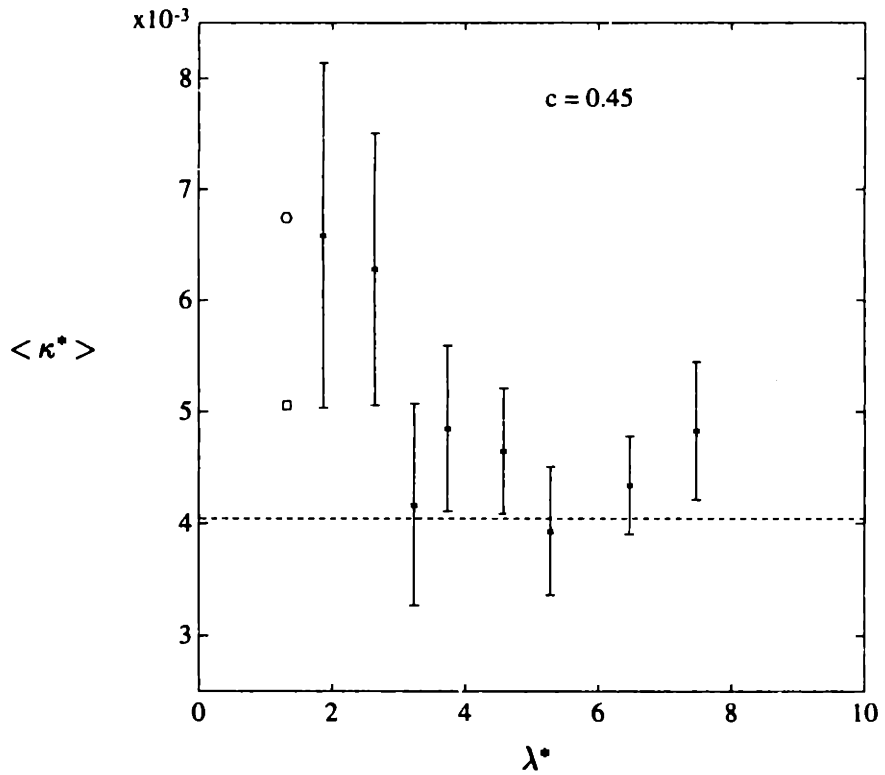

Figure 4-22: Permeability $< \kappa^* >$ and corresponding Monte–Carlo confidence intervals $CI(< \kappa^* >)$ (I–shaped bars) for the concentration $c = 0.45$.

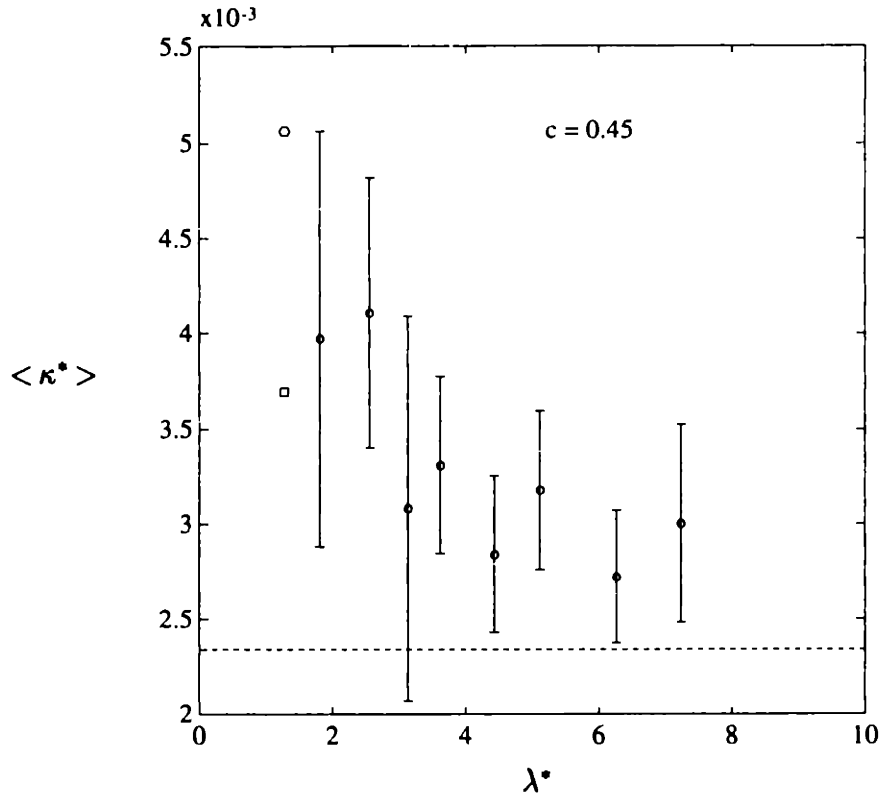

Figure 4-23: Permeability $< \kappa^* >$ and corresponding Monte–Carlo confidence intervals $CI(< \kappa^* >)$ (I-shaped bars) for the concentration $c = 0.48$.

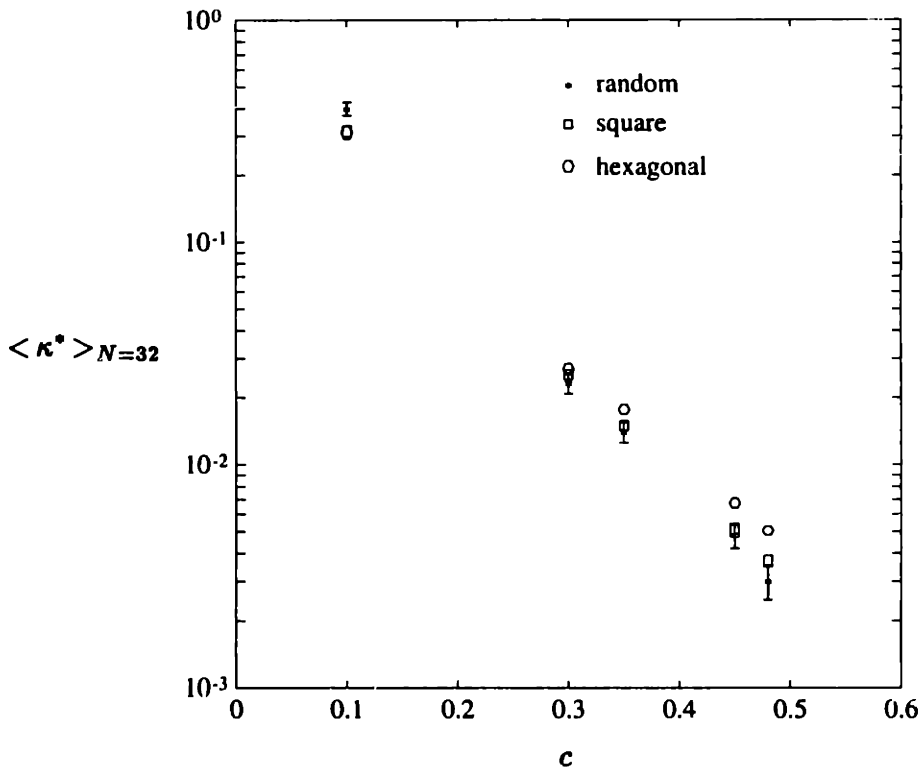

Figure 4-24: Permeability $< \kappa^* >_{N=32}$ versus concentration c.

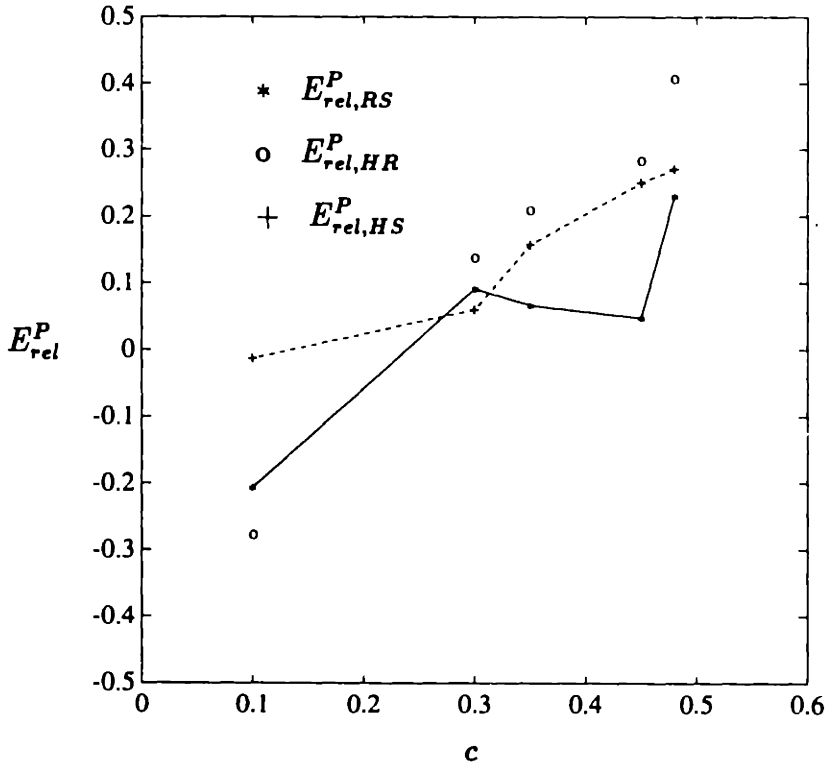

Figure 4-25: Relative differences, E^P_{rel}, between the permeabilities of random and regular arrays, in terms of the concentration c.

Appendix A

Application of Homogenization Theory to the Conduction Problem

The purpose of this Appendix is to, first, briefly present the main ideas of homogenization theory (also called method of homogenization), and, second, to apply it to our conduction mesoscale problem, and derive equations (2.37) and (2.19) of Section 2.1.3. A general and rigorous treatment of the subject is given in Bensoussan, Lions & Papanicolaou (1978); this Appendix draws heavily on their Chapter 1, Sections 1 and 2.

A survey of applications of (periodic) homogenization theory to many different areas can be found in Babuška (1975); Larsen (1975), and Bensoussan, Lions & Papanicolaou (1979) applied it to the fields of radiative and neutron transport; more recently, it has been used by Bendsøe & Kikuchi (1988) in a procedure for shape optimization of structures. Homogenization theory has also been applied to the multicomponent media problems we are interested in: Auriault (1983) determined the effective conductivity of certain types of laminated periodic composites; Mei & Auriault (1989) formulated the creeping flow problem through periodic porous media with several spatial scales, and Mei & Auriault (1991) extended their previous analysis to include the effect of weak inertia.

The outline of this Appendix is as follows. First, in Section A.1, we define what homogenization theory is, and give a physical correspondence to the mathematical problems involved. In Section A.2, we give a brief overview of the analytical techniques that may be employed in homogenization theory. In Section A.3, we apply it to a general, elliptic model problem, using the strong form. Finally, in Section A.4, we apply the method of homogenization to our problem of conduction in unidirectional fibrous composite materials, using the variational form and results obtained in Section A.3; although the final equations are also shown in Auriault (1983), we present a more detailed derivation here, included in the thesis for completeness.

A.1 Definition

Before defining what the method of homogenization is, we first introduce, from a purely mathematical point of view, the following three types of boundary value problems (BVP's):

1. BVP-1

$$A^\epsilon u_\epsilon = f \text{ in } \Omega \tag{A.1}$$

$$u_\epsilon \text{ subject to Dirichlet, Neumann, or mixed b.c.'s on } \partial\Omega \tag{A.2}$$

The domain Ω is an open (say bounded) set of $\mathcal{R}^n$, $\partial\Omega$ is its bounding surface in $\mathcal{R}^{n-1}$, and A^ϵ is a general partial differential operator with periodically varying and *continuous* coefficients. The characteristic length scale of the domain Ω is L, and that of the periods, λ; the positive parameter ϵ is the ratio of such scales, and it is assumed here that

$$\epsilon \equiv \frac{\lambda}{L} << 1. \tag{A.3}$$

Thus, this boundary value problem is said to have rapidly oscillating coefficients. Problem BVP-1 corresponds, in our (conduction) context, to the original multiscale problem of Section 2.1.1, but with an underlying *periodic* medium, rather than truly random. The domain Ω corresponds to the macroscale region

$\Omega_{ma} = \Omega_{co} \cup \Omega_{di}$. The oscillating coefficient (a function of x_1 and x_2) is in fact discontinuous, and takes the values of the component conductivities k_{co} and k_{di} on Ω_{co} and Ω_{di}, respectively; the discontinuity of such coefficient requires a special (variational) treatment, presented in Section A.4.

2. BVP-2

$$A^H u_H = f \text{ in } \Omega \tag{A.4}$$

$$u_H \text{ subject to Dirichlet, Neumann, or mixed b.c.'s on } \partial\Omega \tag{A.5}$$

The partial differential operator A^H has constant coefficients, i.e., it is a homogeneous operator; thus, this boundary value problem is said to be homogenized. Problem BVP-2 corresponds to our macroscale problem, but with constant concentration function.

3. BVP-3

$$A^c u_c = f^c \text{ in } \Omega^c \tag{A.6}$$

$$u_c \text{ subject to Dirichlet, Neumann, or mixed b.c.'s on } \partial\Omega^c \tag{A.7}$$

The domain Ω^c, an open bounded set of $\mathcal{R}^n$, is a periodicity cell of characteristic size λ, i.e., with dimensions proportional to λ in all directions. The partial differential operator A^c may have constant or variable coefficients within Ω^c, and u_c and f^c are λ–periodic functions (i.e., they admit period λ_j^0 in the direction x_j, $j = 1, \ldots, n$). This boundary value problem is called a cell problem. Clearly, problem BVP-3 corresponds to our mesoscale supercell problem.

We can now define the method of homogenization: it is a rigorous mathematical technique whereby one can replace, in the limit $\epsilon \to 0$, a boundary value problem with rapidly varying coefficients (type BVP-1) with a homogenized problem (type BVP-2), whose coefficients are determined by solving a cell problem (type BVP-3). Although all three problems are, in general, very hard to solve analytically, the method of homogenization has the distinct advantage that problems of the types BVP-2 and BVP-3 are much easier to solve numerically than those of the type BVP-1, since the

latter require $O(1/\epsilon^n)$ more degrees of freedom.

From a physical point of view, problem BVP-1 can represent heat transfer, creeping flow, or a neutron transport process in a multicomponent medium of typical macroscale L, with a spatially periodic microstructure of period λ. Problem BVP-2 (respectively BVP-3) can represent the same phenomena in a homogeneous medium of typical macroscale L (respectively in a periodic cell of size λ). Note that the coefficients of A^H in BVP-2 correspond, by definition, to the effective macroscopic properties of the original multicomponent medium. Since the determination of such coefficients involves solving a cell problem on the periodic structure of the medium, of size $\lambda << L$, it is said that the method of homogenization allows one to macroscopically describe the behavior of a multicomponent medium through the analysis of the behavior of its underlying microscopic structure.

The lack of a unique precise definition of effective properties of multicomponent media has led to many discrepancies in the past [Babuška (1975)]. The method of homogenization not only provides a consistent way of computing effective properties for materials with periodic microstructure, but it also relates the quantities (e.g., bulk heat flow) defined for the original multicomponent medium to those computed for the equivalent homogeneous one (in general, anisotropic). It should be pointed out that, typically, real random media has no period λ, in which case the method does not directly apply. As we mentioned in Section 2.1.3, the correlation length is proposed as the bridge for the transition *periodic* $\rightarrow$ *random*; naturally, for self-consistency of the methodology, the correlation length must (turn out to) be small compared to the macroscale L.

A.2 Overview

While investigating a given physical phenomenon, one typically sets up a mathematical model to describe it, often arriving at a problem of the type BVP-1. Homogenization theory can then be used to solve it. In order to replace the operator A^ϵ of BVP-1 with the operator A^H of BVP-2, several methods can be used [Bensoussan,

Lions & Papanicolaou (1978)], based on:

1. asymptotic expansions using multiple scales: fast scale, proportional to λ, and slow scale, proportional to L;

2. energy estimates;

3. probabilistic arguments;

4. spectral decomposition of A^ϵ.

In this section we describe the main ideas involved in using method 1 above, and in the next section it is applied to a model problem.

The basis for the use of the method of asymptotic expansions is the presence of a natural separation of scales in problems of the type BVP-1, as expressed by equation (A.3). The procedure is to look for the solution $u_\epsilon = u_\epsilon(\mathbf{x})$, $\mathbf{x} \in \mathcal{R}^n$, of BVP-1 in the form of an asymptotic expansion in terms of the small positive parameter ϵ:

$$u_\epsilon = u_0 + \epsilon\, u_1 + \epsilon^2\, u_2 + \dots , \tag{A.8}$$

where the functions u_j, $j = 0, 1, \dots$, are now the new unknowns. Next, by inserting (A.8) into (A.1)-(A.2) and collecting equal powers of ϵ, a problem of the type BVP-2 is obtained for u_0, with boundary conditions dependent on those prescribed for the original problem. The main result of the method, shown in Bensoussan, Lions & Papanicolaou (1978), is that u_ϵ converges weakly to u_0 as $\epsilon \to 0$ (weak convergence means convergence of suitable averages). The explicit analytical construction of the homogenized operator A^H is crucial for the actual solution of the problem; it involves solving a λ-periodic cell problem (type BVP-3), which yields the correct constant coefficients of A^H. In general, the homogenized and cell problems have to be solved numerically.

A.3 A Model Problem

A.3.1 Strong form

In BVP-1, let

$$A^\epsilon = -\frac{\partial}{\partial x_i}\left[a_{ij}(\mathbf{y})\frac{\partial}{\partial x_j}\right] + a_0(\mathbf{y})\,, \tag{A.9}$$

where $\mathbf{x} \in \mathcal{R}^2$, $\mathbf{y} \equiv \mathbf{x}/\epsilon$, and $a_{ij}(\mathbf{y})$, $i,j = 1,2$, and $a_0(\mathbf{y})$ are continuous λ–doubly periodic functions. Formally, a function is said to be λ–doubly periodic if it admits periods proportional to λ in both coordinate directions.

The second-order elliptic operator A^ϵ in (A.9) models the simplest possible situations of composite materials with periodic microstructure. We are now interested in determining the behavior of the solution u_ϵ of BVP-1, with A^ϵ given in (A.9), as $\epsilon \to 0$.

A.3.2 Method of asymptotic expansions

As mentioned before, the presence of the small parameter ϵ (reflecting the two disparate scales L and λ) in BVP-1 motivates the application of the method of asymptotic expansions using multiple scales, whereby one looks for the solution $u_\epsilon = u_\epsilon(\mathbf{x})$ in the form

$$u_\epsilon(\mathbf{x}) = u_0(\mathbf{x},\mathbf{x}/\epsilon) + \epsilon\, u_1(\mathbf{x},\mathbf{x}/\epsilon) + \epsilon^2\, u_2(\mathbf{x},\mathbf{x}/\epsilon) + \dots\,, \tag{A.10}$$

where the $u_j(\mathbf{x},\mathbf{y})$, $\mathbf{y} \equiv \mathbf{x}/\epsilon$, $j = 1,2$, are λ–doubly periodic. The variable $\mathbf{y}$ is introduced to allow the functional separation of the periodic and non-periodic parts of u_ϵ. The new boundary value problems for the unknown functions u_j are determined by first inserting (A.10) into (A.1), with A^ϵ given in (A.9), and then by collecting the terms with equal powers of ϵ.

When inserting (A.10) into (A.1), care is necessary with the operator $\partial/\partial x_j$; treating $\mathbf{x}$ and $\mathbf{y}$ as independent variables and subsequently replacing $\mathbf{y}$ with $\mathbf{x}/\epsilon$, it

becomes

$$\frac{\partial}{\partial x_j} = \frac{\partial}{\partial x_j} + \frac{1}{\epsilon}\frac{\partial}{\partial y_j} . \tag{A.11}$$

Carrying out the algebra and collecting the powers ϵ^{-2}, ϵ^{-1}, and ϵ^0, one obtains:

$$A^\epsilon = \epsilon^{-2} A_1 + \epsilon^{-1} A_2 + \epsilon^0 A_3 , \tag{A.12}$$

where

$$A_1 = -\frac{\partial}{\partial y_i}[a_{ij}(\mathbf{y})\frac{\partial}{\partial y_j}] , \tag{A.13}$$

$$A_2 = -\frac{\partial}{\partial y_i}[a_{ij}(\mathbf{y})\frac{\partial}{\partial x_j}] - \frac{\partial}{\partial x_i}[a_{ij}(\mathbf{y})\frac{\partial}{\partial y_j}] , \tag{A.14}$$

$$A_3 = -\frac{\partial}{\partial x_i}[a_{ij}(\mathbf{y})\frac{\partial}{\partial x_j}] + a_0 ; \tag{A.15}$$

the equations involving A_1 , A_2 , A_3, and u_0 , u_1 , u_2 are:

$$A_1 u_0 = 0 , \tag{A.16}$$

$$A_1 u_1 + A_2 u_0 = 0 , \tag{A.17}$$

$$A_1 u_2 + A_2 u_1 + A_3 u_0 = f . \tag{A.18}$$

We now state a result that will be used below. The solvability condition (i.e., uniqueness up to an additive constant) for the problem

$$\begin{cases} A_1 \phi = F \text{ in Y} \\ \phi \text{ periodic in Y} , \end{cases}$$

where A_1 is given in (A.13) and Y is a region in $\mathcal{R}^2$, is [see Bensoussan, Lions & Papanicolaou (1978)]

$$\int_Y F(\mathbf{y})\, d\mathbf{y} = 0 . \tag{A.19}$$

Because of the condition (A.19) and the fact that the operator A_1 involves $\mathbf{y}$ only,

equation (A.16) implies that u_0 is a function of $\mathbf{x}$ only, i.e.,

$$u_0(\mathbf{x},\mathbf{y}) = u_0(\mathbf{x})\,. \tag{A.20}$$

Inserting equations (A.14) and (A.20) into (A.17), we obtain

$$A_1\,u_1 = \left[\frac{\partial}{\partial y_i}a_{ij}(\mathbf{y})\right]\frac{\partial u_0(\mathbf{x})}{\partial x_j}\,, \tag{A.21}$$

where separation of the variables $\mathbf{x}$ and $\mathbf{y}$ on the right–hand side of (A.21) is clearly seen. If $\varphi^j = \varphi^j(\mathbf{y})$ is defined as the λ–doubly periodic solution (up to an additive constant) of

$$A_1\,\varphi^j = -\frac{\partial}{\partial y_i}a_{ij}(\mathbf{y})\,, \tag{A.22}$$

then the general solution of (A.21) is given by

$$u_1(\mathbf{x},\mathbf{y}) = -\varphi^j(\mathbf{y})\,\frac{\partial u_0}{\partial x_j} + \tilde{u}_1(\mathbf{x})\,. \tag{A.23}$$

The problem for u_1 then reduces to finding $\varphi^j(\mathbf{y})$; since A_1 involves $\mathbf{y}$ only and both $a_{ij}(\mathbf{y})$ and $\varphi^j(\mathbf{y})$ are λ–doubly periodic, equation (A.22) (with proper boundary conditions) constitutes the cell problem BVP-3.

From the condition (A.19), one can solve (A.18) for u_2 ($\mathbf{x}$ being a parameter) if

$$\int_Y (A_2\,u_1 + A_3\,u_0)\,d\mathbf{y} = \int_Y f\,d\mathbf{y} \tag{A.24}$$

(notice that, here, Y has dimensions proportional to λ in both directions); using (A.14), (A.15) and (A.23), and the fact that $f = f(\mathbf{x})$, then (A.24) becomes

$$-\frac{1}{|Y|}\left[\int_Y (a_{ij} - a_{ik}\,\frac{\partial\varphi^j}{\partial y_k})\,d\mathbf{y}\right]\,\frac{\partial^2 u_0}{\partial x_i \partial x_j} + \frac{1}{|Y|}\left[\int_Y a_0(\mathbf{y})\,d\mathbf{y}\right]u_0 = f\,, \tag{A.25}$$

where $|Y|$ is the measure of the entire region Y,

$$|Y| = \int_Y d\mathbf{y}\,. \tag{A.26}$$

Clearly, the coefficients

$$C_{eff_{ij}} \equiv -\frac{1}{|Y|}\int_Y (a_{ij} - a_{ik}\frac{\partial \varphi^j}{\partial y_k})\, d\mathbf{y} \tag{A.27}$$

and

$$C_0 \equiv \frac{1}{|Y|}\int_Y a_0(\mathbf{y})\, d\mathbf{y} \tag{A.28}$$

are constants ($\mathbf{y}$ is integrated out), so that equation (A.25) (with proper boundary conditions) constitutes the homogenized problem BVP-2. We can write the homogenized operator A^H explicitly as

$$A^H = C_{eff_{ij}}\frac{\partial^2}{\partial x_i \partial x_j} + C_0\,; \tag{A.29}$$

defining, in general,

$$m(\phi) \equiv \frac{1}{|Y|}\int_Y \phi(\mathbf{y})\, d\mathbf{y}\,, \tag{A.30}$$

then

$$C_{eff_{ij}} = -m(a_{ij}) + m(a_{ik}\frac{\partial \varphi^j}{\partial y_k}) \tag{A.31}$$

and

$$C_0 = m(a_0)\,. \tag{A.32}$$

Mathematically, $C_{eff_{ij}}$ and C_0 are the effective coefficients of the operator A^ϵ; physically, they are the effective bulk properties of the non-homogeneous medium for which BVP-1 was derived.

In the context of our conduction problem, we remark at this point that the division by $|Y|$ in (A.27) ultimately leads to the factor $(1-c)$ in equation (2.19), Section 2.1.3. Notice that $|Y|$ appeared with no ambiguity; it represents the total area of the supercell ($\lambda^2 = \int_{\Omega_{sc}} d\mathbf{y}$), and not just the area of the matrix ($\int_{\Omega_{ma}} d\mathbf{y}$).

Finally, it is worthwhile to state the following results, which are shown in Bensoussan, Lions & Papanicolaou (1978):

1. If A^ϵ is symmetric ($a_{ij} = a_{ji}$), then A^H is also symmetric.

2. A^H is elliptic.

3. If A^ϵ is diagonal ($a_{ij} = 0$ for $i \neq j$), A^H is not necessarily diagonal.

4. The method of asymptotic expansions is justified for both Dirichlet and Neumann boundary conditions; the end result for the error estimate is

$$\| u_\epsilon - u_0 \|_{L^\infty(\Omega)} \leq C\,\epsilon\,,$$

where C depends on Ω, f, a_{ij}, but not on ϵ.

5. Using "energy" ("weak") arguments, it can be proved that the solution u_ϵ of BVP-1 converges to u_0 weakly as $\epsilon \to 0$, where $u_0 \in V(\Omega)$ is the solution of ($a_0 = 0$)

$$a^H(u_0, v) = (f, v) \quad \forall v \in V(\Omega)\,,$$

where $V(\Omega)$ is an appropriate function space, and

$$a^H(u_0, v) \equiv \int_\Omega -C_{eff_{ij}} \frac{\partial u_0}{\partial x_j} \frac{\partial v}{\partial x_i}\, d\mathbf{x}.$$

A.4 Application to the Conduction Problem

We want to solve the original multiscale problem of Section 2.1.1, given by

$$-\frac{\partial}{\partial x_j}[k_{ra} \frac{\partial T}{\partial x_j}] = 0 \quad \text{in } \Omega_{ma,\#}\,, \tag{A.33}$$

$$-k_{co} \frac{\partial T}{\partial x_i} n_i = 0 \quad \text{on } \partial\Omega_{di,\#}\,, \tag{A.34}$$

$$T \text{ subject to Dirichlet and Neumann, b.c.'s on } \partial\Omega_{ma,\#} \tag{A.35}$$

($\partial\Omega_{ma,\#} = \Gamma_0 \cup \Gamma_1 \cup \Gamma_{ad}$). The conductivity of the random multicomponent medium, k_{ra}, is given by

$$k_{ra} = \begin{cases} k_{co} & \text{on } \Omega_{co,\#} \\ k_{di} = 0 & \text{on } \Omega_{di,\#}\,. \end{cases} \tag{A.36}$$

Notice that now the original problem is defined on a medium with an underlying periodic microstructure, indicated by the additional subscript $\#$; the corresponding domain is $\Omega_{ma,\#} = \Omega_{co,\#} \cup \Omega_{di,\#}$. Comparing equation (A.33) with (A.9), we see that the coefficient $a_{ij}(\mathbf{y})$ is the discontinuous scalar k_{ra}, and $a_0(\mathbf{y})$ is zero.

A variational formulation of the problem (A.33)-(A.35) is advantageous, because: first, by transposing the derivatives, it bypasses (see below) the problem introduced by the discontinuity of k_{ra} (notice that the right-hand-side of (A.22) cannot be evaluated, though A_1, from (A.13) and (A.36), is simply $-\partial/\partial y_i\,[k_{co}\,\partial/\partial y_i]$, which appears on the left-hand-side of (2.9), Section 2.1.3); second, it can automatically take care of the zero-flux boundary conditions at the inclusion surfaces, (A.34). The variational formulation (obtained by multiplying (A.33) by the test function v and integrating by parts) is given by

$$\int_{\Omega_{co,\#}} k_{co}\,\frac{\partial T}{\partial x_i}\frac{\partial v}{\partial x_i}\,d\mathbf{x} = 0 \quad \forall v \in H_0^1(\Omega_{co,\#})\,, \tag{A.37}$$

where the Dirichlet boundary conditions in (A.35) have been incorporated into the space H_0^1. Notice that integration by parts allows us to keep only the non-zero integral contribution from (A.36), and the discontinuity of k_{ra} is properly handled.

We now follow the procedure in Section A.3.2, but using the form (A.37). Writing the multiple length scale expansion for the temperature,

$$T(\mathbf{x}) = T_0(\mathbf{x}) + \epsilon\,T_1(\mathbf{x},\mathbf{y}) + O(\epsilon^2)\,, \tag{A.38}$$

and for the test function,

$$v(\mathbf{x}) = v_0(\mathbf{x}) + \epsilon\,v_1(\mathbf{x},\mathbf{y}) + O(\epsilon^2)\,, \tag{A.39}$$

where $\mathbf{y} \equiv \mathbf{x}/\epsilon$ is the rapidly varying variable, and inserting them into (A.37), we obtain to leading order, using the differentiation rule (A.11),

$$\int_{\Omega_{co,\#}} k_{co}\left(\frac{\partial T_0}{\partial x_j} + \frac{\partial T_1}{\partial y_j}\right)\left(\frac{\partial v_0}{\partial x_j} + \frac{\partial v_1}{\partial y_j}\right)\,d\mathbf{x} = 0 \quad \forall v_0, v_1 \in H_0^1(\Omega_{co,\#})\,. \tag{A.40}$$

We can break (A.40) into two equations: choosing, first, $v_1 = 0$, and, second, $v_0 = 0$, we obtain, respectively,

$$\int_{\Omega_{co,\#}} k_{co} \left(\frac{\partial T_0}{\partial x_j} + \frac{\partial T_1}{\partial y_j} \right) \left(\frac{\partial v_0}{\partial x_j} \right) d\mathbf{x} = 0 \quad \forall v_0 \in H_0^1(\Omega_{co,\#}) \,, \tag{A.41}$$

and

$$\int_{\Omega_{co,\#}} k_{co} \left(\frac{\partial T_0}{\partial x_j} + \frac{\partial T_1}{\partial y_j} \right) \left(\frac{\partial v_1}{\partial y_j} \right) d\mathbf{x} = 0 \quad \forall v_1 \in H_0^1(\Omega_{co,\#}) \,. \tag{A.42}$$

We now assume, as was motivated by solvability in Section A.3.2 (equation (A.19)), that

$$T_1(\mathbf{x}, \mathbf{y}) = -\chi^p(\mathbf{y}) \frac{\partial T_0(\mathbf{x})}{\partial x_p} \,, \tag{A.43}$$

where summation over p is implied, $p = 1, 2$. Notice that, since χ^p is a temperature, the factor $-\frac{L}{\Delta T}$ (used in Section 2.1.3) is necessary on the right-hand-side of (A.43) to preserve dimensionality; however, the factor is omitted in this Appendix for clarity of exposition. Inserting (A.43) in (A.42), yields

$$\int_{\Omega_{co,\#}} k_{co} \left(\delta_{jp} - \frac{\partial \chi^p}{\partial y_j} \right) \frac{\partial T_0}{\partial x_p} \frac{\partial v_1}{\partial y_j} d\mathbf{x} = 0 \quad \forall v_1 \in H_0^1(\Omega_{co,\#}) \,. \tag{A.44}$$

Equation (A.44) can be transformed into an integral over the region Ω_{me} of the periodic supercell, using the following relation proved in Keller (1980) (also used by Bendsøe & Kikuchi (1988)):

$$\lim_{\epsilon \to 0} \int_\Omega g(\mathbf{x}, \mathbf{y}) \, d\mathbf{x} = \int_\Omega \left(\frac{1}{|Y|} \int_Y g(\mathbf{x}, \mathbf{y}) \, d\mathbf{y} \right) d\mathbf{x} \,; \tag{A.45}$$

equation (A.45) states that integration over Ω just captures the average over the cell, since the latter, as $\epsilon \to 0$, is essentially a point to the former. In order to apply (A.45) to (A.44), we first identify Ω with $\Omega_{ma,\#}$, $|Y|$ with λ^2, and Y with Ω_{sc}; second, we notice that the integral contributions over $\Omega_{di,\#}$ are null (from (A.36)), so that only the parts $\Omega_{co,\#}$ and Ω_{me} from the original domain and the supercell, respectively, contribute to the integrals on the right-hand-side of (A.45). We then

obtain, combining (A.44) and (A.45),

$$\int_{\Omega_{co,\#}} \frac{\partial T_0}{\partial x_p} \left[\frac{1}{\lambda^2} \int_{\Omega_{me}} k_{co} \left(\delta_{jp} - \frac{\partial \chi^p}{\partial y_j} \right) \frac{\partial v_1}{\partial y_j} \, d\mathbf{y} \right] d\mathbf{x} = 0 \quad \forall v_1 \in H^1_0(\Omega_{co,\#}) \,, \tag{A.46}$$

which implies that

$$\frac{1}{\lambda^2} \int_{\Omega_{me}} k_{co} \left(\delta_{jp} - \frac{\partial \chi^p}{\partial y_j} \right) \frac{\partial v}{\partial y_j} \, d\mathbf{y} = 0 \quad \forall v \in H^1_{\#,0}(\Omega_{co,\#}) \,. \tag{A.47}$$

From (A.47), we finally arrive at

$$\int_{\Omega_{me}} k_{co} \frac{\partial \chi^p}{\partial y_j} \frac{\partial v}{\partial y_j} \, d\mathbf{y} = \int_{\Omega_{me}} k_{co} \frac{\partial v}{\partial y_p} \, d\mathbf{y} \quad \forall v \in H^1_{\#,0}(\Omega_{me}) \,, \tag{A.48}$$

which is equivalent, with $p = 1$, to equation (2.37) of Section 2.1.3, and corresponds to the cell problem BVP-2 of Section A.1.

In order to derive the homogenized problem for T_0, we first insert (A.43) into (A.41), to obtain

$$\int_{\Omega_{co,\#}} k_{co} \left(\delta_{jp} - \frac{\partial \chi^p(\mathbf{y})}{\partial y_j} \right) \frac{\partial T_0}{\partial x_p} \frac{\partial v_0}{\partial x_j} \, d\mathbf{x} = 0 \quad \forall v_0 \in H^1_0(\Omega_{co,\#}) \,, \tag{A.49}$$

where $\chi^p(\mathbf{y})$ is now known from (A.48); using (A.45) (see previous comments regarding proper domain choices),

$$\int_{\Omega_{co,\#}} \left[\frac{1}{\lambda^2} \int_{\Omega_{me}} k_{co} \left(\delta_{jp} - \frac{\partial \chi^p}{\partial y_j} \right) d\mathbf{y} \right] \frac{\partial T_0}{\partial x_p} \frac{\partial v_0}{\partial x_j} \, d\mathbf{x} = 0 \quad \forall v_0 \in H^1_0(\Omega_{co,\#}) \,. \tag{A.50}$$

We clearly recognize the (tensorial) effective conductivity as the constant coefficient in (A.50):

$$k'_{e_{pq}} = \frac{1}{\lambda^2} \int_{\Omega_{me}} k_{co} \left(\delta_{qp} - \frac{\partial \chi^p(\mathbf{y})}{\partial y_q} \right) d\mathbf{y} \,, \tag{A.51}$$

which is equivalent, with $p = q = 1$, to equation (2.19) of Section 2.1.3. Notice the presence, in equation (A.51), of the factor $1/\lambda^2$, and the integral of the Kronecker delta over Ω_{me}; such combination leads to the factor $(1 - c)$ in (2.19). We can physically motivate this result by realizing that the homogenized medium has no holes, *and* it

has the total extension of the supercell. Consequently, division by λ^2 is required to determine the correct averages over the supercell; this fact is mathematically proven in Keller (1980).

The properties of $k'_{e_{pq}}$ can now be easily shown. From equation (A.48), taking $v = \chi^q$,

$$\int_{\Omega_{me}} k_{co} \frac{\partial \chi^q}{\partial y_p} \, d\mathbf{y} = \int_{\Omega_{me}} k_{co} \frac{\partial \chi^p}{\partial y_j} \frac{\partial \chi^q}{\partial y_j} \, ; \tag{A.52}$$

therefore, switching p and q, we get

$$\frac{\partial \chi^q}{\partial y_p} = \frac{\partial \chi^p}{\partial y_q} \, ; \tag{A.53}$$

from (A.51) and (A.53), we conclude that $k'_{e_{pq}}$ is symmetric. We now show that $k'_{e_{pq}}$ can be written as

$$k'_{e_{pq}} = k_{co} \frac{1}{\lambda^2} \int_{\Omega_{me}} \frac{\partial}{\partial y_j}(y_p - \chi^p) \frac{\partial}{\partial y_j}(y_q - \chi^q) \, d\mathbf{y} \ : \tag{A.54}$$

expanding the right-hand-side (RHS) of (A.54),

$$\text{RHS} = k_{co} \frac{1}{\lambda^2} \int_{\Omega_{me}} \left[\delta_{jp}\delta_{jq} - \frac{\partial \chi^p}{\partial y_j}\delta_{jq} - \frac{\partial \chi^q}{\partial y_j}\delta_{jp} + \frac{\partial \chi^p}{\partial y_j}\frac{\partial \chi^q}{\partial y_j} \right] d\mathbf{y} \, ; \tag{A.55}$$

simplifying the δ terms, using (A.52) for the last term, and using symmetry, we obtain (A.51). Thus, for any function $\psi_p \in \mathcal{R}^2$,

$$\psi_p \, k'_{e_{pq}} \psi_q \ = k_{co} \frac{1}{\lambda^2} \int_{\Omega_{me}} \frac{\partial}{\partial y_j} \psi_p (y_p - \chi^p) \frac{\partial}{\partial y_j} \psi_q (y_q - \chi^q) \, d\mathbf{y} \, , \tag{A.56}$$

which is simply the square of the modulus of the gradient of $\psi_p(y_p - \chi^p)$ integrated over Ω_{me}, hence a positive quantity. We conclude that $k'_{e_{pq}}$ is positive-definite, which guarantees well-posedness and uniqueness for (A.50) (Lax-Milgram lemma).

Appendix B

Derivation of Equations (2.52) and (2.56)

B.1 Derivation of equation (2.52)

In order to minimize $L^C_{\Omega_{nip}}$ given in (2.51), we take the functional's first variation, $\delta L^C_{\Omega_{nip}}$, and equate to zero:

$$\delta L^C_{\Omega_{nip}}(\chi_{UB,ni}) = 2\int_{\Omega_{nip}} \frac{\partial \chi_{UB,ni}}{\partial y_k}\frac{\partial v}{\partial y_k}\,d\mathbf{y} = 0\,, \tag{B.1}$$

where $\chi_{UB,ni}$ is the minimizing function. Since $\chi_{UB,ni}$ is a function of y_2 only (for the case $\theta = 0$), equation (B.1) becomes

$$\int_{y_2=-b}^{y_2=+b} \frac{\partial \chi_{UB,ni}}{\partial y_2}\frac{\partial v}{\partial y_2}\,l\,dy_2 = 0\,, \tag{B.2}$$

where $l = l(y_2) = (1 + \alpha - \sqrt{1-4\eta^2})\,d$ is the inter–inclusion distance parallel to y_1, $\alpha \equiv a/d$ (Figure 2-4), and $\eta \equiv y_2/d$. Integrating (B.2) by parts, we obtain

$$v\,l\left[\frac{\partial \chi_{UB,ni}}{\partial y_2}\right]_{-b}^{+b} - \int_{-b}^{+b} v\,\frac{\partial}{\partial y_2}\left(l\,\frac{\partial \chi_{UB,ni}}{\partial y_2}\right)\,dy_2 = 0\,. \tag{B.3}$$

Since $\chi_{UB,ni}$ is constrained to be constant over the segments $y_2 = \pm b$, v is zero on these segments (no variations allowed), and so the first term on the left-hand-side of (B.3) is zero; now, since (B.3) holds for any $v \in X_{UB}(\Omega_{nip})$, we then obtain the Euler equation:

$$\frac{\partial}{\partial y_2}\left(l\,\frac{\partial \chi_{UB,ni}}{\partial y_2}\right) = 0\,. \tag{B.4}$$

Equation (B.4) can be easily solved (to within an arbitrary constant, set to zero):

$$\frac{\partial \chi_{UB,ni}}{\partial y_2} = \frac{C_{UB}}{l}\,, \tag{B.5}$$

where C_{UB} is a constant. Integrating (B.5) in the nip, we obtain

$$\left[\chi_{UB,ni}|_{\Gamma_{ni,1}} - \chi_{UB,ni}|_{\Gamma_{ni,2}}\right] = C_{UB}\int_{y_2=-b}^{y_2=+b}\frac{1}{l}\,dy_2\,, \tag{B.6}$$

where

$$\chi_{UB,ni}|_{\Gamma_{ni,1}} = \chi_{UB,ni}(y_2 = +b)$$

and

$$\chi_{UB,ni}|_{\Gamma_{ni,2}} = \chi_{UB,ni}(y_2 = -b)$$

are unknown, but constant, values. The fact that $l(y_2)$ is symmetric about the centerline perpendicular to the segment connecting the inclusion centers (this centerline is parallel to the y_2 axis for $\theta = 0$) can be used to rewrite the integral on the right-hand-side of (B.6); we then obtain

$$C_{UB} = \left[\chi_{UB,ni}|_{\Gamma_{ni,1}} - \chi_{UB,ni}|_{\Gamma_{ni,2}}\right]\cdot\left[2\int_0^{\beta}\frac{d\eta}{1+\alpha-\sqrt{1-4\eta^2}}\right]^{-1}\,, \tag{B.7}$$

where $\beta \equiv \frac{b}{d}$. Defining

$$G(\alpha,\beta) \equiv \left[2\int_0^{\beta}\frac{d\eta}{1+\alpha-\sqrt{1-4\eta^2}}\right]^{-1}\,, \tag{B.8}$$

we finally derive, from (B.5), (B.7) and (B.8),

$$\frac{\partial \chi_{UB,ni}}{\partial y_2} = \frac{1}{l} G(\alpha,\beta) \left[\chi_{UB,ni}|_{\Gamma_{ni,1}} - \chi_{UB,ni}|_{\Gamma_{ni,2}} \right] , \tag{B.9}$$

which is identical to equation (2.52) of Section 2.1.4.

B.2 Derivation of equation (2.56)

We first notice that, in the problem for χ_{UB}, the average imposed temperature gradient is still

$$< \nabla T_{UB} >_v = < \nabla T >_v = -\frac{\Delta T}{L} \mathbf{e}_1 \tag{B.10}$$

(Section 2.1.3). The average flux, however, becomes

$$< \mathbf{q}_{UB} >_v = \frac{1}{\lambda^2} \left[\int_{\Omega_{me}} k_{co} \frac{\Delta T}{L} \, d\mathbf{y} + \int_{\Omega_{me}} -k_{co} \frac{\partial \chi_{UB}}{\partial y_1} \, d\mathbf{y} \right] \mathbf{e}_1 , \tag{B.11}$$

where $\lambda^2 = \int_{\Omega_{sc}} d\mathbf{y}$, and, in equation (2.21), χ has been replaced by χ_{UB}. The first integral on the right-hand-side of (B.11) simplifies, as before, to $k_{co}(\Delta T/L)(1-c)$. The second integral is split into

$$\int_{\Omega_{me}} -k_{co} \frac{\partial \chi_{UB}}{\partial y_1} \, d\mathbf{y} = \int_{\tilde{\Omega}_{me}} -k_{co} \frac{\partial \chi_{UB}}{\partial y_1} \, d\mathbf{y} + \int_{\Omega_{nip}} -k_{co} \frac{\partial \chi_{UB}}{\partial y_1} \, d\mathbf{y} . \tag{B.12}$$

But since in the nip region, for the case $\theta = 0$, $\chi_{UB} = \chi_{UB}(y_2)$, the integral over Ω_{nip} in (B.12) vanishes. Therefore, we obtain

$$< \mathbf{q}_{UB} >_v = \left[k_{co} \frac{\Delta T}{L}(1-c) + \frac{1}{\lambda^2} \int_{\tilde{\Omega}_{me}} -k_{co} \frac{\partial \chi_{UB}}{\partial y_1} \, d\mathbf{y} \right] \mathbf{e}_1 . \tag{B.13}$$

From equations (2.2), (B.10) and (B.13), and using the definition of the functional I^C_{Ω} in Section 2.1.3 (equation (2.31)), we finally derive

$$k'_{e,UB}(c,\lambda,\{\mathbf{y}\}_N) = k_{co} \left\{ (1-c) - \frac{L^2}{\Delta T^2 \lambda^2} I^C_{\tilde{\Omega}_{me}}(\chi_{UB}) \right\} , \tag{B.14}$$

which is identical to equation (2.56) in Section 2.1.4.

Appendix C

Extension to Sedimentation

In this Appendix we extend the methodology described in Chapter 2 for the conduction and creeping flow problems, to the Stokes sedimentation problem. We address the (physically and mathematically dubious) case of two–dimensional sedimentation; furthermore, the formulation assumes a prescribed particle joint probability density function, though the particles are now moving relative to an inertial laboratory frame. Further extensions of the methodology include: addition of the third dimension, to treat particulate, rather than fibrous, media; formulation and solution of the "self–consistent" analog, in which the particle distribution is *calculated*, by following the motion of the particles; treatment of nonlinear effects, such as field–dependent properties, and inertial motion of the fluid and/or particles. Here, a sketch of the micro–meso–macro formulation of the sedimentation problem is presented, together with a brief discussion of accompanying numerical issues.

Description of the Original Multiscale Problem The original problem for Stokes sedimentation is analogous to the original problems for heat conduction in composites (Section 2.1.1) and creeping flow through porous media (Section 2.2.1): the continuous phase is a fluid with viscosity μ_{co} and density ρ_{co}; the inclusions are now cylindrical non-colloidal *particles* of homogeneous density ρ_{di} (for purposes of presentation we assume $\rho_{di} > \rho_{co}$); the boundary $\partial\Omega_{ma}$ now defines, e.g., the walls of a bounding container, as illustrated in Figure C-1. We focus our attention on

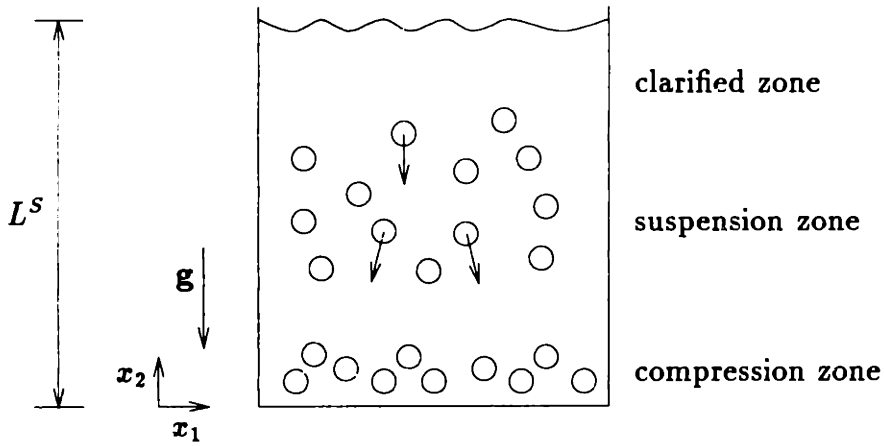

Figure C-1: Batch Stokes sedimentation.

the region of Ω_{ma} between the upper clarified and lower compression zones; within this homogeneous, suspension–filled subdomain we assume zero net (fluid and particle) volume flux. We are interested in determining, for given continuous–phase and distributed–phase parameters, $\mathbf{p}$, the *average sedimentation velocity* (or settling rate) of the particles, $\mathcal{U}(\mathbf{p})$, in the presence of a homogeneous body force (here gravity, $\mathbf{g}$). Extension of Batchelor's low–concentration hindered settling result [Batchelor (1972)] to medium and high concentrations is thus within the reach of the proposed methodology.

Macroscale Our homogeneous, steady–state, quantity of interest, $\mathcal{U}(\mathbf{p})$, in fact *defines* the macroscale problem. We thus pass directly to the mesoscale.

Mesoscale For the prescribed–JPDF formulation, the Level 2, 3, and 4 procedures are analogous to the corresponding composite and porous–medium processes, and we thus focus on the Level 1 formulation. In addition to the definitions associated with Figures 2-1 and 2-5, we require: the acceleration of gravity, $-g\mathbf{e}_2$; the decomposition of the mesoscale boundary $\partial\Omega_{me}$ into the N boundaries of the individual particles, $\partial\Omega_{me} = \cup_{k=1}^{N} \partial\Omega_k$. In the mesoscale supercell (in practice, the V–supercell) we then write the pressure as $p(\mathbf{y}) = -\rho_{co}\, g y_2 - \tau y_2 + p'(\mathbf{y})$, where τ is the fluid "backflow" pressure gradient. The mesoscale velocity, $\mathbf{u}(\mathbf{y}) = (u_1(y_1, y_2), u_2(y_1, y_2))$, perturbation

pressure, $p'(\mathbf{y})$, and backflow gradient, τ, must satisfy the steady Stokes equations,

$$-\frac{\partial}{\partial y_j}[\mu_{co}(\frac{\partial u_i}{\partial y_j}+\frac{\partial u_j}{\partial y_i})]+\frac{\partial p'}{\partial y_i}-\tau\,\delta_{2i}=0 \text{ in } \Omega_{me} \text{ for } i=1,2\,, \tag{C.1}$$

$$-\frac{\partial u_i}{\partial y_i}=0 \text{ in } \Omega_{me}\,, \tag{C.2}$$

$$-(\int_{\Omega_{me}} u_2\,d\mathbf{y}+\frac{\pi d^2}{4}\sum_{k=1}^{N}(U_2)_k)=0\,, \tag{C.3}$$

subject to the no-slip and dynamical boundary conditions

$$\mathbf{u}|_{\partial\Omega_k}=\mathbf{U}_k+\omega_k\,\mathbf{e}_3\times(\mathbf{y}-\mathbf{y}_k)\,,\quad k=1,\ldots,N\,, \tag{C.4}$$

and

$$\int_{\partial\Omega_k}(\mathbf{T}\cdot\mathbf{n})\,ds=(\tau\,\frac{\pi d^2}{4}-W)\mathbf{e}_2\,,\quad k=1,\ldots,N\,, \tag{C.5}$$

$$\int_{\partial\Omega_k}(\mathbf{y}-\mathbf{y}_k)\times(\mathbf{T}\cdot\mathbf{n})\,ds=0\,,\quad k=1,\ldots,N\,. \tag{C.6}$$

The velocity and perturbation pressure must be λ-doubly periodic; in addition, we require for uniqueness that $\int_{\Omega_{me}} u_1\,dy = \int_{\Omega_{me}} p'\,dy = 0$ (the former is permitted by horizontal homogeneity). Here $\mathbf{U}_k$ and ω_k are the translational and rotational velocity, respectively, of the k^{th} particle; $\mathbf{e}_3=\mathbf{e}_1\times\mathbf{e}_2$; $(\,)\times(\,)$ refers to the usual cross product; $\mathbf{T}$ is the stress tensor in the fluid, $T_{ij}=\mu_{co}\,(\partial u_i/\partial y_j+\partial u_j/\partial y_i)-p\,\delta_{ij}$; δ_{ij} is the Kronecker delta; $\mathbf{T}\cdot\mathbf{n}=T_{ij}\,n_j$; and W is the buoyancy-corrected weight (per unit length) of a particle, $W=(\rho_{di}-\rho_{co})g\pi d^2/4$. Note that τ and the $(\mathbf{U}_k\,,\omega_k)$ are not specified, but, rather, are *part* of the solution; in essence, the zero net volume flux and particle force equilibrium equations, (C.3) and (C.5)-(C.6), respectively, are the complementary conditions from which the backflow gradient and particle velocities can be deduced. The strong-form equations (C.1)-(C.6) are the point of departure of Batchelor's analysis.

In this sedimentation problem, the effective property of interest is the average settling velocity of the particles; as opposed to the effective conductivity and permeability, it is a scalar property, by virtue of horizontal homogeneity, and for a particular

configuration $\{\mathbf{y}\}_N$, it is defined as

$$\mathcal{U}'(c, \lambda, \{\mathbf{y}\}_N) = \frac{1}{NW} I^S(\mathbf{u}) , \tag{C.7}$$

where, for $\mathbf{v}$ satisfying $\mathbf{v}|_{\partial\Omega_k} = \mathbf{V}_k + \zeta_k \, \mathbf{e}_3 \times (\mathbf{y} - \mathbf{y}_k)$,

$$I^S(\mathbf{v}) = -W \sum_{k=1}^{N} (V_2)_k . \tag{C.8}$$

We also introduce the dissipation functional $J^S(\mathbf{v})$,

$$J^S(\mathbf{v}) = 2I^S(\mathbf{v}) - \mu_{co} \frac{1}{2} \int_\Omega (\frac{\partial v_i}{\partial y_j} + \frac{\partial v_j}{\partial y_i})(\frac{\partial v_i}{\partial y_j} + \frac{\partial v_j}{\partial y_i}) \, d\mathbf{y} . \tag{C.9}$$

By multiplying equation (C.1) by $\mathbf{u}$, integrating over Ω_{me}, and using the divergence theorem and (C.2)–(C.6), we derive

$$I^S(\mathbf{u}) = J^S(\mathbf{u}) = \mu_{co} \frac{1}{2} \int_{\Omega_{me}} (\frac{\partial v_i}{\partial y_j} + \frac{\partial v_j}{\partial y_i})(\frac{\partial v_i}{\partial y_j} + \frac{\partial v_j}{\partial y_i}) \, d\mathbf{y} . \tag{C.10}$$

From (C.10) it is clear that the settling velocity $\mathcal{U}'$ will always be positive.

As for the conduction and creeping flow problems, both our microscale analytical techniques and our numerical methods will be founded upon the variational form of (C.1)–(C.6) and (C.7),

$$\mathbf{u} = \arg \max_{\mathbf{v} \in B} J^S(\mathbf{v}) , \tag{C.11}$$

where

$$B = \{\mathbf{v} \in Y \mid \operatorname{div} \mathbf{v} = 0 , \int_{\Omega_{me}} v_2 \, d\mathbf{y} - \frac{\pi d^2}{4W} I^S(\mathbf{v}) = 0 , \int_{\Omega_{me}} v_1 \, d\mathbf{y} = 0\} ,$$

and

$$Y = \{ (v_1, v_2) \in (H^1_{\#,0}(\Omega_{me}), H^1_{\#,0}(\Omega_{me})) \mid \forall k \in \{1, \ldots, N\}, \\ \mathbf{v}|_{\partial\Omega_k} = \mathbf{V}_k + \zeta_k \, \mathbf{e}_3 \times (\mathbf{y} - \mathbf{y}_k), \mathbf{V}_k \in \mathcal{R}^2, \zeta_k \in \mathcal{R} \} .$$

Related variational expressions for the sedimentation problem can be found in Hill

& Power (1956), Keller, Rubenfeld & Molyneux (1967), Nir, Weinberger & Acrivos (1975), and Kim & Karrila (1991). To arrive at the unconstrained weak form, similarly to the porous medium problem, we now introduce two Lagrangian multipliers, the pressure, $p'(\mathbf{y})$, associated with the divergence condition, and the backflow gradient, τ, associated with the zero volume flux condition: Find $(\mathbf{u}, p', \tau) \in (Y, L^2_{\#,0}(\Omega_{me}), \mathcal{R})$ such that

$$\mu_{co} \int_{\Omega_{me}} \frac{\partial v_i}{\partial y_j} \left(\frac{\partial u_i}{\partial y_j} + \frac{\partial u_j}{\partial y_i}\right) d\mathbf{y} \; - \; \int_{\Omega_{me}} \frac{\partial v_i}{\partial y_i} p \, d\mathbf{y} - \tau \left[\int_{\Omega_{me}} v_2 \, d\mathbf{y} - \frac{\pi d^2}{4W} I^S(\mathbf{v})\right] = I^S(\mathbf{v}) \quad \forall \mathbf{v} \in Y \,, \tag{C.12}$$

$$- \int_{\Omega_{me}} q \frac{\partial u_i}{\partial y_i} \, d\mathbf{y} = 0 \quad \forall q \in L^2_{\#,0}(\Omega_{me}) \,, \tag{C.13}$$

$$- \eta \left[\int_{\Omega_{me}} u_2 \, d\mathbf{y} - \frac{\pi d^2}{4W} I^S(\mathbf{u})\right] = 0 \quad \forall \eta \in \mathcal{R} \,. \tag{C.14}$$

From (C.7)–(C.11) we can derive the following expression for the settling velocity,

$$\mathcal{U}'(c, \lambda, \{\mathbf{y}\}_N) = \frac{1}{NW} \max_{\mathbf{v} \in B} J^S(\mathbf{v}) \,. \tag{C.15}$$

Related extremum statements for the settling velocity can be found in Keller, Rubenfeld & Molyneux (1967). Levels 2, 3, and 4 of the mesoscale analysis follow directly from (C.7)–(C.14) and Chapter 2.

Microscale At the microscale, we can, due to the maximization property (C.15), once again pursue computation–reducing bounds which are motivated by physical considerations and mathematically rigorized by variational arguments. For example, to generate upper bounds for the settling velocity for a particular configuration, we can: reduce the diameters of very–close pairs from d to d', thereby opening up the associated nip region; remove a particle shielded by many close neighbors. The latter is, in fact, a special case of a hindered settling conclusion which follows directly from (C.15) and embedding arguments: for any subset of particles in a particular

configuration,

$$\mathcal{U}'(c,\lambda,\{\mathbf{y}\}'_M) \geq \mathcal{U}'(c,\lambda,\{\mathbf{y}\}_N)\ ,\ \{\mathbf{y}\}'_M \subset \{\mathbf{y}\}_N\ ,\ M < N\ .$$

The proofs for these claims are based upon rigid–body inclusion arguments, found in Hill & Power (1956), Keller, Rubenfeld & Molyneux (1967), Nir, Weinberger & Acrivos (1975), and Kim & Karrila (1991); in the present context, care must be taken to ensure that comparison solutions honor *all* constraints associated with the space B. Lower bounds for the settling velocity can be developed by restricting the space over which the functional $J^S(\mathbf{v})$ is maximized. For example, the nip–region fluid flow between two close particles can be assumed to take the form of analytical asymptotic solutions for $\alpha \to 0$ already available in the literature [Happel & Brenner (1983), Kim & Karrila (1991)]; this approach will lead to a modified Stokes problem involving nip–interfacial conditions similar to those appearing in (2.55). In summary, bounds provide rigor, but often lack precision, whereas local asymptotic solutions offer precision, but often lack generality and quantitative error estimates; the strength of the proposed approach is not necessarily in the development of new bounds or new analytical procedures, but, rather, in the combination of these two strategies into a general and efficient numerical procedure.

Numerical Methods Turning now to numerical treatment, we address only three issues. First, the rather complex natural boundary conditions (C.5)–(C.6) are automatically reflected in (C.12) and the admissible space, Y. This variational formulation leads to a firmer theoretical foundation, a less communication–intensive parallel algorithm, and a simpler implementation than more standard, for example discrete Green's function, implementations of (C.5)–(C.6). Second, we note that transfer operators [Anagnostou, Maday, Mavriplis & Patera (1990)] can be devised which permit the function space Y to be represented by *standard* nodal finite element bases. Specifically, consider a standard mesh associated with some mesoscale domain, in which the cylinder surfaces are meshed with no reference to the special space Y. Then, to evaluate the action of the dissipation component of the discrete operator derived from

(C.12) (for example, in Uzawa iteration): we transfer each particle velocity to the nodes on the boundary of the associated particle via a simple interpolation matrix Q; we evaluate the dissipation contribution based on this now–standard nodal representation; we transfer the residuals back to the actual particle–velocity degrees–of–freedom via Q^T; we include the residual contributions from $I^S(\mathbf{v})$. Third, the zero net volume flux constraint in B, and associated additional Lagrange multipler, τ, introduce apparently new terms in the weak form (C.12)–(C.14); in fact, (C.12)–(C.14) can also be interpreted as a standard Stokes weak form with the periodic pressure space expanded to include a linear contribution in y_2. Accordingly, we expect Taylor–Hood finite element discretization (Section 3.2.3), and subsequent Uzawa iteration (Section 3.2.4), of (C.12)–(C.14) to have all the good properties (e.g., mesh–independent "inf–sup" condition [Girault & Raviart (1986), Gunzburger (1989)]) usually associated with this velocity–pressure approximation. As regards implementation, the new constraint slightly modifies the discrete divergence and gradient operators.

Appendix D

The ϵ-Smoothing Procedure

In the periodic domain generation process for the mesoscale problems (see Sections 2.1.3, 2.2.3, and 3.2.1), a (special) Voronoi diagram is constructed, whose generators are replicas of the set of inclusion positions $\{\mathbf{y}\}_N$ over 25 square–arranged S–supercells. The desired domain, now called a V–supercell, is then an appropriately extracted subset of such diagram. This simple, efficient process, however, generates (Voronoi) edges whose lengths, l_{VE}, are either zero (i.e., virtual edges, see Figure 3-3) or very small, $l_{VE}/d \approx O(\epsilon_p)$, where ϵ_p is a typical 32–bit machine precision. The objective of the ϵ–smoothing procedure is to remove *all* Voronoi edges whose lengths obey

$$\frac{l_{VE}}{d} \leq \epsilon_s \,, \tag{D.1}$$

where ϵ_s is a chosen parameter such that

$$\epsilon_p \ll \epsilon_s < 1 \,. \tag{D.2}$$

(notice that ϵ_s is a fraction of the unit nondimensional inclusion diameter). The parameter ϵ_s was chosen to be on the order of the normalized default mesh spacing h_0^* (see Section 3.2.2); typically, for the conduction problem, $\epsilon_s \approx h_0^* = 0.1$, and for the creeping flow problem, $\epsilon_s \approx h_0^* = 0.2$ (as mentioned in Section 4.3, the second order approximation of the velocity field allows a larger nondimensional mesh spacing for the creeping flow problem). For simplicity of exposition, small Voronoi edges (virtual

or not) are here denoted $VE_{s,b}$ if they lie on the external boundary of the V–supercell, or $VE_{s,i}$ if they are internal. The execution of ϵ–smoothing (i.e., removal of all the $VE_{s,b}$'s and $VE_{s,i}$'s) ensures that the mesh generator, discrete equations, and solver do not fail *artificially* (notice that they might still fail due to other reasons, e.g. the presence of almost touching inclusions, see Sections 4.2 and 4.3.)

The ϵ–smoothing procedure is constrained to preserve two properties of the V–supercell: periodicity (crucial), and no cutting of inclusions by any Voronoi edge (highly desired). In order to characterize the role of ϵ–smoothing in the domain generation process, we outline below the major steps of the (serial) preprocessing phase (more details in Sections 3.2.1 and 3.2.5):

Preprocessing: start
initialize data
take input $\{\mathbf{y}\}_N$
replicate $\{\mathbf{y}\}_N$ over the 25 S–supercells
construct Voronoi diagram
extract V–supercell geometrical and topological data
identify and match periodic edge pairs: tolerate mismatches
perform ϵ–smoothing
identify and match periodic edge pairs: mismatch $\Rightarrow$ ERROR
setup parallel data constructs
export to parallel processors
Preprocessing: end

(The generation of an input set $\{\mathbf{y}\}_N$, as well as of sequences of $\{\mathbf{y}\}_N$'s for the Monte–Carlo Level–2 driver, is described in Section 3.2.1.) Periodic edge pairs are matched based on topological and geometrical data, the latter being the decisive factor. Periodic edges have equal length, and their midpoints are separated by a distance of λ or $\sqrt{2}\,\lambda$. These geometrical tests are made robust by the guaranteed presence of only long enough edges ($l_{VE} > \epsilon_s\, d$); any round-off errors will scale with machine precision, therefore much smaller than l_{VE}/d, allowing for accurate matching. We remark that no ERROR case arose, after ϵ–smoothing of the V–supercells generated

in this study.

The main issues related to the ϵ–smoothing procedure are now described, followed by an outline of the algorithm. A $VE_{s,b}$ and its partner have to be simultaneously and coherently eliminated, so that periodicity is not destroyed. Figures D-1 and D-2 display *all* the cases that were found to happen on the boundary of the V–supercells. Periodic edge pairs are marked with '/', '//', or '///'; the arrows indicate that the boundaries of the V–supercells wrap around, and are being traversed counterclockwise; thin lines correspond to the original, extracted, configuration, and thick lines show the displaced, kept, edges. If no partner is found for a $VE_{s,b}$, then such a $VE_{s,b}$ is a virtual edge, thus readily eliminated. For any $VE_{s,b}$ or $VE_{s,i}$, the edges that connect to its endpoints have to be identified: they will be the ones displaced due to the elimination process. Before any elimination of a $VE_{s,b}$ or $VE_{s,i}$ can take place, however, potential cutting of a inclusion by the displaced edges is investigated; the small edge is kept if any cutting would happen. Although some alternatives may be devised for such "cutting" cases (e.g., testing for all possible endpoint movements for $VE_{s,i}$'s, or minimal stretching of $VE_{s,b}$'s), it turned out that all small, by–force kept edges had lengths a little smaller than the default mesh spacing h_0 (a quarter, say), therefore well above machine precision. Finally, when a $VE_{s,i}$ touches the boundary, only the internal edges connecting to the other extremity are displaced, and they will in turn touch the boundary.

The ϵ–smoothing algorithm proceeds as follows:

ϵ–smoothing: start

loop over Voronoi edges

if $\frac{l_{VE}}{d} > \epsilon_s$, go to next edge; otherwise,

create duplicate (backup) of V–supercell data

get list of edges that connect to this small edge

if virtual $VE_{s,b}$ or $VE_{s,i}$, then

simply eliminate

update V–supercell data

else if finite $VE_{s,b}$, then

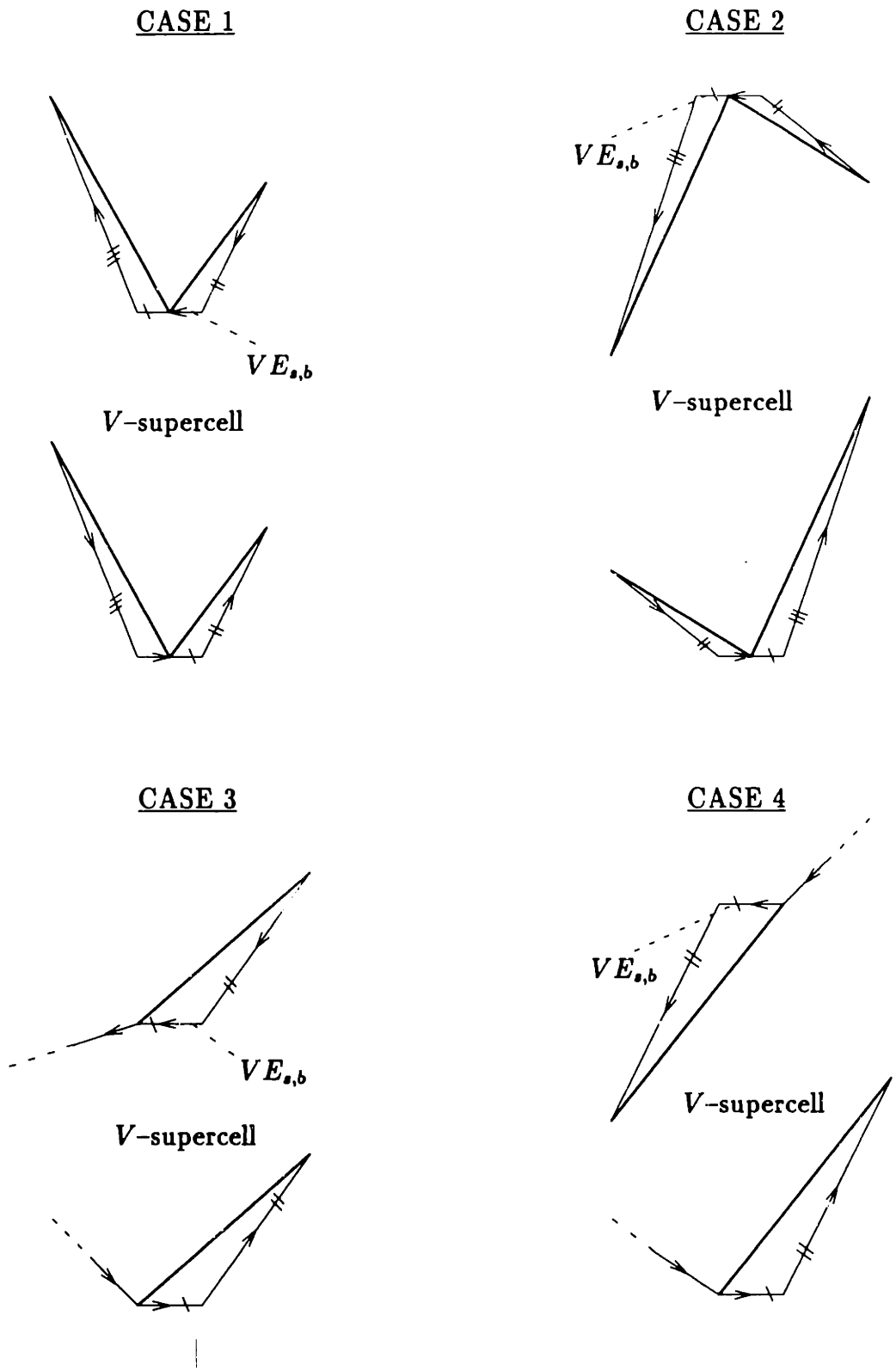

Figure D-1: The ϵ–smoothing procedure: cases 1, 2, 3 and 4 for small Voronoi edges on the boundary of a V–supercell, $VE_{a,b}$. Periodic edge pairs are marked with '/', '//', or '///'; arrows indicate that the boundaries wrap around; thin and thick lines correspond to original and modified edge–configurations, respectively.

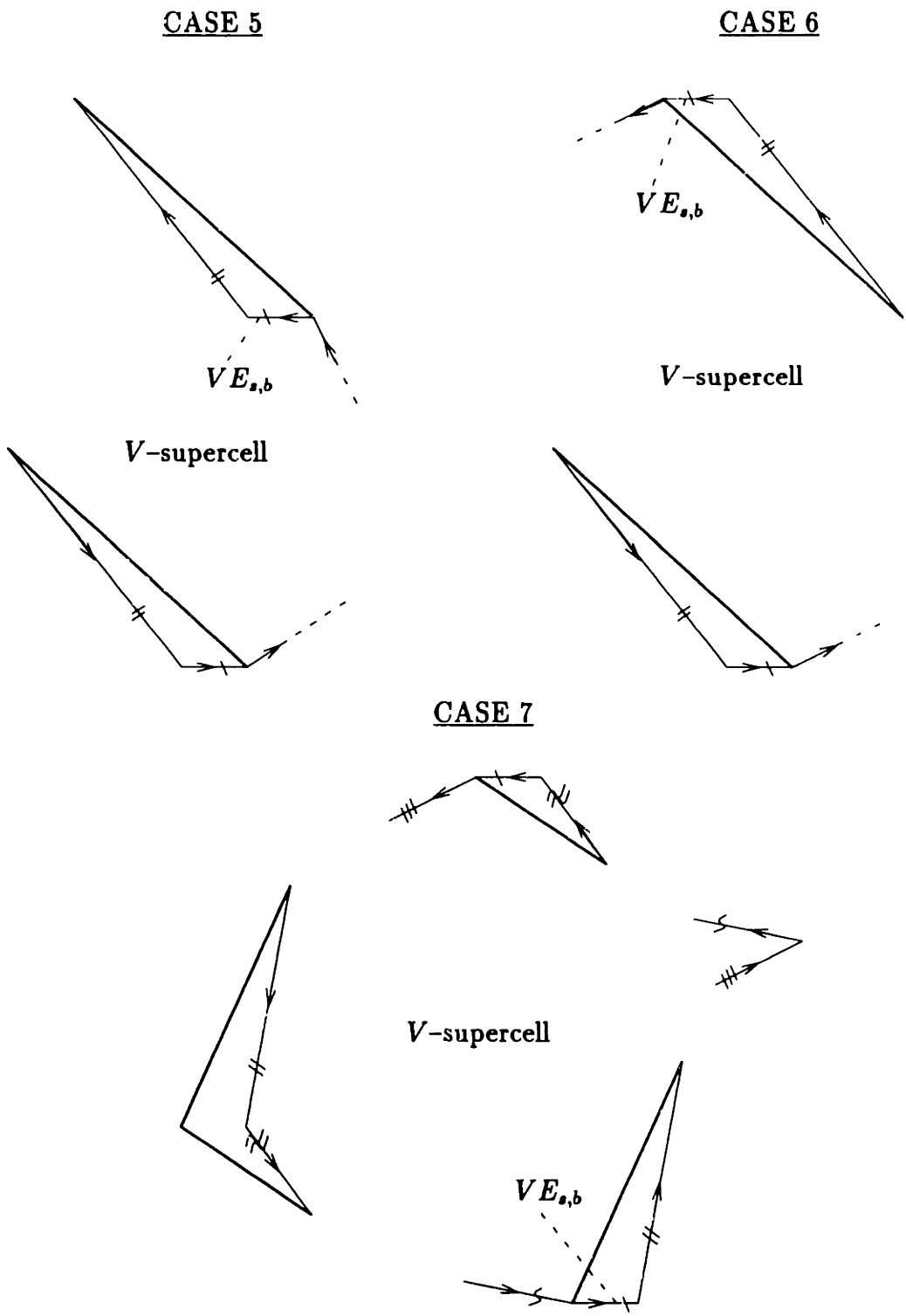

Figure D-2: The ϵ–smoothing procedure: cases 5, 6 and 7 for small Voronoi edges on the boundary of a V–supercell, $VE_{a,b}$. Periodic edge pairs are marked with '/', '//', or '///'; arrows indicate that the boundaries wrap around; thin and thick lines correspond to original and modified edge–configurations, respectively.

identify partner

displace connecting edges according to Figures D-1 and D-2

if no cutting happens, then

eliminate $VE_{s,b}$ pair

update V–supercell data

else

keep small $VE_{s,b}$ pair

retrieve V–supercell data from backup

endif

else if finite $VE_{s,i}$, then

if $VE_{s,i}$ touches boundary, then

displace internal connecting edges to touch boundary

else

displace connecting edges to the midpoint of $VE_{s,i}$

endif

if no cutting happens, then

eliminate $VE_{s,i}$

update V–supercell data

else

keep small $VE_{s,i}$

retrieve V–supercell data from backup

endif

endif

endloop

go back to start and repeat process,

until no more $VE_{s,b}$ or $VE_{s,i}$ exists

ϵ–smoothing: end

As a simple example, the trivial case with only one inclusion is degenerate (Figure 3-2). After construction of the Voronoi diagram and extraction of the resulting V–(super)cell, 7 boundary edges result, 4 of length λ (as expected), and 3 of length

zero (virtual $VE_{s,b}$'s). Before ϵ–smoothing, matching of periodic pairs fails (odd number of boundary edges). The 3 $VE_{s,b}$ edges are then simply eliminated, and matching becomes successful.

Figures D-3 and D-4 show pairs of V–supercells: in each figure, the top configuration shows a V–supercell as extracted from the corresponding (special) Voronoi diagram, *before* ϵ–smoothing; the bottom configuration shows the V–supercell *after* ϵ–smoothing; the dashed circles highlight the differences between the two configurations. The top V–supercells in Figures D-3 and D-4 are shown together in Figure 3-6, Section 3.2.1.

It should be pointed out that, by displacing Voronoi edges relative to the inclusions, the ϵ–smoothing procedure introduces some asymmetries in the V–supercell. In particular, cases 2, 4 and 6 (Figures D-1 and D-2) slightly reduce the matrix volume ($O(\epsilon_s)$ effect); however, these cases happened very rarely, and mostly with $N = 2$, so that they cause no concern. Also, in these cases, the distance between the midpoints of the displaced periodic edges is slightly different from λ or $\sqrt{2}\lambda$, and the matching criterion has to allow for this change. Finally, when meshing two local edges corresponding to the same *displaced* Voronoi (global) edge (see Sections 3.2.2 and 3.2.5), the inclusion from the neighboring two tiles closest to the local edge(s) is chosen (for *both* edges) in order to compute the Hausdorff distances for the points on the edge(s), with respect to the inclusion. Therefore, each global edge has associated with it an inclusion center, used for both corresponding local edges to ensure conforming triangles when meshing.

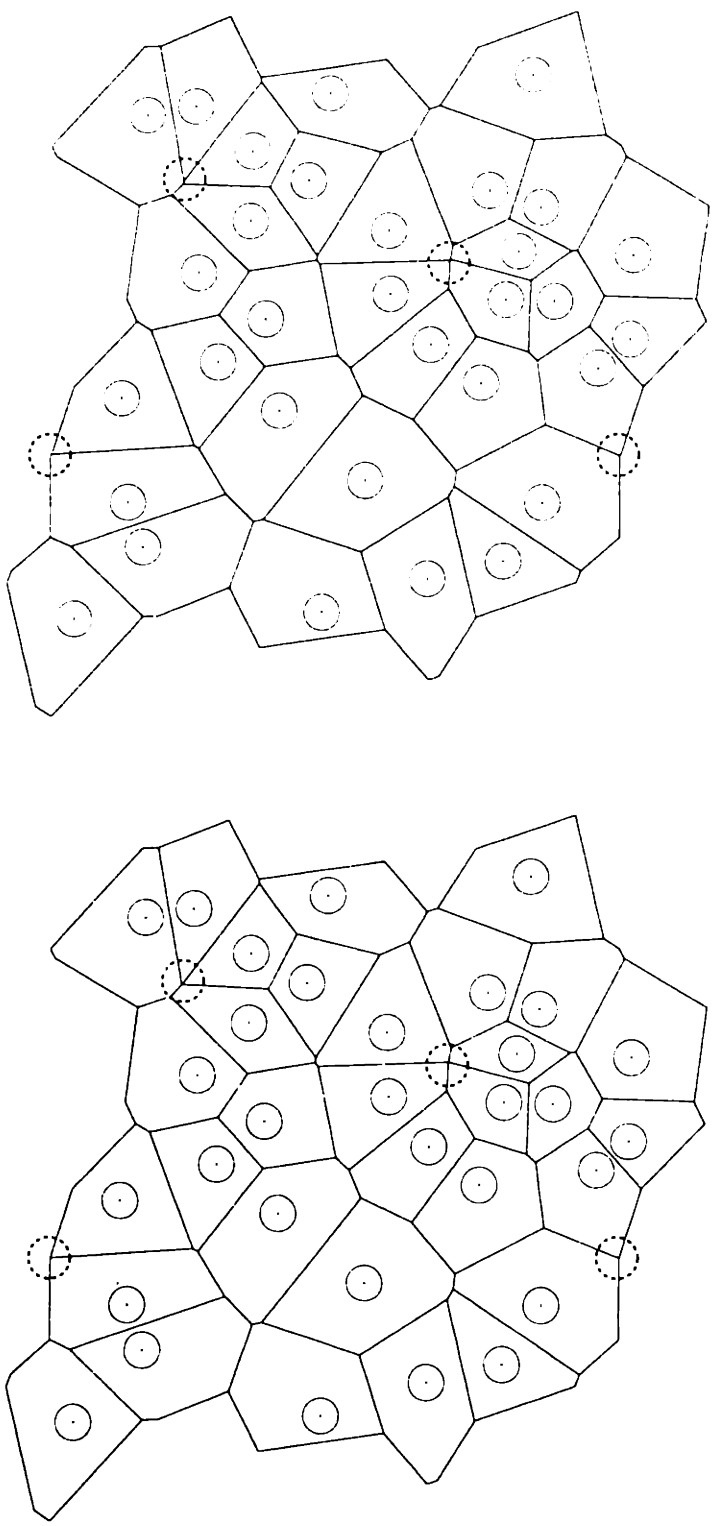

Figure D-3: Typical 32–inclusion V–supercell (concentration $c = 0.10$) before (top) and after (bottom) ϵ–smoothing. Dashed circles highlight the differences due to the elimination of small edges.

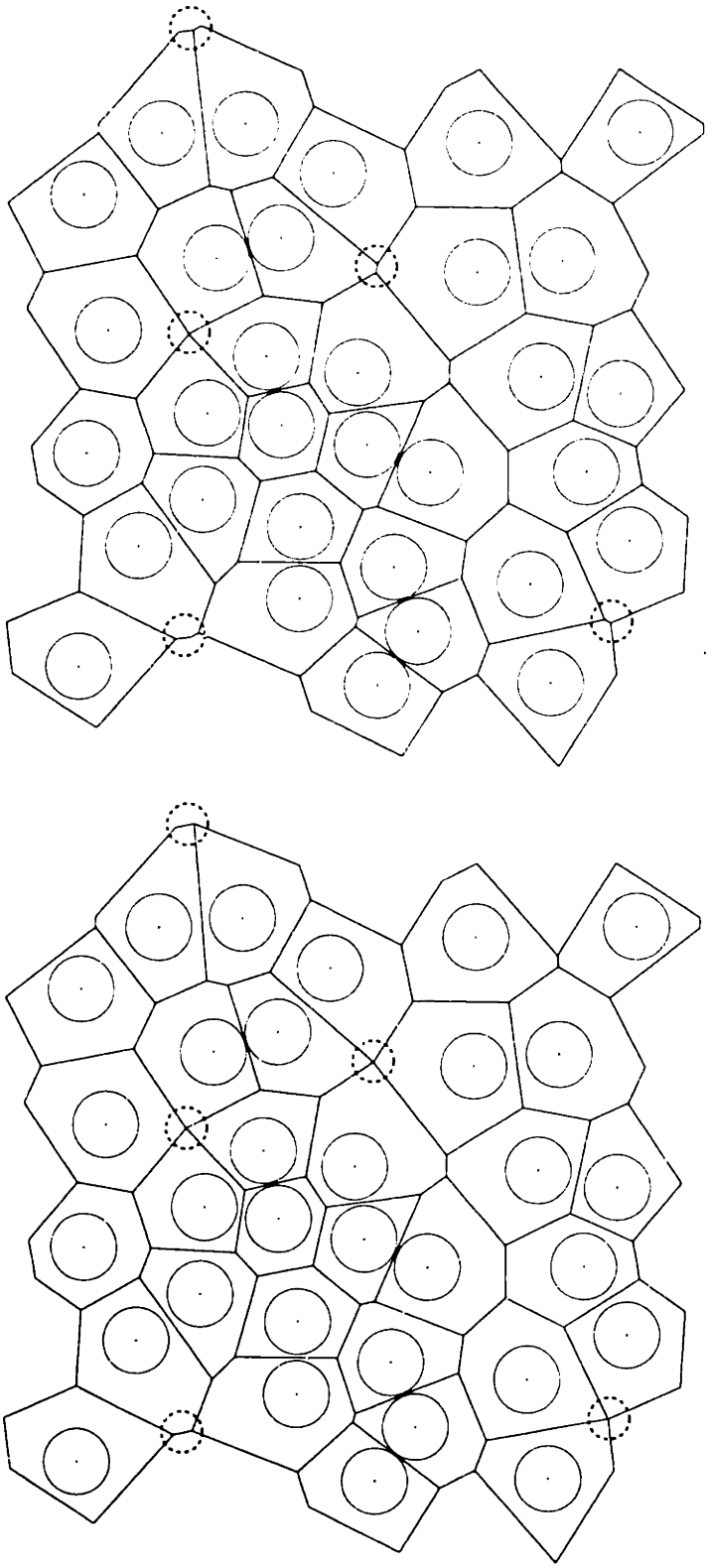

Figure D-4: Typical 32-inclusion V-supercell (concentration $c = 0.30$) before (top) and after (bottom) ϵ-smoothing. Dashed circles highlight the differences due to the elimination of small edges.

Appendix E

A Stopping Criterion for the Conjugate Gradient Iteration

Note: This appendix follows very closely the contents in pages 93 and 94 of the Revised Lecture Notes (1990) for the MIT Computational Fluid Dynamics course (2.274), taught by Prof. Anthony T. Patera. It is included here to allow for a self–contained presentation of the incomplete iteration error criterion for the conduction problem in Section 3.1.4.

In this appendix, we consider the discrete Poisson model problem

$$\underline{\mathbf{A}}\,\underline{u} = \underline{f}\,, \tag{E.1}$$

where $\underline{\mathbf{A}}$ is the finite element Laplacian operator, $\underline{u}$ is the vector of unknown global values of the scalar field u, and $\underline{f}$ is the global forcing vector. The $\underline{\mathbf{A}}$ operator is symmetric and positive–definite, suitable for conjugate gradient iteration. Notice that $\underline{u}$ here corresponds to $\underline{\chi}_h$ in the conduction problem, and to the Cartesian components of the velocity vector, $\underline{u}_{1,h}$ and $\underline{u}_{2,h}$, in the creeping flow problem.

The conjugate gradient algorithm, in the absence of round–off error, converges in at most N_{dof} steps (N_{dof} being the number of system degrees of freedom) to the exact solution $\underline{u}$ of (E.1). Typically, it is *interrupted* after m_f steps, or iterations, $m_f < N_{dof}$. The incomplete iteration error is then defined as a suitable norm of the

difference $(\underline{u}-\underline{u}^{m_f})$; the H^1–seminorm is employed here: in the absence of quadrature errors,

$$|\,\underline{u}-\underline{u}^{m_f}\,|_{H^1} \;=\; [(\underline{u}-\underline{u}^{m_f})^T\,\underline{\mathbf{A}}\,(\underline{u}-\underline{u}^{m_f})]^{\frac{1}{2}}\,, \tag{E.2}$$

where $\underline{u}^m$ is the m^{th} iterate of $\underline{u}$ and the superscript ^{T} denotes the transpose operation. The right–hand–side of (E.2) is the discrete equivalent of the (square root of) the bilinear form a in (3.5). The choice of $|\ |_{H^1}$ rather than the full norm $||\ ||_{H^1}$ is motivated by the facts that, first, $||\ ||_{H^1}$ must be scaled due to the different dimensions of $|\ |_{H^1}$ and $||\ ||_{L^2}$, and second, $|\ |_{H^1}$ is unaffected by the level of the solution, and is the natural norm for conjugate gradient. Notice that, by virtue of the Poincaré–Friedrichs inequality [Girault & Raviart (1986)], bounding $|\ |_{H^1}$ implies bounding $||\ ||_{H^1}$; as a consequence, $||\ ||_{L^2}$ is also bounded.

We express $\underline{u}^m$ as

$$\underline{u}^m = \underline{u} - \underline{\epsilon}^m\,, \tag{E.3}$$

where $\underline{\epsilon}^m$ is the absolute error vector at iteration m. The (conjugate gradient) residual is given by

$$\underline{r}^m = \underline{f} - \underline{\mathbf{A}}\,\underline{u}^m = \underline{\mathbf{A}}\,\underline{\epsilon}^m\,; \tag{E.4}$$

clearly, a non–zero residual induces error. The squared H^1–seminorm of the difference $(\underline{u}-\underline{u}^m)$ is written as

$$|\,\underline{u}-\underline{u}^m\,|^2_{H^1} = |\,\underline{\epsilon}^m\,|^2_{H^1} = \underline{\epsilon}^{m^T}\,\underline{\mathbf{A}}\,\underline{\epsilon}^m = \underline{\epsilon}^{m^T}\underline{r}^m\,. \tag{E.5}$$

Introducing the (non–singular) finite element mass matrix, $\underline{\mathbf{M}}$, in (E.5), and using the Cauchy–Schwarz inequality in $\underline{\mathbf{M}}$, we obtain

$$|\,\underline{u}-\underline{u}^m\,|^2_{H^1} = \underline{\epsilon}^{m^T}\,\underline{\mathbf{M}}\,\underline{\mathbf{M}}^{-1}\,\underline{r}^m \;\leq\; (\underline{\epsilon}^{m^T}\,\underline{\mathbf{M}}\,\underline{\epsilon}^m)^{\frac{1}{2}}\,(\underline{r}^{m^T}\,\underline{\mathbf{M}}^{-1}\,\underline{r}^m)^{\frac{1}{2}} \tag{E.6}$$

$$\leq\; \left(\max\,\frac{\underline{\epsilon}^{m^T}\,\underline{\mathbf{M}}\,\underline{\epsilon}^m}{\underline{\epsilon}^{m^T}\,\underline{\mathbf{A}}\,\underline{\epsilon}^m}\right)^{\frac{1}{2}}\,|\,\underline{u}-\underline{u}^m\,|_{H^1}\,(\underline{r}^{m^T}\,\underline{\mathbf{M}}^{-1}\,\underline{r}^m)^{\frac{1}{2}}\,. \tag{E.7}$$

Using the Rayleigh quotient principle in equation (E.7) yields

$$| \underline{u} - \underline{u}^m |_{H^1}^2 \leq \frac{1}{\varrho_{min}^{1/2}} | \underline{u} - \underline{u}^m |_{H^1} (\underline{r}^{m^T} \underline{\mathbf{M}}^{-1} \underline{r}^m)^{\frac{1}{2}} , \tag{E.8}$$

or

$$| \underline{u} - \underline{u}^m |_{H^1} \leq \frac{1}{\varrho_{min}^{1/2}} (\underline{r}^{m^T} \underline{\mathbf{M}}^{-1} \underline{r}^m)^{\frac{1}{2}} , \tag{E.9}$$

where ϱ_{min} is the minimum eigenvalue of the generalized eigenvalue problem $\underline{\mathbf{A}}\,\underline{X} = \varrho\,\underline{\mathbf{M}}\,\underline{X}$. The left–hand–side of (E.9) is the incomplete iteration error at iteration m. At iteration m_f, we want to ensure that such error is less than a *specified* small tolerance ϵ_{iter}; therefore, from (E.9), the iterative procedure (3.34)–(3.38) is stopped at m_f if

$$(\underline{r}^{m_f^T} \underline{\mathbf{M}}^{-1} \underline{r}^{m_f})^{\frac{1}{2}} < \varrho_{min}^{1/2} \epsilon_{iter} . \tag{E.10}$$

Due to the Rayleigh quotient, we can conservatively replace ϱ_{min} in (E.10) with the corresponding continuous quantity; in practice, a non–rigorous (necessarily conservative) but good estimate for ϱ_{min} is

$$\varrho_{min} \approx \frac{\pi^2}{S_D^2} , \tag{E.11}$$

where S_D is an appropriate scale for the domain size. Also, we can typically approximate $\underline{\mathbf{M}}^{-1} \underline{r}^m$ by

$$\underline{\mathbf{M}}^{-1} \underline{r}^m \approx \sum_{i=1}^{N_{dof}} \frac{r_i^m}{\tilde{M}_i} , \tag{E.12}$$

where r_i^m is the i^{th} component of $\underline{r}^m$, $i = 1, \ldots, N_{dof}$; the denominator in (E.12) denotes an entry of a normalized, "lumped" (one–column) mass matrix $\underline{\tilde{\mathbf{M}}}$, and is given by

$$\tilde{M}_{i=i(k,j)} = \sum_k{}' \mathcal{A}^k \frac{\hat{M}_{jj}^k}{\sum_{m=1}^{3\mathcal{N}_o} \hat{M}_{mm}^k} , \tag{E.13}$$

where $i(k,j)$, $k = 1, \ldots, \mathcal{K}$, $j = 1, \ldots, 3\mathcal{N}_o$, is the global node corresponding to local node j of element k, $\mathcal{N}_o$ is the degree of the interpolants, $\mathcal{A}^k$ is the area of element k, $\hat{M}^k$ is the elemental mass matrix, $\hat{M}_{mm}^k$, $m = 1, \ldots, 3\mathcal{N}_o$, is a diagonal component of $\hat{M}^k$, and $\sum_k'$ represents the direct stiffness operation (Section 3.2.5 and Appendix

F). Notice that the denominator in (E.13) is the trace of $\hat{M}^k$. We then finally arrive, from (E.10), (E.11) and (E.12), at the practical realization of the stopping criterion: the iteration is stopped when

$$\left\{ \sum_{i=1}^{N_{dof}} \frac{(r_i^m)^2}{\tilde{M}_i} \right\}^{\frac{1}{2}} < \frac{\pi}{S_D} \epsilon_{iter} \,. \tag{E.14}$$

Clearly in our case, the appropriate scale for the domain is the V–supercell characteristic size, i.e., $S_D = \lambda^*$.

Appendix F

Parallel Direct Stiffness Summation: Implementation Details

We first describe the nomenclature. A V-supercell has one collection, col, for every inclusion, so that $col = 1, \ldots, N_c$, $N_c = N$. We denote, for collection data structures,

- a local vertex, a local edge, and an element: lv_c, ie_c, and el_c, respectively;
- total number of local vertices, local edges and elements: N_{lv}, N_{le}, and $\mathcal{K}$, respectively;
- a node corresponding to a local vertex: n_v, $n_v = 1, \ldots, N_v$, $N_v = N_{lv}$;
- total number of nodes on local edge le_{c_j}, $j = 1, \ldots, N_{le}$: $N_{e,j}$;
- a node on local edge le_{c_j}: n_e, $n_e = (N_{prev} + 1), \ldots, (N_{prev} + N_{e,j})$, $N_{prev} = N_v + (\sum_{i=1}^{j-1} N_{e,i})$;
- a node of an element: n_{el}, $n_{el} = (N_{prev'} + 1), \ldots, (N_{prev'} + 3\mathcal{N}_o\mathcal{K})$, $\mathcal{N}_o = 1, 2$, $N_{prev'} = N_v + \sum_{i=1}^{N_{le}} N_{e,i}$.

Here, coincident geometrical points, at which location the value of the unknown field variable is desired, belonging to different identified collection structures, are called

nodes; they ultimately correspond to a global degree of freedom. A value for a degree of freedom is kept at all corresponding (local) nodes (i.e., at all memory locations assigned to them). Direct stiffness ensures that such value becomes global (correct) after local evaluation of the action of the appropriate operator (Section 3.1.4).

We denote, for the higher level, global data structures,

- a global vertex: gv^c ;
- a global edge: ge^u ;
- total number of global vertices and global edges: N_{gv} and N_{ge} , respectively;
- a node corresponding to a global vertex: n_{gv} , $n_{gv} = 1, \ldots, N_{gv}$;
- total number of nodes on global edge ge^u_j , $j = 1, \ldots, N_{ge}$: $N_{ge,j}$;
- a node on global edge ge^u_j : n_{ge} , $n_{ge} = 1, \ldots, N_{ge,j}$.

The superscripts c and u indicate that the data structure is, respectively, resident on all processors (thus *c*opied), and resident on one processor only (thus *u*ncopied). Notice that any unknown field variable is uncopied. Collections and global edges, since they are distributed among processors, have both local (to the processor) and global numberings, not particularly distinguished below. The collection and global data structures listed above are schematically shown in Figure F-1.

Using the geometry/topology description of the V–supercell, and of the triangulation T_h (obtained, respectively, from the domain (Section 3.1.1) and mesh (Section 3.1.2) generation steps), the following mappings, M^u, are constructed:

- M^u_1 : local vertex $lv_c \rightarrow$ global vertex gv^c ;
- M^u_2 : local edge $le_c \rightarrow$ global edge ge^u ;
- M^u_3 : global edge $ge^u \rightarrow$ local edges le_c (here, two);
- M^u_4 : global edge $ge^u \rightarrow$ collections *col* containing corresponding le_c ;

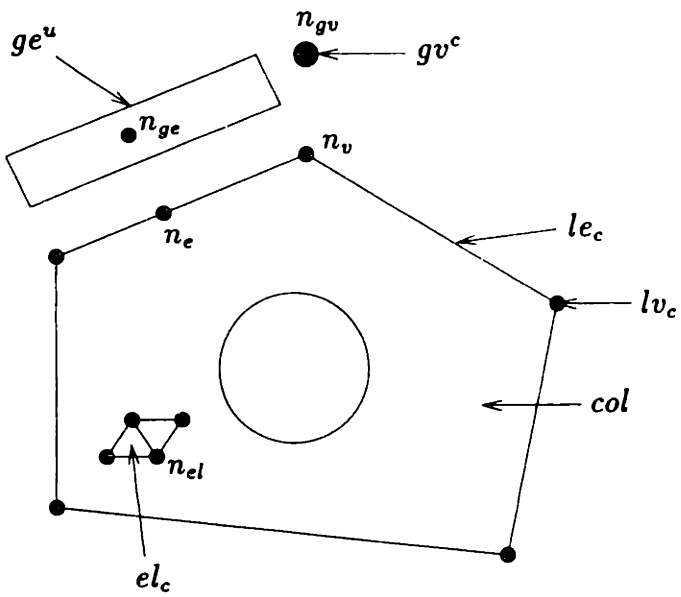

Figure F-1: Collection and global data structures.

- M_5^u : each node n_v , n_e and n_{el} $\rightarrow$ total number of other interacting nodes, N_{int} (notice, for example, that for a node n_{el} inside a collection, it interacts only with other n_{el} nodes, and N_{int} is equal to the node's multiplicity minus 1);

- M_6^u : each node n_v , n_e and n_{el} $\rightarrow$ list of the (discriminated) N_{int} interacting nodes.

Additional collection–to–processor (M_7^c) and global–edge–to–processor (M_8^c) mappings are necessary for sending and receiving edge–data–messages; they are determined from the adopted work–distribution algorithm, applied subsequently to domain partitioning. We simply distribute the collections sequentially among the processors, without particular post–partitioning attention to load balancing; the global edges are distributed, such that each lies (almost always) in one of the processors containing at least one of the two neighboring collections. Consequently, a global edge, most likely, will receive *one* set of data from another processor, corresponding to a local edge; the other set is copied (on the same processor) directly from the local edge data. We remark that the set received second by the global edge is *summed to* the first set, rather than copied over it (this sum operation is implied below).

Direct stiffness summation (DSSUM) then proceeds, *after* local evaluation of the action of the appropriate operator, as follows (where the current value of the unknown at one node, e.g. at n_v, is denoted by a capital V, e.g. V_{n_v}):

- on each processor P, zero out all V_{n_v}'s and V_{n_e}'s;
- on each processor P, perform (standard, serial-type) DSSUM on $V_{n_{el}}$'s inside resident collections, using mappings M_5^u and M_6^u;
- using mapping M_1^u, perform parallel DSSUM on local vertices:
  - on each processor P, accumulate V_{n_v}'s into corresponding $V_{n_{gv}}$'s;
  - invoke global gather–scatter to sum $V_{n_{gv}}$'s across processors, and broadcast result;
  - on each processor P, using M_1^u, M_5^u and M_6^u, redistribute $V_{n_{gv}}$'s back to "interacting" $V_{n_{el}}$'s (redistribution to V_{n_v}'s is unnecessary);
- finally, perform parallel DSSUM on local edges:
  - accumulate local edges le_c's into corresponding global edges ge^u's, using M_2^u; on each processor P,

```
loop over col's, and over le_c's
      pack data: V_{n_e}'s
      find target processor, P_tar, from M_2^u and M_8^c
      communicate: send data to P_tar (or copy if P=P_tar)
      loop over resident ge^u's
            check for incoming V_{n_e}-message
            receive V_{n_e}-message, if arrived
            copy to V_{n_ge}'s
      endloop
endloop, endloop
synchronize processors
loop over resident ge^u's twice
```

(a ge^u can potentially receive two V_{n_e}-messages)

receive *all* previously sent, pending V_{n_e}-messages

endloop;

- redistribute global edges ge^u's to respective local edges le_c's, using M_3^u, M_4^u; on each processor P,

loop over ge^u's, and over number of corresponding le_c's (here, two)

pack data: $V_{n_{ge}}$'s

find target processor, P_{tar}, from M_3^u, M_4^u, and M_7^u

communicate: send data to P_{tar}

(or redistribute, as below, if $P=P_{tar}$)

loop over *col*'s, and over le_c's

check for incoming $V_{n_{ge}}$-message

receive incoming $V_{n_{ge}}$-message, if arrived

flag receipt (caution: a le_c can receive *only one* $V_{n_{ge}}$-message)

redistribute $V_{n_{ge}}$'s, using M_5^u and M_6^u, down to "interacting" $V_{n_{el}}$'s (redistribution down to V_{n_e}'s is unnecessary)

endloop, endloop

endloop, endloop

synchronize processors

loop over *col*'s, and over le_c's again

receive all *all* previously sent, pending $V_{n_{ge}}$-messages

endloop.

Figure F-2 schematically shows the "role hierarchy" of the various collection and global data structures in the above parallel direct stiffness summation procedure. Finally, one last detail: when numbering the n_e's, one chooses a direction around the collections, e.g. counterclockwise; therefore, care is needed in accumulating and redistributing the V_{n_e}'s / $V_{n_{ge}}$'s to ensure that the sums/assignments occur in the proper node order. Sending global, "hidden", tags together with the edge-data is one possible solution, adopted here.

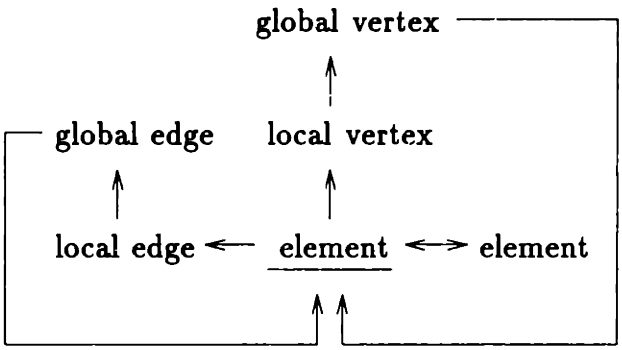

Figure F-2: "Hierarchy" of collection and global data structures.

Appendix G

Random Number Generation

In this Appendix, we first provide some background on random numbers (Section G.1) and on the linear congruential algorithm (Section G.2); next, we report the actual random number generator used, as well as the shuffling routine that was coupled to it, in order to avoid sequential correlation on pairing (Section G.3). Lastly, we present the results of the chi-square and Kolmogorov-Smirnov goodness-of-fit tests that were conducted, to evaluate the combined generator-shuffling statistical performance (Section G.4).

G.1 Random Numbers

Random numbers can be defined as a sequence of numbers in some interval, typically [0,1), having some probability density function, usually taken as the uniform distribution. They are, in fact, random variables associated with random events (e.g, if we record the number of cars crossing the Harvard Bridge every day (events), we will end up with a sequence of random integers). When the sequence of numbers is deterministic, they are called pseudo-random numbers. The key idea is that, although they are generated in a well specified manner, they appear, for all statistical purposes, random.

The generation of (pseudo-)random numbers is very important in a variety of applications [Knuth (1969)]: simulation of stochastic natural phenomena (radioactive

decay is probably the most obvious example), sampling from a distribution (*as in this thesis*, or in the study of random walks), numerical analysis (Monte–Carlo integration (*also in this thesis*), Buffon's needle problem), and computer programming (testing of algorithms, e.g. sorting). In all such applications, the deterministic rule for the generation of numbers should have no meaningful interpretation in the context of the problem being analysed.

A number of procedures and algorithms have been devised to generate random numbers, for example, various machines in games of chance, RAND Corporation's table of one million random digits, and Von Neumann's "middle–square method". Many of these suffer from serious practical problems, such as portability, ease of use, non–reproducibility, short cyclic periods etc. The most successful, well-accepted, and common pseudo–random number generators in use today are based on the linear congruential method, which we briefly describe below (using notation specific to this Appendix).

G.2 Linear Congruential Generators

Linear congruential generators are based on the following fundamental congruence relationship:

$$X_{n+1} = (aX_n + c) \; mod \; m \,, \quad n \geq 0 \,, \tag{G.1}$$

where all numbers are nonnegative integers, a, $a > 0$, is the multiplier, c, $c \geq 0$, is the increment, m, $m > X_0$, $m > a$, $m > c$, is the modulus, and X_0, $X_0 \geq 0$, is the starting value of the sequence, also called the *seed*. A real random number in [0,1) is obtained by dividing X_n by m.

The special case $c = 0$ corresponds to multiplicative generators, which are faster than mixed generators ($c \neq 0$). The sequences generated by (G.1) are cyclic, with period $P_g \leq m$. In practical applications, m should be as large as possible, so as to allow generation of "many" numbers, and also to avoid introduction of bias in the sequence, by confining the numbers to a small set. An obvious limit for m, which turns out to be computationally efficient, is the maximum integer that can be represented

by the word size of the machine being used.

Much theoretical work has been done on such generators [Knuth (1969), Rubinstein (1981)], and perhaps this is why they are so successful (and probably vice–versa). The proper choice of a, c, and m is not arbitrary. For example, in order to achieve $P_g = m$, c cannot be zero. As shown in Knuth (1969), $P_g = m$ is achieved if and only if

1. c is relatively prime to m;

2. $(a-1)$ is a multiple of p, for every prime p dividing m;

3. $(a-1)$ is a multiple of 4, if m is a multiple of 4.

G.3 Description of Tests

In this thesis, we used the system supplied linear congruential generator for the Stardent 3000 machine [Stardent (1990)], which has the following characteristics:

$$m = 2^{48}\,, \tag{G.2}$$

$$a = \text{'}273673163155\text{'O} \approx 2.5214903 \cdot 10^{10}\,, \tag{G.3}$$

and

$$c = \text{'}13\text{'O} = 11\,, \tag{G.4}$$

where "O" means octal system. Notice that conditions 1, 2, and 3 of Section G.2 are satisfied by (G.2)–(G.4), so that the generator has full period. The generator is implemented as a FORTRAN library routine named "ERAND48", which works with special 48–bit integer arithmetic, and generates double precision uniform random deviates in [0,1).

The particular implementation used of the Bays and Durham shuffling algorithm, was subroutine RAN0 from Press, Flannery, Teukolsky & Vetterling (1989). Essentially, an auxiliary array is first initialized with (ERAND48–generated) random

numbers. Next, on each call of the generator, the random number stored in a pointer is used to choose a random element in this auxiliary array; the element becomes the actual output random number, and also the new pointer. The element's entry in the array is refilled by the invoked system routine. The coupling ERAND48–RAN0 then generates, successively, one random number per call.

We are interested in generating inclusion centers $\mathbf{y}_i$, $i = 1, \ldots, N$, uniformly distributed in the region $\Omega_{sc} \in \mathcal{R}^2$ (plus no–overlapping constraint). The output numbers of two successive calls to ERAND48–RAN0 are then paired to form the random pair $\mathbf{Y}_p = (Y_{p,1}, Y_{p,2})$, which will be checked for acceptance by the algorithm described in Section 3.2.1. Consequently, we test our generator coupling against the following (desired) two–dimensional probability density function:

$$P_{\mathbf{Y}_p}(\mathbf{y}_p) = \begin{cases} 1 & \text{in } [0,1) \times [0.1)\,, \\ 0 & \text{elsewhere}\,. \end{cases} \tag{G.5}$$

The corresponding cumulative distribution function, $F_{\mathbf{Y}_p}(\mathbf{y}_p)$, is given by

$$F_{\mathbf{Y}_p}(\mathbf{y}_p) = Pr(Y_{p,1} \leq y_{p,1}\,, Y_{p,2} \leq y_{p,2}) = y_{p,1}\, y_{p,2}\,, \tag{G.6}$$

where $Pr(E)$ is the probability that event E happens, and $(y_{p,1}\,, y_{p,2}) \in \{[0,1)\}^2$. We perform two standard statistical tests: the chi–square and the Kolmogorov–Smirnov goodness–of–fit tests [see e.g. Knuth (1969) and Daniel (1990)].

The chi–square test is a hypothesis test which assesses the null hypothesis that the sample under consideration (here, pairs $\mathbf{Y}_p$'s) has been drawn from a specified distribution (here, $F_{\mathbf{Y}_p}(\mathbf{y}_p)$). The chi–square test is based on a comparison of expected and observed frequencies (see statistic V below). The Kolmogorov–Smirnov test assesses the null hypothesis that two cumulative distribution functions, the hypothesized (here, $F_{\mathbf{Y}_p}(\mathbf{y}_p)$) and the actual (here, the one from which ERAND48–RAN0 samples from), are equal; the test is based on the so–called Kolmogorov statistic, D (see below), which measures the maximum absolute difference between the two distributions being compared.

For the chi-square tests, the unit box $\{[0,1)\}^2$ is first partitioned into $N_{bin} = n_{bin}^2$ square, labelled bins, each of edge-length $\frac{1}{n_{bin}}$. Next, a large number of independent observations, M_{chi}, are made, which consist in generating pseudo-random pairs $\mathbf{Y}_p$, and determining in which bin each pair falls; N_{bin} thus corresponds to the number of different categories to which $\mathbf{Y}_p$ may belong. The following statistic is then computed [Knuth (1969)],

$$V = \frac{1}{M_{chi}} \sum_{k=1}^{N_{bin}} \frac{V_k^2}{p_k} - M_{chi} , \tag{G.7}$$

where p_k is the expected (normalized) frequency, i.e., the probability that each observation falls into category (or bin) k, and V_k is the observed frequency, i.e., the actual number of observations that fall into category k. Notice that, from (G.5),

$$p_k = \frac{1}{N_{bin}} , \quad k = 1, \ldots, M_{chi} . \tag{G.8}$$

The statistic V is distributed, for $M_{chi} \rightarrow \infty$, as the chi-square distribution with $(N_{bin} - 1)$ degrees of freedom. The computed value of V for a given (N_{bin}, M_{chi}, p_k) test may then be assigned a confidence level, by looking up tabulated values for such distribution. In order to ensure the asymptotic properties of V, it is recommended that $M_{chi}\, p_k > 5$.

For the Kolmogorov-Smirnov tests, we make M_{KS} independent observations of the random pair $\mathbf{Y}_p$ (i.e., we generate M_{KS} successive $\mathbf{Y}_p$'s). We then compute the empirical distribution function $F^e_{\mathbf{Y}_p}(\mathbf{y}_p)$ at the sampled values $\mathbf{y}_p^j$, $j = 1, \ldots, M_{KS}$, of $\mathbf{Y}_p$:

$$F^e_{\mathbf{Y}_p}(\mathbf{y}_p^j) = \frac{N_{KS}^j(\mathbf{Y}_p)}{M_{KS}} , \tag{G.9}$$

where $N_{KS}^j(\mathbf{Y}_p)$, $j = 1, \ldots, M_{KS}$, is the number of *observed* pairs $\mathbf{Y}_p$ such that

$$Y_{p,1} \leq y_{p,1}^j \quad \text{and} \quad Y_{p,2} \leq y_{p,2}^j . \tag{G.10}$$

The Kolmogorov-Smirnov test (here, two-sided) is based on the D statistic [Daniel

(1990)], estimated here by

$$D \approx \max_{1 \le j \le M_{KS}} | F^e_{\mathbf{Y}_p}(\mathbf{y}_p^j) - F_{\mathbf{Y}_p}(\mathbf{y}_p^j) | , \tag{G.11}$$

where $F_{\mathbf{Y}_p}(\mathbf{y}_p^j)$ is obtained from (G.5). Notice that the exact value of D is the maximum over all possible values of $\mathbf{Y}_p$, i.e., over all $\mathbf{y}_p \in \{[0,1)\}^2$. The estimate (G.11) improves as M_{KS} increases. Values for the D statistic distribution are also tabulated, and confidence levels may therefore be assigned.

G.4 Results of Tests

The results of the tests are summarized below. The total CPU time to run the tests, on the Stardent 3000 computer, was about fourteen hours (the sorting algorithm used to compute values of $F^e_{\mathbf{Y}_p}(\mathbf{y}_p)$ in (G.9) was $O(M_{KS}^2)$). In what follows, for definiteness, a test is considered passed if the value of the appropriate statistic has probability between 10% and 90% of happening.

Chi–square We conducted tests with N_{bin} ranging from 4 to 40000, in order to test for both local and global randomness. The number of observations for each N_{bin}, given the recommendation in Section G.3 and equation (G.8), was set to $20N_{bin}$. Individual tests for $N_{bin} \in \{4, 100, 2500, 10000, 40000\}$ were all passed. More importantly, however, out of 1000 tests that were performed for $N_{bin} \in \{100, 2500\}$, 82.1% and 80.3%, respectively, passed. These results are consistent with the confidence level band $10\% - 90\%$. Notice that, for all individual tests, we had

$$1 \ll M_{chi} \ll m , \tag{G.12}$$

and also, for the multiple tests,

$$1 \ll 1000\, M_{chi} \ll m , \tag{G.13}$$

where $m = 2^{48} \approx 10^{14}$ is given in (G.2); (G.12) and (G.13) should both hold, so the samples appear to stem from an infinite set.

Kolmogorov–Smirnov Again with the purpose of testing both local and global randomness, individual tests with M_{KS} ranging from 2 to 200000 were performed, and the vast majority passed. Notice that 200000 was usually well above the total number of random pairs generated for a typical Level–2 calculation. More importantly, since the number of inclusions N is in the range 1–50, for $M_{KS} \in \{2, 5, 10, 20, 30, 40, 50, 60\}$, out of 1000 tests, 83.4%, 84.3%, 84.1%, 81.3%, 80.0%, 77.0%, 78.1% and 76.9%, respectively, passed.

Conclusion We conclude, based on the above quantitative statistical results, that the ERAND48–RAN0 coupling is satisfactory for generating random pairs $\mathbf{Y}_p$ uniformly distributed in $\{[0, 1)\}^2$. This conclusion is not at all surprising, given the large, full period of ERAND48 (in general, $m \approx 2^{32}$, as opposed to 2^{48}).

Bibliography

[1] A. Acrivos and E. Chang (1986), "A model for estimating transport quantities in two–phase materials," *Phys. Fluids*, **29**:3-4.

[2] A. Acrivos and E. S. G. Shaqfeh (1988), "The effective thermal conductivity and elongational viscosity of a nondilute suspension of aligned slender rods," *Phys. Fluids*, **31**:1841-1844.

[3] P. M. Adler (1992), *Porous Media: Geometry and Transports*, Butterworth–Heinemann, Boston, Massachusetts.

[4] G. Anagnostou, Y. Maday, C. Mavriplis and A. T. Patera (1990), "On the mortar element method: Generalizations and Implementation." In *Domain Decomposition Methods for Partial Differential Equations*, T. F. Chan, R. Glowinski, J. Periaux and O. B. Widlund (eds.), SIAM, Philadelphia.

[5] J.-L. Auriault (1983), "Effective Macroscopic Description for Heat Conduction in Periodic Composites," *Int. J. Heat Mass Transfer*, **26**:861-869.

[6] I. Babuška (1975), "Homogenization and Its Application. Mathematical and Computational Problems," *Technical Note BN-821*, University of Maryland, Maryland.

[7] G. K. Batchelor (1967), *An Introduction to Fluid Dynamics*, Cambridge University Press, Cambridge, Great Britain.

[8] G. K. Batchelor (1972), "Sedimentation in a dilute dispersion of spheres," *J. Fluid Mech.*, **52**:245-268.

[9] G. K. Batchelor (1974), "Transport Properties of Two–Phase Materials with Random Structure," *Ann. Rev. Fluid Mech.*, **6**:227-255.

[10] E. Behrens (1968), "Thermal Conductivities of Composite Materials," *J. Composite Materials*, **2**:2-17.

[11] M. P. Bendsøe and N. Kikuchi (1988), "Generating Optimal Topologies in Structural Design Using a Homogenization Method," *Comput. Methods Appl. Mech. Eng.*, **71**:197-224.

[12] A. Bensoussan, J.-L. Lions and G. C. Papanicolaou (1978), *Asymptotic Analysis for Periodic Structures*, North–Holland, Amsterdan.

[13] A. Bensoussan, J.-L. Lions and G. C. Papanicolaou (1979), "Boundary Layers and Homogenization of Transport Processes," *Publ. RIMS, Kyoto Univ.*, **15**:53-157.

[14] M. J. Beran (1965), "Use of the Variational Approach to Determine Bounds for the Effective Permittivity in Random Media," *Nuovo Cimento*, **38**:771-782.

[15] M. J. Beran (1968), *Statistical Continuum Theories*, Interscience Publishers, New York.

[16] J. G. Berryman (1983), "Random close packing of hard spheres and disks," *Phys. Rev. A*, **27**:1053-1061.

[17] J. G. Berryman and G. W. Milton (1985), "Normalization constraint for variational bounds on fluid permeability," *J. Chem. Phys.*, **83**:754-760.

[18] J. F. Brady and G. Bossis (1985), "The rheology of concentrated suspensions of spheres in simple shear flow by numerical simulation," *J. Fluid Mech.*, **155**:105-129.

[19] J. F. Brady and G. Bossis (1988), "Stokesian Dynamics," *Ann. Rev. Fluid Mech.*, **20**:111-157.

[20] H. C. Brinkman (1947), "A Calculation of the Viscous Force Exerted by a Flowing Fluid on a Dense Swarm of Particles," *Appl. Sci. Res.*, A**1**:27-34.

[21] P. C. Carman (1937), "Fluid Flow Through Granular Beds," *Trans. Inst. Chem. Eng.*, **15**:150-166.

[22] L. K. Chau and P. D. Chinh (1991), "On bounding the effective conductivity of isotropic composite materials," *J. Appl. Math. Phys. (ZAMP)*, **42**:614-622.

[23] S. Childress (1972), "Viscous Flow Past a Random Array of Spheres," *J. Chem. Phys.*, **56**:2527-2539.

[24] R. Clift, J. R. Grace and M. E. Weber (1978), *Bubbles, Drops, and Particles*, Academic Press, San Diego, California.

[25] P. B. Corson (1974), "Correlation functions for predicting properties of heterogeneous materials. IV. Effective thermal conductivity of two-phase solids," *J. Appl. Phys.*, **45**:3180-3182.

[26] F. E. Curry and C. C. Michel (1980), "A Fiber Matrix Model of Capillary Permeability," *Microvascular Research*, **20**:96-99.

[27] W. W. Daniel (1990), *Applied Nonparametric Statistics*, 2nd. edition, PWS-KENT Publishing Company, Boston.

[28] C. N. Davies (1952), "The Separation of Airborne Dust and Particles," *Inst. Mech. Eng., Proc.*, 1B:185-198.

[29] C. N. Davies (1973), *Air Filtration*, Academic Press, London.

[30] D. A. Edwards, M. Shapiro, P. Bar-Yoseph and M. Shapira (1990), "The influence of Reynolds number upon the apparent permeability of spatially periodic arrays of cylinders," *Phys. Fluids A*, **2**:45-55.

[31] H. G. Elrod (1974), "Two Simple Theorems for Establishing Bounds on the Total Heat Flow in Steady-State Heat-Conduction Problems with Convective Boundary Conditions," *Trans. ASME, J. Heat Transfer*, **96**:65-70.

[32] P. F. Fischer (1989), *Spectral Element Solution of the Navier-Stokes Equations on High Performance Distributed-Memory Parallel Processors*, Ph.D. Thesis, Massachusetts Institute of Technology.

[33] P. F. Fischer and A. T. Patera (1991), "Parallel Spectral Element Solution of the Stokes Problem," *J. Comput. Phys.*, **92**:380-421.

[34] B. R. Gebart (1992), "Permeability of Unidirectional Reinforcements for RTM," *J. Composite Materials*, **26**:1190-1133.

[35] C. K. Ghaddar (1994), Ph.D. Thesis, Massachusetts Institute of Technology, in progress.

[36] V. Girault and P.-A. Raviart (1986), *Finite Element Methods for Navier-Stokes Equations: Theory and Algorithms*, Springer-Verlag, Berlin.

[37] G. H. Golub and C. F. Van Loan (1989), *Matrix Computations*, 2nd. edition, The Johns Hopkins University Press, Baltimore, Maryland.

[38] M. D. Gunzburger (1989), *Finite Element Methods for Viscous Incompressible Flows: A Guide to Theory, Practice, and Algorithms*, Academic Press, San Diego, California.

[39] L. S. Han and A. A. Cosner (1981), "Effective Thermal Conductivities of Fibrous Composites," *Trans. ASME, J. Heat Transfer*, **103**:387-392.

[40] J. Happel (1959), "Viscous Flow Relative to Arrays of Cylinders," *AIChE J.*, **5**:174-177.

[41] J. Happel and H. Brenner (1983), *Low Reynolds Number Hydrodynamics*, Martinus Nijhoff, The Hague.

[42] Z. Hashin (1970), "Theory of Composite Materials." In *Mechanics of Composite Materials*, F. W. Wendt, H. Liebowitz & N. Perrone (eds.), pp. 201-242, Pergamon Press, New York.

[43] Z. Hashin (1983), "Analysis of Composite Materials — A Survey," *Trans. ASME, J. Applied Mechanics*, **50**:481-505.

[44] Z. Hashin and S. Shtrikman (1962), "A Variational Approach to the Theory of the Effective Magnetic Permeability of Multiphase Materials," *J. Appl. Phys.*, **33**:3125-3131.

[45] H. Hasimoto (1959), "On the periodic fundamental solutions of the Stokes equations and their application to viscous flow past a cubic array of spheres," *J. Fluid Mech.*, **5**:317-328.

[46] D. P. H. Hasselman (1993), *Private communication.*

[47] D. P. H. Hasselman, H. Bhatt, K. Y. Donaldson and J. R. Thomas, Jr. (1992), "Effect of Fiber Orientation and Sample Geometry on the Effective Thermal Conductivity of a Uniaxial Carbon Fiber–Reinforced Glass Matrix Composite," *J. Composite Materials*, **26**:2278-2288.

[48] F. Hecht and E. Saltel (1990), "Emc2: Editeur de maillages et de contours bidimensionnels," Manuel d'utilisation, Rapport Technique No. 118, INRIA.

[49] R. Hill and G. Power (1956), "Extremum Principles for Slow Viscous Flow and the Approximate Calculation of Drag," *Quart. J. Mech. Appl. Math.*, **9**:313-319.

[50] H. H. Hu, D. D. Joseph and M. J. Crochet (1992), "Direct Simulation of Fluid Particle Motions," *Theoret. Comput. Fluid Dynamics*, **3**:285-306.

[51] S. J. Karrila, Y. O. Fuentes and S. Kim (1989), "Parallel Computational Strategies for Hydrodynamic Interactions Between Rigid Particles of Arbitrary Shape in a Viscous Fluid," *J. Rheol.*, **33**:913-947.

[52] J. B. Keller (1964), "A Theorem on the Conductivity of a Composite Medium," *J. Math. Phys.*, **5**:548-549.

[53] J. B. Keller (1980), "Darcy's Law for Flow in Porous Media and the Two-Space Method." In *Nonlinear Partial Differential Equations in Engineering and*

Applied Science, R. L. Sternberg, A. J. Kalinowski & J. S. Papadakis (eds.), pp. 429-443, Proceedings of a Conference Sponsored by ONR, Univ. of Rhode Island, Rhode Island.

[54] J. B. Keller, L. A. Rubenfeld and J. E. Molyneux (1967), "Extremum principles for slow viscous flows with applications to suspensions," *J. Fluid Mech.*, **30**:97-125.

[55] A. Kelly (1987), "Composites for the 1990s," *Phil. Trans. R. Soc. Lond.*, A**322**:409-423.

[56] J. J. Kibler (1991), "Integration of Theoretical and Practical Micro Mechanics Procedures into the Design and Analysis of Composite Materials." In *Composites: Design, Manufacture, and Application*, S. W. Tsai and G. S. Springer (eds.), pp. 1R1-1R12, Proceedings of the Eighth International Conference on Composite Materials, Honolulu.

[57] N. Kikuchi (1986), *Finite element methods in mechanics*, Cambridge University Press, Cambridge.

[58] S. Kim and S. J. Karrila (1991), *Microhydrodynamics: Principles and Selected Applications*, Butterworth–Heinemann, Boston, Massachusetts.

[59] S. Kim and R. T. Mifflin (1985), "The resistance and mobility functions of two equal spheres in low–Reynolds–number flow," *Phys. Fluids*, **28**:2033-2045.

[60] D. E. Knuth (1969), *The Art of Computer Programming: Seminumerical Algorithms*, Vol. 2, Addison–Wesley, Reading, Massachusetts.

[61] A. J. C. Ladd (1990), "Hydrodynamic transport coefficients of random dispersions of hard spheres," *J. Chem. Phys.*, **93**:3484-3494.

[62] E. W. Larsen (1975), "Neutron transport and diffusion in inhomogeneous media. I," *J. Math. Phys.*, **16**:1421-1427.

[63] J. R. Levick (1987), "Flow Through Interstitium and Other Fibrous Matrices," *Quarterly Journal of Experimental Physiology*, **72**:409-438.

[64] Y. Maday, D. Meiron, A. T. Patera and E. M. Rønquist (1993), "Analysis of Iterative Methods for the Steady and Unsteady Stokes Problem: Application to Spectral Element Discretizations," *SIAM J. Sci. Comput.*, **14**:310-337.

[65] Y. Maday and A. T. Patera (1993), "A General Estimate for the Thermal Time-to-Steady-State for a Solid Body Suddenly Immersed in a Fluid Stream," *Int. J. Heat Mass Transfer*, to appear.

[66] M. Magen, B. B. Mikiç and A. T. Patera (1988), "Bounds for conduction and forced convection heat transfer," *Int. J. Heat Mass Transfer*, **31**:1747-1757.

[67] P. K. Mallick (1988), *Fiber-Reinforced Composites: Materials, Manufacturing, and Design*, Marcel Dekker, Inc., New York.

[68] R. C. McPhedran and D. R. McKenzie (1978), "The conductivity of lattices of spheres I. The simple cubic lattice," *Proc. R. Soc. Lond.*, A**359**:45-63.

[69] R. C. McPhedran and G. W. Milton (1981), "Bounds and Exact Theories for the Transport Properties of Inhomogeneous Media," *Appl. Phys.*, A**26**:207-220.

[70] C. C. Mei and J.-L. Auriault (1989), "Mechanics of heterogeneous porous media with several spatial scales," *Proc. R. Soc. Lond.*, A**426**:391-423.

[71] C. C. Mei and J.-L. Auriault (1991), "The effect of weak inertia on flow through a porous medium," *J. Fluid Mech.*, **222**:647-663.

[72] K. S. Mendelson (1975), "Effective conductivity of two-phase material with cylindrical phase boundaries," *J. Appl. Phys.*, **46**:917-918.

[73] G. W. Milton (1981), "Bounds on the Electromagnetic, Elastic, and Other Properties of Two-Component Composites," *Phys. Rev. Lett.*, **46**:542-545.

[74] A. M. Mood, F. A. Graybill and D. C. Boes (1974), *Introduction to the Theory of Statistics*, 3rd. edition, McGraw-Hill, New York.

[75] J. von Neumann (1951), "Various techniques used in connection with random digits," *U. S. Nat. Bur. Stand. Appl. Math. Ser.*, **12**:36-38.

[76] A. Nir, H. F. Weinberger and A. Acrivos (1975), "Variational inequalities for a body in a viscous shearing flow," *J. Fluid Mech.*, **68**:739-755.

[77] W. T. Perrins, D. R. McKenzie and R. C. McPhedran (1979), "Transport properties of regular arrays of cylinders," *Proc. R. Soc. Lond.*, A**369**:207-225.

[78] R. Pitchumani and S. C. Yao (1991), "Correlation of Thermal Conductivities of Unidirectional Fibrous Composites Using Local Fractal Techniques," *Trans. ASME, J. Heat Transfer*, **113**:788-796.

[79] R. Pitchumani and S. C. Yao (1992), "Evaluation of transverse thermal diffusivity of unidirectional fiber–reinforced composites," *Int. J. Heat Mass Transfer*, **35**:2185-2194.

[80] S. Prager (1961), "Viscous Flow through Porous Media," *Phys. Fluids*, **4**:1477-1482.

[81] F. P. Preparata and M. I. Shamos (1988), *Computational Geometry: An Introduction*, 2nd. printing, Springer–Verlag, New York.

[82] W. H. Press, B. P. Flannery, S. A. Teukolsky and W. T. Vetterling (1989), *Numerical Recipes: The Art of Scientific Computing (FORTRAN Version)*, Cambridge University Press, Cambridge.

[83] Lord Rayleigh (1892), "On the Influence of Obstacles arranged in Rectangular Order upon the Properties of a Medium," *Phil. Mag.*, **34**:481-502.

[84] G. J. Rodin and Y.-L. Hwang (1990), "The Overall Elastic Response of Materials Containing Spherical Inhomogeneities," submitted to *Proc. R. Soc. Lond.*, A.

[85] E. M. Rønquist (1988), *Optimal Spectral Element Methods for the Unsteady Three-Dimensional Incompressible Navier-Stokes Equations*, Ph.D. Thesis, Massachusetts Institute of Technology.

[86] R. Y. Rubinstein (1981), *Simulation and the Monte Carlo Method*, John Wiley & Sons, New York.

[87] J. Rubinstein and S. Torquato (1989), "Flow in random porous media: mathematical formulation, variational principles, and rigorous bounds," *J. Fluid Mech.*, **206**:25-46.

[88] P. G. Saffman (1973), "On the Settling Speed of Free and Fixed Suspensions," *Stud. Appl. Math.*, **52**:115-127.

[89] A. S. Sangani and A. Acrivos (1982a), "Slow Flow Past Periodic Arrays of Cylinders with Application to Heat Transfer," *Int. J. Multiphase Flow*, **8**:193-206.

[90] A. S. Sangani and A. Acrivos (1982b), "Slow Flow Through a Periodic Array of Spheres," *Int. J. Multiphase Flow*, **8**:343-360.

[91] A. S. Sangani and C. Yao (1988a), "Transport processes in random arrays of cylinders. I. Thermal conduction," *Phys. Fluids*, **31**:2426-2434.

[92] A. S. Sangani and C. Yao (1988b), "Transport processes in random arrays of cylinders. II. Viscous flow," *Phys. Fluids*, **31**:2435-2444.

[93] A. E. Scheidegger (1974), *The physics of flow through porous media*, 3rd. edition, University of Toronto Press, Toronto.

[94] M. Shapiro and H. Brenner (1990), "Dispersion/Reaction Model of Aerosol Filtration by Porous Filters," *J. Aerosol Sci.*, **21**:97-125.

[95] R. A. P. Spencer (1983), "Developments in Pultrusion." In *Developments in GRP Technology - 1*, B. Harris (ed.), pp. 1-36, Applied Science Publishers, London.

[96] L. Spielman and S. L. Goren (1968), "Model for Predicting Pressure Drop and Filtration Efficiency in Fibrous Media," *Environ. Sci. Technol.*, **2**:279-287.

[97] G. S. Springer and S. W. Tsai (1967), "Thermal Conductivities of Unidirectional Materials," *J. Composite Materials*, **1**:166-173.

[98] Stardent Computer Inc. (1990), *Fortran Reference Manual*, Sunnyvale, California.

[99] G. Strang and G. J. Fix (1973), *An Analysis of the Finite Element Method*, Prentice–Hall, Englewood Cliffs, New Jersey.

[100] K. Sugihara and M. Iri (1989a), "VORONOI2 Reference Manual: Topology–Oriented Version of the Incremental Method for Constructing Voronoi Diagrams," *Research Memorandum RMI 89-04*, Department of Mathematical Engineering and Information Physics, University of Tokyo.

[101] K. Sugihara and M. Iri (1989b), "Construction of the Voronoi Diagram for One Million Generators in Single–Precision Arithmetic," *Research Memorandum RMI 89-05*, Department of Mathematical Engineering and Information Physics, University of Tokyo.

[102] S. Torquato and F. Lado (1988), "Bounds on the conductivity of a random array of cylinders," *Proc. R. Soc. Lond.*, A**417**:59-80.

[103] S. Torquato and G. Stell (1982), "Microstructure of two–phase random media. I. The n–point probability functions," *J. Chem. Phys.*, **77**:2071-2077.

[104] D. Y. Tzou (1991), "A Universal Model for the Overall Thermal Conductivity of Porous Media," *J. Composite Materials*, **25**:1064-1084.

[105] H. L. Weissberg and S. Prager (1970), "Viscous Flow through Porous Media. III. Upper Bounds on the Permeability for a Simple Random Geometry," *Phys. Fluids*, **13**:2958-2965.

[106] P. H. Winterfeld, L. E. Scriven and H. T. Davis (1981), "Percolation and conductivity of random two–dimensional composites," *J. Phys. C: Solid State Phys.*, **14**:2361-2376.

[107] S. Yeşilyurt and A. T. Patera (1993), "Statistical Modelling Methods for Deterministic Computational Systems," *J. Comput. Phys.*, submitted.